8-1-2023

Magmatic Processes Leading to Compositional Diversity in the Mars Crust

Amanda Marie Ostwald
University of Nevada, Las Vegas

MAGMATIC PROCESSES LEADING TO COMPOSITIONAL DIVERSITY IN THE MARS CRUST

By

Amanda Marie Ostwald

Bachelor of Science – Geoscience
University of Texas at El Paso
2017

A dissertation submitted in partial fulfillment
of the requirements for the

Doctor of Philosophy – Geoscience

Department of Geoscience
College of Sciences
The Graduate College

University of Nevada, Las Vegas
August 2023

UNLV | GRADUATE COLLEGE

Dissertation Approval

The Graduate College
The University of Nevada, Las Vegas

August 1, 2023

This dissertation prepared by

Amanda Marie Ostwald

entitled

Magmatic Processes Leading to Compositional Diversity in the Mars Crust

is approved in partial fulfillment of the requirements for the degree of

Doctor of Philosophy – Geoscience
Department of Geoscience

Arya Udry, Ph.D.
Committee Chair

Alyssa Crittenden, Ph.D. *Examination*
Vice Provost for Graduate Education &
Dean of the Graduate College

Shichun Huang, Ph.D.
Examination Committee Member

Elisabeth Hausrath, Ph.D.
Examination Committee Member

Andrew Martin, Ph.D.
Examination Committee Member

Aude Picard, Ph.D.
Graduate College Faculty Representative

Abstract

The ancient Mars crust can yield insights into planet formation and evolution that Earth cannot. Direct investigation of the martian surface is limited to studies on meteorites and rover-obtained analyses. The nakhlites and chassignites, two classes of martian meteorites, are together the largest suite of martian meteorites derived from a single location on the surface. As such, they present a rare opportunity to study the Mars crust in detail using samples bearing a contextual relationship. Rover studies have found a surprising amount of compositional diversity in surface materials, the formation mechanisms of which are not well-constrained. This dissertation leverages meteorites and rover analyses in order to better understand what magmatic processes contributed to the formation and compositional diversification of the martian crust.

In Chapter 1, I conducted thermodynamic modeling to model a magmatic process known as assimilation and fractional crystallization, wherein minerals are removed from the magma as they form (fractional crystallization) and the crust surrounding the magma chamber is incrementally melted and added to the bulk magma (assimilation). I found that assimilation and fractional crystallization may have contributed to early evolution of the Mars crust.

In Chapter 2, I studied melt inclusions in a representative suite of martian nakhlite and chassignite meteorites. Melt inclusions are pockets of magma entrapped in minerals as they form, and can represent an initial magmatic composition if they are entrapped early and remain unaltered. I found that nakhlite and chassignite melt inclusions record evidence of crystal storage in changing magma compositions.

In Chapter 3, I analyzed elemental patterns (called “zoning”) in nakhlite and chassignite minerals. Zoning of elements in a mineral record formation conditions such as changes in temperature and composition of the magma. I found that minerals in the nakhlites and chassignites

formed initially very rapidly, and that minerals were stored in changing magma compositions, adding to a growing body of evidence that such formation conditions are very common on Mars.

In this dissertation, I apply a variety of modeling and analytical methods to both samples and to rover analyses in order to study the formation and evolution of the Mars crust. I demonstrate that magmatic processes common on Earth (such as assimilation and fractional crystallization, magma mixing, and crystal storage) evidently contribute to the compositional diversity of the martian crust as well.

Acknowledgments

Thank you to my advisor, Arya Udry, for investing so much of her time and care and patience and attention in me. I consider myself a scientist, truly, only because of her mentorship and the myriad opportunities she granted me. Thank you to my labmates past and present: Rachel Rahib and Zoë Wilbur for showing me the ropes; Evan O'Neal for his constant help and friendship; Sierra Ramsey for her thoughtful scientific advice and delicious baked goods; and Gabriela Motta for her tireless work ethic and willingness to learn from me while I'm still just learning to teach.

Thank you to the faculty and the staff at the Geoscience Department at UNLV. I have always felt supported (even celebrated!) here, and will never forget this experience. Thank you especially to the members of my committee: Libby Hausrath, Shichun Huang, Simon Jowitt, Aude Picard, Andrew Martin, and Dennis Bazylinski. The classes I took with them, their feedback and guidance for my work, and their enthusiasm and support have made me a well-rounded professional. Thank you to the other graduate students at UNLV who are friends now, but who I hope will be colleagues in the future. Thank you, too, to the faculty at my undergraduate *alma mater* UTEP, who have kept in close touch and have continued to offer me support and opportunities all these years.

Thank you to my collaborators. To Peiyu Wu and Esteban Gazel for their help in thermodynamic modeling and grounding my findings in terrestrial realities. To Valerie Payré for her many powerful insights and statistics guidance. To Sammy Griffin for her counsel on shock effects in meteorites. To James Day for his wordsmithing and his LA-ICP-MS expertise. And to Juliane Gross for her sharing her experience and her microanalytical mastery. To all, I am fortunate for your mentorship and hope we continue to work together.

Lastly and most importantly, thank you to my family. My dog, Mira, who kept watch on late nights and kept me moving and calm during stressful days. My mother-in-law, Sharon, whose phone calls and visits kept me motivated even through a difficult deployment. And most of all, my husband Levi. Circumstances kept us apart all this time, but he ensured I never went through any of this alone. I am only able to write this dissertation with his strength, because he sees in me something I cannot not see myself. I am fortunate to be so loved.

Dedication

To Levi and to Mira.

Table of Contents

List of Tables

List of Figures

Chapter 1: Introduction

1.1 How, and Why, We Study the Martian Crust

The crust of Mars is ancient. The oldest bulk Earth crust is the continental crust, which is on average ~2 Ga (Kemp and Hawkesworth, 2003). Exposures of the oldest crust on Earth have been weathered and metamorphosed so that primary formation processes are often obscured. The southern highlands of Mars averages, in contrast, are notably older at ~3.9 Ga (Frey et al., 2002). Weathering on Mars over the last ~3.2 Ga has been globally dominated by aeolian processes and thin film formation, both of which minimize alteration of primary igneous features (e.g., Ehlmann and Edwards, 2014). The dearth of plate tectonics on Mars prevents most regional orogenic metamorphism seen in Earth rocks. Exploration of the martian surface can therefore reveal the processes that form terrestrial crusts, and those which diversify crustal compositions over spans of deep time not resolvable on Earth.

In order to define what magmatic processes played a role in the formation of the martian crust, we rely primarily on the only samples we currently have from Mars: meteorites. The origins of meteorites can be traced to their parent bodies by isotopic or other chemical analyses, particularly by shared oxygen isotopic signatures (e.g., Ali et al., 2016). Meteorites are ejected from their parent bodies when they are liberated by another impact. At the time of authorship, there are 353 identified martian meteorites ("unpaired" stones, meaning that they possibly originate from the same parent meteorite that was separated upon atmospheric entry). Martian meteorite classes, their dominant mineralogies, and their crystallization ages are detailed in Table 1.1. With outlying classes aside, there are three primary classes of martian meteorites: the shergottites, the nakhlites, and the chassignites. The shergottites, the most common type of martian meteorites, are further divided by relative trace element and isotopic enrichment (enriched, depleted, or intermediate), or

by petrologic type. Shergottites may be basaltic or gabbroic, containing pyroxene and either plagioclase or a diaplectic glass formed from plagioclase during shock metamorphism (called maskelynite) caused by ejection (Gross and Filiberto, 2014; Udry et al., 2020). The olivine-phyric shergottites are porphyritic basalts containing large olivine megacrysts (up to ~2 mm) with smaller olivine, pyroxene, and maskelynite (Balta et al., 2017; Udry et al., 2020). Lastly, shergottites may also be classified as poikilitic in reference to volumetrically abundant pyroxene poikilitically enclosing olivine chadacrysts (Combs et al., 2019; Rahib et al., 2019; Udry et al., 2020). The nakhlites are clinopyroxene-rich cumulate rocks, also containing fayalitic olivine, plagioclase, and minor phases in intercumulus glass (Treiman, 2005). The chassignites are dunites, cumulate rocks containing >90 vol.% olivine. The nakhlites and chassignites share largely overlapping crystallization (~1.3 Ga) ages and ejection ages (~11 Ma), likely because both classes originate from the same magmatic edifice on Mars (Nyquist et al., 2001; Cohen et al., 2017; Udry and Day, 2018; Udry et al., 2020). There have been 35 total identified unpaired nakhlite and chassignite stones, making the suite just 10% of all martian meteorites, but they still represent the largest suite of rocks originating from the same location on Mars (Udry and Day, 2018; Udry et al., 2020). As such, the nakhlites and chassignites present a rare opportunity to approach the study of martian magmatic processes with relative context and detail.

The Mars crust can be delineated into three major time periods, each distinguished by distinct mineralogy seen at the surface: the Noachian (>3.7 Ga, containing clay-bearing units), the Hesperian (3.7 Ga–3.1 Ga, containing sulfate-bearing units), and the Amazonian (<3.1 Ga, characterized by oxidation and low degrees of secondary alteration) (e.g., Ehlmann and Edwards, 2014). Meteorites preferentially sample younger martian terrain, likely because younger volcanic centers have a higher elevation to aid in escape from the gravitational well (Udry et al., 2020).

However, exploration of older crust by rovers has led to surprising findings concerning igneous processes. Highly alkaline and even primary mafic melts were discovered at Gusev crater by the *Spirit* rover (Squyres et al., 2004, 2007; McSween et al., 2006; Filiberto et al., 2010). Felsic (> 55 wt.% SiO_2) igneous materials were found at Gale crater by the *Curiosity* rover (Sautter et al., 2015; Cousin et al., 2017; Payré et al., 2017). Ultimately, rover findings challenge a long-standing notion that the crust of Mars was primarily tholeiitic basalt similar to that comprising the ocean floor on Earth, but the means by which such compositional diversity is achieved is not well understood.

In this dissertation, we seek to better constrain what magmatic processes play a part in the formation and diversification of the Mars crust. More specifically, we attempt to answer the following questions:

1. Can assimilation, a process by which magma partially melts and incorporates surrounding crust, lead to evolved magma compositions on Mars? Gale crater felsic (> 55 wt.% SiO_2) igneous materials were found to be chemically similar to early continental crust on Earth, and so crustal recycling was initially implicated in the required magmatic evolution (Sautter et al., 2015). Later work found that fractional crystallization (the continual removal of solid material from a cooling magma body) alone could form martian felsic materials, but only at high degrees of solid fractionation (Udry et al., 2018). The addition of assimilated crust to a fractionating magma is a common process leading to compositional evolution on Earth, but it had not been tested for Mars.
2. What were the initial magma (or "parental magma") compositions that formed the nakhlites and chassignites? While we know the two subclasses formed together on the martian surface, the relationship of the magmas that formed them is not well understood. To better constrain that magmatic relationship, we studied melt inclusions in a representative

selection of nakhlites and chassignites. Melt inclusions are pockets of magma that are entrapped in crystals as they form, and represent the initial magma composition (e.g., Schiano, 2003; Kent, 2008; Wallace et al., 2021).

3. What magmatic processes are recorded in cumulus minerals (minerals which accumulated together after emplacement) in the nakhlites and chassignites? Zoning, or shapes formed by differing distributions of elements within individual crystals, can reveal intrinsic and extrinsic magmatic conditions during mineral formation (e.g., Donaldson, 1976; Milman-Barris et al., 2008; Ubide and Kamber, 2018). I seek to constrain zoning patterns in mineral phases in a representative selection of nakhlites and chassignites in order to elucidate what magmatic and emplacement conditions formed them.

1.2 Tables

Table 1.1 Martian meteorites, ages, and dominant mineralogy†

Class	Subclass	Mineralogy	Crystallization ages
Shergottite	Gabbroic, Basaltic	Pyroxene, maskelynite or plagioclase	~150 Ma–2.4 Ga
	Poikilitic	Pyroxene enclosing olivine; olivine, pyroxene, maskelynite	
	Olivine-phyric	Olivine (up to 2 mm), pyroxene, maskelynite	
Nakhlite	–	Pyroxene, olivine, plagioclase, glass, sulfides, oxides, phosphates	~1.3 Ga
Chassignite	–	Olivine, plagioclase, orthopyroxene, phosphates	~1.3 Ga
Polymict regolith breccia	–	Variable: comprised of igneous clasts (basalt, norite, trachyandesite, gabbro, monzonite, mugearite)	~4.5 Ga
Orthopyroxenite	–	Orthopyroxene, chromite, augite, glass, apatite, olivine	~4.1 Ga

† Udry et al., 2020 and references therein

1.3 References:

Ali, A., Jabeen, I., Gregory, D., Verish, R., Banerjee, N., 2016, New triple oxygen isotope data of bulk and separated fractions from SNC meteorites: Evidence for mantle homogeneity of Mars: Meteoritics and Planetary Science, v. 51, p. 981–995.

Balta, B., Sanborn, M.E., Mayne, R.G., Wadhwa, M., McSween, H.Y., and Crossley, S.D., 2017, Northwest Africa 5790: A previously unsampled portion of the upper part of the nakhlite pile: Meteoritics and Planetary Science, v. 52, p. 36–59, doi:10.1111/maps.12744.

Cohen, B.E., Mark, D.F., Cassata, W.S., Lee, M.R., Tomkinson, T., and Smith, C.L., 2017, Taking the pulse of Mars via dating of a plume-fed volcano: Nature Communications, v. 8, doi:10.1038/s41467-017-00513-8.

Combs, L.M., Udry, A., Howarth, G.H., Righter, M., Lapen, T.J., Gross, J., Ross, D.K., Rahib, R.R., and Day, J.M.D., 2019, Petrology of the enriched poikilitic shergottite Northwest Africa 10169: Insight into the martian interior: Geochimica et Cosmochimica Acta, v. 266, p. 435–462, doi:10.1016/j.gca.2019.07.001.

Cousin, A. et al., 2017, Classification of igneous rocks analyzed by ChemCam at Gale crater, Mars: Icarus, v. 288, p. 265–283, doi:10.1016/j.icarus.2017.01.014.

Donaldson, C.H., 1976, An experimental investigation of olivine morphology: Contributions to Mineralogy and Petrology, v. 57, p. 187–213, doi:10.1007/BF00405225.

Ehlmann, B.L., and Edwards, C.S., 2014, Mineralogy of the Martian Surface: Annual Review of Earth and Planetary Sciences, v. 42, doi:10.1146/annurev-earth-060313-055024.

Filiberto, J., Dasgupta, R., Kiefer, W.S., and Treiman, A.H., 2010, High pressure, near-liquidus phase equilibria of the Home plate basalt Fastball and melting in the Martian mantle: Geophysical Research Letters, v. 37, p. 1–4, doi:10.1029/2010GL043999.

Frey, H. V., Roark, J.H., Shockey, K.M., Frey, E.L., and Sakimoto, S.E.H., 2002, Ancient lowlands on Mars: Geophysical Research Letters, v. 29, p. 22-1-22–4, doi:10.1029/2001gl013832.

Gross, J., and Filiberto, J., 2014, Granitic compositions in gabbroic martian meteorite NWA 6963 and a possible connection to felsic compositions on the martian surface, *in* 45th Lunar and Planetary Science Conference, p. #1440.

Kemp, A.I.S, and Hawkesworth, C.J., 2003, 3.11 Granitic perspectives on the generation and secular evolution of the continental crust: Treatise on Geochemistry, v. 3, p. 349–410.

Kent, A.J.R., 2008, Melt inclusions in basaltic and related volcanic rocks: Reviews in Mineralogy and Geochemistry, doi:10.2138/rmg.2008.69.8.

McSween, H.Y. et al., 2006, Alkaline volcanic rocks from the Columbia Hills, Gusev crater, Mars: Journal of Geophysical Research E: Planets, v. 111, p. 1–15, doi:10.1029/2006JE002698.

Milman-Barris, M.S., Beckett, J.R., Baker, M.B., Hofmann, A.E., Morgan, Z., Crowley, M.R., Vielzeuf, D., and Stolper, E., 2008, Zoning of phosphorus in igneous olivine: Contributions to Mineralogy and Petrology, v. 155, p. 739–765, doi:10.1007/s00410-007-0268-7.

Nyquist, L.E., Bogard, D.D., Greshake, A., and Eugster, O., 2001, Ages and geologic histories of martian meteorites: Chronology and Evolution of Mars, p. 105–164.

Payré, V. et al., 2017, Alkali trace elements in Gale crater, Mars, with ChemCam: Calibration update and geological implications: Journal of Geophysical Research: Planets, v. 122, p. 650–679, doi:10.1002/2016JE005201.

Rahib, R.R., Udry, A., Howarth, G.H., Gross, J., Paquet, M., Combs, L.M., Laczniak, D.L., and Day, J.M.D., 2019, Mantle source to near-surface emplacement of enriched and intermediate poikilitic shergottites in Mars: Geochimica et Cosmochimica Acta, v. 266, p. 463–496,

doi:10.1016/j.gca.2019.07.034.

Sautter, V. et al., 2015, In situ evidence for continental crust on early Mars: Nature Geoscience, v. 8, p. 605–609, doi:10.1038/ngeo2474.

Schiano, P., 2003, Primitive mantle magmas recorded as silicate melt inclusions in igneous minerals: Earth-Science Reviews, v. 63, p. 121–144, doi:10.1016/S0012-8252(03)00034-5.

Squyres, S.W. et al., 2007, Pyroclastic activity at home plate in Gusev crater, Mars: Science, v. 316, p. 738–742, doi:10.1126/science.1139045.

Squyres, S.W. et al., 2004, The Spirit Rover's Athena Science Investigation at Gusev Crater, Mars: Science, v. 305, p. 794–799, doi:10.1210/jcem-10-10-1361.

Treiman, A.H., 2005, The nakhlite meteorites: Augite-rich igneous rocks from Mars: Elsevier GmbH, v. 65, p. 203–270, doi:10.1016/j.chemer.2005.01.004.

Ubide, T., and Kamber, B.S., 2018, Volcanic crystals as time capsules of eruption history: Nature Communications, v. 9, doi:10.1038/s41467-017-02274-w.

Udry, A., and Day, J.M.D., 2018, 1.34 billion-year-old magmatism on Mars evaluated from the co-genetic nakhlite and chassignite meteorites: Geochimica et Cosmochimica Acta, v. 238, p. 292–315, doi:10.1016/j.gca.2018.07.006.

Udry, A., Gazel, E., and McSween, H.Y., 2018, Formation of Evolved Rocks at Gale Crater by Crystal Fractionation and Implications for Mars Crustal Composition: Journal of Geophysical Research: Planets, v. 123, p. 1525–1540, doi:10.1029/2018JE005602.

Udry, A., Howarth, G.H., Herd, C., Day, J., Lapen, T.J., and Filiberto, J., 2020, What martian meteorites reveal about the interior and surface of Mars: Earth and Space Science Open Archive, p. 55, https://doi.org/10.1002/essoar.10503123.2.

Wallace, P.J., Plank, T., Bodnar, R.J., Gaetani, G.A., and Shea, T., 2021, Olivine-hosted melt

inclusions: A microscopic perspective on a complex magmatic world: Annual Review of Earth and Planetary Sciences, v. 49, p. 465–494, doi:10.1146/annurev-earth-082420-060506.

Chapter 2: The Role of Assimilation and Fractional Crystallization in the Evolution of the Mars Crust

2.1 Copyright Disclaimer

The article citation citation and DOI is as follows:

Ostwald, A. M., Udry, A., Payré, V., Gazel, E., and Wu, P., 2022, The role of assimilation and fractional crystallization in the evolution of the Mars crust: Earth and Planetary Science Letters, v. 585, p. 117514, doi:10.1016/j.epsl.2022.117514.

2.2 Abstract

Recent findings of evolved martian crustal materials by orbiters and rovers challenged the longstanding notion of an only-tholeiitic basaltic crust. Models exploring intraplate magmatic processes like fractional crystallization show that unrealistic amounts of solid accumulation are sometimes required for the formation of martian evolved materials, including evolved materials analyzed by the *Curiosity* rover at Gale crater. Assimilation and fractional crystallization (AFC) play an important role in the diversification of magmas on Earth, but has not been explored for its

role in the generation of evolved martian crustal compositions. In this study, we conduct a series of thermodynamic AFC models using the Magma Chamber Simulator (MCS) model interfacing with the Rhyolite-MELTS algorithm to better understand the controls on assimilation and whether it contributed to the evolution of the martian crust. We find that AFC models replicate evolved Gale crater targets effectively at different pressures and water contents. AFC likely contributed to martian crustal formation, particularly evolved compositions. Higher crustal temperatures likely lead to a higher volume of evolved magmas formed by AFC processes on early (rather than modern) Mars. AFC may have also occurred during the Amazonian, especially in the fractured upper layers of crust, although in lower volume than during the Noachian.

2.3 Introduction

A not-so-mafic martian crust

The long-enduring understanding that the crust of Mars is largely comprised of mafic and ultramafic material has been challenged in recent years by observations of evolved materials from orbit (e.g., Brož et al., 2015; Christensen et al., 2005; Rogers & Nekvasil, 2015; Hewins et al., 2017), as limited-scale evolved material in martian meteorites (e.g., Gross & Filiberto, 2014; Santos et al., 2015), and with findings of surficial felsic materials (containing >55 wt.% SiO_2) via *in situ* investigations conducted by rovers (e.g., Cousin et al., 2017; Payré et al., 2020, Sautter et al., 2015). Some authors have found that felsic materials analyzed by the *Curiosity* rover at Gale crater could possibly be early continental crust akin to tonalite-trondhjemite-granodiorite (TTG) suites or icelandites on Earth (Sautter et al., 2015). Other work has determined that intraplate magmatic processes, such as fractional crystallization alone, can reproduce those felsic targets (Udry et al., 2018; Wu et al., 2021). However, resultant modeled felsic compositions derived from mafic magmas from fractional crystallization alone require large degrees of crystallization (>55%) and thus, extraction and eruption of the residual magma is likely to be slowed or stalled without intermediate processes such as volatile decompression or filter pressing (Udry et al., 2018; Payré et al., 2020; Wu et al., 2021; Brophy 2009).

Assimilation and fractional crystallization (AFC) is a process common in igneous systems on Earth and is a significant control on crustal evolution (e.g., DePaolo, 1981; Grove and Brown, 2018). Fractional crystallization, an exothermic process, may heat crust (surrounding a magma chamber) until it partially melts. Assimilation is the incorporation of partially melted wallrock into a magma body. The combined effects of the chemical removal of compatible elements by fractional crystallization and the addition of heat and incompatible elements from partially melting

wallrock drives the evolution of the magma chamber. Such open-system processes contribute significantly to the diversity of Earth's crust in all magmatic settings, including intracontinental magmas at hotspots, arc and backarc settings, and it is possibly responsible for the presence of highly silicious materials in some mid-ocean ridges (MOR) (e.g., Grove & Brown, 2018). Despite its importance in the evolution of the Earth's crust, AFC has not been explored for its role in the diversification of the crust on Mars or other terrestrial planets and their evolved lithologies.

Here we investigate the potential role of AFC in the compositional evolution of the martian crust through time using a new modeling tool called the Magma Chamber Simulator (MCS) (Bohrson et al., 2014). We use martian primary or near-primary magma compositions as initial magma compositions, which have undergone no crystallization or open-system processes, into which we assimilate proposed Mars crustal compositions. We explore the process of AFC under a range of Mars-relevant conditions, including varying depths and pressures, water contents, oxygen fugacities (fO_2), and areothermal (Mars geothermal) gradients. We compare our results to fractional crystallization- (FC-) only models. In addition, we model assimilation of permeable crust using smaller wallrock to magma ratios, as recent results from seismic studies on the Mars *InSight* lander reveal a possible ~8–11 km depth global blanket of brecciated or altered crust (Lognonné et al., 2020). We endeavor to find the possible influence of assimilation on magmatic diversification on Mars, and make qualitative suggestions as to its role elsewhere in the solar system.

2.4 Methods

2.4.1 Magma Chamber Simulator Assimilation Modeling

We performed all models presented in this paper using the Magma Chamber Simulator (MCS), which is designed to mimic open-system magmatic processes including AFC (see Fig. 2.1) (Bohrson et al., 2014). The MCS commands MELTS thermodynamic phase equilibria calculators to simultaneously conduct models for fractional crystallization of a magma chamber subsystem as well as partial melting of a wallrock subsystem (Fig. 2.1; Bohrson et al., 2014). We conducted all models using Rhyolite-MELTS v.1.2.0, which is best suited to fluid-bearing magmas that may approach quartz or feldspar saturation (under 1.0 GPa) (Ghiorso & Gualda, 2015; Gualda et al., 2012). The MCS partially melts the wallrock to preferentially remove incompatible elements and mix the partial melt into the residual magma with each temperature decrement (Fig. 2.1; Bohrson et al., 2014). Fractional crystallization- (FC-) only models are also possible in MCS.

For the purposes of this study, we modeled three subsystems: 1. the magma, 2. the wallrock (assimilant), and 3. the cumulate reservoir (the combined solid and liquid products of fractional crystallization) (Fig. 2.1). As the magma cools, it transfers heat to the surrounding wallrock (crust) which then approaches its solidus (melting temperature). The cooling magma also forms a cumulate reservoir that no longer interacts with the magma chemically or thermally. When the wallrock reaches its solidus, it partially melts. The wallrock partial melt, because of boundary layer effects, does not interact with the magma until it reaches a threshold volume (a variable referred to as "FMZero" in the model) (Bohrson et al., 2014). When the threshold partial melt is exceeded, the wallrock and magma subsystems perfectly mix (i.e., chemistry is immediately mixed in the entire volume of the magma; Bohrson et al., 2014; see Appendix A material for model assumptions). The process continues until both the magma and wallrock subsystems reach thermal equilibrium (i.e., the wallrock cannot be further heated by the magma chamber) and the process of

fractional crystallization dominates. To calculate bulk residual wallrock, we used the "Cumulate and residual wallrock major element calculation tool" (by Jussi Heinonen) from the MCS website.

2.4.2 Initial Compositions and Model Parameters

Magma and Wallrock Subsystems

For the magma subsystem compositions, we use the Fastball and experimental melt composition averaged Adirondack compositions from Collinet et al. (2015; reported in Table 1.1). Fastball is a near-primary ~3.65 Ga basaltic clast located in a pyroclastic deposit at Home Plate in Gusev crater, where it was analyzed by the *Spirit* rover (Squyres et al., 2007; Filiberto et al., 2010). In addition to Fastball, the averaged Adirondack-class basalts found at Gusev crater were also experimentally confirmed by Monders et al. (2007) to be near-primary melts. The experimental averaged Adirondack basalt compositions were obtained through partial melting experiments of a Dreibus and Wänke (1988) primitive mantle composition at 1.5 GPa (Collinet et al., 2015). We employed a varied amount of initial water contents in our magma subsystems including 0.07 wt.% H_2O, 0.5 wt.% H_2O, and 1.0 wt.% H_2O. Martian primary magmas and estimates for mantle volatile reservoirs have had suggested water contents ranging from 0 wt.% to 2 wt.% H_2O (e.g., McCubbin et al., 2016; Usui et al., 2015). All H_2O content estimates are given in Table 1.1.

Crustal compositions are used for the wallrock subsystems, including the bulk composition of Northwest Africa (NWA) 7034 and the bulk Mars crustal composition. We used the bulk rock composition of NWA 7034 as reported by Agee et al. (2013), including water contents (0.63 wt.%), to represent Noachian-aged wallrock (crustal) composition (Table 1.1). The bulk Mars crustal composition was modeled using the composition of volatile-free soils measured by the Alpha-Particle X-Ray Spectrometer (APXS) instruments onboard the Mars Exploration and

Reconnaissance (*MER*) rovers *Spirit* and *Opportunity* (Taylor and McLennan, 2009). Water contents for the average martian crust is taken from McCubbin et al. (2016) (1410 ppm) as it is not reported otherwise in Taylor and McLennan (2009). All wallrock compositions are reported in Table 1.1.

Model Parameters

We selected model pressures of 1.0 kbar (~8 km), 2.0 (~16 km), 4.0 (~30 km), and 6.0 kbar (~50 km) corresponding to magma pressures at depths ranging from the shallow martian subsurface to the bottom of the average modern martian crust (Wieczorek & Zuber, 2004). We tested thermal gradient estimates of 6°C/km, 15°C/km, and 22°C/km (Table A1). The estimates for the martian crustal thermal gradient range from 5°C/km to 21°C/km which can vary laterally, and it was likely hotter on early (≥3.7 Ga) Mars (Babeyko & Zharkov, 2000; Ehlmann et al., 2011; Semprich & Filiberto, 2020). Hahn et al. (2011) estimated the Gale crater region to have a thermal gradient of 15°C/km in the Noachian. We assumed a surface temperature of 0°C for model simplicity.

To evaluate the effects of fO_2 on our evolving magma and wallrock subsystems, we tested both constrained and unconstrained fO_2 values. Constrained models were conducted at the fayalite-magnetite-quartz (FMQ) buffer. Unconstrained fO_2 model compositions are found in Table A2. Unconstrained models were tested at an Fe^{2+}/Fe^{3+} ratio equivalent to FMQ+2, FMQ, and FMQ–3 (see Appendix A). These values encompass estimates for the reduced martian upper mantle to correspond to melts in the lower crust (FMQ–3), as well as estimates for the martian nakhlite meteorites (FMQ+1.5) which formed at shallow depths (Herd et al., 2002). The effects of fO_2 are included in Appendix A.

For regional melting models, we selected a 1:1 ratio of thermal activity between the wallrock and magma subsystems in the case of a simplified intrusive body, as per the recommendation in Bohrson et al. (2014). To mimic assimilation of porous, impact-fractured crust, we increase the mass of magma relative to the wallrock (10:3) in order to mimic larger exposed surface wallrock surface area within a range common to terrestrial systems (Bohrson et al., 2020). We selected an FMZero (the threshold partial wallrock melt volume required for mixing with the magma) value of 5% for every model, consistent with experimental estimates of liquid interconnectivity for basaltic partial melts (Vigneresse et al., 1996). Enthalpy convergence steps were kept at 30 for each model, and temperature steps for the magma subsystem were calculated at 5°C decrements. The interplay of each model parameter and each modeled subsystem is illustrated in Figure 2.1.

2.4.3 Evolved Martian Compositions

All modeled resulting melts from AFC described above are compared to a number of felsic and alkaline compositions observed by the *Curiosity* rover at Gale crater, as well as the felsic late-stage material in NWA 6963 (Table A3). Gale materials dated from Noachian (>3.7 Ga, Sautter et al., 2015) are analyzed using the Laser Induced Breakdown Spectrometer (LIBS) part of the ChemCam suite onboard *Curiosity* and are reported in Table 1.1 (Cousin et al., 2017; Sautter et al., 2015). ChemCam LIBS is accurate within 0.2 wt.% to ~7 wt.% for major oxides depending on their concentrations (Clegg et al., 2017; Cousin et al., 2017). Targets include alkaline intermediate to felsic targets like Harrison and Becraft, as well as sub-alkaline dacites (~65 wt.% SiO_2) such as Sparkle (Fig. A1; Cousin et al., 2017; Sautter et al., 2015).

The martian meteorite NWA 6963, an enriched gabbroic shergottite (the ages of which are 165–225 Ma), contains interstitial granite with two distinct textures (Filiberto et al., 2018; Gross & Filiberto, 2014). The Type 1 granite contains quartz and alkali feldspar with microscopic cuneiform texture, while the Type 2 granite is glassy (Gross & Filiberto, 2014). Extensive fractional crystallization might result in the observed granitic compositions (Gross & Filiberto, 2014) (Table 1.1).

2.4.4 Model fit selection and comparison to target compositions

To find the best-fit composition along each modeled liquid line of descent (LLD, or the compositional change in a magma at each temperature decrement), we calculate the root-mean-square (RMS) of the model against the target composition at each temperature step. The following equation is used to calculate RMS (x_{RMS}):

$$x_{RMS} = \sqrt{\frac{1}{n}\sum_{i=1}^{n}([f_o - f_e]^2)}$$

where f_o are modeled oxides, f_e are target oxides, and n is the number of oxides (n = 8) considered. RMS calculations highlight the magnitudes of differences between all oxides combined in models at individual temperature decrements against target compositions to allow us to define the best-fit temperature, pressure, and composition. The smallest RMS value is taken to be the best-fit composition along the modeled LLD for that given target composition. For additional information on RMS, see Appendix A.

2.5 Results

2.5.1 AFC Model Comparison by Initial Magma and Wallrock Compositions

To compare the effects of initial magma and wallrock compositions on AFC models, we modeled our selected initial magmas, Fastball and averaged experimental Adirondack basalt, and we assimilated wallrock compositions of either the bulk rock composition of NWA 7034 (Agee et al., 2013) or an estimate for the average Mars crust (Taylor & McLennan, 2009). The average Mars crust wallrock has a solidus temperature of ~920°C and NWA 7034 at ~875°C as calculated by the MCS. The liquidus temperature of Fastball was found to be 1513°C, and the Adirondack basalt average to be ~1525°C (see Appendix A for additional considerations). Residual wallrock compositions undergo little change (Fig. A2). All models presented are constrained at the FMQ fO_2 buffer. Additional unconstrained models are presented in Fig. A3.

Fastball Initial Magma Composition

In Fastball initial magma AFC models including NWA 7034 wallrock that are constrained at the FMQ fO_2 buffer, high pressure models (4–6 kbar) begin assimilation at crystallinities of ~1–12% at ~1280–1500°C. Low pressure models (1–2 kbar) of similar compositions begin assimilation at 30–70% at 1100–1050°C. The average Mars crust models assimilate at ~1–21% crystallinity and 1269–1400°C at 4–6 kbar pressures, and 1–2 kbar pressure models begin assimilation at ~75–50% crystallinity and 1040–1400°C, respectively.

In Fastball and NWA 7034 models, at 6 kbar and constrained at the FMQ buffer, whitlockite ($Ca_9[MgFe][PO_4]_6PO_3OH$) and orthopyroxene accumulate early to remove CaO and concentrate Na_2O relative to lower pressure models, where clinopyroxene crystallization removes Na_2O from the melt as well (Fig. 2.2). All modeled Fastball magmas, regardless of initial water content, increase in CaO as MgO is depleted until ~3–5 wt.% MgO remains, after which there is a sharp decrease in CaO and TiO_2 content, when augite begins to crystallize (Fig. 2.2–2.3).

Magmatic values for SiO_2 increase and FeO_T decrease as iron-rich spinel forms at ~2 wt.% MgO (Fig. 2.3–2.4). Feldspar crystallization occurring at around ~1 wt.% remaining MgO sharply depletes Al_2O_3. Only in 0.07 wt.% initial magmatic water models, 1–4 kbar models onset feldspar crystallization at 2–4 wt.% MgO, which significantly depletes the magmas in Al_2O_3 until feldspar accumulation decreases and Al_2O_3 increases at <1 wt.% MgO (Fig. 2.2–2.3). This trend similarly enriches the magma in FeO_T and TiO_2.

Adirondack Basalt Average Initial Magma Composition

In models wherein averaged Adirondack basaltic magma assimilates the average Mars crust and is constrained at the FMQ buffer, high pressure (6 kbar) assimilation begins between 1400–1480°C (with solid accumulation as low as ~1 wt.%), while low pressure assimilation begins from 990–1060°C (at ~60 wt.% accumulation). In NWA 7034 wallrock models, low pressure assimilation occurs between 1000–1060°C and high-pressure models between 1480–1550°C. Some high-pressure models (4–6 kbar) gain significant fractions of liquid magma, reaching thermal equilibrium and ceasing assimilation after the total magma chamber mass increased ~10–20%, regardless of wallrock composition.

In all AFC models with Adirondack initial magma compositions, the rapid decrease of Al_2O_3 at MgO contents of ~2–4 wt.% and its subsequent increase is noticeable in 1–2 kbar models of 0.50 wt.% H_2O magmas in addition to 0.07 wt.% H_2O magmas, which is reflected in increases in FeO_T and TiO_2 values (Fig. 2.5–2.6). Adirondack initial magma with 0.07 wt.% H_2O assimilating the average Mars crust contains the most Al_2O_3 of all models (~16.4 wt.%) as it accumulates the least feldspar overall (~11 wt.%). Adirondack initial magma models lose CaO

after ~3–5 wt.% MgO remains in the magma due to augite crystallization (Fig. 2.5–2.6). Iron-rich spinel increases FeO_T and decreases SiO_2 at ~2 wt.% MgO (Fig. 2.4–2.6).

2.5.2 Modeled Cumulate Mineralogy

High pressure models (4–6 kbar) form less feldspar overall than lower pressure models (1–2 kbar), with ~25–35 wt.% feldspar at 1 kbar compared to 11–25 wt.% at 6 kbar (Fig. 2.7). Fastball initial magma models accumulate more feldspar than do Adirondack initial magmas with the same wallrock compositions (35 wt.% and 31 wt.%, respectively) (Fig. 2.7). Adirondack initial magmas form upwards of 40 wt.% total pigeonite and Fastball initial magmas form 29 wt.% in total (Fig. 2.7). Together, the models form a variety of pyroxene minerals, including orthopyroxene (~4–34 wt.%), pigeonite (~11–40 wt.%), and augite (3–23 wt.%; Fig. 2.7). Additional common phases include olivine, spinel, whitlockite, apatite, and occasionally late-stage quartz or garnet.

2.5.3 Effects of Initial Wallrock Temperature

In order to test the effect of the initial wallrock temperature, as possibly the areothermal gradient has changed over time or varies laterally (e.g., with proximity to volcanic centers), we conducted AFC models with initial wallrock temperatures corresponding to a low-end estimate of 6°C/km and a high-end estimate of 21°C/km (Babeyko & Zharkov, 2000). The high-end estimate areothermal gradient typically prompts magmas to reach thermal equilibrium with larger volumes of liquid magma still present. Higher initial wallrock temperatures lead to more rapid melting of the wallrock at higher magma temperatures, and thus, lower amounts of solid accumulation (Fig. A4a). Conversely, the lower-end estimate for the areothermal gradient results in thermal equilibrium at smaller volumes of liquid magma overall. Cooler initial wallrock temperatures

along the 6°C/km gradient typically reach their solidus at higher magma temperatures and smaller residual magma volumes (Fig. A4a).

Wallrock heats up at the same rate in all areothermal gradient models (Fig. A4b). Water-undersaturated (0.07 wt.% H_2O) magma subsystems along a 6°C/km gradient reach thermal equilibrium from ~900°C at 1 kbar pressures to ~1000°C at 4 kbar (Fig. A4b). Water undersaturated models along a 21°C/km gradient reach thermal equilibrium at ~980°C at 1 kbar, and 1100°C at 4 kbar (Fig. A4b). Increasing water contents typically result in a lower temperature thermal equilibrium in all models by upwards of 50°C. Areothermal temperatures of 21°C/km cannot be modeled with the MCS at pressures larger than 4 kbar as the wallrock exceeds the typical basalt solidus, and non-brittle rheologies and high-pressure wallrock mineralogies are not accounted for.

2.5.4 FC-Only Models

Fastball magmas undergoing only FC constrained at an fO_2 of FMQ reach 55 wt.% SiO_2 at 82% crystallinity at 6 kbar, and reach 75% crystallinity in 0.07 wt.% H_2O initial magmas at 1 kbar. FC models at 6 kbar reach the same SiO_2 at 66% crystallinity, and 45% crystallinity at 1 kbar (Fig. 2.8). Adirondack initial magmas with 0.07 wt.% H_2O in the same conditions reach 89% and 83% crystallinity at 6 and 1 kbar respectively, and they reach 74% and 56% crystallinity at 6 and 1 kbar with 1.0 wt.% H_2O models (Fig. 2.8).

2.5.5 Effects of Crustal Permeability

Recent findings from the *Insight* mission show a possible 8–11 km depth blanket of crust with a low seismic velocity, indicative of relatively high porosity or permeability possibly due to

impact fracturing and/or secondary alteration (Lognonné et al., 2020). To mimic permeable martian upper crust, we conducted comparative AFC modeling wherein the magma (Fastball) to wallrock (NWA 7034) ratio is 10:3, effectively increasing the surface area of the wallrock in contact with the magma subsystem. At 1 kbar pressure (8 km depth, within the modeled permeable blanket), models of a Fastball magma intruding permeable NWA 7034 wallrock begin assimilation at 1200–1340°C for all initial magma water contents, and reach thermal equilibrium at 1130–1280°C and 3–16% crystallinity (Fig. A5). In contrast, similar models not accounting for permeability initiate assimilation at 990–1050°C, and reach thermal equilibrium at 930–970°C and 60–70% crystallinity. In permeable wallrock models, hotter magma temperatures and larger volumes of magma result in increased evolution with less overall solid accumulation. In permeable wallrock models, the initial Fastball magma containing 0.07 wt.% H_2O reaches 53 wt.% SiO_2 (basaltic trachyandesite) by 55% crystallinity, while a non-permeable model reaches 47 wt.% SiO_2 by the same degree of crystallinity (Fig. A5). A 1.0 wt.% H_2O, permeable model reaches 65 wt.% SiO_2 by 55% solid accumulation. A non-permeable model in the same conditions reaches 62 wt.% SiO_2 (Fig. A5).

2.6 Discussion

2.6.1 Model Comparisons and Best Fits

Comparing Models to Evolved Martian Igneous Materials

Models of Fastball initial magma assimilating NWA 7034 at 6 kbar, 0.07 wt.% H_2O model mimics Gale crater alkaline target Harrison composition with 54% cumulate material in the magma chamber. The model underestimates Al_2O_3 by ~7 wt.% and contains ~4 wt.% more FeO than the Harrison target (Fig. 2.2). In the 6 kbar, 0.07 wt.% H_2O model, 27% of total solid accumulation is

feldspar. Models at 4 kbar with 0.07 wt.% H_2O approach highly-alkaline targets Chakonipau and Becraft (trachyte) around ~76% crystallinity (Fig. 2.4).

Fastball assimilating the average Mars crust results in overall higher crystallinities when compared to Gale crater target compositions, reaching the target Harrison composition at 2 kbar pressure and with 0.50 wt.% H_2O at 57% crystallinity (Fig. 2.4). Another model at 1 kbar pressure, with 0.07 wt.% H_2O also replicates Harrison, but at 70 wt.% crystallinity and with an underestimation of Al_2O_3 by ~9.5 wt.% (Fig. 2.3). Fastball assimilating the average Mars crust at 2 kbar with 0.07 wt.% H_2O reaches Sledgers (~64 wt.% SiO_2) after 80% crystallinity (Fig. 2.4).

The Adirondack basalts assimilating a bulk NWA 7034 wallrock composition reaches andesitic compositions (Sparkle, 59 wt.% SiO_2) at 56% crystallinity at 1 kbar with 1.0 wt.% H_2O (Fig. 2.4). At 4 kbar pressure, with both 0.07 wt.% H_2O and 1.0 wt.% H_2O, the model combination reaches Sledgers at ~80% crystallinity (Fig. 2.4). At 6 kbar, a 1.0 wt.% H_2O model replicates the silica content of Harrison at 50% crystallinity. At 1 kbar and with 1.0 wt.% H_2O, Adirondack basaltic magma assimilating the composition of the average Mars crust reaches Sparkle (59 wt.% SiO_2) target within 64% crystallinity, and with 0.5 wt.% H_2O reaches Angmaat by 77% crystallinity (Fig. 2.4). Models with 0.07 wt.% H_2O at 2 kbar and 4 kbar replicate alkaline basaltic trachyandesite Harrison only by 75% and 86% crystallinity, respectively. At 6 kbar and with 1.0 wt.% H_2O, the combination replicates Harrison within 85% crystallinity as well (Fig. 2.4).

Comparing AFC Models to FC-Only Models

Modeling only the process of FC in both the Fastball and Adirondack basalt initial magma compositions yields similar LLD results as AFC models, especially at pressures of 1 kbar (Fig. 2.8). However, the FC-only models reach felsic (>55 wt.% SiO_2) compositions after significant

amounts of fractionation (60–70%). At 6 kbar, the FC-only model for the Fastball initial magma composition reaches the trachy-basalt field (~45–50 wt.% SiO_2) by 55% fractionation (Fig. 2.8). In contrast, the AFC model at 6 kbar featuring Fastball magma and NWA 7034 wallrock reaches trachy-andesite (~ 53–56 wt.% SiO_2) by 55% fractionation (Fig. 2.8). Higher pressure AFC models (4–6 kbar) have slight differences in their LLD when compared to FC models. In Fig. 2.8, this effect is best seen in the results for the initial Fastball magma containing 0.07 wt.% H_2O, the FC-only model of which becomes more silica-depleted at high temperatures than the AFC model does under the same conditions. Silica depletion likely occurs when the addition of wallrock partial melt to the magma enriches it in SiO_2 to offset the crystallization of orthopyroxene in the AFC model only.

In terrestrial basaltic systems, critical crystallinity occurs when a magma chamber accumulates around 55% solid material and the viscosity is such that the magma behaves as a solid (Marsh, 1981). In terrestrial systems, magma compaction, filter pressing, and devolatilization release liquid from intercumulate spaces in critically crystalline magmas (e.g., Brophy, 2009), but these effects on Mars are not well-understood. Lower crystallinity magmas are thus more likely to erupt, particularly those at or below the critical crystallinity limit. FC-only models always reproduce target compositions at higher crystallinities (Fig. 2.8) than comparable AFC models, making FC-only felsic magma less likely to erupt overall.

Formation of Evolved Target Compositions

In this study, we use the best-fit models, as calculated by RMS, to make predictions of formation conditions for observed evolved martian compositions. Best-fit model descriptions, compositions, and magmatic conditions are found in Table A3. All Gale crater targets are best

replicated with initial Adirondack basaltic magmas and wallrock composed of the average Mars crust, but with different initial water contents and at different pressures (Fig. 2.6). Gale crater basaltic trachyandesite Harrison (52.9 wt.% SiO_2) is the best reproduced composition, replicated by an AFC model at high pressure (6 kbar) and with an initial water content of 0.07 wt.% H_2O. The trachyte Sledgers (63.9 wt.% SiO_2) is best replicated by a 0.07 wt.% H_2O model at 6 kbar pressure, after the largest amount of accumulation of all best-fit models (90%). The diorite Angmaat (62.9 wt.% SiO_2) is replicated by a 1.0 wt.% H_2O magma at 2 kbar depth at the lowest degree of crystallinity among the best-fit models (67%). The trachyte Becraft (60.1 wt.% SiO_2) is best-fit by a model with 0.50 wt.% H_2O at 6 kbar. The trachyte Chakonipau (61.9 wt.% SiO_2) is replicated by a 0.07 wt.% H_2O model at 6 kbar. The diorite Sparkle (59.4 wt.% SiO_2) is best represented by an Adirondack basaltic magma assimilating the average Mars crust, with initial magmatic water of 1.0 wt.% at 2 kbar pressure. Best-fit models generally fall within ~2 wt.% of ChemCam compositions, which is in the range of the instrument precision, with Al_2O_3 typically underestimated by models and FeO_T overestimated by ~3–4 wt.%. Thus, AFC at a range of possible depths (2–6 kbar) and initial water contents (0.07–1.0 wt.%) may explain observed evolved compositions at the surface of Mars. Generally, subalkaline compositions are best modeled by hydrous magma at 2 kbar depth, while alkaline evolved targets are reproduced by higher pressure models (4–6 kbar, Fig. 2.4).

At comparable conditions to the best-fit AFC models, FC-only models provide significantly poorer fits overall. For instance, an RMS value of 1.5 for the best fit AFC model for Harrison is 4.8 for fractional crystallization alone. An AFC RMS value for Chakonipau is 2.5, while a fractional crystallization best fit yields an RMS value of 6.7. Most of the best fit fractional-

crystallization models occur at or near the end of the model calculations, when there are ~90% accumulated solids.

Our AFC models provide generally poor fits to the NWA 6963 granitic glasses. Both are best represented by an Adirondack basaltic magma assimilating NWA 7034 wallrock at low pressure (1 kbar) with initial water contents of 1.0 wt.% (Fig. 2.4). Both best-fits occur only after significant fractionation of over 77% solid material. The NWA 6963 granitic glasses occur as interstitial material to more mafic cumulate phases (Gross and Filiberto, 2014). We can therefore reasonably expect that similarly siliceous compositions must require significant fractionation of a cumulate reservoir. Alternatively, the initial magma and wallrock compositions tested in this paper could provide generally poor model fits for this composition.

2.6.2 Controls on Assimilation

Coupled Roles of Pressure, Temperature, Depth, and Crustal Thickness

Magmatic system pressures and wallrock initial temperatures increase with depth along the areothermal gradient. The wallrock temperature approaches its solidus at pressures relevant to the crust-mantle boundary, which results in increased amounts of partial melting. Areothermal gradients are affected by a number of factors, which include proximity to volcanic centers, the abundance of radiogenic isotopes, and the age of the planet as younger Mars is expected to have had more residual energy shortly after accretion and differentiation (Babeyko & Zharkov, 2000; Ehlmann et al., 2011; Yoshizaki & McDonough, 2020). Modeled estimates of the areothermal gradient range as low as 2.7°C/km for modern Mars (Yoshizaki & McDonough, 2020) to as high as 21°C/km for “hot” Mars (Babeyko & Zharkov, 2000).

Recent estimates for crustal thickness (and thus potential magma chamber depths) find an average of 35–85 km, but can be as thin as 0 km in Hellas Basin or exceed 100 km in volcanic centers (Plesa et al., 2018). When the contribution of features such as volcanoes and impact basins are removed from crustal thickness estimates, the Mars crust appears to be comprised of distinct blocks of crust with differing thicknesses and geochemical characteristics (Bouley et al., 2020). Terrains vary laterally in composition in correlation with their ages, implying that volcanism (as parental material to subsequent secondary processes) was different between eras (Taylor and McLennan, 2009). The effects of assimilation are expected to be more pronounced in areas of the crust near to volcanic centers with an enhanced areothermal gradient and thickened crust (i.e., primarily in the southern highlands).

As thickened crust and an elevated areotherm provide an important control on the degree to which assimilation occurs, the same constraints affect the erupted volume of magma as well. On the first order, melting of a wallrock system partially replenishes the liquid volume of crystallizing magma (Fig. A4a). More assimilation, under higher pressure and thicker crust, would also result in larger volumes of erupted material. Mars, with its depressed areothermal gradient when compared to Earth's geotherm (~25°C/km), would have overall smaller erupted volumes of felsic lavas where assimilation played a key role in their formation. Where the crust was thicker and areothermal gradient high on Mars, more extensive assimilation may have led to evolved outcrops larger in scale than where crust was thinner or cooler. Furthermore, a thicker crust results in increasingly alkaline magmas forming under higher pressures. New estimates for Mars crustal densities find that even small volumes of magma may be stored at various depths, evolve, and erupt efficiently (Brož et al., 2015). Thus, AFC may play an important role in the potential presence of small, evolved (i.e., viscous) flows wherever the crust is sufficiently thickened. Unerupted felsic

material formed by AFC may also contribute to observations of anomalously low density martian crust (Baratoux et al., 2014; Wieczorek and Zuber, 2014; Goossens et al., 2017).

Bulk cumulate mineralogy calculations from AFC process show a variety of ultramafic (olivine, orthopyroxene), mafic (pyroxene), and more evolved phases (feldspar, quartz) (Fig. 2.7). AFC would especially play a role in the mineralogical evolution of the surface if underplating resulted in a progressively thicker crust to allow for deeper-seated magmas to intrude hotter wallrock, or in volcanic centers where the crust would maintain an elevated areothermal gradient and prolonged volcanism to similarly thicken the crust (e.g., Baratoux et al., 2013). Exhumed cumulate bodies or cumulate phases entrained in lavas may bear low-Ca pyroxene (formed early in cumulate bodies), while extrusive phases may include later-formed high-Ca pyroxene and feldspar phases, thus diversifying the mineralogy of the Mars crust early in its history. AFC models with oxidized and reduced unconstrained fO_2 formed no olivine, and the normative mineralogy of all best fit models finds very little olivine (Fig. A6), in keeping with the dearth of directly observed olivine at Gale crater (Payré et al., 2020).

The Role of Initial Compositions on LLDs

Water content in magma at low pressure is a significant control on alkalinity during magma evolution in our models. Lower pressure models (1–2 kbar) with 1.0 wt.% H_2O are less alkaline than higher pressure models (4–6 kbar) with 1.0 wt.% H_2O and the same initial magma and wallrock compositions (Fig. 2.4). Low pressure (1–2 kbar) models with 0.50 and 0.07 wt.% H_2O have higher overall alkalinity than do 1.0 wt.% H_2O models under the same conditions as expected. Increasing water in low-pressure systems prompts generally greater feldspar accumulation and drives alkalinity values lower as those oxides are taken up by the crystallizing phases (Fig. 2.7).

At higher pressures (4–6 kbar), where assimilation occurs to a greater extent, water behaving as an incompatible element is efficiently extracted from wallrock and mixed into the magma subsystem, and the LLDs for different initial magmas containing variable initial water contents merge (Fig. 2.4). At high pressures, initial water contents in the magma subsystem play a smaller role in the evolution of the magma chamber than at lower pressures, as wallrock-derived water is readily added to the magma.

Wallrock compositions control magmatic evolution during AFC primarily by their solidus temperatures. Wallrock compositions with lower solidus temperatures melt more readily and contribute more assimilant to the magma than wallrock compositions with higher solidus temperatures. At high pressures, such as 4–6 kbar, substantial additions of incompatible elements (e.g., SiO_2, Al_2O_3, Na_2O) from assimilant may further drive evolution, although the effect on the LLD on the magma subsystem is small overall. This is especially noticeable when comparing AFC to FC-only models, as in Fig. 2.8. However, the primary control on the LLD, and on mineralogy of the cumulates generated during fractionation, is the initial magma composition (Fig. 2.2–2.6).

The Nature of the Crust

We found that assimilation onsets rapidly in magma evolution and contributes somewhat to melt evolution in permeable crust. It is likely that melt diversification occurs even at low pressures, such as along shallowly emplaced sills or dikes. Thus, magma evolution in the shallow crust increases over time, with more evolved magmas forming after significant impact cratering had brecciated the uppermost layers of crust. It is important to note that we conducted idealized modeling that may not account for thermal annealing and rapid crystallization where magma is

thin and exposed to large surfaces of cold wallrock, i.e., along veins, the effects of which may limit magmatic evolution.

2.6.3 AFC in the Solar System

Assimilation and fractional crystallization contributes to Earth's own crustal diversity (e.g., DePaolo, 1981; Grove and Brown, 2018), and it may play a similarly significant role in the crustal compositions of other terrestrial bodies as well, including Mars, Vesta, the Moon, and iron meteorite parent bodies. Assimilation has been implicated as a contributor to the negative europium anomalies in diogenites, and therefore may have played a role in the formation of the crust of Vesta (e.g., Barrat et al., 2010). Low degrees of assimilation may have occurred in the presence of FC at the core-mantle boundary in planetesimals, as shown by the trace element in IIAB and IIIAB type iron meteorites (Malvin, 1988). Assimilation prompted by recharge (magmatic replenishment) may have also contributed to the rare earth element profile of the green picritic glass collected from the lunar surface by the Apollo 15 crew (Elkins-Tanton et al., 2003).

As we found by conducting Mars-relevant AFC modeling, the primary controls on assimilation are depth and wallrock initial temperatures along a (geo)thermal gradient. To a lesser extent, the solidus temperature of wallrock is also a significant determinant in the degree to which assimilation occurs. On Venus, where surface temperatures exceed 450°C (Gilmore et al., 2017), the venusian thermal gradient may be inherently high enough to promote significant partial melting of wallrock within even shallow intrusions. Venus has volcanic features that may be felsic, such as the tesserae (Gilmore et al., 2017). Modeling by Shellnutt (2013) showed that FC may account for felsic volcanics on Venus, but only after significant crystallinity (~90% solid accumulation) which may be unlikely to erupt without significant volatilization or compaction. Thus, assimilation

may play an important and, as of yet unexplored, role in the formation of felsic outcrop on Venus and modeling should be conducted in advance of upcoming missions.

The mercurian crust contains terrains with abundant and exotic sulfides (e.g., Vander Kaaden et al., 2017). Sulfide minerals typically have a lower melting temperature than oxide minerals, and will likely more rapidly melt and assimilate into upwardly-mobile magma. Assimilated graphite from the crust or regolith has been implicated in the removal of O from oxides to smelt metals at the surface of Mercury (McCubbin et al., 2017). In the next decade of planetary exploration, should we send missions to Venus or Mercury to explore their crusts with higher resolution, the planetary community should give careful consideration to open-system processes like AFC.

2.7 Conclusions

Open-system processes like AFC promote significant diversification of terrestrial magmas, and may have been common on Mars throughout its geologic history. The primary controls on martian AFC, and the effects of AFC on magmatic evolution, are detailed below and are visualized in Fig. 2.9:

- AFC models provide good fits to Gale crater target compositions within generally low degrees of crystallinity. AFC models provide significantly better fits at consistently lower degrees of crystallinity than do FC-only models. AFC models are not ideal fits for NWA 6963 granitic interstitial glass, which must have required significant fractionation to form instead.

- Assimilation works to promote magmatic diversification over FC alone as the influx of partially melted wallrock maintains higher volumes of magma as solids continuously fractionate.
- Increasing depth (and thus pressure) in a magma system implies an increase in initial temperature of the surrounding wallrock. Higher temperatures at higher pressures leads to increased volumes of assimilant added to the magma chamber, and increased evolution of the magma.
- Early Mars, with a hotter areothermal gradient and a thinner crust, would have allowed for assimilation and silicic evolution of magmas at pressures as low as 2–4 kbar and higher volumes of magmas. Later Mars would have formed less voluminous evolved magma, although AFC processes could have occurred especially in the upper fractured crust.
- Estimates for the areothermal gradient of Mars are overall colder than the average geothermal gradient of Earth. Thus, assimilation on Mars would result in lower volumes of erupted evolved magmas than on Earth.
- Water in magmas plays a more significant role in their evolution when assimilation is limited. As water behaves like an incompatible element in most mafic to intermediate magmatic systems, it is readily removed from melting wallrock and added to the magma.
- The overall compositional trends of an evolving magma undergoing AFC are controlled by its initial composition, but it will evolve to felsic compositions with lower degrees of crystallinity than in FC alone.

Future work should address additional open-system processes, such as recharge and assimilation fractional and crystallization (RAFC), as AFC rarely works alone in producing felsic compositions from initial basaltic magmas (e.g., Grove et al., 1998). Additionally, returned

samples from the *Perseverance* rover mission to Jezero crater may help resolve the role of assimilation in the diversification of Mars' crust. The crater counting-derived age estimates for the mafic floor unit ranges from as low as 1.4 Ga to as high as 3.45 Ga between studies (Goudge et al., 2015; Shahrzad et al., 2019). If the crater floor unit is an igneous unit and if it is Noachian or formed in a shallow and impact-fractured crust, it may preserve isotopic characteristics of assimilation due to higher areothermal temperatures or increased wallrock surface area. If, however, the unit is Amazonian and lacked an elevated areothermal gradient, it may be unlikely to display isotopic or trace element evidence of assimilation. We must collect igneous samples of different ages and locations to better make predictions about what temporal and lateral magmatic evolution we might expect for Mars, and what processes played a role in that evolution.

2.8 Acknowledgments, Samples, and Data

This study was supported by NASA Mars Data Analysis Program 80NSSC17K0477 awarded to A. U. and E. G.

2.9 Tables

Table 2.1. Initial compositions and evolved compositions used in this study.

		Rock Type	SiO_2	TiO_2	Al_2O_3	Cr_2O_3	FeO_T	MnO	MgO	CaO	Na_2O	K_2O	P_2O_5
Initial magma compositions*	Fastball[1]	Basalt	48.3	0.71	8.36	0.52	19.0	0.50	12.8	6.18	2.50	0.25	0.84
	Averaged Adirondack Basalt (*DW04* [2])	Basalt	47.8	0.37	8.40	0.63	19.3	0.53	14.0	6.90	1.50	0.20	0.46
Initial wallrock compositions	NWA 7034 bulk[3]	—	49.8	1.03	11.8	0.19	13.6	0.29	8.18	9.36	3.92	0.36	0.80
	Bulk Silicate Mars[4]	—	49.3	0.98	10.5	0.38	18.2	0.36	9.06	6.92	2.97	0.45	0.90
Gale crater target compositions	Harrison[6]	Trachy-andesite	52.9	0.98	18.0	—	10.1	—	2.35	6.14	3.34	2.17	—
	Sledgers[7]	Trachyte	63.9	0.29	16.3	—	6.62	—	1.81	2.19	5.14	7.08	—
	Chakonipau[7]	Trachyte	61.9	0.83	16.3	—	6.62	—	0.92	0.92	5.43	7.08	—
	Becraft[7]	Trachyte	60.1	1.31	14.8	—	9.93	—	1.31	1.69	4.22	6.65	—
	Sparkle[7]	Dacite	59.4	0.37	17.3	—	5.40	—	1.40	11.9	3.45	0.74	—
	Angmaat[7]	Andesite	62.9	0.91	16.9	—	10.1	—	1.31	3.02	2.52	2.41	—
Northwest Africa 6963[8]	Type 1	Granite	80.4	0.23	12.1	—	0.69	0.01	0.03	3.44	3.61	0.43	0.20
	Type 2	Granitic glass	78.6	0.52	11.8	—	0.65	0.02	0.01	0.49	3.32	5.16	0.19

*H_2O Content is varied between marked models to include 0.07, 0.50, and 1.0 wt.%, and final compositions are normalized to 100%

[1]Squyres et al., 2007
[2]Collinet et al., 2015
[3]Agee et al., 2013
[4]Taylor & McLennan, 2009
[5]McCubbin et al., 2016
[6]Cousin et al., 2017
[7]Sautter et al., 2015
[8]Gross & Filiberto, 2014

2.10 Figures

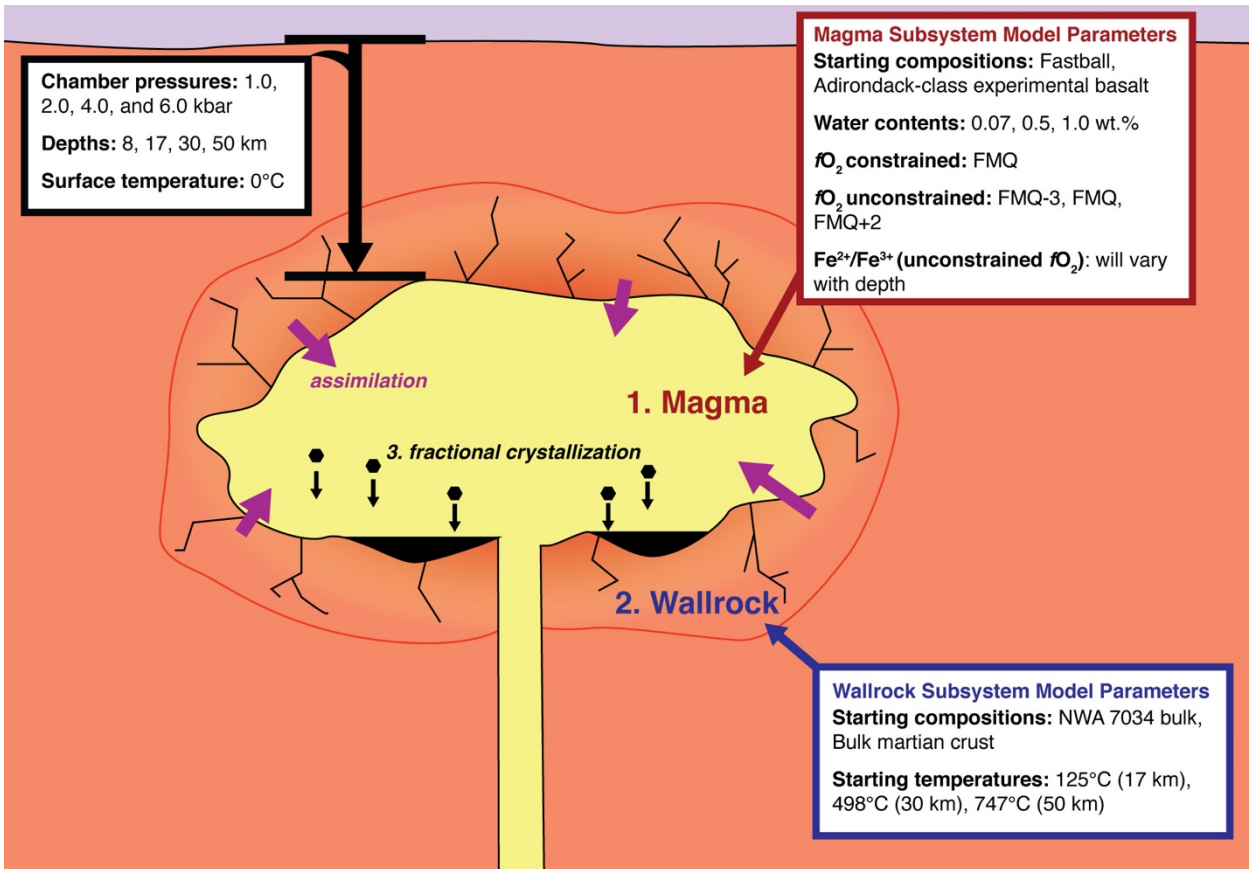

Figure 2.1: Schematic view of assimilation and fractional crystallization (AFC) as it is modeled by the Magma Chamber Simulator. The process of AFC occurs in three steps: 1) intrusion of the magma into a surrounding wallrock, 2) fractionation and accumulation of solid material, 3) exothermic heating and partial melting of the wallrock leading to assimilation. Fastball composition is from Squyres et al., 2007. Adirondack experimental basalt composition is from Collinet el al., 2015. Bulk NWA 7034 is from Agee et al., 2013. Bulk martian crust composition is from Taylor and McLennan, 2009.

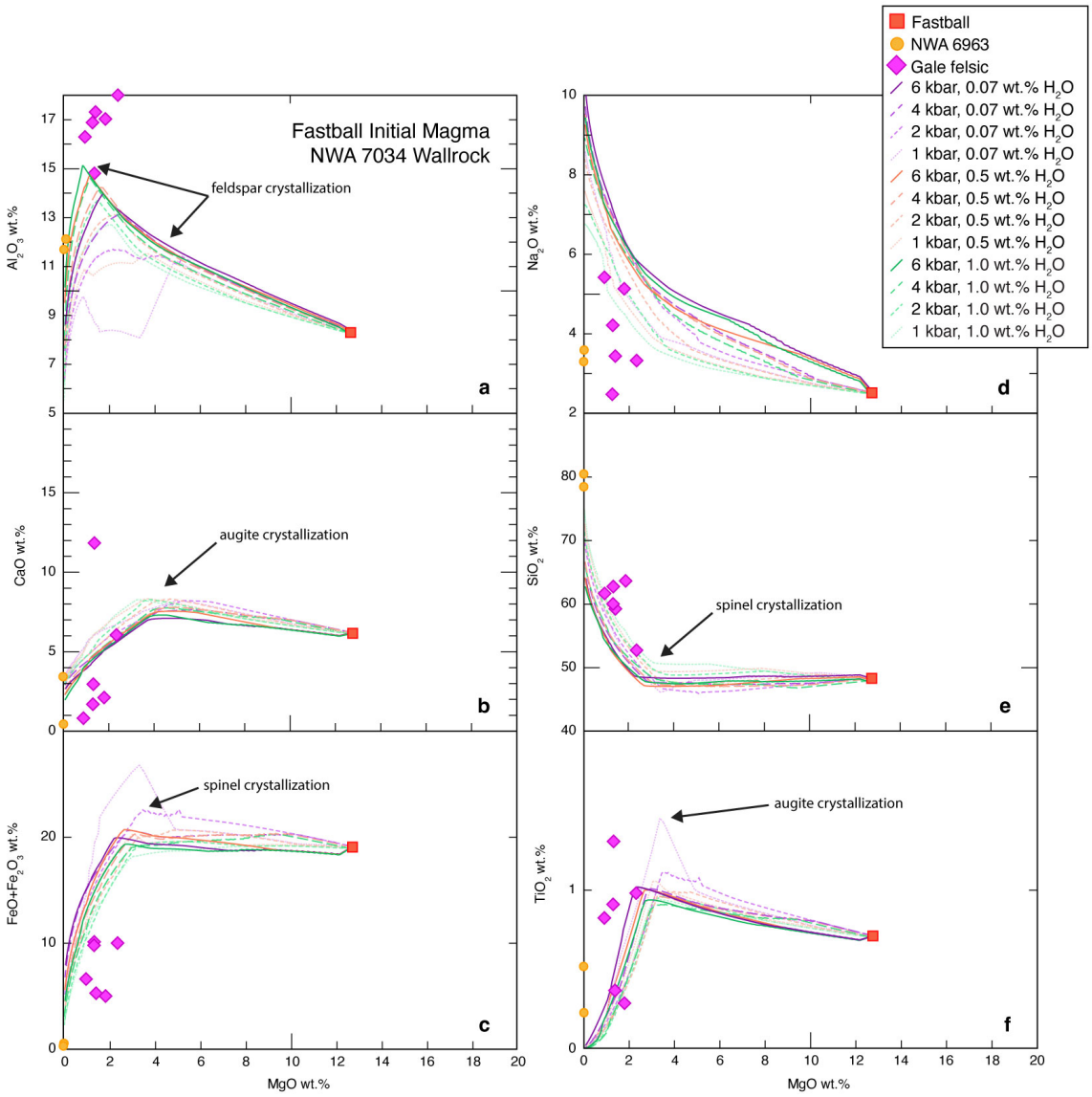

Figure 2.2: Magmatic evolution during AFC starting from Fastball initial composition (Squyres et al., 2007), assimilating NWA 7034 wallrock (Agee et al., 2013) along a 15°C/km thermal gradient. MgO versus a) Al_2O_3, b) CaO, c) FeO + Fe_2O_3, d) Na_2O, e) SiO_2, and f) TiO_2. Increasingly dark shades represent increasing pressures. Purple colors are magmas with an initial 0.07 wt.% H_2O, orange with 0.50 wt.% H_2O, and green with 1.00 wt.% H_2O.

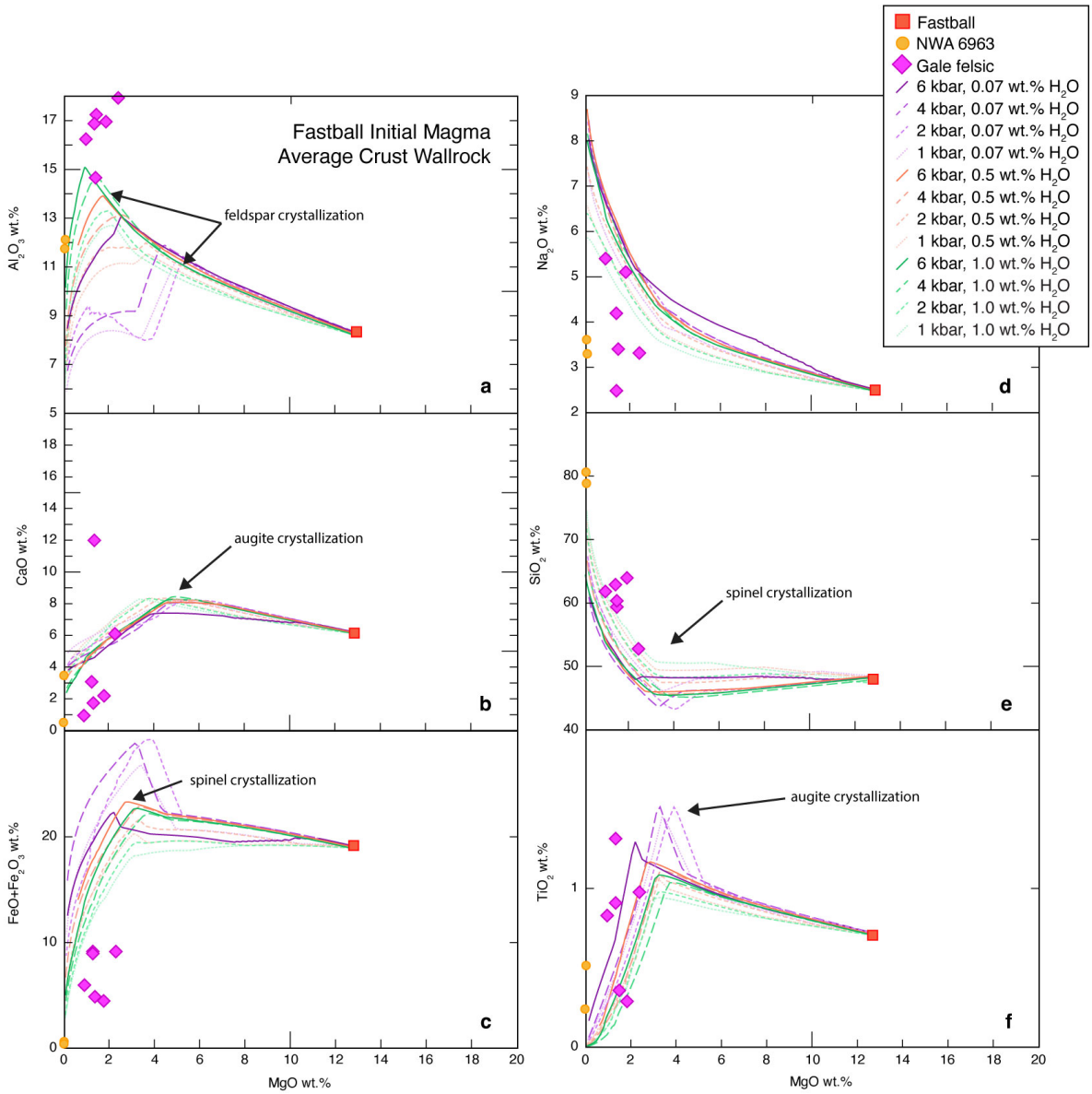

Figure 2.3: Magmatic evolution during AFC starting from Fastball initial composition (Squyres et al., 2007), assimilating the average Mars crust (Taylor and McLennan, 2009) along a 15°C/km thermal gradient. MgO versus a) Al_2O_3, b) CaO, c) FeO + Fe_2O_3, d) Na_2O, e) SiO_2, and f) TiO_2 diagrams. Increasingly dark shades represent increasing pressures. Purple colors are magmas with an initial 0.07 wt.% H_2O, orange with 0.50 wt.% H_2O, and green with 1.00 wt.% H_2O.

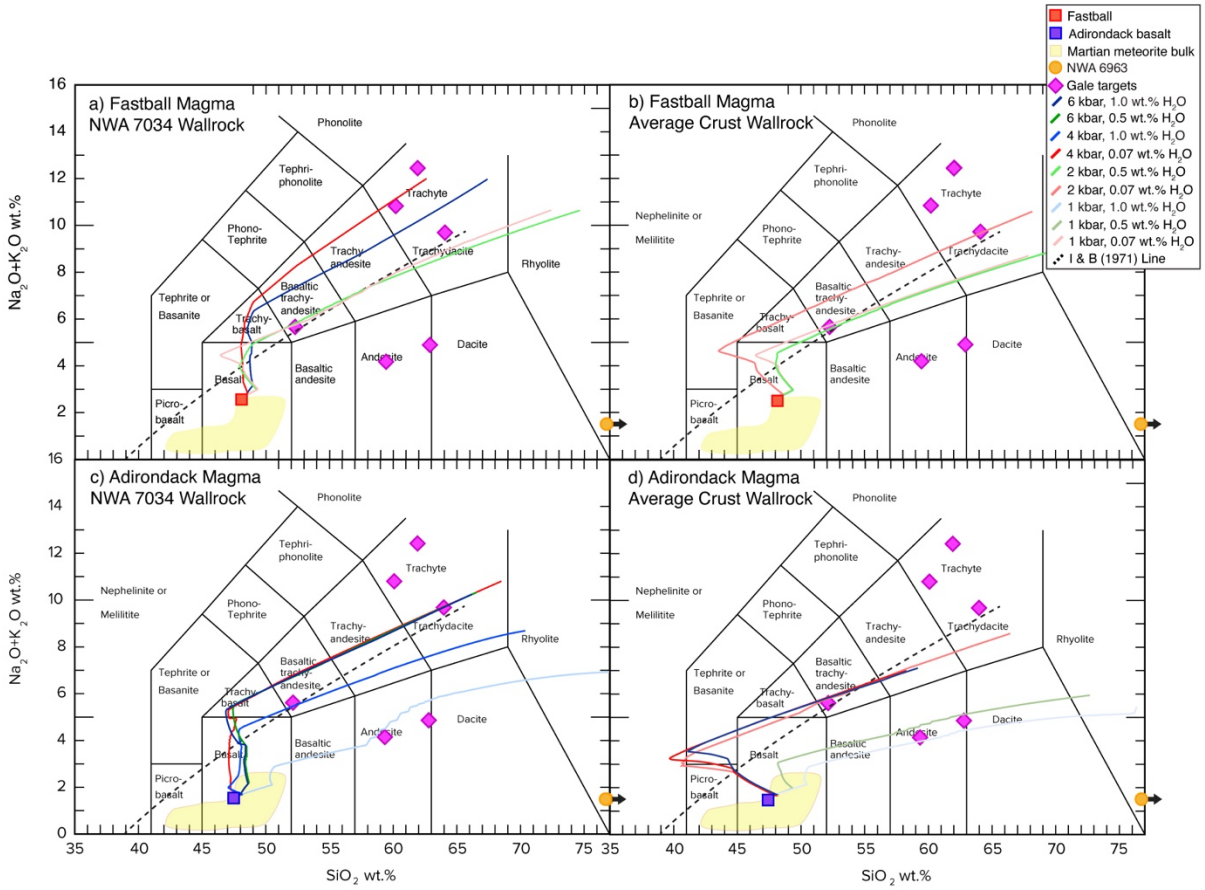

Figure 2.4: Total alkali elements (Na_2O + K_2O) versus SiO_2 diagrams for: a) Fastball magma assimilating NWA 7034 wallrock; b) Fastball magma assimilating the average Mars crust wallrock; c) Adirondack basalt magma assimilating NWA 7034 wallrock; and d) Adirondack basalt magma assimilating the average Mars crust wallrock all along a 15°C/km thermal gradient. Increasing pressures correspond to increasing wallrock temperatures, and higher-pressure models undergo more overall assimilation calculations and are typically more alkaline than lower pressure models. At 78 wt.% SiO_2 and greater, the NWA 6963 targets fall off of the diagram. Bulk martian meteorite compositions from Udry et al., 2020.

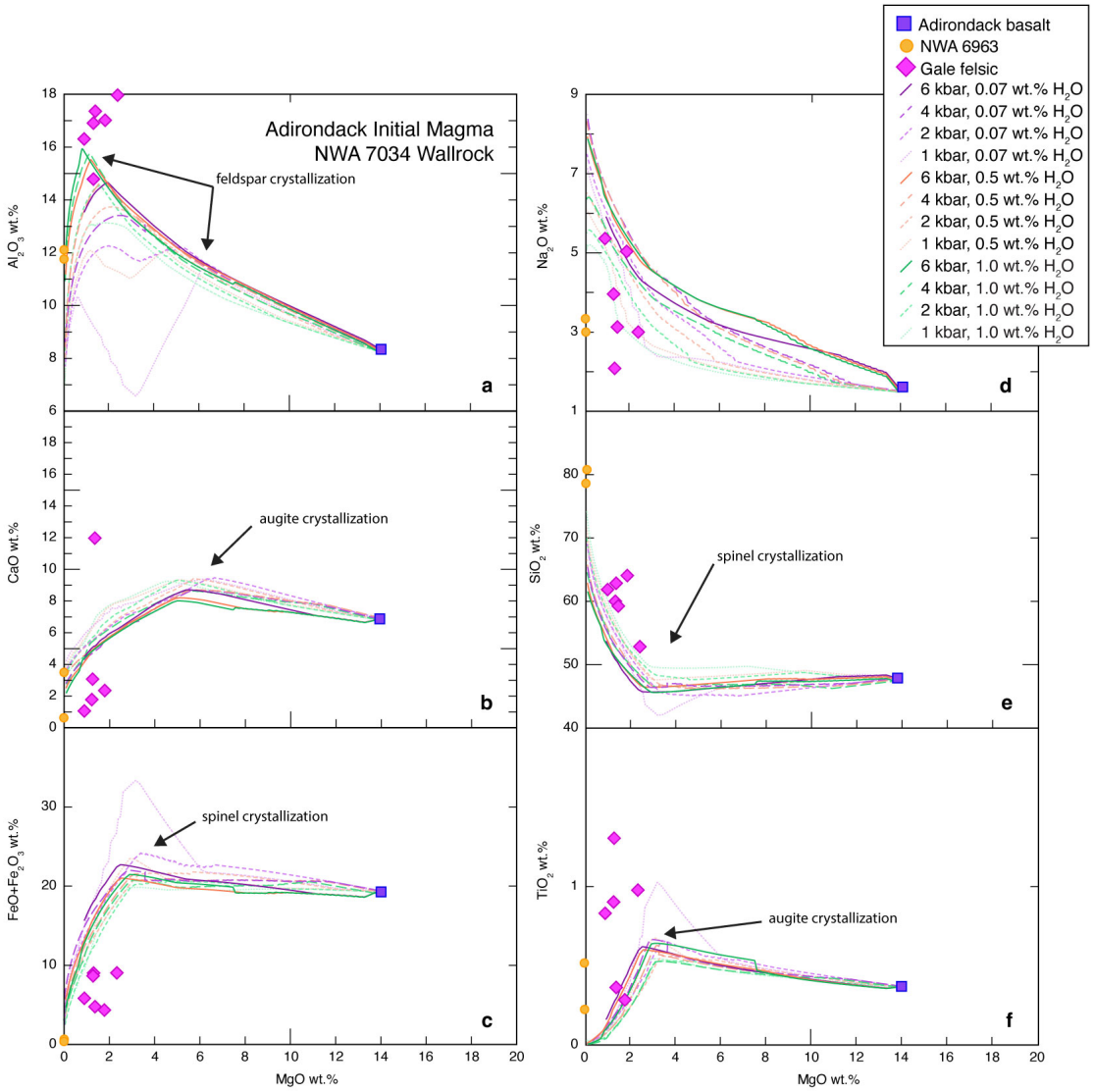

Figure 2.5: Magmatic evolution during AFC starting from Adirondack basalt initial composition (Collinet et al., 2015), assimilating NWA 7034 wallrock (Agee et al., 2013) along a 15°C/km thermal gradient. MgO versus a) Al_2O_3, b) CaO, c) FeO + Fe_2O_3, d) Na_2O, e) SiO_2, and f) TiO_2 diagrams. Increasingly dark shades represent increasing pressures. Purple colors are magmas with an initial 0.07 wt.% H_2O, orange with 0.50 wt.% H_2O, and green with 1.00 wt.% H_2O.

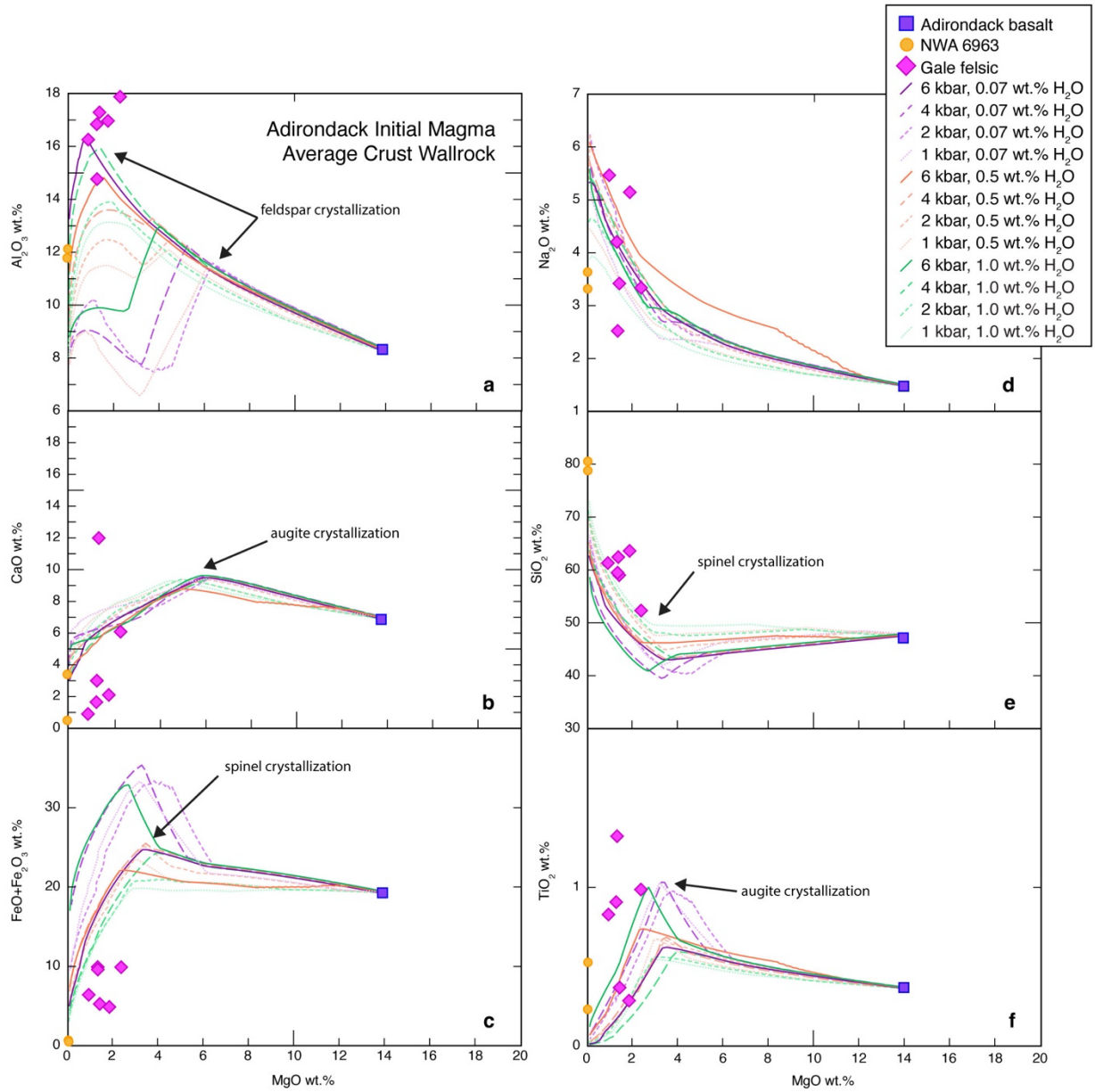

Figure 2.6: Magmatic evolution during AFC starting from Adirondack basalt initial composition (Collinet et al., 2015), assimilating the average Mars crust (Taylor and McLennan, 2009) along a 15°C/km thermal gradient. MgO versus a) Al_2O_3, b) CaO, c) FeO + Fe_2O_3, d) Na_2O, e) SiO_2, and f) TiO_2 diagrams. Increasingly dark shades represent increasing pressures. Purple colors are magmas with an initial 0.07 wt.% H_2O, orange with 0.50 wt.% H_2O, and green with 1.00 wt.% H_2O.

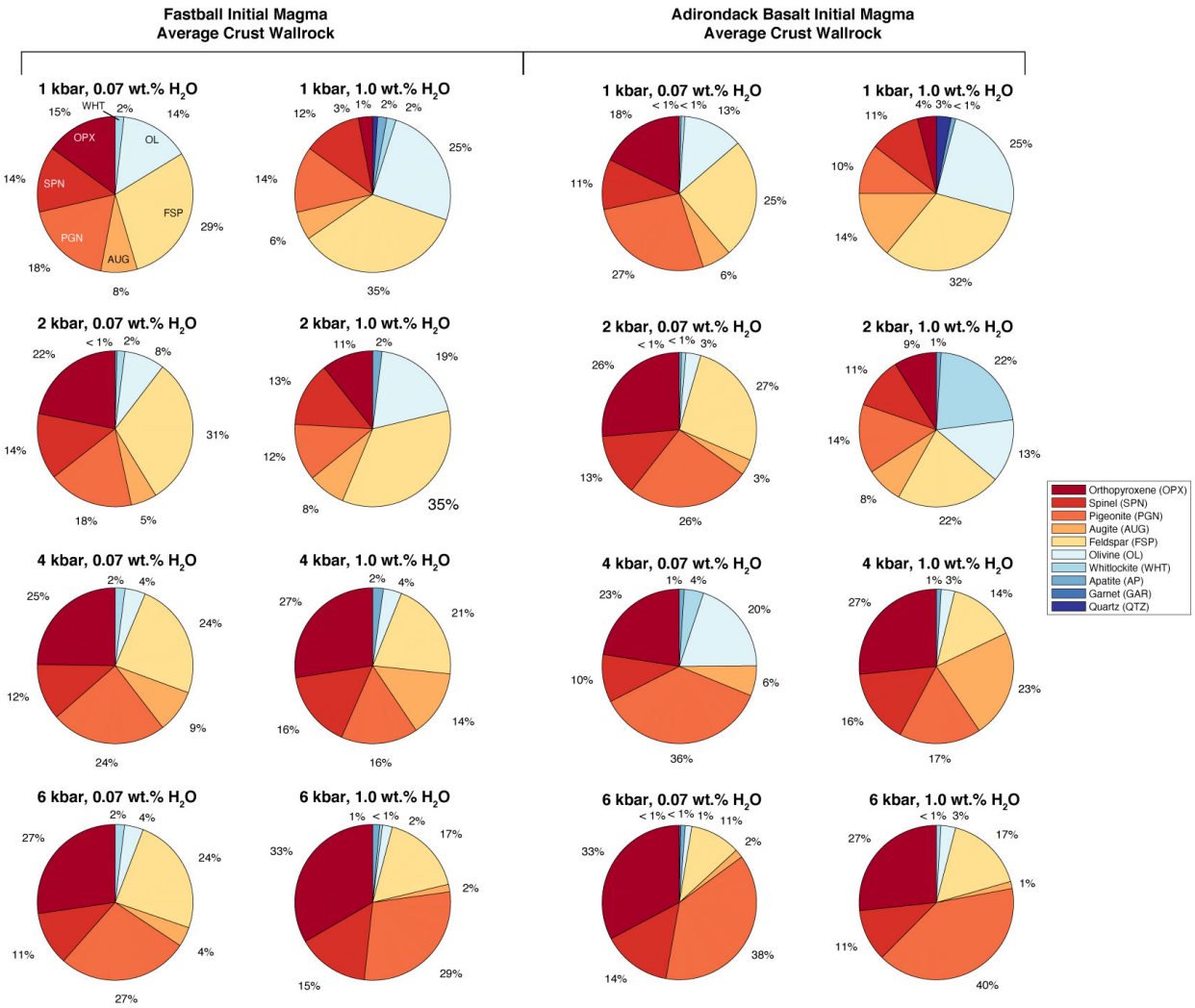

Figure 2.7: Total bulk mineralogy (by total system, including magma and wallrock partial melt, mass percentage) of cumulate reservoir for average crust wallrock assimilated by Fastball initial magmas at 0.07 and 1.0 wt.% H2O (left) and Adirondack basalt initial magmas at 0.07 and 1.0 wt.% H2O (right). Mineralogy across all models is diverse and includes an abundance of both high- and low-Ca pyroxene (augite and pigeonite, respectively).

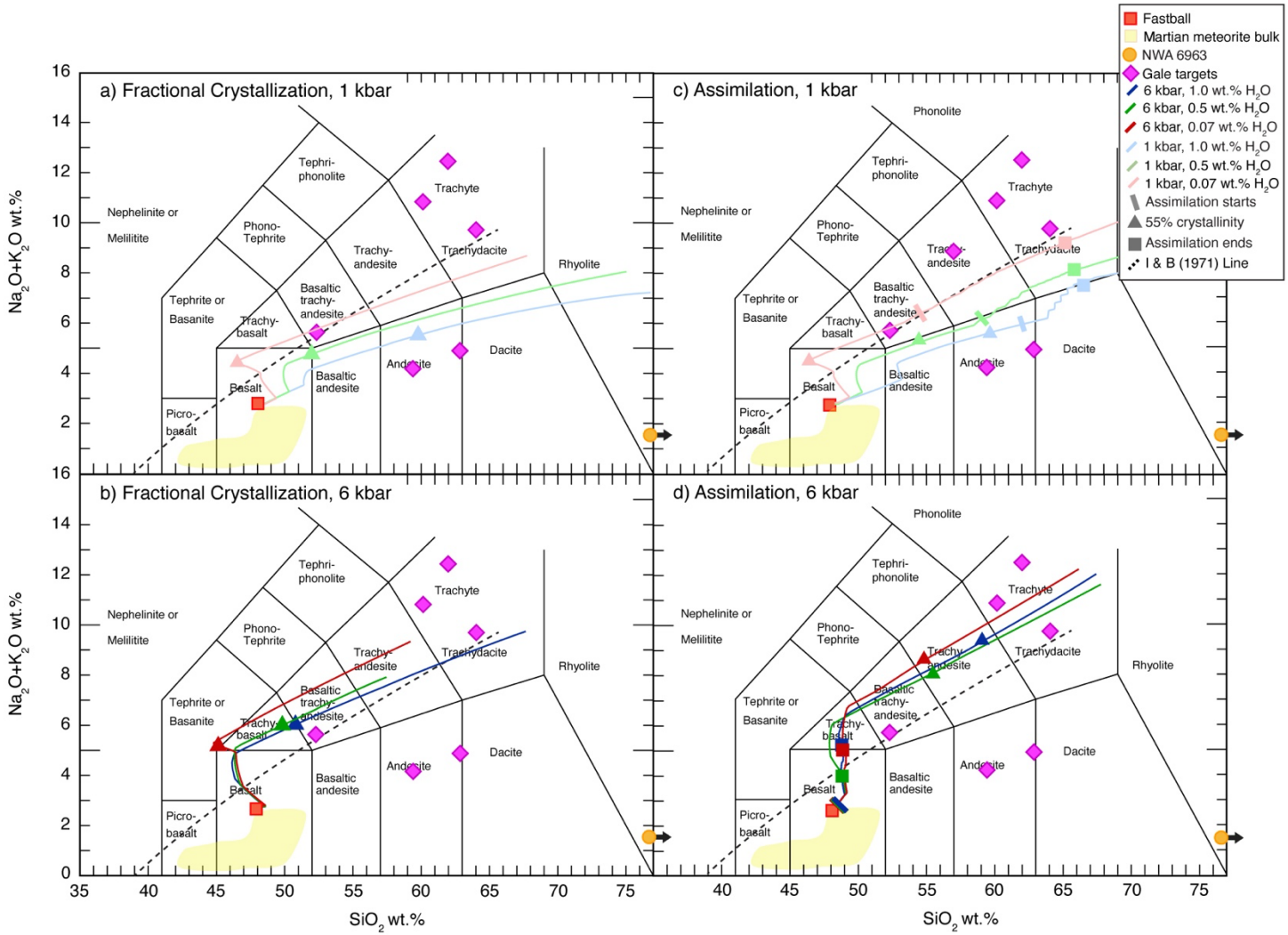

Figure 2.8: Total alkali elements versus silica diagrams of a) fractional-crystallization only of: Fastball magma at 1 kbar and b) 6 kbar; assimilation and fractional crystallization of Fastball magma and NWA 7034 wallrock at 1 kbar and d) 6 kbar. Assimilation of a wallrock adds larger amounts of silica to the magma at lower degrees of crystallinity than fractional crystallization alone. At 78 wt.% SiO_2 and greater, the NWA 6963 targets fall off of the diagram. Bulk martian meteorite compositions from Udry et al., 2020.

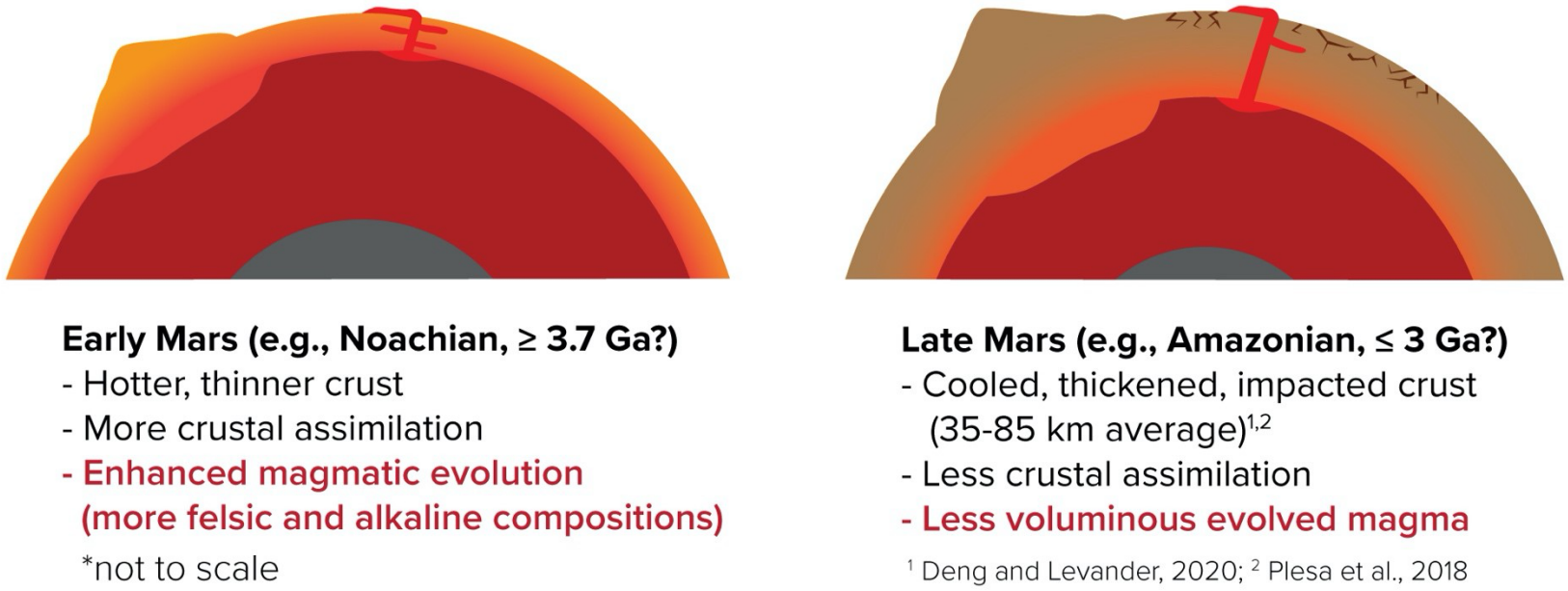

Figure 2.9: Schematic detailing major takeaways. Generally, early Mars had an elevated areothermal gradient which allowed for a greater extent of crustal assimilation. The effect may be overall enhanced magmatic and crustal evolution. As Mars aged, its crust cooled, which likely inhibited assimilation and magmatic evolution, except at depth and where brecciation increased surface area of crustal material in contact with shallowly intruding magmas. Crustal thickening likely resulted in increased alkalinity in magmas as well, but timing of crustal thickening is not well constrained. Other factors, such as volatile evolution over time, are also difficult to constrain, but may play a role in the efficacy of assimilation.

2.11 References

Agee, C.B. et al., 2013, Unique meteorite from early Amazonian Mars: Water-rich basaltic breccia Northwest Africa 7034: Science, v. 339, p. 780–785, doi:10.1126/science.1228858.

Babeyko, A.Y., and Zharkov, V.N., 2000, Martian crust: A modeling approach: Physics of the Earth and Planetary Interiors, v. 117, p. 421–435, doi:10.1016/S0031-9201(99)00111-9.

Baratoux, D., Toplis, M.J., Monnereau, M., and Sautter, V., 2013, The petrological expression of early Mars volcanism: Journal of Geophysical Research E: Planets, v. 118, p. 59–64, doi:10.1029/2012JE004234.

Barrat, J.A., Yamaguchi, A., Zanda, B., Bollinger, C., and Bohn, M., 2010, Relative chronology of crust formation on asteroid Vesta: Insights from the geochemistry of diogenites: Geochimica et Cosmochimica Acta, v. 74, p. 6218–6231, doi:10.1016/j.gca.2010.07.028.

Bohrson, W.A., Spera, F.J., Ghiorso, M.S., Brown, G.A., Creamer, J.B., and Mayfield, A., 2014, Thermodynamic model for energy-constrained open-system evolution of crustal magma bodies undergoing simultaneous recharge, assimilation and crystallization: The magma chamber simulator: Journal of Petrology, v. 55, p. 1685–1717, doi:10.1093/petrology/egu036.

Bohrson, W.A., Spera, F.J., Heinonen, J.S., Brown, G.A., Scruggs, M.A., Adams, J. V., Takach, M.K., Zeff, G., and Suikkanen, E., 2020, Diagnosing open-system magmatic processes using the Magma Chamber Simulator (MCS): part I—major elements and phase equilibria: Contributions to Mineralogy and Petrology, v. 175, p. 1–29, doi:10.1007/s00410-020-01722-z.

Bouley, S. et al., 2020, A thick crustal block revealed by reconstructions of early Mars highlands: Nature Geoscience, v. 13, p. 105–109, doi:10.1038/s41561-019-0512-6.

Brophy, J.G., 1991, Composition gaps, critical crystallinity, and fractional crystallization in

orogenic (calc-alkaline) magmatic systems: Contributions to Mineralogy and Petrology, v. 109, p. 173–182, doi:10.1007/BF00306477.

Brož, P., Hauber, E., Platz, T., and Balme, M., 2015, Evidence for Amazonian highly viscous lavas in the southern highlands on Mars: Earth and Planetary Science Letters, v. 415, p. 200–212, doi:10.1016/j.epsl.2015.01.033.

Christensen, P.R. et al., 2005, Evidence for magmatic evolution and diversity on Mars from infrared observations: Nature, v. 436, p. 504–509, doi:10.1038/nature03639.

Clegg, S.M. et al., 2017, Recalibration of the Mars Science Laboratory ChemCam instrument with an expanded geochemical database: Spectrochimica Acta - Part B Atomic Spectroscopy, v. 129, p. 64–85, doi:10.1016/j.sab.2016.12.003.

Collinet, M., Médard, E., Charlier, B., Vander Auwera, J., and Grove, T.L., 2015, Melting of the primitive martian mantle at 0.5-2.2 GPa and the origin of basalts and alkaline rocks on Mars: Earth and Planetary Science Letters, v. 427, p. 83–94, doi:10.1016/j.epsl.2015.06.056.

Cousin, A. et al., 2017, Classification of igneous rocks analyzed by ChemCam at Gale crater, Mars: Icarus, v. 288, p. 265–283, doi:10.1016/j.icarus.2017.01.014.

DePaolo, D.J., 1981, Trace element and isotopic effects of combined wallrock assimilation and fractional crystallization: Earth and Planetary Science Letters, v. 53, p. 189–202, doi:10.1016/0012-821X(81)90153-9.

E. Vander Kaaden, K., M. McCubbin, F., R. Nittler, L., N. Peplowski, P., Z. Weider, S., A. Frank, E., and J. McCoy, T., 2017, Geochemistry, mineralogy, and petrology of boninitic and komatiitic rocks on the mercurian surface: Insights into the mercurian mantle: Icarus, v. 285, p. 155–168, doi:10.1016/j.icarus.2016.11.041.

Ehlmann, B.L., Mustard, J.F., Murchie, S.L., Bibring, J.P., Meunier, A., Fraeman, A.A., and

Langevin, Y., 2011, Subsurface water and clay mineral formation during the early history of Mars: Nature, v. 479, p. 53–60, doi:10.1038/nature10582.

Elkins-Tanton, L.T., Chatterjee, N., and Grove, T.L., 2003, Experimental and petrological constraints on lunar differentiation from the Apollo 15 green picritic glasses: Meteoritics and Planetary Science, v. 38, p. 515–527, doi:10.1111/j.1945-5100.2003.tb00024.x.

Filiberto, J. et al., 2018, Shergottite Northwest Africa 6963: A Pyroxene-Cumulate Martian Gabbro: Journal of Geophysical Research: Planets, v. 123, p. 1823–1841, doi:10.1029/2018JE005635.

Filiberto, J., Dasgupta, R., Kiefer, W.S., and Treiman, A.H., 2010, High pressure, near-liquidus phase equilibria of the Home plate basalt Fastball and melting in the Martian mantle: Geophysical Research Letters, v. 37, p. 1–4, doi:10.1029/2010GL043999.

Ghiorso, M.S., and Gualda, G.A.R., 2015, An H2O–CO2 mixed fluid saturation model compatible with rhyolite-MELTS: Contributions to Mineralogy and Petrology, v. 169, p. 1–30, doi:10.1007/s00410-015-1141-8.

Gilmore, M., Treiman, A., Helbert, J., and Smrekar, S., 2017, Venus Surface Composition Constrained by Observation and Experiment: Space Science Reviews, v. 212, p. 1511–1540, doi:10.1007/s11214-017-0370-8.

Goossens, S., Sabaka, T.J., Genova, A., Mazarico, E., Nicholas, J.B., and Neumann, G.A., 2017, Evidence for a low bulk crustal density for Mars from gravity and topography: Geophysical Research Letters, v. 44, p. 7686–7694, doi:10.1002/2017GL074172.

Goudge, T.A., Mustard, J.F., Head, J.W., Fassett, C.I., and Wiseman, S.M., 2015, Journal of geophysical research: Journal of Geophysical Research: Planets, v. 120, p. 775–808, doi:10.1038/175238c0.

Gross, J., and Filiberto, J., 2014, Granitic compositions in gabbroic martian meteorite NWA 6963 and a possible connection to felsic compositions on the martian surface, *in* 45th Lunar and Planetary Science Conference, p. #1440.

Grove, T.L., and Brown, S.M., 2018, Magmatic processes leading to compositional diversity in igneous rocks: Bowen (1928) revisited: American Journal of Science, v. 318, p. 1–28, doi:10.2475/01.2018.02.

Gualda, G.A.R., Ghiorso, M.S., Lemons, R. V., and Carley, T.L., 2012, Rhyolite-MELTS: A modified calibration of MELTS optimized for silica-rich, fluid-bearing magmatic systems: Journal of Petrology, v. 53, p. 875–890, doi:10.1093/petrology/egr080.

Hahn, B.C., and McLennan, S.M., 2007, Evolution and Geochemistry of the Martian Crust: Integrating Mission Datasets: Seventh International Conference on Mars, v. 1353, p. 3179, http://adsabs.harvard.edu/abs/2007LPICo1353.3179H%0Ainternal-pdf://0.0.1.201/2007LPICo1353.html.

Herd, C.D.K., Borg, L.E., Jones, J.H., and Papike, J.J., 2002, Oxygen fugacity and geochemical variations in the martian basalts: Implications for martian basalt petrogenesis and the oxidation state of the upper mantle of Mars: Geochimica et Cosmochimica Acta, v. 66, p. 2025–2036, doi:10.1016/S0016-7037(02)00828-1.

Hewins, R.H. et al., 2017, Regolith breccia Northwest Africa 7533: Mineralogy and petrology with implications for early Mars: Meteoritics and Planetary Science, v. 52, p. 89–124, doi:10.1111/maps.12740.

Lognonné, P. et al., 2020, Constraints on the shallow elastic and anelastic structure of Mars from InSight seismic data: Nature Geoscience, v. 13, p. 213–220, doi:10.1038/s41561-020-0536-y.

Marsh, B.D., 1981, On the crystallinity, probability of occurrence, and rheology of lava and magma: Contributions to Mineralogy and Petrology, v. 78, p. 85–98, doi:10.1007/BF00371146.

McCubbin, F.M., Boyce, J.W., Srinivasan, P., Santos, A.R., Elardo, S.M., Filiberto, J., Steele, A., and Shearer, C.K., 2016, Heterogeneous distribution of H2O in the Martian interior: Implications for the abundance of H2O in depleted and enriched mantle sources: Meteoritics and Planetary Science, v. 51, p. 2036–2060, doi:10.1111/maps.12639.

McCubbin, F.M., Vander Kaaden, K.E., Peplowski, P.N., Bell, A.S., Nittler, L.R., Boyce, J.W., Evans, L.G., Keller, L.P., Elardo, S.M., and McCoy, T.J., 2017, A Low O/Si Ratio on the Surface of Mercury: Evidence for Silicon Smelting? Journal of Geophysical Research: Planets, v. 122, p. 2053–2076, doi:10.1002/2017JE005367.

Payré, V., Siebach, K.L., Dasgupta, R., Udry, A., Rampe, E.B., and Morrison, S.M., 2020, Constraining Ancient Magmatic Evolution on Mars Using Crystal Chemistry of Detrital Igneous Minerals in the Sedimentary Bradbury Group, Gale Crater, Mars: Journal of Geophysical Research: Planets, v. 125, doi:10.1029/2020JE006467.

Plesa, A.C., Padovan, S., Tosi, N., Breuer, D., Grott, M., Wieczorek, M.A., Spohn, T., Smrekar, S.E., and Banerdt, W.B., 2018, The Thermal State and Interior Structure of Mars: Geophysical Research Letters, v. 45, p. 12,198-12,209, doi:10.1029/2018GL080728.

Rogers, A.D., and Nekvasil, H., 2015, Feldspathic rocks on Mars: Compositional constraints from infrared spectroscopy and possible formation mechanisms: Geophysical Research Letters, v. 42, p. 2619–2626, doi:10.1002/2015GL063501.Received.

Santos, A.R., Agee, C.B., McCubbin, F.M., Shearer, C.K., Burger, P. V., Tartèse, R., and Anand, M., 2015, Petrology of igneous clasts in Northwest Africa 7034: Implications for the

petrologic diversity of the martian crust: Geochimica et Cosmochimica Acta, v. 157, p. 56–85, doi:10.1016/j.gca.2015.02.023.

Sautter, V. et al., 2015, In situ evidence for continental crust on early Mars: Nature Geoscience, v. 8, p. 605–609, doi:10.1038/ngeo2474.

Semprich, J., and Filiberto, J., 2020, High-pressure metamorphic mineralogy of the Martian crust with implications for density and seismic profiles: Meteoritics & Planetary Science, v. 15, p. 1–15, doi:10.1111/maps.13535.

Shahrzad, S., Kinch, K.M., Goudge, T.A., Fassett, C.I., Needham, D.H., Quantin-Nataf, C., and Knudsen, C.P., 2019, Crater Statistics on the Dark-Toned, Mafic Floor Unit in Jezero Crater, Mars: Geophysical Research Letters, v. 46, p. 2408–2416, doi:10.1029/2018GL081402.

Shellnutt, J.G., 2013, Petrological modeling of basaltic rocks from Venus: A case for the presence of silicic rocks: Journal of Geophysical Research E: Planets, v. 118, p. 1350–1364, doi:10.1002/jgre.20094.

Squyres, S.W. et al., 2007, Pyroclastic activity at home plate in Gusev crater, Mars: Science, v. 316, p. 738–742, doi:10.1126/science.1139045.

Taylor, S.R., and McLennan, S.M., 2009, Planetary Crusts: Their Composition, Origin and Evolution: Cambridge, UK, Cambridge University Press.

Udry, A., Gazel, E., and McSween, H.Y., 2018, Formation of Evolved Rocks at Gale Crater by Crystal Fractionation and Implications for Mars Crustal Composition: Journal of Geophysical Research: Planets, v. 123, p. 1525–1540, doi:10.1029/2018JE005602.

Udry, A., Howarth, G.H., Herd, C., Day, J., Lapen, T.J., and Filiberto, J., 2020, What martian meteorites reveal about the interior and surface of Mars: Earth and Space Science Open Archive, p. 55, https://doi.org/10.1002/essoar.10503123.2.

Usui, T., Alexander, C.M.O.D., Wang, J., Simon, J.I., and Jones, J.H., 2015, Meteoritic evidence for a previously unrecognized hydrogen reservoir on Mars: Earth and Planetary Science Letters, v. 410, p. 140–151, doi:10.1016/j.epsl.2014.11.022.

Vigneresse, J.L., Barbey, P., and Cuney, M., 1996, Rheological transitions during partial melting and crystallization with application to felsic magma segregation and transfer: Journal of Petrology, v. 37, p. 1579–1600, doi:10.1093/petrology/37.6.1579.

Wieczorek, M.A., and Zuber, M.T., 2004, Thickness of the Martian crust: Improved constraints from geoid-to-topography ratios: Journal of Geophysical Research E: Planets, v. 109, p. 1–16, doi:10.1029/2003je002153.

Wu, P., Gazel, E., Udry, A., Setera, J.B., and Ostwald, A., 2021, Melt inclusions in chassignite NWA 2737: A link between processes recorded in Martian meteorites and rocks at Gale crater: Meteoritics and Planetary Science, v. 56, p. 1328–1349, doi:10.1111/maps.13700.

Yoshizaki, T., and Mcdonough, W.F., 2020, ScienceDirect The composition of Mars: Geochimica et Cosmochimica Acta, v. 273, p. 137–162, doi:10.1016/j.gca.2020.01.011.

Chapter 3: Melt Inclusion Heterogeneity in Nakhlite and Chassignite Meteorites and Evidence for Complicated, Multi-Generational Magmas

3.1 Notice of Publication Submission

This chapter has been formatted from an article that has been accepted for publication in Meteoritics and Planetary Science Journal pending revisions. Authors include Amanda M. Ostwald, Arya Udry, James M. D. Day, and Juliane Gross. Amanda Ostwald performed all analyses and writing for this chapter.

3.2 Abstract

Nakhlite and chassignite meteorites are cumulate rocks thought to originate from the same location on Mars. Petrogenetic relationships between nakhlites and chassignites are not fully constrained, and the two cumulus phases in nakhlites—olivine and clinopyroxene—possibly formed together from one magma, or separately from different magmas. Primary magma compositions can be determined from studies of melt inclusions trapped within early-formed mineral phases. Melt inclusions frequently undergo post-entrapment effects (e.g., cation exchange), and when such processes occur, there can be significant changes to their compositions. Here, we report major-, minor-, and trace-element abundances for melt inclusions in cumulus phases in nakhlites and chassignites. The melt compositions that they record are variable (MgO = 2.50–13.5 wt.%, K2O = 0.03–3.03 wt.%, La/Yb = 2.46–16.4) and indicate diffusive reequilibration with changing magma composition outside of their host mineral phases. Evidence for diffusive reequilibration suggests that nakhlite and chassignite magmas were generated in an open-system, and cumulus phases underwent magma storage and mixing. Such processes may be akin to those

which occur in terrestrial intrusive magmatic systems by open-system magma recharge. The nakhlite and chassignite suite therefore provide insights into magmatic processes during magma storage and transit on Mars.

3.1 Introduction

The nakhlites and chassignites are cumulate rocks with similar crystallization and ejection ages (~1.3 Ga and ~11 Ma, respectively), originating from the same location on Mars (Nyquist et al. 2001; Cohen et al. 2017; Udry and Day 2018; Udry et al. 2020). At the time of writing (spring 2023), there are 27 unpaired (of which 17 are paired) nakhlites and three chassignites, making the two classes together the largest single-origin suite of rocks from Mars. Despite their shared provenance, their petrogenetic and emplacement histories are not fully constrained, largely due to the lack of knowledge concerning their field relations prior to ejection from Mars. The two sample classes may have been emplaced separately as flows or sills at or near the martian surface (Day et al. 2006; Sautter et al. 2015; Jambon et al. 2016; Udry and Day 2018). Nakhlites are clinopyroxene-rich, otherwise containing variable amounts of fayalitic olivine, glass, plagioclase, and minor phosphate, sulfide minerals, intercumulus olivine, and titanomagnetite (e.g., Treiman 2005). Chassignites are dunites, and they are primarily comprised of olivine with minor amounts of chromite, plagioclase, orthopyroxene, and phosphate (Beck et al., 2006). The bulk nakhlites and chassignites share similar trace element patterns, and so their magmas are thought to have formed from partial melting of a single, depleted source that was likely oxidized relative to the martian mantle as sampled by shergottites (Treiman 2005; McCubbin et al. 2013; Cohen et al. 2017b; Udry and Day 2018; Day et al. 2018; Udry et al. 2020; Nicklas et al. 2021).

Mantle-derived igneous rocks form from parental partial melts, which are initially unaffected by later processes such as mineral accumulation, assimilation, or the addition of exogenous fluids. For example, the bulk composition of a cumulate rock, which has undergone fractionation, cannot be used to determine its parental melt composition. Instead, a common method to determine the parental melt for a cumulate rock is to study melt inclusions contained

within the earliest-formed mineral phases. A melt inclusion is a pocket of magma entrapped in mineral phases as they crystallize, and if entrapment occurs immediately in an early-crystallizing host, it may be considered a parental melt composition for that host phase and bulk rock (e.g., Kent 2008; Schiano, 2003; Wallace et al. 2021).

Past studies concerning the nakhlite parental melt composition have relied heavily on just three meteorites in the suite: Nakhla, Governador Valadares, and Miller Range (MIL) 03346 (Harvey and McSween 1992; Treiman 1993; Varela et al. 2001; Stockstill et al. 2005; Imae and Ikeda 2007; Sautter et al. 2012; Goodrich et al. 2013). These studies arrived at different conclusions concerning nakhlite petrogenesis, in part because they used different techniques for melt inclusion analysis (reheating an inclusion to homogenize versus *in situ* analyses). There are a limited number of studies on the chassignite parental magma using melt inclusion analysis (e.g., Johnson et al. 1991; He et al. 2013); however, consistently applied methods to a coherent analysis of both nakhlite and chassignite melt inclusions has not been done. This omission is important for several reasons. First, McCubbin et al. (2013) demonstrated that a Cl-rich exogenous fluid may have interacted with the nakhlite magma after the chassignite olivine cumulates formed to account for variation in volatile species. Second, Udry and Day (2018) found that fractional crystallization, in addition to a Cl-rich magmatic fluid, contributed to relative LREE-enrichment in chassignites, but these authors noted that more than one parental magma from the same depleted mantle source may have generated the complex suite. Third, there is little consensus on the relative formation history of the nakhlite cumulus phases (olivine and pyroxene). Some authors have found that nakhlite olivine forms together with the pyroxene and intercumulus material, and is phenocrystic (e.g., Harvey and McSween 1992; Stockstill et al. 2005; Udry and Day 2018), while others have suggested that olivine forms from a distinct magma composition and is entrained in the bulk

nakhlite magma as a xenocryst, or "foreign" crystal cargo (e.g., Sautter et al. 2012; Goodrich et al. 2013).

Here we present the first combined melt inclusion study of nakhlite and chassignite meteorites. All melt inclusions were studied using the same methods, and so results within the study are internally consistent within both olivine and clinopyroxene. Furthermore, we present data for major, minor and trace elements in nakhlite and chassignite melt inclusions providing the most comprehensive study to date of melt inclusions in the nakhlites and chassignites.

3.2 Methods

3.2.1 Major Element Compositional Analysis

Melt Inclusion and Sample Selection

We analyzed melt inclusions (MIs) in nakhlite polished thin sections for nakhlite samples Miller Range (MIL) 090030 (n=3, denoting number of MIs), MIL 090032 (n=4), Governador Valadares (n=1), Caleta el Cobre (CeC) 022 (n=14), and Northwest Africa (NWA) 10645 (n=8). We also analyzed MIs in chassignite polished thin sections for samples NWA 2737 (n=6), and Chassigny (n=10). All MIs were examined on a *Nikon* Eclipse LV100N POL petrographic microscope and were subsequently imaged using electron probe microanalysis (EPMA). These steps were taken to determine the overall nature of the MIs: that they did not fall on fractures within their host mineral, and to ensure that they were not visibly altered (i.e., by iddingsite, a mixture of alteration phases common in nakhlites). For analysis by electron microprobe, MIs must be larger than the excitation volume caused by an electron beam to avoid mixing the signal with that of the host phase, making melt inclusions smaller than ~10 μm in diameter unsuitable for microprobe analyses. Additionally, prior work has indicated that syn-entrapment effects (such as

boundary layer enrichments) may affect compositions in small (<15 μm diameter) inclusions more significantly effects, although such effects are typically negligible in natural MIs (e.g., Kent 2008; Sonzogni and Treiman 2015). Selection bias was therefore for MIs with diameters greater than 15 μm. Detailed sample and MI selection, as well as all other methodological steps in data collection and reduction, are outlined in Fig. B1.

Major and minor element analytical methods

There are two approaches to MI analysis: *in situ* analysis of a thin section, or experimental reheating and rehomogenization of an uncut mineral or bulk sample. Experimental treatment of MIs is intended to reverse post-entrapment effects by restoring the inclusion to its initial liquid state, at which point it is quenched and studied (e.g., Schiano 2003; Adam J.R. Kent 2008; Goodrich et al. 2013). Heating a sample without first observing the MI *in situ* leads to certain risks, including the melting and addition of cognate (large, separately entrapped phases which do not crystallize from the entrapped melt) and alteration phases (see Goodrich et al. [2013] supplemental files for detailed discussion). Since the MI are three-dimensional objects, there is no guarantee this method will be effective, especially if formation temperatures are over- or under-estimated. Additional uncertainties arise with rapid diffusion of volatile elements and compounds through the host phase, or cation exchange during heating (Goodrich et al. 2013). Equally, there are uncertainties associated with *in situ* analysis of unheated samples, such as: matrix effects or phase mixing in electron beam analysis of complex and small inclusions, and key limitations imparted with two-dimensional sectioning of three-dimensional inclusions. Notably, some authors (e.g., Treiman 1993; Goodrich et al. 2013) average MI bulk compositions in thin section by size in an effort to reconstruct their three-dimensional composition; we elect to treat each inclusion

composition separately for reasons explained later. Notwithstanding these issues, both experimental and *in situ* methods have found utility, with the non-destructive thin-section method being particularly appropriate to limited mass extraterrestrial materials (e.g., Treiman 1993).

Different approaches to *in situ* electron microprobe studies of unheated samples have also been explored with the goal of minimizing analytical errors. Goodrich et al. (2013) conducted gridded EMP analyses by systematically analyzing a rectangle filled with focused beam points with a spacing determined by excitation volume typical of the beam size and instrument settings. Conducting an analysis of small, heterogenous inclusions with a grid of focused points has the benefit of reducing phase mixing compared to diffuse beam methods, discussed later. Grid techniques, however, require significant analytical time. Additional issues arise from calibration of diverse compositional components of MI using an EPMA, and collateral effects on ZAF corrections for matrix effects, as the atomic number (Z), absorption (A), and fluorescence (F) inherent to a given phase must be corrected for against a standard with a similar matrix (e.g., Goldstein et al., 2018).

We elected to analyze individual phases present in MI for their major and minor element chemistry on the *JEOL* JXA-8900 EPMA at the University of Nevada, Las Vegas and the *JEOL* JXA-8200 Superprobe at Rutgers University under similar analytical conditions (Fig. B1). An accelerating voltage of 15 kV, with a 10 nA beam current for MIs and a 20 nA beam current for host phases was employed. Where glassy phases (with or without microlytic material) were large enough, a spread beam between 2 μm and 5 μm diameter was used to minimize volatile migration. Peak counts for all elements were 30 seconds, except Na, which was measured with a 10 second peak count time. Analyses were calibrated against standards, which are listed in Table B2, and raw data were treated with standard PAP corrections. Some MI analyses overlapped with the host

phase, and those MIs were then excluded from further consideration. In one glassy MI within MIL 090032, we conducted both a defocused gridded analysis (5 μm beam diameter) and a focused (1 μm beam diameter) traverse for comparison; the PTL results can be found in Appendix B (Fig. B2) and results fall within ± 1 wt.% oxides (within model uncertainties). Elemental maps and concurrent backscattered electron (BSE) images of MIs were conducted at accelerating voltages of 15 kV on four spectrometers to discern between glass, pyroxene, and amphibole: Na Kα on TAP, Mg Kα on TAP, K Kα on PETJ, and Ca Kα on PETH.

Present Bulk Composition to Parental Trapped Liquid

We used *Fiji* software for pixel counting in order to determine the volume contribution of each phase present in the analyzed MIs (Schindelin et al. 2012) (Fig. B1). We used both BSE and elemental maps to constrain the volume abundances of each phase present. All volume percentages were multiplied by the densities of their respective phases to arrive at the modal abundances of each phase. The major and minor element composition of each phase was then multiplied by its modal abundance and the total was then normalized to 100%. We refer to the resultant composition as the Present Bulk Composition (PBC), which is an intermediate step in the calculation for the parental melt composition.

The PBC, as the untreated bulk composition of the MI is the compositional result of the post-entrapment process of diffusion that must be corrected for in order to obtain a melt composition at the time of entrapment (called the parental trapped liquid, or PTL) (e.g., Basu Sarbadhikari et al. 2011; Danyushevsky et al. 2000; Goodrich et al. 2009; Danyushevsky and Plechov 2011; Sonzogni and Treiman 2015). Melt inclusions inevitably nucleate their host phase along their margins during cooling to achieve equilibrium (Danyushevsky et al. 2000). This host

phase becomes increasingly depleted in MgO as crystallization progresses, which in turn prompts diffusive reequilibration and Fe-loss in the bulk inclusion. If the inclusion is reheated, the host phase may melt and result in Fe-gain. These effects can be corrected for in the *Petrolog3* software, which conducts mass-balance calculations that return the bulk inclusion composition to a user-defined initial FeO_T (total FeO, or FeO + Fe_2O_3) condition (Danyushevsky and Plechov 2011) (Fig. B1). A key assumption made during *Petrolog3* calculations is that the host mineral is contained within a closed system bulk magma and is not a xenocryst entrained in a distinct magma.

Nakhlite olivine cores are typically diffusively homogenized in terms of FeO and MgO content, and some authors suggest nakhlite olivine reequilibrated with an unrelated external magma (e.g., Longhi and Pan 1989; Treiman 1993; 1986). Because an initial composition for nakhlite olivine cores cannot be established, there is no simple solution for FeO_T of nakhlite melts in equilibrium with unequilibrated nakhlite olivine. To test the effects of different FeO_T values on the PTL, we elected to use high and low ranges of FeO_T from other calculated nakhlite parental melts: 28.9 wt.% (Goodrich et al. 2013) and 22.2 wt.% (Imae and Ikeda 2007) FeO_T. Following the same procedure, we selected 20.3 wt.% FeO_T for the MI in Chassigny (Filiberto 2008), and 19.0 wt.% FeO_T for MI in NWA 2737 (He et al. 2013). Selected FeO_T values encompass both experimentally-determined (Filiberto 2008) and analytically-determined (Imae and Ikeda 2007; Goodrich et al. 2013; He et al. 2013) parental melt compositions.

Pyroxene-hosted MI PTLs were processed with Rhyolite-MELTS using the alphaMELTS interface (Fig. B1). Rhyolite-MELTS is an algorithm for the alphaMELTS thermodynamic modeling software that is calibrated for low pressure (0–1 GPa) mafic to felsic systems (Gualda et al. 2012; Ghiorso and Gualda 2015). Pyroxene-hosted MIs typically contain two phases: glass and a halo of pyroxene that is chemically distinct from the host phase. Goodrich et al. (2013) found

that halo pyroxene in Nakhla MIs likely reequilibrated with their host minerals. Per their methods, we calculated the original halo volume for pyroxene in equilibrium with its melt by adjusting the modal abundance of the measured halo pyroxene until Rhyolite-MELTS models yielded a similar composition of pyroxene as the liquidus phase (the first phase to crystallize). The resultant modeled bulk liquid and pyroxene composition, when the two are in equilibrium, was then taken to be the PTL for a given pyroxene-hosted MI. Pyroxene-hosted MI PTLs and all other comparative models were conducted as constrained at the FMQ boundary and low pressure (1 kbar), similar to Goodrich et al. (2013), but these conditions are also appropriate for nakhlites as shallowly-emplaced magma sills, or as lavas (e.g., Balta et al. 2017; Corrigan et al. 2015; Jambon et al. 2016; Udry et al. 2020; Udry and Day 2018).

3.2.2 Trace Element Compositions

LA-ICP-MS analysis: Spot Measurements

All spot (single point) trace element measurements were conducted at the Scripps Institution of Oceanography on a *Thermo Fisher Scientific* iCAP Qc inductively coupled plasma mass spectrometer coupled to an *Elemental Scientific* NWR UP213 laser ablation system (LA-ICP-MS) (Fig. B1). Analysis employed a fluence of 3.5 J/cm^2 at a 5 Hz repetition rate and flushed the 3 cm^3 ablation cell with a He carrier gas prior to mixing with Ar mix at a flow of ~1 L/min. Spot sizes were dependent on the inclusion size. A 100 μm beam size was used for inclusions larger than ~50 μm in diameter, while a 50 μm beam size was used for inclusions smaller than 50 μm in diameter. Analytical sessions only used a single spot size for unknowns and standards. All analyses were bracketed with analyses of standards BHVO-2g, BCR-2g, and BIR-1g conducted with the same instrument settings and spot sizes (i.e., MIs measured with a 100 μm beam were bracketed

with 100 μm beam standard measurements). Data was collected for ~60 s, with ~20 s of background and ~40 s of ablation. Analyses were buffered by a 120 s washout time. The time-resolved data was processed offline at UNLV using *iolite 4*, a software which allows for visually-aided selection of data, automated quantification against internal standards, and quality checks against external standards (Paton et al. 2011). All data were processed using the trace element data reduction scheme with linear smoothing, and data were selected to remove any outlying points caused by zoning, unseen inclusions, or penetration into underlying phases. Melt inclusion data were specifically chosen by first ratioing elements that were compatible in the host phase against incompatible elements (e.g., Ca/La in pyroxene) throughout the analysis, and then selecting a smooth plateau of the time-resolved ratioed data to ensure consistent host to ratio proportions throughout.

LA-ICP-MS analysis: host phase removal corrections

For MI point analyses, the laser beam diameter frequently overlapped the host phase on the polished thin section surface and at depth. Host compatible and incompatible elements in the laser output data were ratioed, and data were only selected along continuous ratio values to ensure relative host and MI volumes remained the same throughout the analysis. We imaged all MIs prior to analysis. We then analyzed images of the MIs and the ablation pits with the *FIJI* software using pixel counting to determine the volume of ablated hosts versus ablated inclusions. All host phases were also analyzed on the LA-ICP-MS separately from, but adjacent to, the analyzed MI. Those host phase trace element data were then normalized to the volume of host phase that was ablated with the MI, and the resultant trace element values were subtracted from the MI trace element profile to isolate the signal from the beam-averaged MI.

Trace Element Maps Using LA-ICP-MS

Trace element maps were collected using an iCAP Qc ICP-MS and NWR193 Excimer laser at UNLV, a TwoVol 2 ablation cell, and He-Ar carrier gas (Fig. B1). Rasters were conducted with a 12 J/cm^2 fluence and 10 Hz repetition rate. Scan speeds were kept at half the numerical value of the size of the square (XYR) beam with 1 μm of overlap between each raster line, per Ubide et al. (2015). For 24 μm beam sizes, we used a 12 s scan speed. For a 12 μm square beam, we used a 6 s scan speed. NIST 610 rasters were conducted under the same conditions in the same sessions. Rasters were conducted in a repeated left-to-right, down, right-to-left, down motion. The raster data was then processed with the semi-quantitative trace element scheme in *iolite 4* and the data was coordinated to a 2D plane using NWR-generated laserlog files (Paton et al. 2011). The distance between the laser and the ICP-MS creates a drag effect in the rasters that cannot be rigorously corrected for, so the effect was retained.

3.3. Results

3.3.1 Melt Inclusion Petrography

A total 47 MIs were studied, with 30 hosted in nakhlites and 17 in chassignites (Table B1). All MIs can be arranged into two general petrographic types: simple or complex. Simple MIs are primarily composed of glass and microlytic phases are 1 μm or less in width, and are qualitatively determined to be pyroxene using Energy Dispersive Spectrometry (EDS). Occasionally, simple MIs may also contain large cognate phases, which likely were enclosed with melt (e.g., Goodrich et al. 2013). Complex MIs are composed of mineral phases (from ~1-10 μm in diameter) that crystallized from the entrapped melt, all of which are contained in a glassy matrix. Both types of

MIs can include void spaces, presumably where volatile elements were once concentrated. All MIs may be crosscut by shear fracturing caused by impact, but this effect is most notable in the chassignite-hosted MIs (Fig. 3.1–3.4). There is no visible devitrification or crushing in any shocked MIs.

Olivine-hosted MIs in the nakhlites range in size from ~10 μm diameter to ~150 μm diameter (as noted previously, only MI with diameters of 15 μm or larger were analyzed) (Fig. 3.1–3.2). Nakhlite olivine-hosted MIs may be either simple or complex. We found that complex nakhlite olivine-hosted MIs variably contain sulfides, oxides (titanomagnetite), and pyroxene (>1 μm) that appear to have mineralized inward from the inclusion rims, leaving a heterogenous glass phase that fills interstices (Fig. 3.1). Some complex MI also contain small (<1 μm) olivine grains along the rim. Simple MIs consist of heterogenous glass containing microlytic pyroxene (Fig. 3.1). All MIs in nakhlite olivine are rounded to subrounded and may display shear effects. The largest of these MIs was hosted in the Governador Valadares meteorite (Fig. 3.1–3.2). X-ray composite element maps show a central glass phase that is somewhat homogenous in SiO_2 but containing a heterogenous distribution of Na_2O_3 and K_2O (Fig. 3.3b–c). A <1 μm rim of olivine is seen around the rim (Fig. 3.2a).

All nakhlite pyroxene-hosted MIs are petrographically simple in the samples analyzed. They consist of a glassy phase containing microlytic pyroxene, and frequently also contain cognate oxides along their perimeters. Pyroxene immediately surrounding MIs (called “halo” pyroxene) appears brighter in backscattered electron images (Fig. 3.1). Pyroxene-hosted MIs are elongated and irregular in shape, although they typically appear to take on right-angled cleavage patterns (Fig. 3.1). Long axes for analyzed pyroxene-hosted MIs ranged from ~10 μm to ~130 μm, with short axes between 5 and 80 μm.

All but one MI in the chassignites occurred in olivine hosts, with one MI contained in an oxide phase. Olivine-hosted MIs in the chassignites are always rounded and complex. (Fig. 3.3). Glass is typically a central phase within the MI. High- and low-Ca pyroxene, and occasionally amphibole (kaersutite) occurs from the rims inward (Fig. 3.3). Oxides (sometimes large, ~10 μm) and small phosphates (<1 μm) may be scattered inside the MIs. All MIs display significant shear displacement along impact fractures but appear to have been rounded to sub-rounded prior to any impacts (Fig. 3.3). Diameters range from ~35 μm to ~150 μm for MI in both NWA 2737 and Chassigny.

3.3.2. Major and Minor Element Abundances

Major and minor element chemistry in MIs may be divided into untreated PBCs (present bulk compositions), and modeled PTL (parental trapped liquid) compositions. Importantly, PBC compositions are not corrected for post-entrapment effects such as reequilibration. These effects are corrected for in the PTL calculations; however, there are limitations to the model as discussed previously.

Present Bulk Composition Results

The PBC calculations for the MIs from nakhlites and chassignites are highly variable (Table 2.1). Some olivine-bearing MIs contain only a glassy phase that was homogenized under the beam (e.g., MIL 090030 olivine-hosted MIs), making their single-phase glass composition the PBC. Such MIs are MgO-depleted, with Mg# (Molar MgO × 100/[Molar MgO + Molar FeO*]) values as low as 1.78. Other olivine-bearing MIs are polycrystalline, such as in Governador Valadares, which has a higher Mg# value of 16.8 likely due to excess contributions from MgO-

bearing pyroxene (Fig. 3.3). Pyroxene-hosted PBCs are more magnesian on average than olivine-hosted PBCs due to the addition of halo pyroxene, with Mg# ranging from 15.4 to 33.2. Pyroxene-hosted PBC also tend to be extremely TiO_2-enriched, with a total wt.% as high as 16.4. This is an effect of contributions from large, likely cognate, Ti-bearing oxides. Chassignite-hosted PBCs are the most mafic, with Mg# ranging from 65.3 to 79.5. The PBC calculations for MIs are variable overall; for instance, CeC 022 ranges from 1.2 to 5.7 wt.% Na_2O, while Chassigny PBCs span 0.1–1.0 wt.% Na_2O.

3.3.3 Parental Trapped Liquid Results

Nakhlites

Olivine-hosted PTLs were calculated in *Petrolog3* with two FeO_T values determining model outcomes. Table 2.2 lists all PTL values for successful MI analyses. Nakhlite olivine-hosted PTLs were reconstructed in two MIs in MIL 090030, three MIs in MIL 090032, and a single MI in Governador Valadares. All olivine-hosted PTLs are listed twice in table 2.2 for a given MI. We use the notation of FeO* for total FeO and Fe_2O_3 in our calculated PTL, in contrast to $FeO_{T,}$ as the predicted value for bulk initial Fe contents in the parental magma (see 2.1.2. above for an explanation). Differences in bulk FeO* vary depending on initial composition. For the MIL 090030 and 090032 MIs, the difference in FeO* between A and B models is ~4.8 wt.%, ranging between ~22.9 and 28.2 wt.% for a ~20% difference in total. Governador Valadares has a larger FeO* range, from 22.8–29.7 wt.%, a difference of ~7 wt.% or ~26%. The three different EMP analytical techniques (gridded analysis, defocused and focused traverse) produce overlapping results when different FeO_T values are applied (Fig. B2).

Major element abundances in PTLs show greater variability with the different FeO_T used when compared to minor element abundances. In MIL 090030, SiO_2 varies by ~5% (46.6 to 48.9 wt.%, and 49.8 to 52.5 wt.%), while P_2O_5 varies by just ~0.1% (0.60 to 0.69 wt.% and 0.80 to 0.70 wt.%) (Fig. 3.5). Changes in MgO are minimal between models, with the largest change (~1.0 wt.% difference) in an MI in Governador Valadares which was between 2.50 and 3.51 wt.% MgO (Fig. 3.5). The MIL PTLs are more primitive than the Governador Valadares PTL, with the latter ranging between ~4.6 and 5.3 in Mg# (Table 2.2). Notably, K_2O is enriched in all nakhlite olivine-hosted MIs, from 0.59 to 1.05 wt.% (Fig. 3.5). Alkali element ratios (K_2O/Na_2O) do not change between A and B models, with MIL 090030 the most Na_2O-rich at 0.31 and Governador Valadares is the most K_2O-enriched at 0.62 (Table 2.2, Fig. 3.5).

Pyroxene-hosted MIs were not processed with *Petrolog3*. Consequently, the 11 MIs have only one PTL (in NWA 10645, MIL 090030, and CeC 022). Pyroxene-hosted MIs fall largely in a narrow range of compositions. The most siliceous PTLs are in CeC 022 pyroxene, ranging from 52.4–58.8 wt.% SiO_2 (Fig. 3.5), whereas NWA 10645 is the least siliceous, with values between 52.9–53.8 wt.% SiO_2 (Fig. 3.5). Pyroxene-hosted PTLs are less ferroan than olivine-hosted PTLs, ranging from 9.28 (CeC 022) to 19.7 (NWA 10645) wt.% FeO* (Fig. 3.6). Despite this, pyroxene-hosted PTLs are more primitive, with Mg#s ranging from 8.3 to 14.1 (both CeC 022) (Table 2.2). Pyroxene-hosted PTLs are also more K_2O enriched than olivine-hosted MIs, ranging from 0.69–3.03 wt.% K_2O (NWA 10645 and NWA 90030, respectively) (Fig. 3.5). Potassium contents are typically larger than those of sodium, with K_2O/Na_2O between 0.29 and 5.41.

Chassignites

Olivine-hosted chassignite MIs were processed in *Petrolog3* using a single literature FeO_T value for each NWA 2737 and Chassigny. The result is that PTL FeO and MgO values within each sample are similar (<1 wt.% difference at most for both oxides, Table 2.2, Fig. 3.5). Despite this, Chassigny PTL SiO_2 abundances range from 45.4 to 51.8 wt.%, and NWA 2737 from 45.0 to 52.0 wt.% (Table 2.2, Fig. 3.5). The PTLs in NWA 2737 contain the least CaO (~4.65 wt.%, compared to ~9.2 wt.% in Chassigny PTLs) (Table 2.2, Fig. 3.5). Alkali metals tend to be depleted in Chassignite PTLs compared to the nakhlites: K_2O ranges from 0.03 to 0.67 wt.%, and Na_2O from 0.16 to 1.88 wt.% in the chassignite PTLs. However, the average K_2O/Na_2O ratio for nakhlite olivine-hosted PTLs and the chassignite PTLs are similar at 0.41 and 0.38, respectively (Table 2.2). Chassignite PTLs are the most mafic of all the MIs studied, with Mg#s ranging from 17 to 26.

3.3.4 Trace Element Abundances

Trace Element Point Analyses

Point analyses on MIs in the nakhlites and chassignites revealed similar rare earth element (REE) trends (Fig. 3.6a). Their CI-normalized REE patterns are also parallel to bulk rock analyses. Some pyroxene-hosted nakhlite MIs display slight negative europium anomalies with Eu/Eu* (= $Eu_{CI}/[Sm_{CI} \times Gd_{CI}] \times 0.5$) ranging between 0.01 and 0.96. Negative Eu are most visible in pyroxene-hosted MIs (Fig. 3.6a). Chondrite-normalized REE values, when ratioed, display significant heterogeneity, but typically show relative enrichment in the LREEs (light REE) relative to the HREEs (heavy REE) (Fig. 3.6b). Ratioed LREEs and HREEs are variable, as seen in La/Lu_{CI} which range from ~1–8. Other element ratios like Ce/Lu_{CI} display a similar range in values (~3–15) despite being less affected by fractional crystallization trends.

Trace element ratios are also variable in ratio plots for Nb, Y, and Zr (Fig. 3.7). Chassignite and nakhlite MI Nb/Y (0.01–3.0) versus Zr/Y (0.62–4.68) barely overlap the nakhlite and chassignite bulk compositional envelope (Fig. 3.7a). The narrowest range for Nb/Y and Zr/Y is found in nakhlite olivine-hosted MIs, which plot together around ~0.6–1, and ~3.7–4.1 respectively. Pyroxene-hosted MIs show the largest range, extending even below the shergottite trendline in Nb/Y space (Fig. 3.7a). When Zr/Nb and Y/Nb are compared in a bivariate plot, most points fall within ~1–54 for Zr/Nb and ~1–81 for Y/Nb (Fig. 3.7b). These values fall outside established values for MIs in the Tissint shergottite analyzed by Sarbadhikari et al. (2017).

Trace Element Map Analyses

Trace element distributions in MIs appear largely dependent on their petrography. Polycrystalline MI contain significant heterogeneities as different phases seem more likely to contain some trace elements than others (Fig. 3.8). Incompatible elements (e.g., Al, REE) are concentrated largely in the MI, while compatible elements (Mg) are not. Melt inclusions that are petrographically simple (in nakhlite olivine and pyroxene), containing only glass and microlytic phases, are much more homogenous than complex inclusions. This is best illustrated with Nb, Y, and Zr compilation maps where elemental distribution throughout a polycrystalline MI is uniquely heterogenous compared to other MI types considered here (Fig. 3.8a). One exception to this rule is the presence of large cognate oxides in some MIs, usually pyroxene-hosted examples, which can contribute larger concentrations of some trace elements (e.g., Ce; Fig. 3.8c).

3.4 Discussion

3.4.1 Nakhlite Olivine as Xenocrysts, Antecrysts, or Phenocrysts

An enduring question concerning nakhlite petrogenesis lies in the relative formation history of primary cumulus phases, olivine and augite. Some authors have argued that olivine co-crystallized with augite, both as phenocrysts, while others have argued that olivine is a xenocryst (formed in another magma and later entrained in the nakhlite bulk). Petrologically, the enclosure of pyroxene by olivine in MIL 03346 suggests olivine crystallized after augite (Day et al. 2006), in contrast to Nakhla, where the opposite sequence has been observed (e.g., Harvey and McSween 1992a, 1992b). For some studies, differing interpretations may arise from the dissimilar methods to determine the parental melt compositions of the cumulus phases in the suite. In two papers using mass-balance calculations and MI analysis to determine the nakhlite parental melt, Treiman (1986; 1993) found that while olivine and pyroxene crystallize from a single magma in Nakhla, the magmatic system was open and pore space between cumulus phases was infiltrated by chemically distinct magmas. In two more parental melt studies using different MI analysis techniques, Sautter et al. (2012) and Goodrich et al. (2013) concluded that megacrystic (large) olivine cores and the MI they contained were not in equilibrium with the bulk nakhlite magmas, possibly because the olivine cores are xenocrystic (a separately-formed crystal entrained into another chemically distinct magma). Balta et al. (2017) found that olivine in nakhlite Northwest Africa (NWA) 5790 originated from an incompatible-enriched magma relative to the bulk rock, and that olivine was xenocrystic. Jambon et al. (2016) proposed that nakhlite pyroxene is frequently resorbed and often enclosed in olivine, making pyroxene xenocrystic but consanguineous with olivine. Other parental melt studies found that olivine and pyroxene were co-saturated in their calculated melt compositions, indicating that they are both phenocryst populations (Harvey and McSween 1992; Stockstill et al. 2005). Udry and Day (2018) also suggested that across the nakhlite suite, olivine

and pyroxene follow fractional crystallization trends and that olivine had to form both before and after pyroxene and so is likely to be phenocrystic.

One possibility that is not explicitly explored in the literature is that one or both cumulus phases of some (or all) the nakhlites are antecrysts, which are minerals formed from different partial melts derived from the same mantle source rock that generated a bulk sample. In this scenario, a mineral may bear similarities in terms of incompatible trace element (ITE) abundances to the bulk rock (i.e., parallel abundances on a REE diagram), but it may also differ in major and minor element chemistry enough that it is not in equilibrium with its bulk host rock in terms of its compatible elements (e.g., Wieser et al. 2019). From major and minor element chemistry alone, it is difficult to determine whether samples or phases are petrogenetically related. To constrain whether cumulus phases are related, we focus on MIL 090030, as this nakhlite is the only analyzed meteorite that contained both pyroxene- and olivine-hosted MIs. We conducted fractional crystallization models using the Rhyolite-MELTS v.1.0.2 algorithm on the alphaMELTS interface using both an olivine-hosted PTL and a pyroxene-hosted PTL as initial magma compositions for individual runs. We used the same model parameters as previously described, which we also used to determine the parental melt composition for nakhlite pyroxene-hosted MIs. We found that olivine-hosted PTLs were unable to generate pyroxene compositions observed in MIL 090030 (Fig. B3). Furthermore, the pyroxene-hosted PTL in MIL 090030 did not generate any olivine (Fig. B4). There are two possibilities for these results: 1) the two phases did not form from a single batch of magma and one or both are xenocrysts or antecrysts, or 2) the PTL calculations are not representative of the initial entrapped liquid compositions. If the second possibility is true, and if post-entrapment effects like subsolidus diffusion occur for a long enough duration or in an open magmatic system, this may lead to an irreversibly altered MI bulk composition.

3.4.2 Link Between the Chassignites and the Nakhlites

Udry and Day (2018) have suggested that chassignites may have been emplaced as cumulates or crystal settling pods in nakhlite lava flows, or separately in shallow sills. McCubbin et al. (2013) found that exogenous Cl-rich fluids likely affected an evolving melt largely following chassignite formation and predating nakhlite formation. We used thermodynamic modeling to determine whether the most primitive chassignite PTL (in NWA 2737) could replicate any PTL entrapped in nakhlites. Because chassignite MIs contain hydrous minerals, we vary the initial water abundance between 0.07 wt.% (the minimum amount for the model, effectively zero) and 2.0 wt.% (the amount predicted to be present in the chassignite mantle source [McCubbin et al., 2010]) If the NWA 2737 PTL replicates any nakhlite PTL, the two PTL would represent different stages of melt evolution in a single magma body.

We found that the NWA 2737 anhydrous model does perfectly overlap multiple CeC 022 pyroxene-hosted PTL with regards to SiO_2 and alkali metals (Fig. 3.9). Despite chemical similarities, however, the models do not replicate nakhlite bulk mineralogy (Fig. 3.10). All NWA 2737 PTL models generate abundant pigeonite and no augite, while the largest modal fraction of CeC 022 is augite. Furthermore, NWA 2737 PTL models fail to generate the intercumulus plagioclase found in CeC 022. Again, there are two possible reasons for the models failing to reproduce observations: 1) the two subgroups are not formed from a single magma composition, or 2) their PTLs are not representative of true parental melt compositions. It is possible that all cumulus phases in the nakhlite and chassignite system have been reequilibrated in evolving magmas or new magmas, and their PTLs cannot be accurately reconstructed using these or similar methods. Furthermore, MI in the nakhlites tend to be petrographically glassy and simple, while

the chassignite MIs are complex and polycrystalline. This, combined with the difference in host Mg# (Table 2.2) may indicate different thermal histories and possibly different magma compositions.

3.4.3 Effects of Shock Processes on MI Compositions

Nakhlite and chassignite MIs are differently affected by shock processes manifesting in different appearances in MIs between the two sample types. While we did not observe evidence of devitrification or crushing, many MIs are cross-cut by fractures. Fractures surrounding MIs are commonly formed during mineral ascent due to pressure contrasts in the host and inclusion (called "decrepitation"; e.g., Wallace et al., 2021). However, we take fractures cross-cutting inclusions to be signs of impact fracturing, especially where inclusions appear to be displaced along the fracture (Fig. 3.1–3.4). The effects of impact-induced shock on MIs are not deeply explored in the MI literature. Loss of volatile elements like Na_2O has been noted in olivine-phyric shergottite MI bulk compositions, and it was attributed to shock volatilization (Goodrich 2003). Some Na_2O volatilization may affect nakhlite and chassignite PBCs as well, lending to some variability in values. However, Na_2O is heterogeneously distributed in some MI glasses, and so variability may be due to misrepresentative sampling in two dimensions (Fig. 3.3b–c). It is possible that shock effects contribute to MI compositional heterogeneity, but the extent of those contributions are not easily constrained.

3.4.4 Potassium Enrichment in Nakhlite PTLs

In agreement with other nakhlite PTL studies (i.e., Goodrich et al. 2013), we found K_2O enrichments and high K_2O/Na_2O. However, the chassignite PTL are alkali-depleted (Fig. 3.5, Table

2.2). Goodrich et al. (2013) attributed K-enrichment in the nakhlites to a mantle source that had been metasomatically enriched in K relative to Na, a process that might occur when low degrees of partial melting generates high-K fluids which then travel from elsewhere in the mantle. However, the chassignites are largely thought to originate from the same source as the nakhlites as they share crystallization ages, isotopic signatures, and CI-normalized rare earth element patterns (e.g., McCubbin et al. 2013; Udry and Day 2018; Udry et al. 2020). Chassignite and nakhlite MIs should bear similar K enrichments if that were the case, as it would be highly unlikely that the suite would consistently bear the same source character aside from K_2O variations. There are several possibilities to explain this discrepancy.

First, it is possible that K was heterogeneously distributed in the nakhlite and chassignite mantle source during metasomatism, or K was progressively enriched during and after the partial melting that generated the chassignite parental melt. This need not happen rapidly, as Cohen et al. (2017) found that nakhlite crystallization may have occurred over a time span of 100 Ma. There are no such high-resolution geochronological constraints on chassignite formation. If chassignites had formed early in the timeline, K enrichment may have progressed from that point onward. However, the probability for this enrichment to happen at this exact timing rather than anytime in the geologic history recorded by nakhlites and chassignites is low. It may also be possible that the magmas themselves were enriched in K by some exogenous fluid, rather than the source having undergone metasomatism. Like the Cl-rich fluid found by McCubbin et al. (2013), this K-bearing fluid may have preferentially enriched the nakhlite melts. This process is also observed in shergottite meteorites (Combs et al. 2019; O'Neal et al. 2022). The K enrichment signals may also be a consequence of the method used to construct PTL compositions, or enrichments may be due to a secondary process affecting melt inclusions which may not be correctable. For instance, K-

enrichments may not be a true signal in PTL calculations. The addition of olivine to the MIs could have diluted minor elements in the chassignites inclusions to a greater extent than the nakhlites. Methods for PTL calculation which rely on adding an olivine component to the bulk inclusion may be subject to significant error if the initial olivine abundance is poorly constrained (see Fig. B2). Lastly, variably K_2O-enriched MIs could simply record changing magma compositions interacting with the host mineral. Cottrell et al. (2013) found that small MIs, or MIs close to their host rims, equilibrate more rapidly with a changing external magma than large MIs or those distant from host rims. If MIs in nakhlites and chassignites are affected by reequilibration with a changing external magma, they will have been affected differently by relative sizes and positioning, lending to overall heterogeneity. Unless closed-system crystallization can be proven, making single PTL reconstructions via size normalized averages of all inclusions in a sample (cf., Treiman 1993; Goodrich et al. 2013) may result in significant uncertainties.

3.4.5 Mantle Source of the Nakhlites and Chassignites

Trace element compositions in MIs have been previously used in shergottites to characterize their sources (e.g., Peters et al. 2015; Basu Sarbadhikari et al. 2011; 2017). The nakhlite and chassignite MIs yielded largely parallel REE patterns, which are in turn parallel to bulk rock values (Fig. 3.6). This indicates that all samples were derived from melting of a single depleted source, which is in accordance with past studies (e.g., Debaille et al. 2013; Armytage et al. 2018; Day et al. 2018; Udry et al. 2020). Generally, MI REE abundances indicate that the melt or melts that formed the nakhlites and chassignites originate from a single mantle source. This source is also significantly more Nb enriched and Zr and Y depleted than the shergottite reservoirs characterized by Peters et al. (2015) and Basu Sarbadhikari et al. (2017) (Fig. 3.7b).

However, there are inconsistencies between individual trace element ratios (Fig. 3.6, 3.7a), which may be due to a few potential effects. The first is that MIs may be singularly chemically heterogenous, which we find to be true particularly of coarsely polycrystalline MIs in qualitative trace element maps (Fig. 3.8). Additionally, mixing different phases in a single beam on the LA-ICP-MS may introduce error due to matrix-dependent fractionation effects (Zhang et al. 2016). Because chassignite-hosted MIs are all polycrystalline, *in situ* trace element abundances may be scattered. However, we attempted to control this effect by selecting representative host:MI ratios, and deselecting outliers in the LA-ICP-MS data reduction step. Secondly, if a host mineral is entrained in a new magma and undergoes diffusive reequilibration of major and minor elements in the grain and the melt inclusion, trace elements should also undergo diffusive reequilibration (Cottrell et al. 2002; Wallace et al. 2021). Incompatible trace elements have long been considered to be unchanged by post-entrapment processes (Gaetani and Watson 2000; Schiano 2003; Basu Sarbadhikari et al. 2011; Basu Sarbadhikari et al. 2017). However, recent terrestrial work on trace elements in MIs find significant heterogeneity to which diffusion into and out of the inclusion host plays a role (Wieser et al. 2019; Wallace et al. 2021). While diffusion rates of trace elements in most mineral systems are poorly constrained, the onset of diffusion into a mineral host seems to be controlled by its compatibility (Cottrell et al. 2002). The final effect that may be contributing to trace element variability is that they may originate from different degrees of partial melting of the source, resulting in slight variations between batches of magma (e.g., Wallace et al 2021). In this scenario, these different partial melts would be considered as distinct parental melts responsible for whatever phases they may form.

As the effects of diffusive reequilibration affect trace elements based on their compatibilities in a host, ratios of elements with similar partition coefficients (such as Nb, Zr, and

Y in olivine, where D ≈ 0.01) must reveal actual change in the parental magma, particularly for homogenous (in this study: glassy) inclusions. In Hawaiian basalts, variability between bulk rock compositions and MIs in Nb/Y and Zr/Y ratios is shown to represent different degrees of partial melting from a single source (Wallace et al. 2021). The same may be true for homogenous, glassy olivine-hosted nakhlite inclusions that plot together in Fig. 3.7. Because glassy, olivine-hosted nakhlite inclusions plot together, but away from bulk rock, their Nb/Y and Zr/Y ratios are representative of a different parental melt than those which produced the rest of the bulk rock. This same method cannot be applied to pyroxene-hosted MIs, as Zr (0.123), Y (0.467), and Nb (0.06) have different partition coefficients in pyroxene and that may contribute to scatter (Fig. 3.7, kdd.earthref.org). Some data scatter for glassy pyroxene-hosted inclusions in Zr, Y, and Nb space may then be attributed to post-entrapment diffusion preferring Y over Nb (Fig. 3.7). Reequilibration of a MI with a host alone is evidence of magma storage. Sufficient time is needed for diffusion and for magma recharge events to maintain an open system, indicating a complicated petrogenetic history encompassing multiple generations of melt and cumulate storage for the nakhlite and chassignite suite.

3.4.6 Post-Entrapment Processes

Because trace element abundances appear scattered and may not represent equilibrium parental melt conditions, it is likely that the major and minor elements in nakhlite and chassignite MIs have been affected by open-system processes as well. The effects of post-entrapment processes such as diffusive reequilibration, especially ones occurring in an open magmatic system, are an area of active research in terrestrial literature. If an MI is entrapped in a mineral phase that comes into contact with a new magma, the host phase will equilibrate with its new exterior magma

while continuing to undergo diffusive exchange with its MI (Cottrell et al. 2002; Brahm et al. 2021; Wallace et al. 2021). Our PTL calculations (and those of other authors) rely on an assumption for an initial condition: how much host was in equilibrium with its MI during entrapment. If the nakhlite system was open, as has previously been postulated (e.g., Treiman 1993; Goodrich et al. 2013), it may not be possible to predict an initial condition for MIs—particularly for those MIs hosted in olivine, which is a mineral considered to be subject to more rapid diffusion than pyroxene (e.g., Goodrich et al. 2013). Indeed, we found that greater variability in PTL data is introduced by a change in initial FeO_T conditions than by differences in analytical techniques (Fig. B2).

Constructing the PTL for olivine-hosted inclusions involves the assumption that the olivine has not been subjected to open-system processes, including loss of solid or liquid phases, reequilibration in chemically heterogenous or rejuvenated magmas, or xenocryst incorporation in new bulk magmas. This is a noted shortcoming in the *Petrolog3* literature (Danyushevsky and Plechov 2011), but any method reliant on adding open-system host phases into a bulk inclusion composition will suffer from the same issue: one cannot simply predict the amount of host phase initially in equilibrium with a MI if that host phase composition had in any way been changed after MI entrapment. Ultimately, major and minor element chemistry of MIs alone is not predictive of closed-system behavior. Instead, MIs (particularly in open-systems) may be better representative of storage conditions following a period of diffusive exchange with an evolving host (Cottrell et al. 2002; Brahm et al. 2021; Wallace et al. 2021).

Although we do not know if chassignites and nakhlites share a common parental melt based on MIs alone, we can conclude that from trace element REE abundances that they originate from a single source, and that they have likely been reequilibrated. In order to show that MIs are in disequilibrium with the carrier liquid (the liquid leading to eruption) for their host mineral, other

authors compare trace element findings for MIs against intercumulus material (e.g., Peters et al. 2015; Wieser et al. 2019). Unfortunately, intercumulus material in nakhlites is typically coarsely heterogenous and suffers from data scatter for many of the reasons that polycrystalline MIs do. Instead, we find that there are significant differences between the bulk rock and MI compositions (i.e., Nb/Y and Zr/Y in olivine-hosted nakhlite MIs), and disequilibrium must be considered. If MIs are not in equilibrium with their bulk rock, and they then represent storage conditions rather than entrapment conditions, they may be either xenocrystic or antecrystic. If nakhlite and chassignite cumulus phases were xenocrystic, their entrapped melts would be produced from incompatible trace element-distinct sources. Instead, MIs across the suite share the same REE patterns, and so their host phases may be antecrystic.

These findings are consistent with a shift in our understanding of terrestrial magma systems away from simplistic systems undergoing discrete crystallization and eruption or emplacement events. Instead, the current view is that magma chambers are dominated by accumulation of crystal "mush" followed by storage that can last for 10–30 Ma in some mafic systems prior to that mush being entrained (e.g., Karlstrom and Richards 2011; Cashman et al. 2017; Wieser et al. 2019). On a planet without plate tectonics, i.e., in a solid-lid regime, these findings have implications for the longevity for magma chamber evolution. Cohen et al. (2017) found that nakhlites could have been emplaced over a period of 100 Ma, which is a significantly longer period than any hotspot-derived magmatic activity on Earth. An outstanding question is how a single depleted source might generate partial melts that differ so little as to produce similar mineralogy for each eruption over such a timespan. It is likely that there was accumulation of mineralogically similar mush material to equilibrate with fresh magma batches.

We propose a model for nakhlite and chassignite formation wherein multiple magmas are generated from melting a chemically homogenous and depleted source (Fig. 3.11). Those magmas fractionate phases containing MIs that are stored in equilibrium with their magma until it significantly evolves away from its initial conditions, or it is mixed or replaced with a new magma. After contact with a new magma, the mush phases reequilibrate with the exterior melt and their MIs also undergo reequilibration. Occasionally in terrestrial magmas, mush cumulates may be entrained in new magmas and emplaced at or near the surface on the order of tens of millions of years. Not all cumulates need to be generated from the same magma chambers, i.e., dunitic chassignites may originate from a unique magma chamber (either separated spatially or temporally from a nakhlite chamber), but all cumulate phases were initially generated from melts at the same source and erupt to the same surface location. Nakhlite MIs are enriched in K_2O relative to chassignite inclusions. The K enrichment may be an effect of rehomogenization of the MI leading to an incorrect PTL calculation. If, however, these relative enrichments are real, the higher K_2O signature may be due to an exogenous crustal fluid that altered the bulk nakhlite melt composition after chassignite MI entrapment. Alternatively, the nakhlites may have been generated by a lower degree of partial melting of a K_2O-rich source, and the chassignites formed from an earlier and higher-degree of partial melting that resulted in relative K_2O depletion. Lastly, K_2O enrichments which vary significantly between MIs may arise simply from interactions with changing magma compositions.

3.5 Summary and Conclusions

The nakhlite and chassignite martian meteorites are the product of magma storage and reequilibration, and these magmas likely supplied a magma chamber that erupted highly similar

materials for tens of millions, upwards of 100 million years. To come to that understanding, we found that:

- There may be no way to reliably determine a parental melt composition for the nakhlites or chassignites from melt inclusions.
    - There are currently no sufficient methods for establishing a mafic parental trapped liquid for any melt inclusion in a cumulus phase that may have been affected by open-system processes such as reequilibration in a new magma composition, but there is significant work being done to address this barrier in current literature (e.g., Brahm et al., 2021).
    - Open-system processes would not be reversible (in order to retrieve an initial parental melt composition) by microanalysis on thin sections, nor by reheating experiments.
- Broad trends in the PTLs still reveal changing storage conditions for cumulus phases. Chassignites are more primitive and more alkali-depleted than the nakhlites. Chassignite olivine may have undergone longer storage and reequilibration than the nakhlite olivine to relatively dilute the alkalinity of its parental melt composition. Alternatively, chassignite inclusions were entrapped prior to the enrichment of the nakhlite magma in K_2O, or that the chassignites were formed by higher degrees of partial melting of a K_2O-rich nakhlite source.
- Thermodynamic fractional crystallization models of chassignite PTLs reproduce pyroxene-hosted PTL bulk chemistry, but not nakhlite mineralogy. Similarly, nakhlite olivine-hosted PTLs cannot reproduce nakhlite pyroxene compositions, and pyroxene-hosted PTLs do not generate olivine. In the case that PTL chemistry is representative of a true parental melt

composition, chassignites and nakhlites, and the two cumulus phases in the nakhlites, all originate from different parental magmas. Alternatively, PTL compositions are subject to analytical and model error and are not representative of parental magmas, or represent changing magmatic compositions in an open-system.

- Trace element abundances co-vary due to diffusive reequilibration only when the trace elements have the same partition coefficient. This means that one reason for trace element scatter is because of differential diffusion into host phases due to reequilibration in an open-system environment. Other contributing factors may include melt inclusion compositional heterogeneities and analytical error.
- All studied nakhlite and chassignite-hosted melt inclusions have similar parallel REE patterns, and thus originate from the same source. This is in keeping with past literature findings.
- Nakhlites and chassignites likely originate in open-magma systems, with pulses of partial melting from a single source contributing to storage and mixing prior to entrainment and eruption of cumulus phases.
- Future work on nakhlite and chassignite melt inclusion analysis may be able to resolve the parental melt composition for these samples if their initial host FeO and MgO contents can be determined, or if extensive studies to constrain the effects of diffusion into and out of melt inclusions can be conducted. To the first point, olivine is the best constrained system for Mg and Fe isotopic diffusion gradients. However, nakhlite olivine also lacks in most major and minor element zoning and is likely heavily reequilibrated. It may be difficult to establish an initial FeO composition using isotopic systematics, but it may be possible. To the second point, constraining differing elemental diffusion gradients abutting melt

inclusion may help to constrain first-order timescales for storage and possibly find the best suited candidates for early-entrapped and largely original melt inclusions. Reequilibrated melt inclusions are helpful for understanding changing conditions in a magma if not the initial magma composition itself.

3.6 Acknowledgments, Samples, and Data

This study was supported by NASA Solar System Workings 80NSSC21K0159 awarded to A. U., J. D., and J. G. Data sources and samples are described in the Methods section with all instrument data reported in Appendix B. Comments by A. Treiman and C. Goodrich are appreciated. We like to thank Paul Burger (Rutgers University) and Minghua Ren (UNLV) for their help in conducting microprobe analyses, as well as Christopher DeFelice (UNLV, Pacific Northwest National Lab) for his assistance in LA-ICP-MS analyses. US Antarctic meteorite samples are recovered by the Antarctic Search for Meteorites (ANSMET) program which has been funded by NSF and NASA, and characterized and curated by the Department of Mineral Sciences of the Smithsonian Institution and Astromaterials Curation Office at NASA Johnson Space Center.

3.7 Tables

Table 3.1. Present bulk compositions of studied melt inclusions (in wt.%).

Chassignites	**SiO_2**	**TiO_2**	**Al_2O_3**	**FeO*†**	**MnO**	**MgO**	**CaO**	**Na_2O**	**K_2O**	**P_2O_5**	**Cr_2O_3**	**Mg#‡**
Chassigny MI 02	47.1	1.04	6.59	13.5	0.39	14.5	9.00	0.94	0.65	2.01	4.07	65.3
Chassigny MI 03	49.3	0.64	3.71	15.5	0.46	21.2	6.89	0.12	0.59	7.93	7.26	70.8
NWA 2737 MI 01	46.4	0.99	7.93	12.2	0.32	17.3	4.81	1.80	0.59	0.14	7.26	71.3
NWA 2737 MI 03	54.8	0.36	6.91	8.89	0.25	19.6	4.98	2.01	0.69	0.83	0.35	79.5
Nakhlite Olivine-hosted												
MIL 090030 MI 01	61.6	1.93	14.6	6.05	0.12	0.46	7.55	4.32	1.50	0.98	0.00	11.7
MIL 090030 MI 02	54.0	2.15	11.7	11.1	0.22	1.97	13.6	2.87	0.87	1.02	0.02	23.9
MIL 090032 MI 01	64.7	0.09	19.2	0.84	0.02	0.01	0.64	2.19	13.5	0.04	0.02	1.78
MIL 090032 MI 02	54.3	2.12	10.8	14.2	028	1.42	13.3	2.22	0.73	0.55	0.31	14.9
Governador V.	61.6	2.43	12.9	9.92	0.13	1.14	4.39	3.74	2.31	1.11	0.06	0.05
Nakhlite Pyroxene-hosted												
NWA10645 MI 02	62.5	0.31	15.5	5.55	0.11	1.18	3.85	4.29	5.44	1.02	0.02	27.1
NWA10645 MI 03	54.7	0.58	8.13	16.5	0.41	4.45	9.60	2.16	2.62	0.68	0.06	32.1
NWA10645 MI 04	57.3	0.36	10.6	12.5	0.32	3.41	7.61	3.07	3.98	0.55	0.05	32.4
NWA10645 MI 05	53.8	0.32	5.80	19.0	0.51	5.82	11.5	2.37	0.69	0.09	0.04	32.4
MIL090030 MI 01	51.2	2.43	10.5	16.1	0.32	1.63	14.7	0.91	0.69	0.62	0.03	15.4
CeC 022 MI 02	47.6	16.4	8.60	9.16	0.19	2.60	8.83	1.73	1.33	1.31	0.10	33.2
CeC 022 MI 04	62.3	3.88	16.0	5.05	0.10	1.25	2.22	5.32	5.07	0.28	0.02	30.3
CeC 022 MI 08	57.4	11.0	13.3	4.94	0.09	0.87	3.24	5.31	1.67	0.17	0.10	23.6
CeC 022 MI 12	51.2	14.1	14.1	6.35	0.13	1.16	4.52	5.74	1.57	0.05	0.10	24.3
CeC 022 MI 13	57.3	6.48	13.2	7.60	0.18	1.34	3.76	3.97	4.38	0.19	0.05	23.7
CeC 022 MI 14	52.3	1.04	5.01	19.1	0.55	5.35	12.8	1.20	2.03	0.27	0.06	33.0

†Reported FeO is not delineated by oxidation state, i.e., FeO* = ($FeO + Fe_2O_3$)

‡ Mg# = (Molar MgO × 100)/(Molar MgO + Molar FeO*)

Abbreviations: NWA = Northwest Africa; MIL = Miller Range; Governador V. = Governador Valadares; CeC = Caleta el Cobre

Table 3.2. Calculated parental trapped liquid compositions of studied melt inclusions (in wt.%).

Chassignites	SiO_2	TiO_2	Al_2O_3	FeO*†	MnO	MgO	CaO	Na_2O	K_2O	P_2O_5	Cr_2O_3	Mg#‡	K_2O/Na_2O	Mean Host Mg#
Chassigny MI 02	45.9	1.07	6.77	17.3	0.40	8.05	9.24	0.97	0.67	2.06	4.18	40.7	0.69	67.6
Chassigny MI 03	51.8	0.87	5.03	17.7	0.62	8.84	9.35	0.16	0.03	1.80	0.92	43.0	0.16	67.8
NWA 2737 MI 01	45.0	0.96	7.66	16.9	0.31	12.8	4.65	1.74	0.57	0.14	7.01	53.9	0.33	79.2
NWA 2737 MI 03	52.0	0.34	6.46	16.8	0.23	13.5	4.65	1.88	0.65	0.78	0.33	55.1	0.34	79.1
Nakhlite Olivine-hosted†‡														
MIL 090030 MI 01-A	52.5	1.35	10.2	22.9	0.08	2.84	5.28	3.02	1.05	0.69	0.00	17.9	0.35	41.5
MIL 090030 MI 01-B	49.8	1.18	8.89	27.8	0.07	3.59	4.60	2.63	0.91	0.60	0.00	18.5	0.35	41.5
MIL 090030 MI 02-A	48.9	1.69	9.18	23.2	0.17	2.64	10.7	2.18	0.68	0.80	0.02	16.7	0.31	40.4
MIL 090030 MI 02-B	46.5	1.46	7.97	28.2	0.15	3.33	9.25	1.89	0.59	0.70	0.01	17.2	0.31	40.4
MIL 090032 MI 01-A	48.9	1.68	8.99	23.4	0.24	2.62	10.4	2.21	0.98	0.59	0.00	16.4	0.44	41.4
MIL 090032 MI 01-B	48.0	1.34	7.48	28.1	0.19	3.46	8.36	1.80	0.79	0.47	0.00	17.8	0.44	41.4
MIL 090032 MI 02-A	50.3	1.26	9.85	22.9	0.15	2.78	8.39	2.41	0.97	0.97	0.00	17.6	0.40	41.4
MIL 090032 MI 02-B	47.9	1.10	8.60	27.7	0.13	3.47	7.33	2.10	0.84	0.85	0.00	18.0	0.40	41.4
MIL 090032 MI 03-A	47.5	1.68	8.89	23.4	0.18	2.64	12.4	1.58	0.57	1.09	0.00	16.5	0.36	41.4
MIL 090032 MI0 3-B	45.5	1.48	7.81	28.0	0.16	3.26	10.9	1.39	0.50	0.96	0.00	17.0	0.36	41.4
Governador V.-A	54.1	1.85	9.77	22.8	0.10	2.50	3.34	2.84	1.76	0.84	0.05	54.1	1.85	39.7
Governador V.-B	49.9	1.51	8.01	29.7	0.08	3.51	2.73	2.33	1.45	0.69	0.04	49.9	1.51	39.7
Nakhlite Pyroxene-hosted														
NWA10645 MI 02	52.9	0.44	5.51	19.7	0.51	5.84	11.7	1.40	1.59	0.30	0.05	34.2	1.14	40.3
NWA10645 MI 03	52.8	0.44	5.38	19.7	0.52	5.84	11.9	1.38	1.57	0.41	0.05	34.2	1.14	51.5
NWA10645 MI 04	52.6	0.44	5.49	19.8	0.52	5.83	11.7	1.48	1.77	0.25	0.05	34.1	1.20	51.5
NWA10645 MI 05	53.8	0.32	5.80	19.0	0.51	5.82	11.5	2.37	0.69	0.09	0.04	35.0	0.29	51.9
MIL090030 MI 01	53.5	0.08	4.81	17.0	0.63	5.77	14.5	0.56	3.03	0.05	0.02	37.4	5.41	60.7
CeC 022 MI 02	58.8	0.63	10.1	9.28	0.26	3.49	11.7	2.02	1.46	1.51	0.03	39.8	0.73	47.6
CeC 022 MI 04	55.7	0.83	8.65	16.1	0.50	3.36	9.17	2.85	2.61	0.16	0.04	26.8	0.92	58.2
CeC 022 MI 08	53.9	0.84	5.80	18.1	0.53	5.03	12.6	2.11	0.67	0.24	0.07	32.9	0.32	54.7
CeC 022 MI 12	55.6	0.74	9.71	14.1	0.42	3.97	10.7	3.79	0.97	0.15	0.04	33.1	0.26	52.4
CeC 022 MI 13	53.4	0.86	6.89	19.6	0.52	3.84	9.96	1.95	1.95	0.50	0.04	25.6	1.00	55.3
CeC 022 MI 14	52.4	0.84	5.05	19.1	0.55	5.35	12.8	1.21	2.05	0.27	0.06	33.0	1.70	60.5

†Reported FeO is not delineated by oxidation state, i.e., FeO* = (FeO + Fe_2O_3)

‡ Mg# = (Molar MgO × 100)/(Molar MgO + Molar FeO*)

†‡ Compositions ending in -A use an FeO_T of 22.2 wt.% (Imae and Ikeda, 2007), and -B of 28.9 wt.% (Goodrich et al., 2013).

Abbreviations: NWA = Northwest Africa; MIL = Miller Range; Governador V. = Governador Valadares; CeC = Caleta el Cobre

3.8 Figures

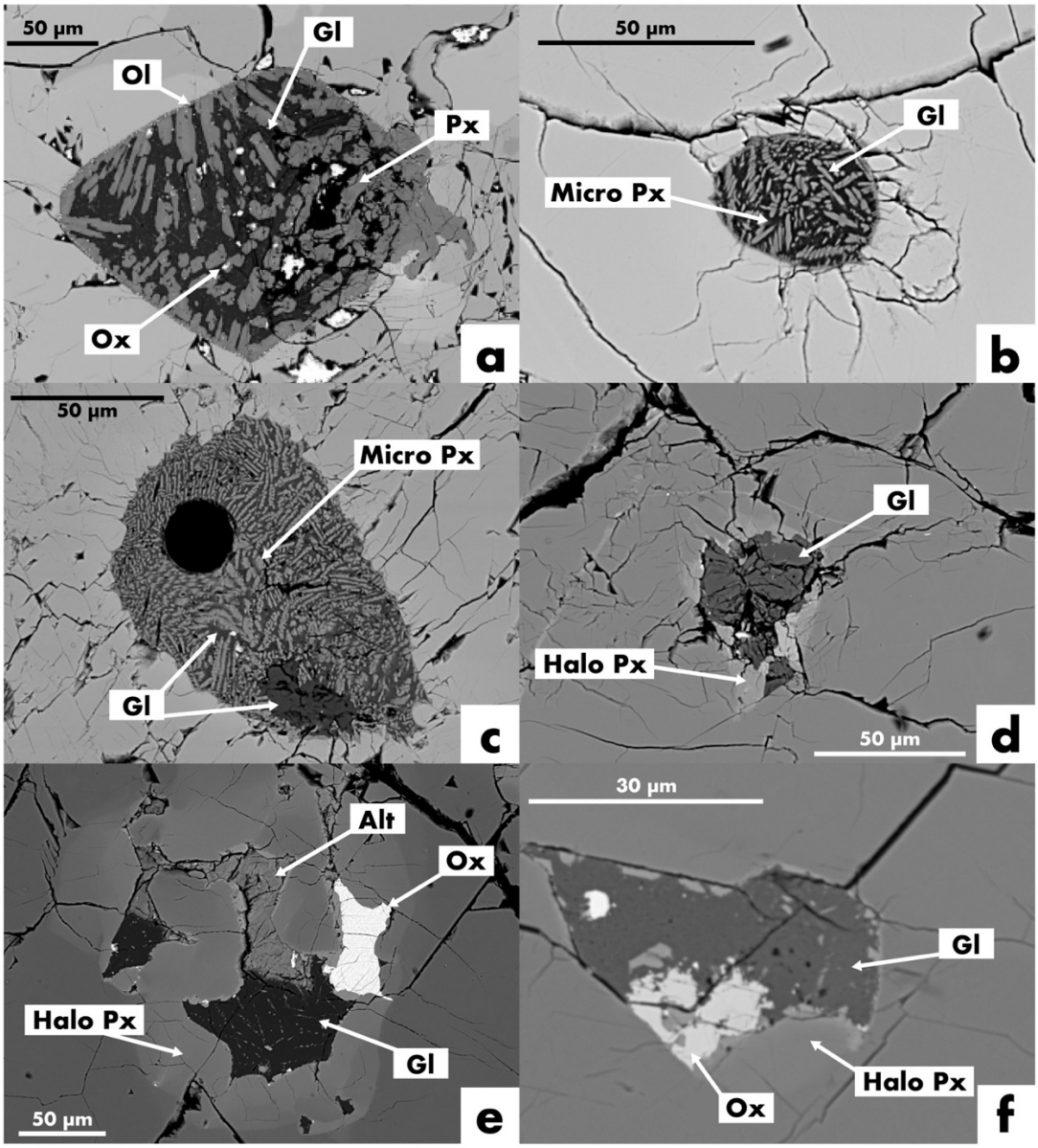

Figure 3.1: Backscattered electron (BSE) images of melt inclusions (MI) contained in nakhlites: a) olivine-hosted MI in Governador Valadares; b) olivine-hosted MI in Miller Range (MIL) 090030; c) olivine-hosted MI in MIL 090032; d) pyroxene-hosted MI in MIL 090030; e) pyroxene-hosted MI in Northwest Africa 10645; f) pyroxene-hosted MI in Caleta el Cobre 022. Abbreviations: Ol = olivine; Gl = glass; Px = pyroxene; Ox = oxide; Micro Px = microlytic pyroxene; Halo Px = halo pyroxene; Alt = alteration.

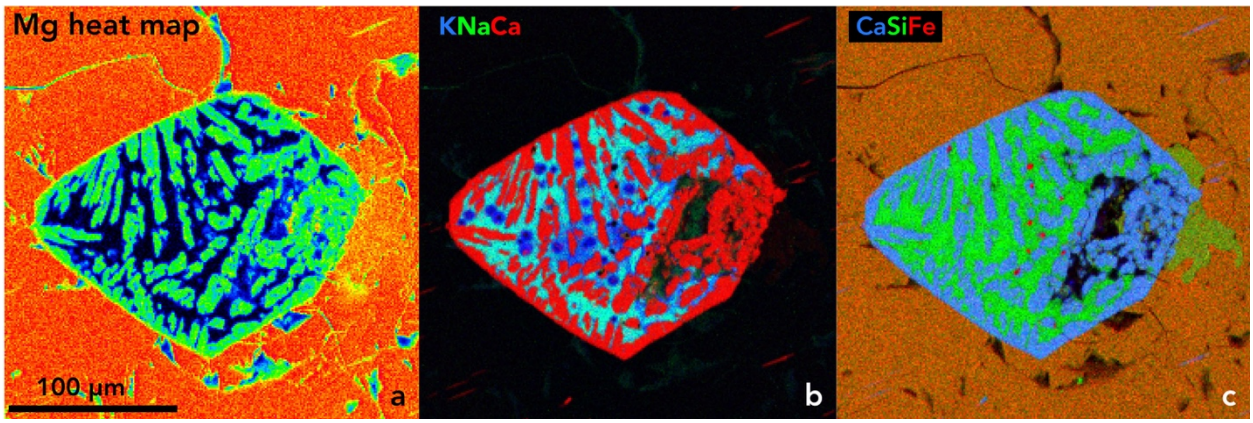

Figure 3.2: Composite maps for Governador Valadares, the largest complex nakhlite olivine-hosted melt inclusion. a) Mg heat map, wherein warmer colors are higher concentrations of Mg. b) X-ray map where K is blue, Na is green, Ca is red. c) X-ray map where Ca is blue, Si is green, Fe is red. A thin (<1 µm), moderately magnesian, rim of olivine can be seen around the inclusion. The glassy phase central to the inclusion has heterogenous K and Na distribution, but largely homogenous Si.

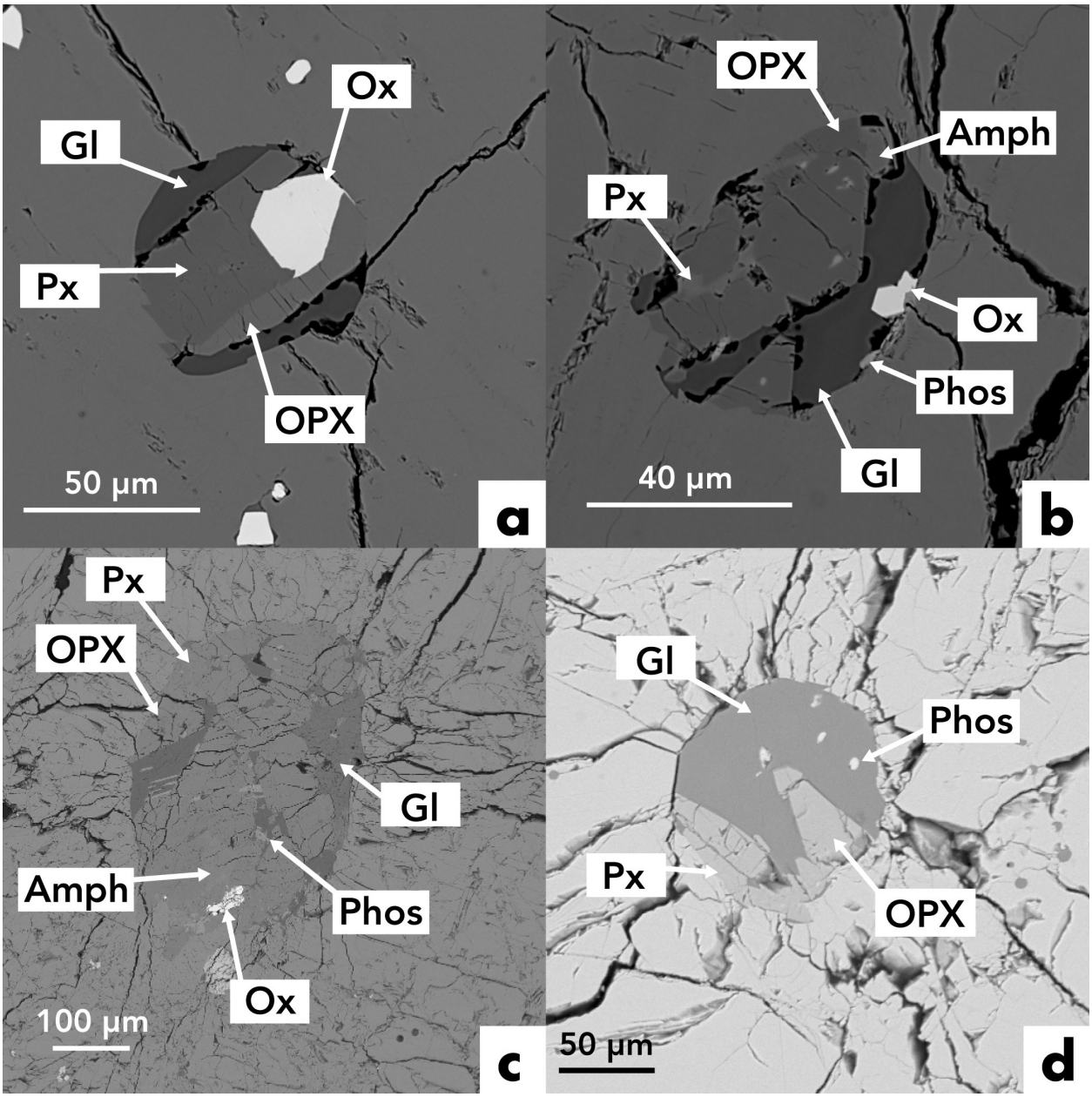

Figure 3.3: BSE images of MI contained in chassignites: a) NWA 2737; b) NWA 2737; c) Chassigny; d) Chassigny. All MI are olivine-hosted. Abbreviations: Ox = oxide; Gl = glass; Px = pyroxene, OPX = orthopyroxene; Amph = amphibole; Phos = phosphate.

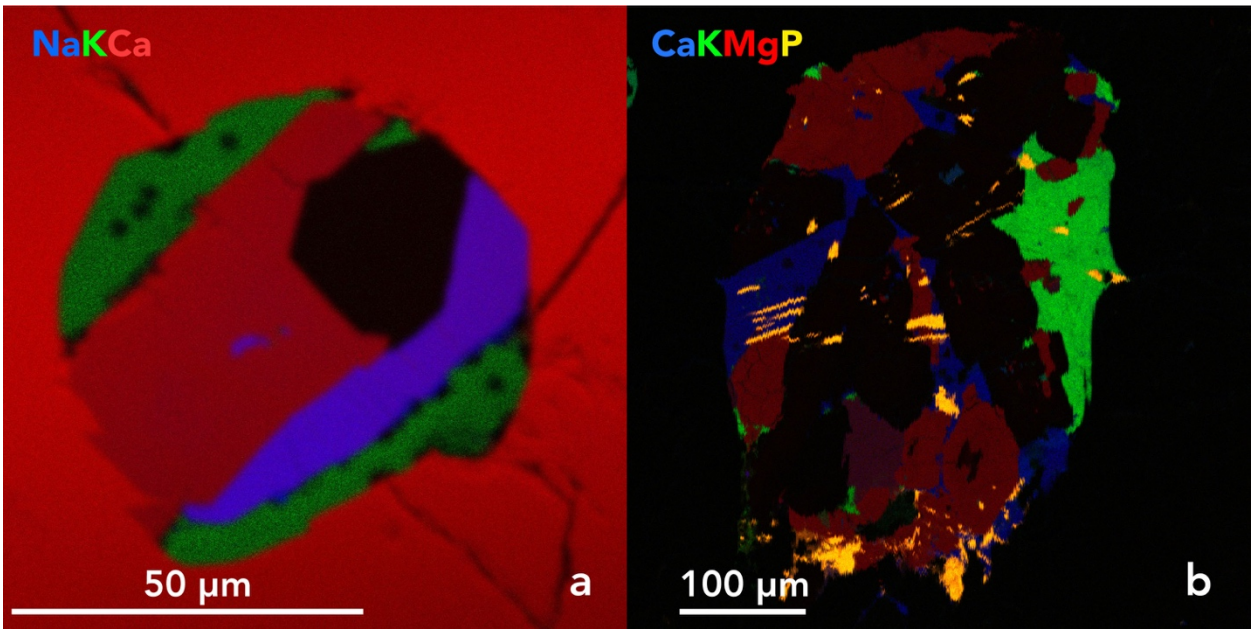

Figure 3.4: Composite maps for melt inclusions in chassignites: a) NWA 2737, where Ca is red, K is green, and Na is blue; b) Chassigny, where Ca is blue, K is green, and Na is blue. Some chassignites contain two glass phases: one containing high K_2O, and another high Na_2O.

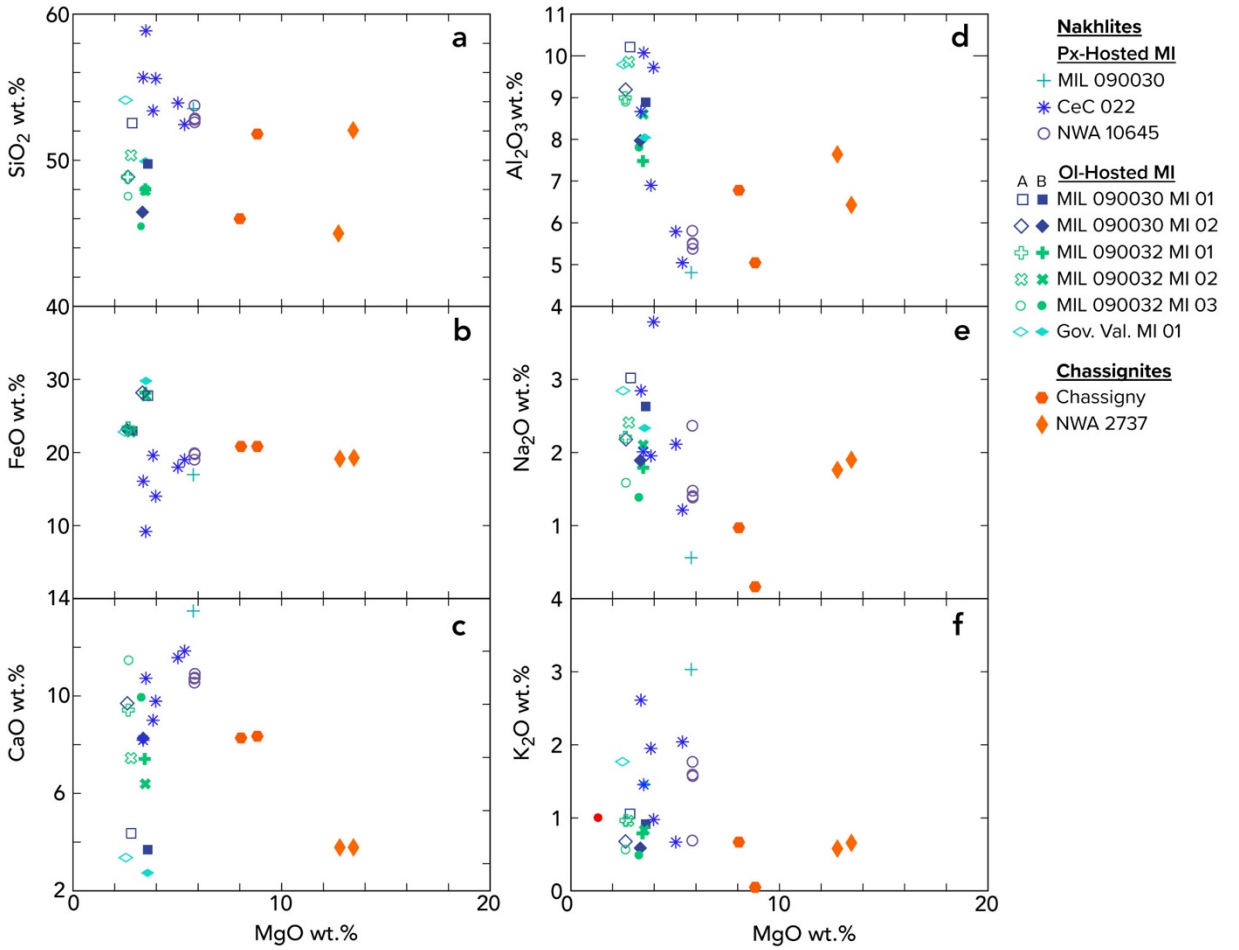

Figure 3.5: PTL results for oxides SiO2, FeO, CaO, Al2O3, Na2O, and K2O plotted against MgO. Olivine-hosted melt inclusions in the nakhlites were processed using two FeO_T (initial FeO + $Fe2O_3$) conditions: A was processed with 22.2 wt.% FeO_T (Imae and Ikeda, 2007) and B was processed with 28.9 wt.% FeO_T (Goodrich et al., 2013).

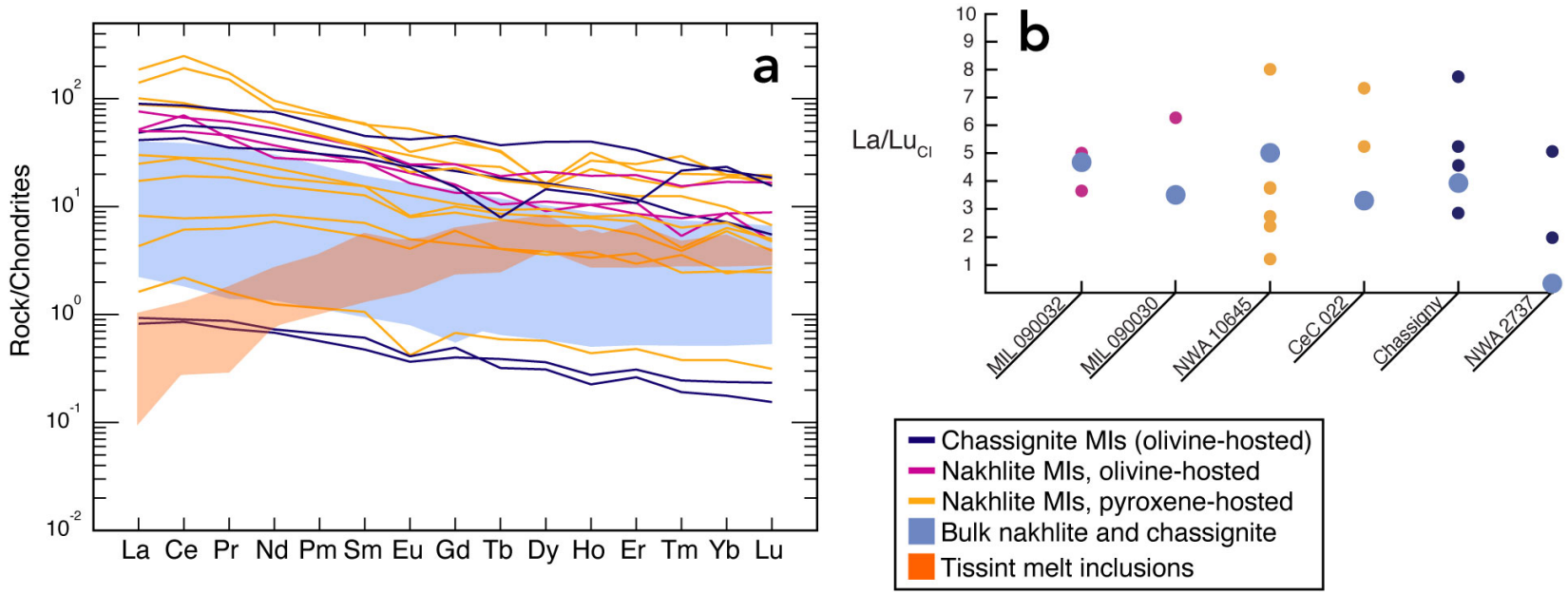

Figure 3.6: Trace element abundances for melt inclusions in nakhlites (olivine- and pyroxene-hosted) and chassignites (olivine-hosted). a) Spider diagram, with bulk inclusion compositions normalized against CI chondritic values (McDonough and Sun, 1995); blue envelope represents bulk sample compositions, taken from Udry et al. 2020. Shergottite Tissint melt inclusion REE abundances (Type I and II) are represented by the orange envelope, and are taken from Basu Sarbadhikari et al. 2017. b) Variation in La/Lu (CI normalized) for melt inclusion REE data presented in a); bulk rock values are also plotted. Profiles for the REE in MI are largely parallel to bulk rock values, however, when individual elements are ratioed, there is significant variability (especially when compared to bulk rock values).

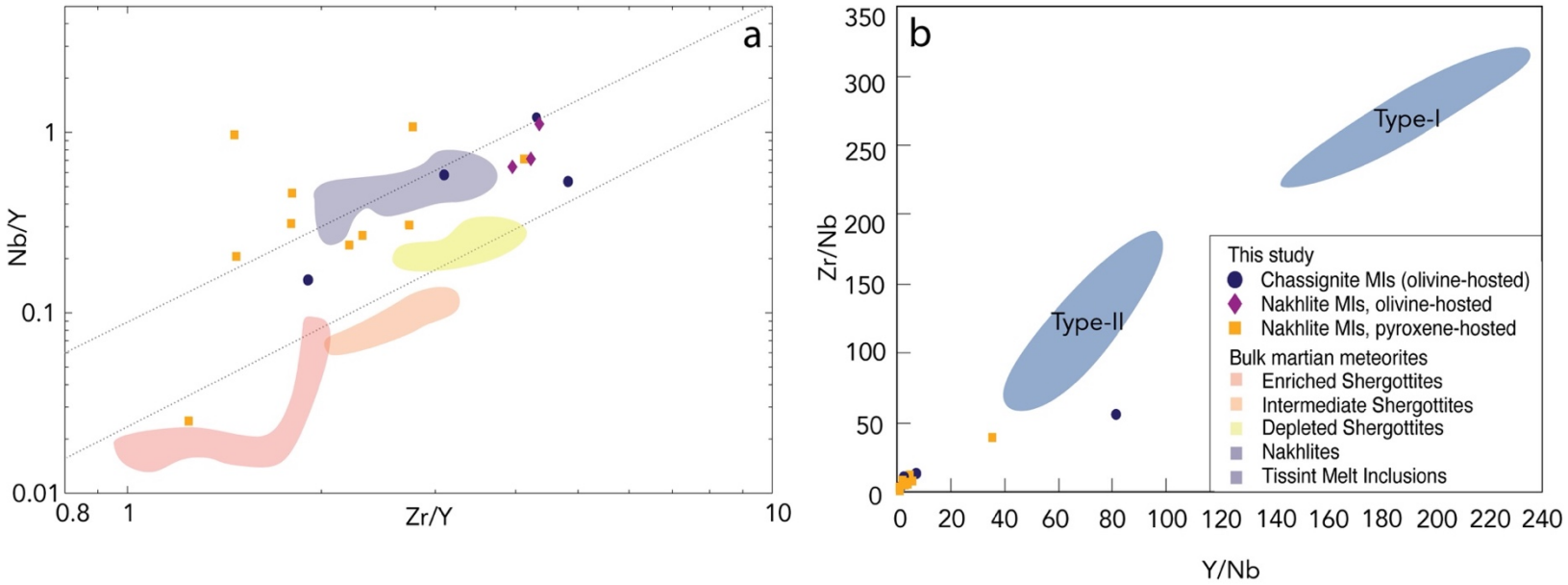

Figure 3.7: Melt inclusion trace element ratios compared to bulk rock nakhlites, and to shergottites. a) Zr/Y and Nb/Y ratio plot adapted from Day et al. (2018). Nakhlite bulk rocks falls on a trendline similar to rejuvenated Hawaiian basalts, and shergottites around typical Hawaiian basalt trends. Only nakhlite melt inclusions (MI) plot together. b) Zr/Nb and Y/Nb ratio plot adapted from Sarbadhikari et al. (2017). No nakhlite or chassignite MI falls within melt inclusions analyzed from Tissint (Type-I and Type-II envelopes).

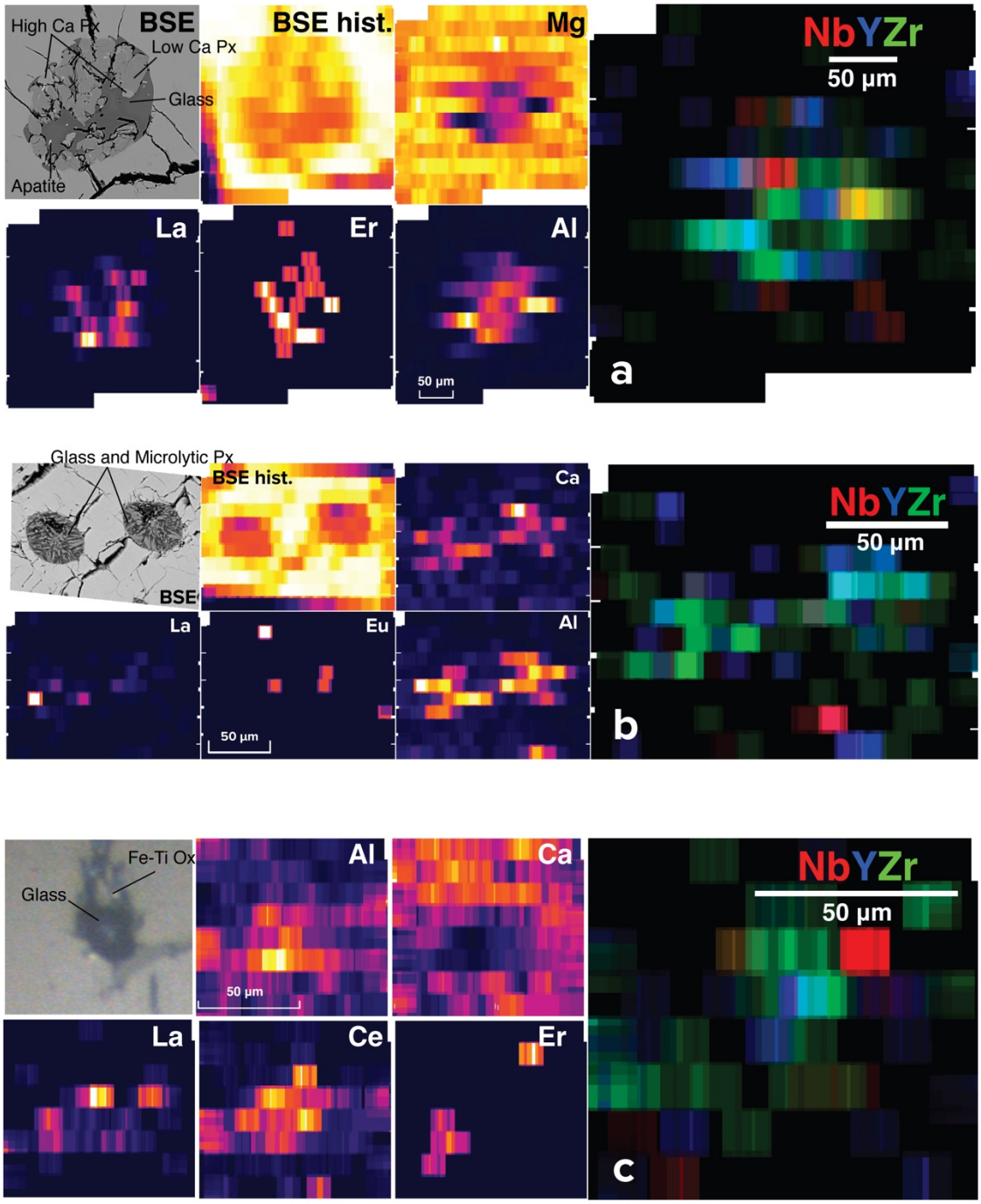

Figure 3.8: Trace element maps of melt inclusions. a): maps made of a polycrystalline inclusion in chassignite NWA 2737, which is highly heterogenous. b): two side-by-side simple (glassy) inclusions in nakhlite NWA 090030. c): simple melt inclusion contained in nakhlite pyroxene in NWA 10645. Px = pyroxene; Fe-Ti Ox = iron-titanium oxide.

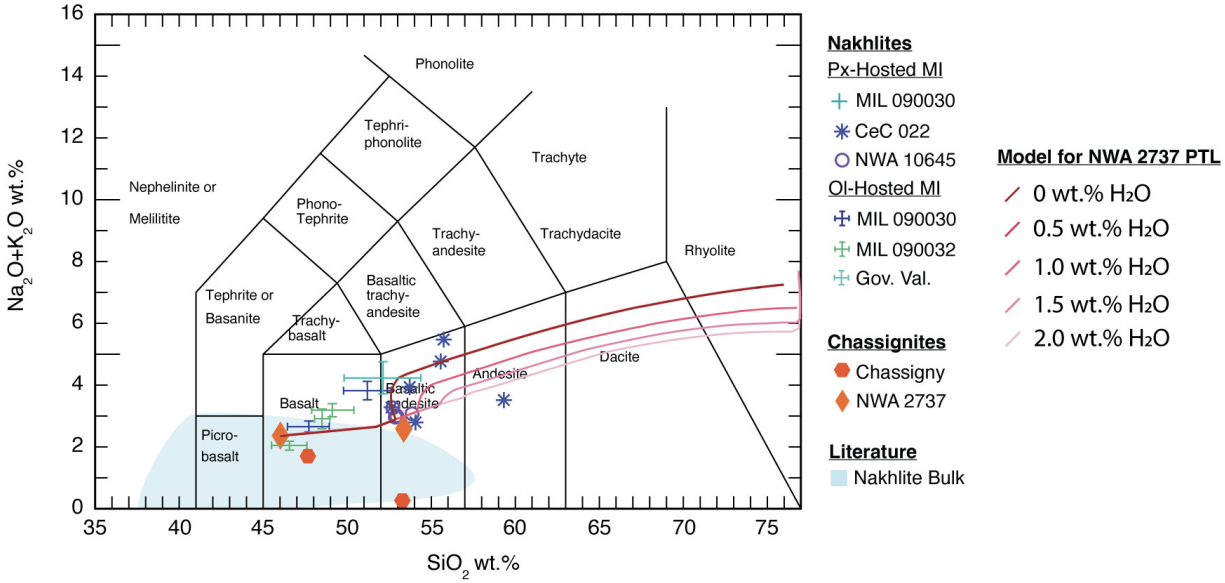

Figure 3.9: Results for thermodynamic modeling of a NWA 2737 PTL. Liquid lines of descent representing different initial water contents in the magma are represented by red lines. Models appear to approach PTLs in nakhlite pyroxene-hosted MIs (particularly in CeC 022).

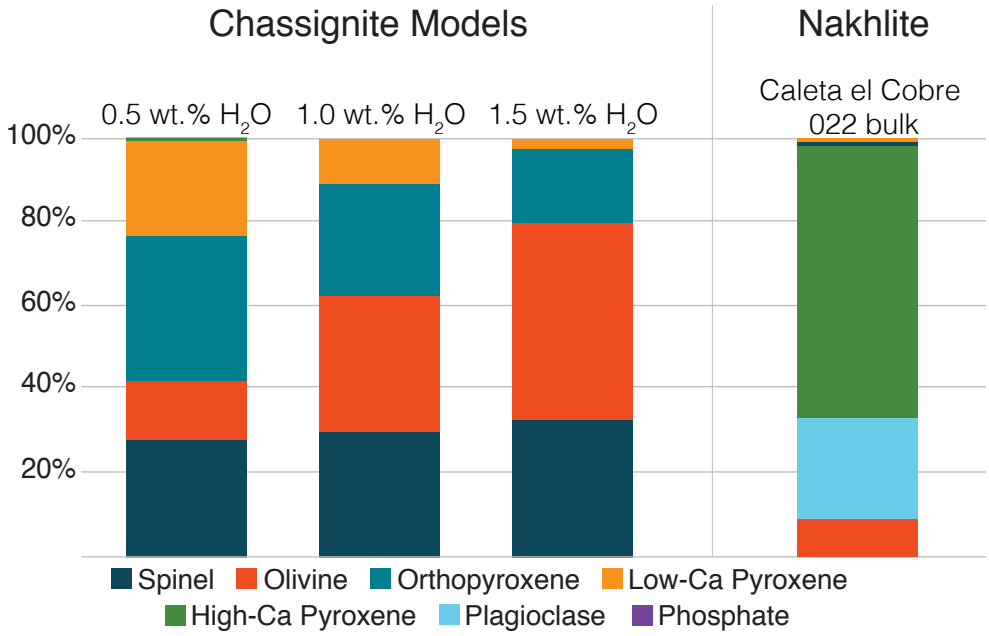

Figure 3.10: Mineralogy for chassignite PTL fractional crystallization models (right) compared to nakhlite (CeC 022) bulk mineralogy (left). While chassignite PTL models are somewhat similar to CeC 022 MI chemistry, the models do not replicate observed mineralogical compositions.

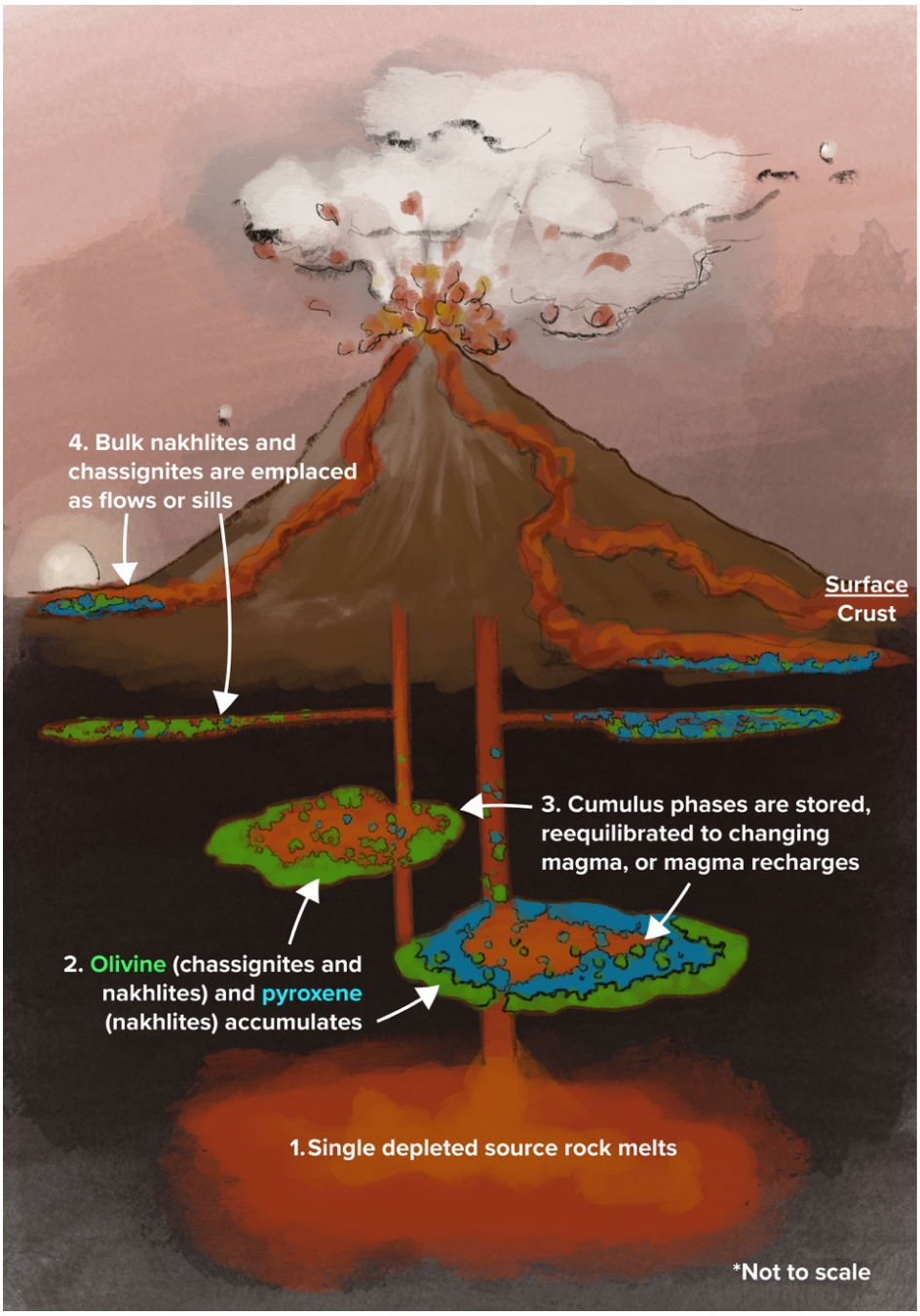

Figure 3.11: Model for nakhlite emplacement (not to scale). A single mantle source partially melts to produce the nakhlite and chassignite parental melts. These melts are stored in magma chambers, where phases such as olivine (in chassignites and nakhlites) and pyroxene (in nakhlites) accumulate. The parental magma shifts away from its initial composition, possibly due to the addition of fresh pulses of magma over time. This leads to disequilibrium between the cumulus phases and their surrounding magma, which in turn causes diffusive reequilibration between melt inclusions and host cumulus phases. The nakhlites and chassignites are later emplaced at or near the surface of Mars as lava flows or sills before they are impacted and ejected (e.g., Corrigan et al., 2015; Treiman, 2005; Udry and Day, 2018; Udry et al., 2020).

2.9 References

Armytage, R.M.G., Debaille, V., Brandon, A.D., and Agee, C.B., 2018, A complex history of silicate differentiation of Mars from Nd and Hf isotopes in crustal breccia NWA 7034: Earth and Planetary Science Letters, v. 502, p. 274–283, doi:10.1016/j.epsl.2018.08.013.

Balta, B.J., Sanborn, M.E., Mayne, R.G., Wadhwa, M., McSween, H.Y., and Crossley, S.D., 2017, Northwest Africa 5790: A previously unsampled portion of the upper part of the nakhlite pile: Meteoritics and Planetary Science, v. 52, p. 36–59, doi:10.1111/maps.12744.

Basu Sarbadhikari, A., Babu, E.V.S.S.K., and Vijaya Kumar, T., 2017, Chemical layering in the upper mantle of Mars: Evidence from olivine-hosted melt inclusions in Tissint: Meteoritics and Planetary Science, v. 52, p. 251–267, doi:10.1111/maps.12790.

Basu Sarbadhikari, A., Goodrich, C.A., Liu, Y., Day, J.M.D., and Taylor, L.A., 2011, Evidence for heterogeneous enriched shergottite mantle sources in Mars from olivine-hosted melt inclusions in Larkman Nunatak 06319: Geochimica et Cosmochimica Acta, v. 75, p. 6803–6820, doi:10.1016/j.gca.2011.09.001.

Beck, P., Barrat, J.A., Gillet, P., Wadhwa, M., Franchi, I.A., Greenwood, R.C., Bohn, M., Cotten, J., van de Moortèle, B., and Reynard, B., 2006, Petrography and geochemistry of the chassignite Northwest Africa 2737 (NWA 2737): Geochimica et Cosmochimica Acta, v. 70, p. 2127–2139, doi:10.1016/j.gca.2006.01.016.

Brahm, R., Zellmer, G.F., Kuritani, T., Coulthard, D., Nakagawa, M., Sakamoto, N., Yurimoto, H., and Sato, E., 2021, MushPEC: Correcting Post-entrapment Processes Affecting Melt Inclusions Hosted in Olivine Antecrysts: Frontiers in Earth Science, v. 8, p. 1–20, doi:10.3389/feart.2020.599726.

Cashman, K. V., Sparks, R.S.J., and Blundy, J.D., 2017, Vertically extensive and unstable

magmatic systems: A unified view of igneous processes: Science, v. 355, doi:10.1126/science.aag3055.

Cohen, B.E., Mark, D.F., Cassata, W.S., Lee, M.R., Tomkinson, T., and Smith, C.L., 2017a, Taking the pulse of Mars via dating of a plume-fed volcano: Nature Communications, v. 8, p. 1–9, doi:10.1038/s41467-017-00513-8.

Cohen, B.E., Mark, D.F., Cassata, W.S., Lee, M.R., Tomkinson, T., and Smith, C.L., 2017b, Taking the pulse of Mars via dating of a plume-fed volcano: Nature Communications, v. 8, doi:10.1038/s41467-017-00513-8.

Combs, L.M., Udry, A., Howarth, G.H., Righter, M., Lapen, T.J., Gross, J., Ross, D.K., Rahib, R.R., and Day, J.M.D., 2019, Petrology of the enriched poikilitic shergottite Northwest Africa 10169: Insight into the martian interior: Geochimica et Cosmochimica Acta, v. 266, p. 435–462, doi:10.1016/j.gca.2019.07.001.

Corrigan, C.M., Velbel, M.A., and Vicenzi, E.P., 2015, Modal abundances of pyroxene, olivine, and mesostasis in nakhlites: Heterogeneity, variation, and implications for nakhlite emplacement: Meteoritics and Planetary Science, v. 50, p. 1497–1511, doi:10.1111/maps.12492.

Cottrell, E., Spiegelman, M., and Langmuir, C.H., 2002, Consequences of diffusive reequilibration for the interpretation of melt inclusions: Geochemistry, Geophysics, Geosystems, v. 3, p. 1–26, doi:10.1029/2001gc000205.

Danyushevsky, L. V., Della-Pasqua, F.N., and Sokolov, S., 2000, Re-equilibration of melt inclusions trapped by magnesian olivine phenocrysts from subduction-related magmas: petrological implications: Contributions to Mineralogy and Petrology, v. 138, p. 68–83.

Danyushevsky, L. V., and Plechov, P., 2011, Petrolog3: Integrated software for modeling

crystallization processes: Geochemistry, Geophysics, Geosystems, v. 12, doi:10.1029/2011GC003516.

Day, J.M.D., Tait, K.T., Udry, A., Moynier, F., Liu, Y., and Neal, C.R., 2018, Martian magmatism from plume metasomatized mantle: Nature communications, v. 9, p. 4799, doi:10.1038/s41467-018-07191-0.

Day, J.M.D.D., Taylor, L.A., Floss, C., and McSween, H.Y., 2006, Petrology and chemistry of MIL 03346 and its significance in understanding the petrogenesis of nakhlites on Mars: v. 41, p. 581–606, doi:10.1111/j.1945-5100.2006.tb00484.x.

Debaille, V., O'Neill, C., Brandon, A.D., Haenecour, P., Yin, Q.Z., Mattielli, N., and Treiman, A.H., 2013, Stagnant-lid tectonics in early Earth revealed by 142Nd variations in late Archean rocks: Earth and Planetary Science Letters, v. 373, p. 83–92, doi:10.1016/j.epsl.2013.04.016.

Filiberto, J., Treiman, A.H., and Le, L., 2008, Crystallization experiments on a Gusev Adirondack basalt composition:, http://meteoritics.org.

Gaetani, G.A., and Watson, E.B., 2000, Open system behavior of olivine-hosted melt inclusions: Earth and Planetary Science Letters, v. 183, p. 27–41, doi:10.1016/S0012-821X(00)00260-0.

Ghiorso, M.S., and Gualda, G.A.R., 2015, An H2O–CO2 mixed fluid saturation model compatible with rhyolite-MELTS: Contributions to Mineralogy and Petrology, v. 169, p. 1–30, doi:10.1007/s00410-015-1141-8.

Goldstein J. I., Newbury, D. E., Michael J. R., Ritchie N. W. M., Scott J. H. J., Joy D. C., 2018, *Scanning electron microscopy and X-Ray microanalysis 4th ed.*, NY: Springer, p. 298–307.

Goodrich, C.A., Fioretti, A.M., and Van Orman, J., 2009, Petrogenesis of augite-bearing ureilites Hughes 009 and FRO 90054/93008 inferred from melt inclusions in olivine, augite and orthopyroxene: Geochimica et Cosmochimica Acta, v. 73, p. 3055–3076,

doi:10.1016/j.gca.2009.02.018.

Goodrich, C.A., Treiman, A.H., Filiberto, J., Gross, J., and Jercinovic, M., 2013, K2O-rich trapped melt in olivine in the Nakhla meteorite: Implications for petrogenesis of nakhlites and evolution of the Martian mantle: Meteoritics and Planetary Science, v. 48, p. 2371–2405, doi:10.1111/maps.12226.

Gualda, G.A.R., Ghiorso, M.S., Lemons, R. V., and Carley, T.L., 2012, Rhyolite-MELTS: A modified calibration of MELTS optimized for silica-rich, fluid-bearing magmatic systems: Journal of Petrology, v. 53, p. 875–890, doi:10.1093/petrology/egr080.

Harvey, R.P., and Mcsween, H.Y., 1992, The parent magma of the nakhlite meteorites: Clues from melt inclusions.:

He, Q., Xiao, L., Hsu, W., Balta, J.B., McSween, H.Y., and Liu, Y., 2013, The water content and parental magma of the second chassignite NWA 2737: Clues from trapped melt inclusions in olivine: Meteoritics and Planetary Science, v. 48, p. 474–492, doi:10.1111/maps.12073.

Imae, N., and Ikeda, Y., 2007, Petrology of the Miller Range 03346 nakhlite in comparison with the Yamato-000593 nakhlite:, http://meteoritics.org.

Jambon, A., Sautter, V., Barrat, J.A., Gattacceca, J., Rochette, P., Boudouma, O., Badia, D., and Devouard, B., 2016, Northwest Africa 5790: Revisiting nakhlite petrogenesis: Geochimica et Cosmochimica Acta, v. 190, p. 191–212, doi:10.1016/j.gca.2016.06.032.

Johnson, M.C., Rutherford, M.J., and Hess, P.C., 1991, Chassigny petrogenesis: Melt compositions, intensive parameters, and water contents of Martian (?) magmas: Geochimica et Cosmochimica Actamica et Cosmochimico Acta, v. 55, p. 349–366.

Karlstrom, L., and Richards, M., 2011, On the evolution of large ultramafic magma chambers and timescales for flood basalt eruptions: Journal of Geophysical Research: Solid Earth, v. 116,

p. 1–13, doi:10.1029/2010JB008159.

Kent, A.J.R., 2008, Melt Inclusions in Basaltic and Related Volcanic Rocks: Reviews in Mineralogy and Geochemistry, doi:10.2138/rmg.2008.69.8.

Longhi, J., and Pan, V., 1989, The parental magmas of the SNC meteorites , in 19th Lunar and Planetary Science Conference, p. 451–464.

McCubbin, F.M., Smirnov, A., Nekvasil, H., Wang, J., Hauri, E., Lindsley, D.H., 2010, Hydrous magmatism on Mars: A source of water for the surface and subsurface during the Amazonian, Earth and Planetary Science Letters, v. 292, p. 132–138.

McCubbin, F.M., Elardo, S.M., Shearer, C.K., Smirnov, A., Hauri, E.H., and Draper, D.S., 2013, A petrogenetic model for the comagmatic origin of chassignites and nakhlites: Inferences from chlorine-rich minerals, petrology, and geochemistry: Meteoritics and Planetary Science, v. 48, p. 819–853, doi:10.1111/maps.12095.

Nicklas, R.W., Day, J.M.D., Vaci, Z., Udry, A., Liu, Y., and Tait, K.T., 2021, Uniform oxygen fugacity of shergottite mantle sources and an oxidized martian lithosphere: Earth and Planetary Science Letters, v. 564, p. 116876, doi:10.1016/j.epsl.2021.116876.

Nyquist, L.E., Bogard, D.D., Greshake, A., and Eugster, O., 2001a, Ages and geologic histories of martian meteorites: Chronology and Evolution of Mars, p. 105–164.

Nyquist, L.E., Bogard, D.D., Greshake, A., and Eugster, O., 2001b, The clan of Martian meteorites , formerly called SNCs after S hergotty , N akhla and C hassigny , now consists of 16 unpaired meteorites of magmatic origin (basalts and ultramafic cumulates). Generally young crystallization ages (with the exception of : , p. 105–165.

O'Neal E. W., Ostwald A. M., Udry A., Gross J., Righter M., Mcquaig D. R., Lapen T. J., Howarth G. H., Johnsen R., 2022, The evolution of poikilitic shergottite magmas from mantle to crust,

85th Meteoritical Society Meeting, Abstract #6178.

Paton, C., Hellstrom, J., Paul, B., Woodhead, J., and Hergt, J., 2011, Iolite: Freeware for the visualisation and processing of mass spectrometric data: Journal of Analytical Atomic Spectrometry, v. 26, p. 2508–2518, doi:10.1039/c1ja10172b.

Peters, T.J., Simon, J.I., Jones, J.H., Usui, T., Moriwaki, R., Economos, R.C., Schmitt, A.K., and McKeegan, K.D., 2015, Tracking the source of the enriched martian meteorites in olivine-hosted melt inclusions of two depleted shergottites, Yamato 980459 and Tissint: Earth and Planetary Science Letters, v. 418, p. 91–102, doi:10.1016/j.epsl.2015.02.033.

Sautter, V., Toplis, M.J., Lorand, J.P., and Macri, M., 2012, Melt inclusions in augite from the nakhlite meteorites: A reassessment of nakhlite parental melt and implications for petrogenesis: Meteoritics and Planetary Science, v. 47, p. 330–344, doi:10.1111/j.1945-5100.2012.01332.x.

Schiano, P., 2003, Primitive mantle magmas recorded as silicate melt inclusions in igneous minerals: Earth-Science Reviews, v. 63, p. 121–144, doi:10.1016/S0012-8252(03)00034-5.

Schindelin, J. et al., 2012, Fiji: an open-source platform for biological-image analysis: Nature Methods, v. 9, p. 676–682.

Sonzogni, Y., and Treiman, A., 2015, Small melt inclusions can record bulk magma compositions: A planetary example from the Martian basalt (shergottite) Tissint: Meteoritics and Planetary Science, v. 50, p. 1880–1895, doi:10.1111/maps.12516.

Stockstill, K.R., Mcsween, H.Y., and Bodnar, R.J., 2005, Melt inclusions in augite of the Nakhla martian meteorite: Evidence for basaltic parental melt:, http://meteoritics.org.

Treiman, A.H., 2005, The nakhlite meteorites: Augite-rich igneous rocks from Mars: Elsevier GmbH, v. 65, p. 203–270, doi:10.1016/j.chemer.2005.01.004.

Treiman, A.H., 1993, The parent magma of the Nakhla (SNC) meteorite, inferred from magmatic inclusions: Geochimica et Cosmochimica Acta, doi:10.1016/0016-7037(93)90198-6.

Treiman, A.H., 1986, The parental magma of the Nakhla achondrite: Ultrabasic volcanism on the shergottite parent body*: Geochemica et Cosmochimico Acta, v. 50, p. 1061–1070.

Ubide, T., McKenna, C.A., Chew, D.M., and Kamber, B.S., 2015, High-resolution LA-ICP-MS trace element mapping of igneous minerals: In search of magma histories: Chemical Geology, v. 409, p. 157–168, doi:10.1016/j.chemgeo.2015.05.020.

Udry, A., and Day, J.M.D., 2018, 1.34 billion-year-old magmatism on Mars evaluated from the co-genetic nakhlite and chassignite meteorites: Geochimica et Cosmochimica Acta, v. 238, p. 292–315, doi:10.1016/j.gca.2018.07.006.

Udry, A., Howarth, G.H., Herd, C., Day, J., Lapen, T.J., and Filiberto, J., 2020, What martian meteorites reveal about the interior and surface of Mars: Earth and Space Science Open Archive, p. 55, https://doi.org/10.1002/essoar.10503123.2.

Varela, M.E., Kurat, G., and Clocchiatti, R., 2001, Glass-bearing inclusions in Nakhla (SNC meteorite) augite: Heterogeneously trapped phases: Mineralogy and Petrology, v. 71, p. 155–172, doi:10.1007/s007100170037.

Wallace, P.J., Plank, T., Bodnar, R.J., Gaetani, G.A., and Shea, T., 2021, Olivine-hosted melt inclusions: A microscopic perspective on a complex magmatic world: Annual Review of Earth and Planetary Sciences, v. 49, p. 465–494, doi:10.1146/annurev-earth-082420-060506.

Wieser, P.E., Edmonds, M., Maclennan, J., Jenner, F.E., and Kunz, B.E., 2019, Crystal scavenging from mush piles recorded by melt inclusions: Nature Communications, v. 10, doi:10.1038/s41467-019-13518-2.

Zhang, S., He, M., Yin, Z., Zhu, E., Hang, W., and Huang, B., 2016, Elemental fractionation and

matrix effects in laser sampling based spectrometry: Journal of Analytical Atomic Spectrometry, v. 31, p. 358–382, doi:10.1039/c5ja00273g.

Chapter 4: Complex Zoning in the Nakhlite and Chassignite Martian Meteorites Reveals Multi-Stage Petrogenesis

4.1 Notice of Publication Submission

This chapter has been formatted from an article that has been submitted for publication. Authors include Amanda M. Ostwald, Arya Udry, Juliane Gross, James M. D. Day, and Sammy Griffin. Quantitative electron probe microanalysis and laser ablation inductively coupled plasma mass spectrometry was performed solely by Amanda Ostwald. Qualitative electron probe mapping was conducted by Amanda Ostwald and Juliane Gross. Writing was led by Amanda Ostwald.

4.2 Abstract

Nakhlites (clinopyroxene-rich cumulates) and chassignites (dunites) are two types of meteorites that were emplaced onto and ejected from the Mars surface together, but their petrogenetic history is otherwise difficult to discern. We study the primary magmatic history preserved in geochemical zoning patterns in the cumulus phases of a representative suite of nakhlites and chassignites. Samples studied include nakhlites Northwest Africa (NWA) 11013, NWA 10645, Governador Valadares, Caleta el Cobre 022, Nakhla, Miller Range 090032, and NWA 817, as well as chassignites NWA 2737 and Chassigny. In nakhlite and chassignite olivine, P preserves primary magmatic signatures, and P_2O_5 ranges from ~<0.01 to 0.21 wt.%; in nakhlite pyroxene, Cr zoning corresponds to Cr_2O_3 abundances between ~0.03 to 0.36 wt.%. We find that nakhlite pyroxene cores uniformly formed initially rapidly for a time at high crustal pressure, and then slowly at near-equilibrium under less crustal pressure. Pyroxene in the nakhlites was then stored through multiple injections of magma prior to eruption and final crystallization. Nakhlite

olivine cores are morphologically heterogenous throughout the suite, but all record rapid initial crystallization prior to equilibrium formation followed by resorption due to changing magma compositions. Both olivine and pyroxene in the nakhlites are antecrysts, as they initially formed in a different magma than the one that they erupted in. Chassignites underwent very rapid initial undercooling followed by rapid changes in magma thermal conditions to result in thin elemental oscillations. Together, the cumulus phases of the nakhlite and chassignite suite combined with other observations on shergottite martian meteorites suggest that rapid initial mineral formation is very common on Mars, possibly due to magmatic conditions or compositions that are unique to the planet.

4.3 Introduction

The nakhlite and chassignite martian meteorites share overlapping crystallization (~1.3 Ga) and ejection ages (~11 Ma), making it likely that they were sourced from a single impact event (Nyquist et al., 2001; Cohen et al., 2017; Udry and Day, 2018; Udry et al., 2020). At the time of writing, there are 32 unpaired nakhlite stones and three unpaired chassignite stones, collectively making them the largest single-origin suite of rocks from Mars. While it can be inferred that the nakhlites and chassignites formed in and were ejected from one location on the Mars surface, that location is unknown.

The nakhlites are clinopyroxene-rich cumulate rocks also containing fayalitic olivine, as well as varying amounts of glass, plagioclase, and other minor phases such as oxide, phosphate, and sulfide minerals (e.g., Treiman, 2005). The two phases with the largest modal fraction in the nakhlites, clinopyroxene and olivine, are in disequilibrium, and literature on their relationship is divided. Some authors contend that olivine and pyroxene form from compositionally different magmas, making one phase or the other xenocrystic, while other authors argue that the two phases form together in a single magma and are thus phenocrystic (e.g., Harvey and Mcsween, 1992; Stockstill et al., 2005; Sautter et al., 2012; Goodrich et al., 2013; Udry and Day, 2018). If one of the nakhlite phases was erupted in a compositionally different magma than it formed in, and if the magmatic system was otherwise closed in terms of trace elements and isotopes, that phase would be considered antecrystic (see Chapter 2; also e.g., Balta et al., 2013; Ubide and Kamber, 2018). Differences in texture, mineralogy, and chemistry among the nakhlites point toward emplacement as multiple lava flows, lava lake infills, or sills near the martian surface (Day et al., 2006; Corrigan et al., 2015; Sautter et al., 2015; Jambon et al., 2016; Udry and Day, 2018; Griffin et al., 2022; Griffin et al., 2022). Furthermore, high-resolution $^{40}Ar/^{39}Ar$ dating shows that the nakhlites were

emplaced over the course of nearly 100 Ma (Cohen et al., 2017). In contrast, the longest-lived magma chambers on Earth are thought to persist for only 30 Ma (Marsh, 2007). The chassignites are dunites (olivine cumulates) which, because of similar trace element enrichments and volatile fluid interactions, are petrogenetically related to the nakhlites and likely sample the same depleted, oxidized source (Treiman, 2005; McCubbin et al., 2013; Udry and Day, 2018; Day et al., 2018; Nicklas et al., 2021).

In this study, we conduct mapping and quantification of major, minor, and trace elements in the cumulus phases of a comprehensive suite of nakhlite and chassignite samples. We focus on minor elements (e.g., Al, Ti, Cr, and P), which best preserve primary magmatic processes, in contrast with divalent cations (i.e., Mg^{2+}, Fe^{2+}), which rapidly diffuse through the mineral grain to erase initial zoning. In olivine, P is incompatible but may be incorporated during periods of rapid, disequilibrium growth due to undercooling (Milman-Barris et al., 2008; Shearer et al., 2013; Welsch et al., 2014; Xing et al., 2022). Pyroxene disequilibrium growth can also be recorded with Al and Ti enrichments relative to more compatible elements Mg or Si (Kouchi et al., 1983; Welsch et al., 2016). Chromium, as a compatible element in pyroxene, can record additions of mafic (Cr-bearing) magmas as enrichments, late-stage crystallization of Cr-depleted melts, and localized compositional variabilities in dynamic magmas (Streck et al., 2002; Tornare et al., 2016; Welsch et al., 2016; Ubide and Kamber, 2018; Ubide et al., 2019). We systematically compare primary magmatic zoning to reconstruct the shared petrogenetic history of the nakhlites and chassignites.

4.4 Methods

4.4.1 Samples

We conducted analyses on a suite of seven of the 32 nakhlites, and two of the three chassignites. Nakhlite samples include thin sections of Northwest Africa (NWA) 11013, NWA 10645, Governador Valadares, Caleta el Cobre (CeC) 022, Nakhla, Miller Range (MIL) 090032, and a thick section of NWA 817. Chassignite samples include thin sections of Chassigny and NWA 2737.

4.4.2 Major and Minor Element Characterization

Major and minor element data were collected using two methods: quantitative traverses, and qualitative mapping. Quantitative traverses were collected on the *JEOL JXA-8900* Electron Probe Microanalyzer (EPMA) at the University of Nevada, Las Vegas using a 15 kV accelerating voltage and a 200 nA beam current and a 1 μm spot size. All elements in both olivine and pyroxene (Si, Ti, Al, Cr, Fe, Ni, Mn, Mg, Ca, Na, K, P, V) were measured against a standard block, which is listed in Table C1. Qualitative maps on all samples, save Chassigny, were conducted on the Rutgers University *JEOL JXA-8200* Superprobe using a 15 kV accelerating voltage, a 300 nA beam current, and a 500 ms dwell time. The Chassigny map was conducted using the *JEOL JXA-8530F+* at the University of Minnesota using a 15.0 kV accelerating voltage, a 500 nA beam current, and a 25 ms dwell time.

Maps of full mineral grains using large (500 ms) dwell times, necessary to collect signal of low abundance elements, frequently take a full day or longer to collect. In order to reduce analytical time, we also used a "strip mapping" method described in Shearer et al. (2013). Using the *JEOL JXA-8200* Rutgers Superprobe, and the same settings (500 nA beam current, 15 kV accelerating voltage, 500 ms dwell time) as in full grain maps, we collected maps composed of 150 μm strips from rim-to-rim which coincided with the locations we collected quantitative traverses. We elected

to conduct full or core-to-rim mineral on recently discovered or understudied samples, and strip maps on samples which are better characterized by the literature. In chassignite olivine, we mapped Ca and P. For nakhlite olivine, we mapped Mg, Fe, Ca, Ni, Mn, Al, Cr, and P. In pyroxene, we mapped Mg, Fe, Ca, Al, Ti, Mn, Cr, and V.

4.4.3 Trace Element Characterization

In order to characterize the trace element abundances present in different compositional zones (i.e., areas of high P or Cr), we selected individual spots using minor element maps and analyzed them using laser ablation inductively coupled plasma mass spectrometry (LA-ICP-MS). All LA-ICP-MS analyses were conducted at UNLV using the *Thermo Fisher Scientific iCAP Qc* ICP-MS coupled to an *Elemental Scientific* Excimer NWR193 laser ablation system. The laser operated at 15 Hz with a fluence of 6.7 J/cm^2 a 20 s period of background gas collection, 40 s dwell time, and 10 s wash delay between analyses. Beam sizes varied between (but not within) individual minerals in order to accommodate differences in zoning sizes, ranging in diameter from 30 μm to 50 μm. We analyzed Li, Na, Al, Sc, V, Cr, Ni, Ba, Nd, Sm, Zr, and La with 2 s dwell time for each element. We bracketed all unknown measurements with measurements of standards NIST-610, BIR-1G, and BHVO-2G using consistently sized beams (30–50 μm to match the bracketed unknown measurement). All LA-ICP-MS data were reduced in *iolite 4* using the trace element reduction scheme (Paton et al., 2011).

4.5 Results

4.5.1 Qualitative Mapping

Element maps provide information on the relative variation of trace metal contents across the mineral grains, and as no standards were measured, these maps provide only qualitative information. All maps presented are heat maps, where warmer colors represent relatively higher abundances (red the highest, followed by orange and yellow). Cooler colors are relatively lower abundances (dark blue is the lowest, followed by cyan and then green). No absolute elemental abundances can be determined from the maps, but correlation and quantification can be inferred by comparing maps with EMPA traverses discussed in a later section.

Pyroxene in the Nakhlites

Qualitative X-Ray mapping in the nakhlites Governador Valadares, MIL 090032, NWA 817, Nakhla, NWA 10645, and NWA 11013 reveals that pyroxenes in those samples have a similar elemental zoning. Pyroxene is subhedral (NWA 10645, NWA 11013, Nakhla) to euhedral (NWA 817, Governador Valadares, MIL 090032) and occurs in clusters typical in cumulate rocks. In all samples, Mg is relatively enriched in large cores—comprising about ~90–95% of the total volume of the mineral—before depleting rapidly to more Fe-rich compositions at the rim (Figs. 4.1, C1). Core shapes are subhedral, except in MIL 090032 and NWA 817, where cores appear euhedral and have a sharp compositional delineation against the rim (Figs. 4.1e, 4.1i). Manganese (Mn) and Vanadium (V) are also consistently enriched along the rims of nakhlite pyroxene (Fig. C1). The distribution of Mg, Fe, Mn, and V appears somewhat patchy throughout the large cores of MIL 090032, NWA 11013, NWA 10645, and Governador Valadares (Figs. 4.1a, 4.1e, 4.1i, 4.1m, 4.1u, C1), but is homogenous in NWA 817 and Nakhla.

Within the Mg-rich cores of all mapped nakhlite pyroxenes, the minor elements Cr, Al, and Ti are distributed in irregular, nonconcentric zones (Figs 4.1, C1). Samples NWA 817, Governador

Valadares, and Nakhla have Cr enrichments and Al, Ti depletions in the center of their cores, but overall chemical distributions are heterogenous. In all samples, Cr does not correlate with Al and Ti. The relationship between Al and Ti is most obvious in sample MIL 090032, where the contrast between areas of high and low Cr is particularly sharp (Fig. 4.1, C1). The margins of pyroxene cores are Ti- and Al-rich, as well as Cr-poor. Therefore, there are two distinct domains in the high-Mg pyroxene cores: Domain 1, containing more abundant Ti and Al; and Domain 2, containing more Cr. The other minor element maps Mn and V do not show distinct preferences for either domain. Melt inclusions and void spaces also do not show domain preferences, except in samples NWA 11013 and Nakhla where they are found in Domain 1.

Pyroxene cores are consistently surrounded by two distinct rims (not seemingly related to the two core Domains): an inner rim of middling Cr, Ti, and Al concentration; and an outer rim of Cr depletion corresponding to Ti and Al enrichment. Inner rims in NWA 11013 and NWA 10645 are thick and display a range in Cr concentrations from relatively Cr-depleted adjacent to the core to relatively Cr-enriched adjacent to the outer rim (Fig. 4.1). Contrast between the core and rims, and between the rims themselves, are frequently sharpest in Cr, Ti, and Al maps, and are less distinct in Mg or Fe maps (Figs. 4.1, C1).

Olivine in the Nakhlites

Olivine in the nakhlites occurs in two general populations: 1) large subhedral megacryst olivine (as imaged in NWA 11013, ~6 mm on a long axis), and 2) smaller anhedral olivine in the interstices of accumulated pyroxene (Fig. 4.2; ~2 mm long axes). Both populations of olivine frequently enclose pyroxene and abut pyroxene at their margins (Fig. 4.2). All nakhlite olivine have higher Mg cores that transition to relatively Fe-enriched rims (Figs. 4.2, C3). The transition

between Mg-rich core and Fe-rich rim can be sharp (NWA 11013, NWA 817, MIL 090032), or gradational (Nakhla, Governador Valadares), and Mg-rich core volumes also vary. Along with Fe, Mn is also slightly enriched in nakhlite olivine rims (Fig. C3). Aluminum, Ni, and Ca maps are homogenous throughout olivine grains (Fig. C3).

Heterogeneity in nakhlite olivine is singularly preserved by P zoning, the shapes of which differ significantly between samples. The largest olivine mapped, the megacryst in NWA 11013, contains a subhedral P-rich core, mantled by oscillatory bands of different widths (~10–100 μm), which alternate between high and low P, and terminate in a P-rich outermost rim (Fig. 4.2f). Central to the grain is a large, P-rich melt inclusion that is surrounded by an irregularly shaped P-poor envelope. Throughout the grain, across the core and all oscillatory bands, P appears more concentrated in the bottom of the mapped image. All interstitial olivine grains contain P-rich regions in their Mg-rich cores, but all P-rich inner cores are differently shaped between samples. Caleta el Cobre 022 olivines contains P-rich cores in dendritic habits mantled by irregular zones of P enrichments and pockets of P depletion (Fig. 4.2b). The Nakhla olivine reveals two general regions of P enrichments: a large grain with irregular, feathery P enrichments crosscut by sharp, rounded P depletions, and a smaller grain attached below, generally P-rich but with feathery oscillations (Fig. 4.2i). Northwest Africa 817 olivine contains an anhedral P-rich inner core that seemingly extends beyond the Mg-rich boundary. The mapped Governador Valadares olivine contains irregular patches of P enrichments, the topmost mantled by thin (~1–10 μm) oscillatory bands that are cross-cut by a depleted envelope containing pyroxene (Fig. 4.2l). Miller Range 090023 olivine P maps reveal a skeletal or hopper inner core, with thin oscillatory bands giving way to irregular P patches toward the rim. Many P-rich areas in MIL 090032 are crosscut by P-depleted region. Among the latter, some are small, rounded, and are marked by sharp edges while

others are gradual and irregular in shape. Pyroxene is not found to be enclosed in any P-rich areas in any olivine in the nakhlites.

Olivine in the Chassignites

Elemental maps in chassignite olivine are featureless, except maps conducted for P (Fig. 4.3). Backscattered electron images of olivine, in which the change in grey tones indicate a change in phase density generally coinciding with a shift between Mg and Fe concentrations, are homogenous. Maps for Ca are likewise homogenous, and only grain boundaries are visible. Maps of P, however, show complex compositional variety. Olivine grains in NWA 2727 frequently contain high-P hopper cores with lower-P infill, often surrounded by thin oscillatory bands of high- and low-P to the rim (Fig. 4.3b, e, h). Olivine in Chassigny is comprised solely of thin oscillatory zoning (~1–10 μm), with concentrations seemingly higher in the lower-left quadrant of each crystal imaged in figure 4.3k. Small fractures crosscut and offset oscillations in both samples. Melt inclusions and interstitial material appear bright in P and Ca maps in both samples.

4.5.2 Quantitative Major, Minor, and Trace Element Traverses

Nakhlite Pyroxene

Broadly, the quantitative data confirm qualitative map results. Magnesium oxide is concentrated in the cores, and gives way to FeO enrichment (~14.0 wt.% FeO in the core, ~16.4 wt.% FeO in the core) at the rims of nakhlite pyroxene (Fig. 4.4). Along traverses, there is some variability in SiO_2 that correlates with changes in MgO (Fig. 4.4, Fig. 4.5a). Calcium oxide is slightly depleted (~18.6 wt.%) in the rims of some nakhlite pyroxene (e.g., NWA 10645), and while trends in CaO do not appear to correlate with other major elements, it is negatively correlated with

MnOd (Fig. 4.4, Fig. 4.5b). Significant change in major elements within nakhlite pyroxene is primarily restricted to the rims, as cores are largely homogenous.

Minor element distributions are, in contrast to the major elements, notably heterogenous throughout pyroxene grains in the nakhlites. Oxides TiO_2, Al_2O_3, MnO, and Na_2O_3 in pyroxenes tend to increase, while Cr_2O_3 is generally depleted (as low as ~0.03 wt.% in the rim, with ~0.36 wt.% average in the core), stepwise in the pyroxene rims (Fig. 4.6). As implied by the Domains 1 and 2 uncovered during elemental mapping, Cr_2O_3 is negatively correlated with Al_2O_3 and TiO_2 (Fig. 4.5c–d) in most samples, but is positively correlated in NWA 817 and Governador Valadares cores (but is negatively correlated in rims). Against other elements, pyroxene Domain 1 Al_2O_3 and TiO_2 share a positive correlation with FeO and Na_2O, while Domain 2 Cr_2O_3 is positively correlated with SiO_2 and MgO (Fig. 4.5e–g). Samples fall into two groups in terms of Na_2O abundances: NWA 817, NWA 11013, and NWA 10645 pyroxenes contain more Na_2O on average (together ~0.28 wt.%) than Nakhla, MIL 090032, and CeC 022 (~0.14 wt.%) (Fig. 4.5f). Spatially, Na_2O increases in sync with Domain 1 oxides in most samples, save for CeC 022, where Na_2O is depleted in the pyroxene outermost rim. Manganese oxide shares a weak positive correlation with Na_2O (Fig. 4.5g). The pyroxene rims of NWA 11013 are more MgO-depleted than in other samples (~5 wt.% versus ~7–10 wt.%), and as a consequence its rims trend differently when oxide abundances are compared to cores (Fig. 4.5). Rare earth elements (such as La) are relatively enriched (~5.3±1.1 ppm) in the outermost rim, where Cr_2O_3 is most depleted (Fig. C2).

Nakhlite Olivine

As seen in pyroxene, nakhlite olivine quantitative traverses complement mapping data. Major elements in the cores of olivine are largely homogenous; MgO becomes depleted (~14.5

wt.%) at the rims, while FeO is relatively enriched (~51.0 wt.%) (Fig. 4.7). Minor variability in SiO_2 (31.0–34.9 wt.%) is positively correlated with MgO (Fig. 4.8a), and negatively correlated with FeO in all samples (Fig. 4.8b). Minor elements CaO, MnO, and P_2O_5 were heterogeneously distributed throughout olivine grains (Fig. 4.9). Of those oxides, MnO is negatively correlated with MgO and SiO_2, but positively correlated with FeO (Fig. 4.8c). Calcium oxide (CaO) and P_2O_5 share no trends with each other, nor do they share trends with other oxides (Fig. 4.8d). Phosphorous oxide is sufficiently low abundance (~0–0.20 wt.%) and is complexly distributed in maps so that trends are not easily discernable from quantitative traverse data alone. Calcium trends were, however, not visible in our maps but do present as patterns in traverse data (Fig. 4.7–4.8).

Chassignite Olivine

As in the maps, chassignite olivine is nearly chemically homogenous in all measurable oxides, save P_2O_5 (Fig. 4.7). Major elements MgO, SiO_2, and FeO are the same throughout the grain. Small variations in CaO do not correspond to any other element (Fig. C4b), but CaO is preferentially depleted around a large melt inclusion lying in the NWA 2737 traverse (Fig. 4.7). The heterogeneity of P_2O_5 in chassignite maps is less apparent in the traverse, and absolute concentrations range as high as 0.21 wt.%.

4.6 Discussion

4.6.1 A Single Story for the Nakhlite Pyroxene

Effective Undercooling Recorded in Pyroxene Cores

The two domains we observe in nakhlite pyroxene cores (Domain 1: Al_2O_3 and TiO_2-rich; Domain 2: Cr_2O_3, MgO, and SiO_2-rich) are also found in the Hawaiian ankaramite pyroxenes

described by Welsch et al. (2016) and Hammer et al. (2016). Ankaramite is an igneous rock defined by up to 60 vol.% crystals wherein pyroxene occurs in a greater abundance than olivine. Ankaramite from the Haleakala volcano on Maui is formed in the post-shield stage of the Hawaiian hotspot, which occurs as the island moves away from the hotspot and undergoes a transition in the degree and frequency of melting as it approaches inactivity. Hawaiian ankaramite pyroxene is defined by two domains: a "spongy" domain characterized by numerous void spaces and relatively higher abundances of MgO, SiO_2, and Cr_2O_3 coinciding with the {100}, {010}, and {110} faces; and a non-spongy domain lacking in void spaces and comprised of higher abundances of Al_2O_3, TiO_2, and Na_2O in the {-111} faces. Welsch et al. (2016) found that the first domain to form was non-spongy during a period of effective undercooling. As the first pyroxene domain formed an hourglass structure, it incorporated incompatible elements Al and Ti because its rapid crystallization outpaced the rate at which those elements diffused through the nearfield melt (Welsch et al., 2016). The second domain then infilled the voids left by the initial hourglass faces at a slower, near-equilibrium pace, incorporating incompatible elements to a lesser degree, and eventually formed the external faces to result in euhedral phenocrysts (Welsch et al., 2016). Crystallization during the formation of the second domain, however, was interrupted by eruption, and volatiles were exsolved from the new crystal face to result in the observed spongy texture (Welsch et al., 2016). Final, low-pressure, late-stage crystallization occurred rapidly thereafter, resulting in a high TiO_2 and Al_2O_3 outermost rim (Welsch et al., 2016).

We do not observe void spaces (vesicles, or even melt inclusions) occurring in any one domain preferentially in the nakhlites, which implies that the nakhlites did not volatize during the second phase of core formation (Fig. 4.1). The two domains of most of the inner nakhlite cores are otherwise largely morphologically similar to the ankaramite pyroxene, indicating that nakhlite

pyroxene cores also formed during two distinct stages of growth. The first stage of growth (Domain 1) was likely rapid, onset by thermodynamic effective undercooling, or supersaturation of clinopyroxene in the melt and enriching the grain in incompatible elements (Al, Ti). Supersaturation occurs during thermal or chemical changes in a magma that prompt rapid nucleation and crystallization (REF). Rapid, or disequilibrium, crystallization can lead to incorporation of incompatible elements from the boundary layer surrounding the mineral (Welsch et al., 2014, 2016; Lee et al., 2022). The second stage of growth (Domain 2) occurred in near-equilibrium conditions, filling the remaining grain with compatible elements (Mg, Si). Variability in the relationship between Cr and Al between samples likely reflects differences in the chemical environment of the magma prompting undercooling. Where Cr and Al are positively correlated, rapid crystal growth may have been prompted by a fresh injection of Cr-rich mafic magma. By contrast, Al and Ti enrichments not associated with elevated amounts of Cr mark periods of effective undercooling prompted by other means (Welsch et al., 2016). The degree to which nakhlite pyroxene was undercooled appears to differ slightly between samples, however, as indicated by the general morphologies of the sector zoning observed, as cores can take on either skeletal or hourglass shapes.

Sector zoning in the ankaramite pyroxenes is often irregular in shape as it likely marks the change between two modes of growth. The first mode is rapid and diffusion-controlled growth, wherein growth outpaces the diffusion rate of Al and Ti in the melt resulting in enrichments in the {-111} sectors (Welsch et al., 2016). Undercooling in this mode was estimated to be $\Delta T = 45°C$ (Welsch et al., 2016). The second mode is closer to equilibrium and interface controlled, entrapping more pyroxene-compatible elements as infill in remaining domains (Welsch et al., 2016). Some sector zoning in the nakhlite pyroxenes (NWA 10645, Nakhla, MIL 090032, and NWA 11013, Fig.

4.1) takes on highly similar irregular hourglass shapes to the ankaramite pyroxenes, implying comparable degrees of undercooling. However, some sector zoning in the nakhlite pyroxenes is irregularly Al, Ti, and Cr enriched through the center of the grain (e.g., NWA 817, Governador Valadares, Fig. 4.1d, 4.1i). Similar morphologies are found in experimental and Etnean pyroxenes with irregular dendritic cores that formed in very high degrees of undercooling (ΔT > 73°C) leading to intense supersaturation and a diffusion-limited crystal growth regime (Masotta et al., 2020).

Magma Mixing and Emplacement Recorded in Pyroxene Rims

Rims in the nakhlite pyroxenes are marked by progressive depletion in Cr, with some samples (e.g., NWA 10645 and NWA 11013) showing Cr variation (from depleted to enriched) in the inner rim producing a sawtooth shape in the chemical traverses (Fig. 4.1, Fig. 4.6). Mantling inner rims in Etnean pyroxenes analyzed by Ubide and Kamber (2018) were attributed to episodes of magma recharge that did not result in eruptions for those pyroxenes. Outermost rims on Etnean pyroxenes are also relatively depleted in Cr, and likely represent late-stage crystallization post-eruption after the magma was depleted in compatible elements (Ubide and Kamber, 2018). Variability in nakhlite inner rim Cr may represent dynamic crystallization blending magma compositions, whereas simple Cr depletion in inner rims may be due to the addition of a locally less-mafic magma than that responsible for the nakhlite pyroxene cores. Outermost nakhlite cores are likely also late-stage crystallization in an evolved magma, especially as rims contain markedly higher concentrations of incompatible trace elements (C2).

Importantly, many Etnean pyroxene cores were stored prior to eruption and underwent periods of additional crystallization as the magma compositions changed; upon eruption, low Cr

outermost rims were likely accompanied by olivine and plagioclase crystallization. Ubide and Kamber (2018) call Etnean pyroxene cores antecrysts, or crystals formed from a previous, petrogenetically-related magma to the one that they erupted in. Recycled, antecrystic Etnean pyroxene cores are often resorbed due to the additions of hotter mafic magma. Core morphologies in nakhlite pyroxenes are variable, with some euhedral shapes sharply preserved (e.g., NWA 817) and others more anhedral and rounded (e.g., Nakhla) (Fig. 4.1). Magma injections into the storage chamber for nakhlite pyroxenes may have had variable temperatures either temporally, or spatial distributions of temperatures may have been heterogenous within the magma chamber to cause variable degrees of resorption around pyroxene cores.

Oxygen Fugacity (fO_2) Changes in Nakhlite Pyroxene

Vanadium exists in a range of valence states in martian basalts, most commonly V^{3+} and V^{4+}, but to a lesser extent V^{2+} and V^{5+}. While V^{3+} is more compatible than V^{4+} in olivine and Ca-rich pyroxene, V incorporation into the crystal lattice of olivine appears to be complicated in martian magmas that are undergoing changes in fO_2 (e.g., Shearer et al., 2013). For instance, coupled V and P enrichments in later stage oscillatory growth of shergottite NWA 1183 olivine was possibly due to an increase in fO_2. The nakhlite pyroxene comparatively record few changes in V as a function of fO_2 in their magmatic environment. There is no discernable correlation between V and any other element in pyroxene cores (Fig. 4.1, 4.5). There is minor V enrichment at pyroxene rims visible in maps, which may be due to late-stage crystallization leading to either oxidation or relative V enrichments in the magma (as also observed in olivine-phyric shergottites; Shearer et al., 2013) (Fig. C1). Indeed, Mckay et al. (2007) found that nakhlite pyroxene cores in

MIL 03346 and Yamato 593 contained distinctive Al, Ti, and Cr zoning that could not be attributed to oxidative changes in the magma.

Pressure Changes During Crystallization

The application of pyroxene geobarometers to specific samples is often tenuous even for terrestrial samples when provenance is known. A liquid-pyroxene thermobarometer was applied to Hawaiian ankaramite samples in Hammer et al. (2016), who found that even after correcting for accumulation, high Al and Ti pyroxene cores were likely not in equilibrium with the liquid and thus barometry data were interpreted as generally representing crystallization first in the lower crust, and then crystallization in the upper crust to allow for the volatilization required for spongy texture formation. The relationship between nakhlite pyroxene and its liquid is also difficult to discern, as nakhlites display cumulate textures and contain disequilibrium ferroan olivine that, as we assert later, may initially form from distinct magma compositions. Furthermore, partitioning behavior of elements are highly dependent on liquid compositions, and martian magmas contain more abundant Fe and less Al than terrestrial magmas (e.g., Collinet et al. 2021; Lessel and Putirka 2015; Payré and Dasgupta 2022). With no known provenance, details about crustal thickness and relative crustal pressures are difficult to discern for the nakhlites. Interpretations for geobarometers applied to the nakhlites are therefore only intended for a first-order comparison against terrestrial systems, and estimates for pressure conditions should be treated with caution.

As the initial crystallization for pyroxene cores in the nakhlites may have been rapid, and therefore in inherent disequilibrium with their melt, we elected to compare atomic Ti and Al (calculated per 6 oxygens) that we measured in pyroxene cores across the suite as a means to compare to the single pyroxene barometer developed for terrestrial silica-saturated alkalic magmas

(hawaiite) by Nekvasil et al. (2004). The same single-pyroxene barometer was applied to olivine-phyric shergottite pyroxene and experimental pyroxene by Filiberto et al. (2010), and again to poikilitic shergottites by Rahib et al. (2019). Applied to the ankaramite pyroxene, Ti/Al ratios fit the observations made in Hammer et al. (2016) using a liquid-pyroxene barometer (Fig. 4.10): pyroxene crystallization pressures range from lower to upper crust, where mid-crust pressures are ~4.3 kbar as determined by Nekvasil et al. (2004). Although nakhlite pyroxene contains less overall Ti and Al, ratios across the suite's cores range from roughly lower terrestrial crust to upper terrestrial crustal pressures (Fig. 4.10).

Nakhlite pyroxenes consistently display two rims, which are progressively depleted in Cr, Mg, and Si, and enriched in Fe, Ti, and Al. Sodium enrichment is coupled with Ti and Al in most nakhlite pyroxenes (Fig. 4.4–4.5) even in the outermost rims. In contrast, the outermost rims of ankaramite pyroxenes are depleted in Na, but enriched in Al and Ti, which is a departure from partitioning behavior preserved in the core where all three elements are positively correlated. Welsch et al. (2016) ascribe Na and Al-Ti decoupling to changes in pressure upon emplacement. The coupled behavior of Na and Ti-Al in pyroxene rims in the nakhlites as opposed to the ankaramites may mark a difference either in partitioning behavior specific to martian magmas, or in a difference in final pressures recorded by emplacement in the nakhlite suite. However, there are two distinct groups of nakhlite pyroxene in terms of bulk grain Na abundances (Figs. 4.5f, 4.5h), which may represent two distinct emplacement pressures, with the high pyroxene grains with the higher Na content being formed at higher pressure (see Hammer et al. 2016). A systematic comparison between ankaramite pyroxene erupted to the surface as lava flows or pyroclastics against ankaramite pyroxene emplaced in sills could elucidate the emplacement mechanisms for the nakhlite pyroxenes. Furthermore, experiments on Na, Al, Ti, and Cr partitioning behavior for

pyroxene in Mars-relevant magmas is needed to better resolve barometry, thermometry, and undercooling controls for the system.

4.6.2 Differing Stories for the Nakhlite Olivine

Olivine, as found in this study, bears considerable morphologic heterogeneity in the nakhlite suite. Nakhlite olivine, regardless of size and crystal morphology, often contains relict cores with high-P, but the morphology of those cores is variable between samples. Cores present as irregular, euhedral, skeletal, anhedral; those cores are variably mantled by oscillatory zoning or are crosscut by resorption and embayments. Pyroxene chadacrysts are only observed within low-P areas in olivine.

Phosphorous in nakhlite olivine bears no correlation with any other element (Figs. 4.2, 4.5, 4.9). In terrestrial olivine, the incompatible charge of P^{5+} appears to be offset by Al and Cr, as they are often spatially correlated, particularly in experimentally-produced olivine (Milman-Barris et al., 2008). The incorporation of P in olivine is prompted by disequilibrium mineral growth that outpaces diffusion of incompatible elements through the silicate melt, and diffusion of P in a melt slightly outpaces Cr and Al, respectively, while divalent cations (Mg, Fe, Mn) diffuse rapidly (Milman-Barris et al., 2008). The martian mantle is thought to be up to ten times more enriched in P than the terrestrial mantle, and martian basalts are typically P-enriched relative to terrestrial ones (Wanke and Dreibus, 1988; Payré and Dasgupta 2022). Martian basalts also tend to be relatively Al-poor (Milman-Barris et al. 2008). Mari et al. (2020) noted a correlation between P and Al in olivine in the olivine-phyric shergottite, Tissint, but did not see a correlation with Cr. Compositional differences between martian and terrestrial magma, in addition to diffusive relaxation of elements with higher diffusion coefficients in olivine, obscure coupling behaviors of

P in nakhlite olivine. Calcium appears to be zoned in the quantitative profiles collected in nakhlite olivine (not in maps), however, it is not spatially correlated with P. Other authors' attempts at cooling rate quantification for the nakhlites that use Ca diffusion modeling found significant thermal heterogeneity in the suite, possibly due to complexities in Ca zoning not obviously visible in quantitative data (Mikouchi and Miyamoto, 2002; Mikouchi et al., 2017). Until any coupled partitioning behavior between Ca and P can be uncovered in nakhlite olivine, care should be taken in leveraging relative diffusion rates of both elements for cooling rate or storage timescales.

The presence of P-rich zones in olivine inherently denotes rapid crystal growth during undercooling, however, even dendritic olivine may form in low to moderate undercooling conditions prompted by magma mixing events (ΔT = 25–60°C) (Shea et al., 2019). Crustal magma chambers containing cumulates could cool hotter, fresh magma on contact. A systematic study of P zoning in olivine in a transect of the Sept Iles layered mafic intrusion found that olivine in basal portions of the intrusion contained dendritic cores, but had formed in just one batch of magma undercooled by surrounding cold wallrock (Xing et al., 2022). In contrast, olivine formed in undercooling caused by the interaction of multiple mixing magmas took on irregular-shaped cores with resorption and embayment features (Xing et al. 2022). Dendritic olivine cores in nakhlites, however, appear to have more complicated histories than those of Sept Iles, as dendritic growth is crosscut by embayments and resorption (e.g., MIL 090030, Fig. 4n). In a further example from the Baima layered intrusion in China, resorbed dendritic P-rich olivine cores likely formed in two stages, the first resulting in core formation and the second resulting in resorption and infill (Xing et al., 2017). Nakhlite olivine likely also underwent multiple formation stages: formation of high-P cores, resorption and embayment of some high-P cores, crystallization resulting in lower-P infill, and final rim overgrowth. Areas of lower P between branches of higher P in dendritic or skeletal

olivine, or filling voids left during resorption, represent slower, interface-controlled, close-to-equilibrium crystallization conditions (Welsch et al., 2014).

4.6.3 The Singular Story of Chassignite Olivine

Chassigny and NWA 2737 olivine morphologies are distinct from the morphologies preserved by P zoning in the nakhlites. Northwest Africa 2737 olivine cores tend to be dendritic or skeletal, and are mantled by thin oscillatory zones at their rims. Chassigny contains olivine comprised of concentric, thin P zoning from core to rim. Invariable zoning widths possibly point to intrinsic factors causing undercooling in the melt, as opposed to variable widths generated by resorption in magma mixing events. Because NWA 2737 olivine ($Fo_{\sim 79}$) is more primitive than that of Chassigny ($Fo_{\sim 67}$), NWA 2737 olivine dendritic cores may mark the initial crystallization conditions of the chassignites, which was prompted by rapid crystallization due to supersaturation and effective undercooling (Donaldson, 1976; Milman-Barris et al., 2008; Welsch et al., 2014; Xing et al., 2022). Crystallization then gave way to regular temperature changes in a dynamic magma environment, which is marked by oscillatory zoning in both NWA 2737 and Chassigny and where areas of low-P formed slowly in conditions close to equilibrium (Xing et al., 2022). Relative P depletions along concentric zones may record growth between two adjacent olivine crystals sharing a melt pool (Shearer et al., 2013). Because we do not observe P depletions in oscillations in adjacent grains, olivine in chassignites likely formed at a distance apart in their magma prior to accumulation. Edges of olivine grains visibly crosscut some oscillatory zoning and cores (Fig. 4.3), likely because of physical damage during the later stages of formation and accumulation as well as possible resorption. Otherwise, resorption and embayment features are not seen to cross-cut zoning as in the nakhlites.

Hewins et al. (2020) found that the relatively ferroan olivine ($Fo_{\sim 54}$) in chassignite NWA 8694 was Ca-depleted at its rims, implying zonation, but that P and Ca were not visible in maps. Preserved Ca zoning despite the element's relatively rapid diffusion rate in olivine served as evidence for quick cooling after emplacement (Hewins et al., 2020). We do not observe Ca depletions in the chassignite olivine rims, nor do we see evidence of zoning in the quantitative or mapping data (Figs. 4.3 and 4.9). However, we do observe Ca depletion around a melt inclusion in NWA 2737 olivine. Mobilization of incompatible elements into a melt inclusion in the subsolidus requires elevated temperatures. Because Ca depletion surrounding the melt inclusion occurred after relaxation of other Ca zoning, depletion likely occurred after prolonged storage and during a thermal event that was not overwritten by additional diffusive relaxation (i.e., emplacement).

4.6.4 Crystallization History of Olivine in Martian Meteorites

Olivine has been extensively studied in the shergottite martian meteorites, because it is a ubiquitous and early-forming phase. One subclass of shergottites is the poikilitic shergottites, which show two textural domains: the poikilitic domain, containing pyroxene poikilitically enclosing olivine; and a non-poikilitic domain representing a later-crystallizing stage, containing olivine, pyroxene, and maskelynite (e.g., Udry et al., 2020). Notably, Rahib et al. (2019) conducted P mapping of olivine in a selection of poikilitic. The authors found that the intermediate poikilitic shergottite Lewis Cliff (LEW) 88516 contained olivine (in a late-crystallizing non-poikilitic zone) bearing a P-enriched skeletal core mantled by thin P-rich oscillatory bands, which was similar in morphology to NWA 2737 P maps collected in this study (supplement in Rahib et al. 2019). In the other poikilitic shergottites that these authors analyzed (NWA 10618, NWA 7755, Allan Hills

77005, and NWA 11065), grains consistently displayed thin oscillatory P-rich and P-poor bands similar to those in Chassigny, despite some minor variation between olivine morphologies. Both trends were attributed to inconsistent growth rates resulting in variable incorporation of P into the olivine crystal structure (Rahib et al., 2019).

Olivine-phyric shergottites are another subclass of shergottites containing olivine in the form of earlier-crystallizing megacrysts, along with smaller olivine, pyroxene, and maskelynite (Udry et al., 2020). Olivine-phyric shergottite NWA 6234 contained olivine with high-P cores surrounded by thin P oscillations (Gross et al., 2013). Again, this trend was explained by initial rapid formation followed by alternating crystallization rates (Gross et al. 2013). Additionally, other minor elements (Ca, Mn, Al, Cr, Ni) were otherwise homogenous throughout the grain because the olivine was exposed to prolonged elevated temperatures to allow for diffusion and annealing (Gross et al. 2013). Olivine-phyric shergottites Yamato 980459 (Y98) and NWA 1183 show more variability in olivine morphologies preserved by phosphorous: NWA 1183 contains olivines with low-P cores surrounded by discontinuous P zoning, and Y98 contains P-rich cores surrounded by continuous P oscillations. The P-poor cores were attributed to single-batch phenocrystic growth of olivine, whereas P-rich cores were considered xenocrystic (Shearer et al., 2013). Larkman Nunatak (LAR) 06319, another olivine-phyric shergottite, contains olivine antecrysts which preserve P zoning, but with diffusively homogenized divalent cation zoning (Balta et al., 2013). Tissint, another olivine-phyric shergottite, contained olivine with oscillatory enrichments of P (Mari et al., 2020). In the absence of evidence for magma mixing, oscillations were attributed to a dynamic magmatic environment, where colder regions of the chamber prompted rapid cooling and solute trapping (Mari et al., 2020). As we do not observe evidence for accumulation during formation in chassignite olivine P zoning, P oscillations may also record a dynamic magmatic environment.

Lastly, Fe and Mg isotope profiles in the primitive, enriched olivine-phyric shergottite NWA 1068 show slow initial growth in a deep crustal magma chamber during a period of storage prior to rapid crystallization during transport and a relatively shallow emplacement (Collinet et al., 2017). Near-equilibrium, low-P overgrowth of olivine in nakhlites and chassignites may also occur during storage.

Interestingly, Eckley (2022) found that 3D reconstructions of shergottite olivine in multiple samples (LAR 12095, LAR 12011, and Elephant Moraine) revealed skeletal and dendritic growth not easily visualized in 2D thin sections. Their intensive literature review of martian meteorite olivine morphologies revealed that many, if not most, martian olivine formed by rapid undercooling to result in skeletal or dendritic olivine (Eckley, 2022). Caleta el Cobre 022 olivine contains a P-rich core that is nearly identical to the mantled dendritic olivine imaged in LAR 12011 as seen cut along the {100} plane view. Likely, even euhedral to subhedral olivine with few melt inclusions may have initially formed from undercooling prior to later equilibrium crystallization, but that magmatic history would not be revealed without P mapping.

Rapid undercooling appears to be common in olivine from various lithologies of shergottites, but is also common to the crystallization of the cumulus phases of the nakhlites as well as the olivine in chassignite NWA 2737. Dynamic magma in a thermally variable chamber resulted in oscillatory compositional changes in Tissint, and the same may have been true for the mantles and rims of the chassignites. Diffusive relaxation of major and most minor elements across olivine in LAR 06319, but retention of P zoning, indicated that some olivine-phyric shergottites contain stored antecrysts. The same is true of nakhlite and chassignite olivine, indicating that crystal storage and recharge in a trace element and isotopically closed system is potentially common on Mars.

4.6.5 Petrogenesis of Nakhlite and Chassignite Cumulus Minerals

The crystallization history of the nakhlites and chassignites, as preserved by zoning, is a complex one. If the chassignites formed together in a single magma, NWA 2737 likely began rapid dendritic crystallization first, which was followed by oscillations of rapid and slow crystallization prompted by intrinsic thermal changes in the magma chamber (Fig. 4.11). Because olivine grains may have formed at some distance from each other, the environment may have been dynamic. Olivine accumulated and was stored for a long enough period that all zoning, except P, was erased by diffusion of cations (e.g., Fe, Mg, Mn) across the grain. For the chassignites observed in this study, diffusive relaxation of Ca across the grain was overwritten by its relative depletion adjacent to melt inclusions, likely representing interaction with a hotter mobilizing magma during emplacement.

Nakhlite pyroxene preserves multiple stages of core formation, one rapid and incorporating Al and Ti at a greater rate and higher pressure than in slower, later stage core formation, which preferentially sampled Si and Mg (Fig. 4.11). There is some minor morphological and chemical variety in nakhlite pyroxene cores, probably representing different mechanisms and rates for growth. Pyroxene cores are surrounded by progressively Cr, Mg, and Si rims in all samples, meaning that pyroxene in the studied nakhlites was subjected to at least one magma mixing event that did not result in eruption. Outermost Mg and Cr depleted rims represent late-stage growth, likely upon emplacement (Fig. 4.11). Because the liquids which formed nakhlite pyroxene are not the eruptive liquid, nakhlite pyroxene is likely antecrystic. Pressures decrease somewhat uniformly during core formation for the nakhlites, and core formation may be restricted to crustal conditions.

Olivine cores in the nakhlites reveal histories of rapid growth onset by varying degrees or means of undercooling. Non-equilibrium growth of both olivine and pyroxene in the nakhlites thus indicates that initial crystallization of the parental melt(s) responsible for the suite began with periods of undercooling (Welsch et al., 2016). Olivine cores were also likely resorbed and reformed under closer to equilibrium conditions during magma mixing events, or as they interacted with melt of different compositions in a dynamic chamber (Fig. 4.11).

The magma, which finally entrained nakhlite pyroxenes, also entrained nakhlite olivine. Clinopyroxene, like the augite in the nakhlites, is more stable in higher pressure mafic magmas, but at lower pressures olivine and plagioclase also become liquidus phases (Hammer et al., 2016). Likely, as the entrained pyroxenes and olivines depressurized, crystallization continued for both phases. Initially closely-spaced pyroxene and olivine may have experienced overlapping growth resulting in poikilitic enclosure of either phase (as we observed: olivine enclosed pyroxene). While zoning (aside from Cr, Al, and Ti in pyroxene and P in olivine) was largely erased by diffusive relaxation across pyroxene and olivine cores, outermost rims still preserve zoning of even divalent cations. Thus, storage preceded emplacement, and cooling upon emplacement occurred rapidly enough to preserve final overgrowth.

Research into terrestrial olivine formation is increasingly finding evidence for rapid onset crystallization (e.g., Welsch et al., 2014), but effective undercooling initiating crystallization in martian magmas seems to be the rule rather than the exception (e.g., Eckley, 2022). Some intrinsic and extrinsic factors controlling initial crystal growth rates could be more common on Mars than on Earth. For instance, the crust of Mars is thicker than that of Earth on average, ranging from 35–85 km (up to 100 km) (Plesa et al., 2018); thicker crust may prohibit frequent eruption and foster more crystal storage. Hot mafic magmas may rapidly cool on contact with cold stored crystals or

crystal mush during injection. Furthermore, undercooling can be prompted not just by heat loss in a magma (more or less rapid, as explained above), but also by raising the liquidus temperature of the crystallizing phase, thus delaying nucleation and lowering the temperature required for formation (Donaldson, 1976; Welsch et al., 2014). As an extreme example, spodumene formation in terrestrial pegmatites may occur during undercooling aided by the localized saturation of Li in the melt (Maneta et al., 2015). Martian magmas may simply share a compositional component that raises the liquidus temperatures of olivine (and possibly pyroxene). For instance, relatively high levels of P in martian magmas favor the stability of pyroxene in mantle residuum, thereby relatively saturating mantle partial melts in less complex silicates like olivine (Payré and Dasgupta, 2022). Future empirical work on martian magmas should seek to address the effects of undercooling in Mars-relevant magma compositions.

4.6.6 A Final Note on the Role of Potential Shock Effects

There are a few nominal petrographic effects of shock on the nakhlites, which include twinning in clinopyroxene and undulatory extinction in olivine (Treiman, 2005). Those observations and the dearth of maskelynite observations render estimates of maximum pressure on the nakhlites to be <15 GPa, with the possibility of two shock events that lead to aqueous alteration of the suite (Daly et al., 2019). Despite the nominal visible presentation of shock in nakhlites, primary magmatic nakhlite petrofabrics are difficult to discern because of shock overprinting (Griffin et al., 2022). The effects of shock on primary zoning are not well-understood. Dislocations that serve as pathways in zircon allow low-mobility elements to move relatively quickly through the crystal lattice in response to deformation on geologic timescales (Piazolo et al., 2016). However, the effects of rapid deformation on zoning in silicate minerals is unknown. It is possible that the

somewhat directional distribution of P in some of the nakhlite and chassignite olivine, such as that in NWA 11013 (Fig. 4.1) is in response to localized shock distribution. Griffin et al. (2022b) conducted grain relative orientation distribution (GROD) mapping on the same CeC 022 thin section analyzed in this study, the results of which are visible in Figure 5 of their publication. When their results are compared to Fig. 4.2 in this dissertation, the high-P inner core of CeC 022 olivine is spatially correlated to an area of low deformation, while the moderately high-P mantle overlaps areas of higher deformation in the grain. The largest amount of deformation occurs in the outermost rim of CeC 022 olivine, and in the surrounding mesostasis (Griffin et al., 2022b). Outer rim deformation is also accompanied by P enrichment. Spatial correlations between P zoning are imperfect in the core and best resolved in the rim, indicating that there is likely some compositional dependence on deformation in shocked grains in nakhlites, but that primary zoning in the cores of large grains is mostly preserved. However, a significant amount of experimental work must be done to address the problem of shock effects on primary magma features in mineral grains.

4.7 Conclusions

Our systematic comparison of primary magmatic textures in the nakhlites reveal considerable homogeneity in pyroxene, but heterogeneity in olivine. Chassignite olivine appears related by magmatic processes. In sum:

- Cores of all nakhlite pyroxene analyzed in this study display sector zoning indicative of initially rapid disequilibrium formation followed by equilibrium infill of voids to the subhedral or euhedral inner rim. The degree of undercooling responsible for small differences in core morphologies may differ, but all nakhlite pyroxene began forming in due to some degree of effective undercooling.

- The two compositional domains of pyroxene cores likely formed over a range of crustal pressures, from lower to upper crust. After entering their new staging chamber, nakhlite pyroxenes were stored during the injection of magmas which did not result in eruption. Final entrainment and eruption are recorded in a Mg-poor outermost rim in all studied pyroxenes. Because the final liquid to entrain them is not the liquid that formed them, nakhlite pyroxene cores are likely antecrystic.
- Nakhlite olivine formed initially in varying degrees of undercooling resulting in phosphorous-enriched relict cores, while later infill was closer to equilibrium and phosphorous-poor; relict cores often show signs of interactions with additional magmas, such as resorption or embayment, and pyroxene is sometimes enclosed in infill growth. Nakhlite olivine cores are therefore antecrysts.
- Chassignite olivine formed initially rapidly to form high-P dendritic cores in NWA 2737, and then formed in rapidly changing conditions to result in thin oscillating bands in both NWA 2737 and Chassigny. Storage was prolonged to result in complete chemical homogeneity, save interactions with melt inclusions possibly during emplacement.
- The parental magma(s) which formed the nakhlite olivine and pyroxene as well as the chassignite olivine in this study always began crystallization in disequilibrium. Similar findings in multiple shergottite subgroups supports a growing body of evidence that initially undercooled magmas were common on Mars, possibly indicating that magma storage is common, or that the compositions of martian magmas affects liquidus behavior of mafic minerals like olivine relative to Earth.
- From the mapping and quantitative data, the relationship between the nakhlites and chassignites is still unclear. The chassignite olivine formed in magmatic conditions that

were different than those recorded by nakhlite olivine. Chassignite olivine underwent rapidly changing conditions to generate thin oscillations, although NWA 2737 formed initially by a high degree of undercooling in a manner similar to nakhlite olivine and pyroxene. Furthermore, likely chassignite olivine underwent accumulation but do not record recharge and resorption events as does nakhlite olivine.

4.8 Acknowledgments, Samples, and Data

This study was funded by NASA Solar System Workings 80NSSC21K0159, which was awarded to A. U., J. D., and J. G. Samples and data sources are described in the Methods section, and all instrument data are reported in Appendix C. Thank you to Burger (Rutgers University) and to Minghua Ren (UNLV) for their help in conducting microprobe analyses. US Antarctic meteorite samples are recovered by the Antarctic Search for Meteorites (ANSMET) program which has been funded by NSF and NASA, and were characterized and curated by the Department of Mineral Sciences of the Smithsonian Institution and Astromaterials Curation Office at NASA Johnson Space Center.

4.9 Figures

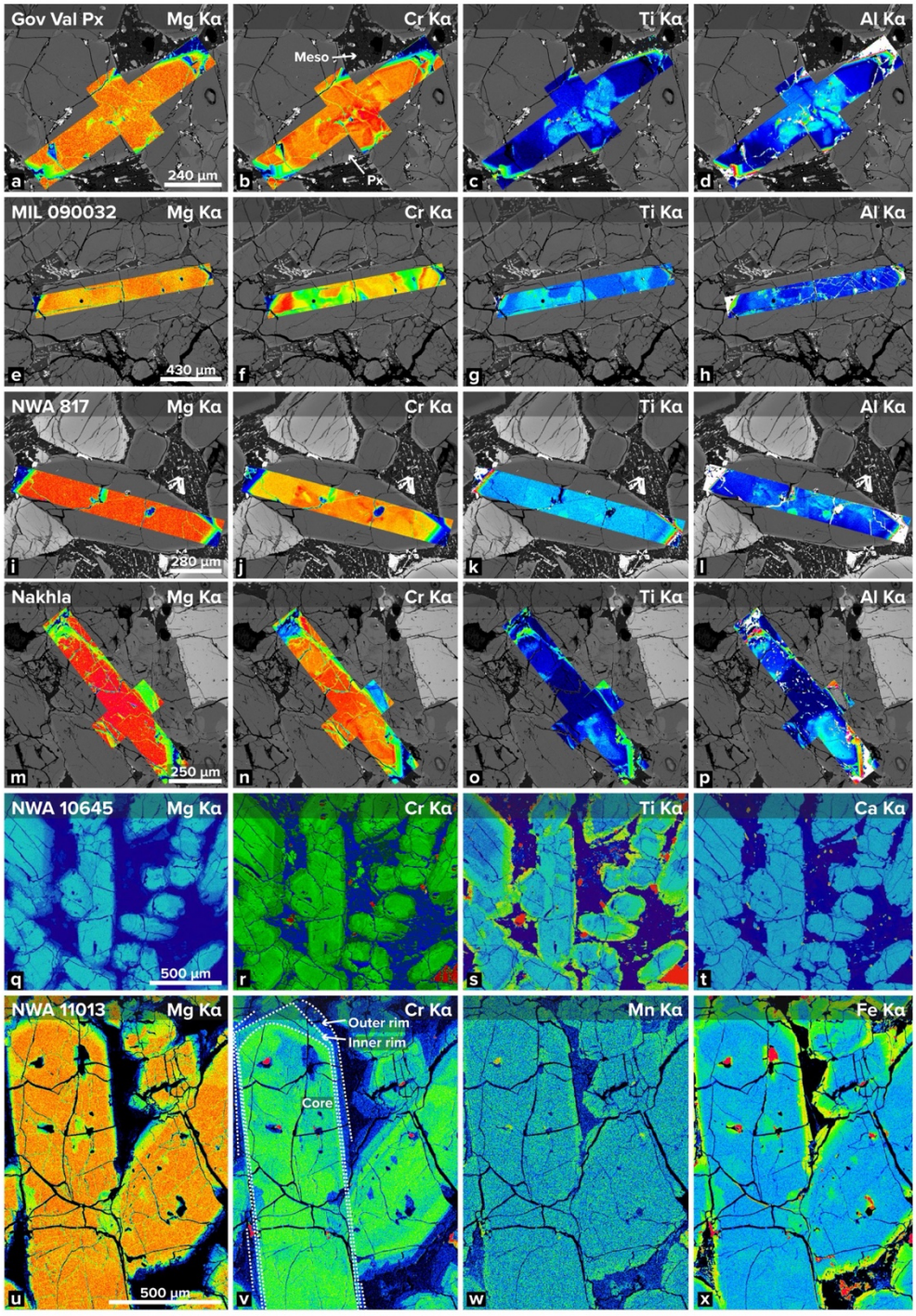

Figure 4.1: Characteristic pyroxene Kα X-Ray maps for nakhlite samples (from top to bottom) Governador Valadares (Gov Val), Miller Range (MIL) 090032, Northwest Africa (NWA) 817, Nakhla, NWA 10645, and NWA 11013. Elements include Mg, Cr, Ti, Al, Ca, Mn, and Fe. Generally, nakhlite pyroxene displays sector zoning in two domains: high Ti and Al; and high Mg and Si. Example core, inner rim, and outer rim are outlined in (v), the NWA 11013 Cr map. Abbreviations: Meso = mesostasis; Px = pyroxene.

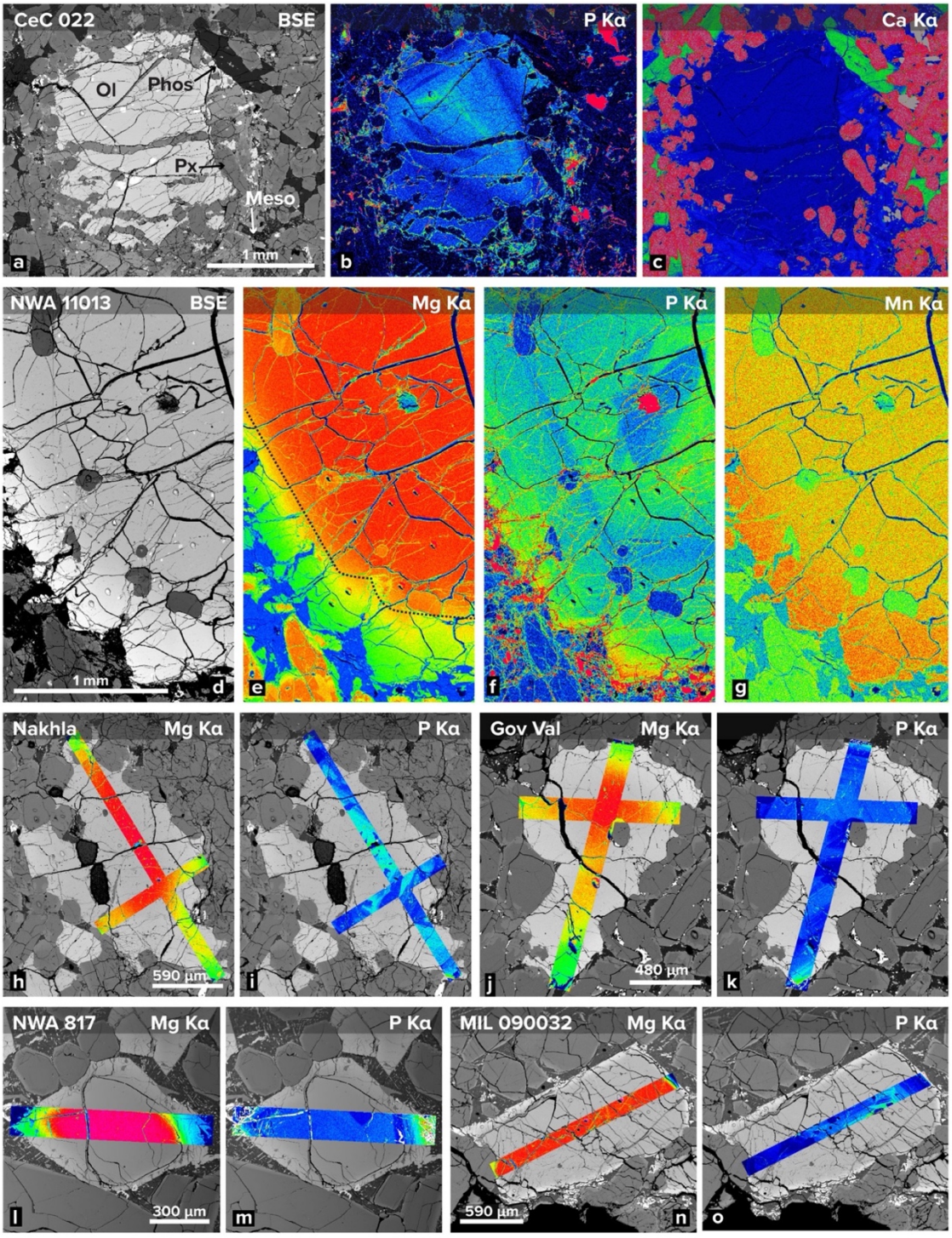

Figure 4.2: Backscattered electron ("BSE") images and P, Ca, Mg, and Mn Ka X-Ray maps in olivine from nakhlites. Samples include, from top to bottom and left to right: CeC 022, NWA 11013, Nakhla, NWA 817, Governador Valadares ("Gov Val"), and MIL 090032. All elements save P are homogenously distributed through the core. P zoning varies between samples. An Mg-rich core is outlined in 2e (NWA 11013 Mg). Abbreviations: Ol = olivine; Phos = phosphate; Px = pyroxene; Meso = mesostasis.

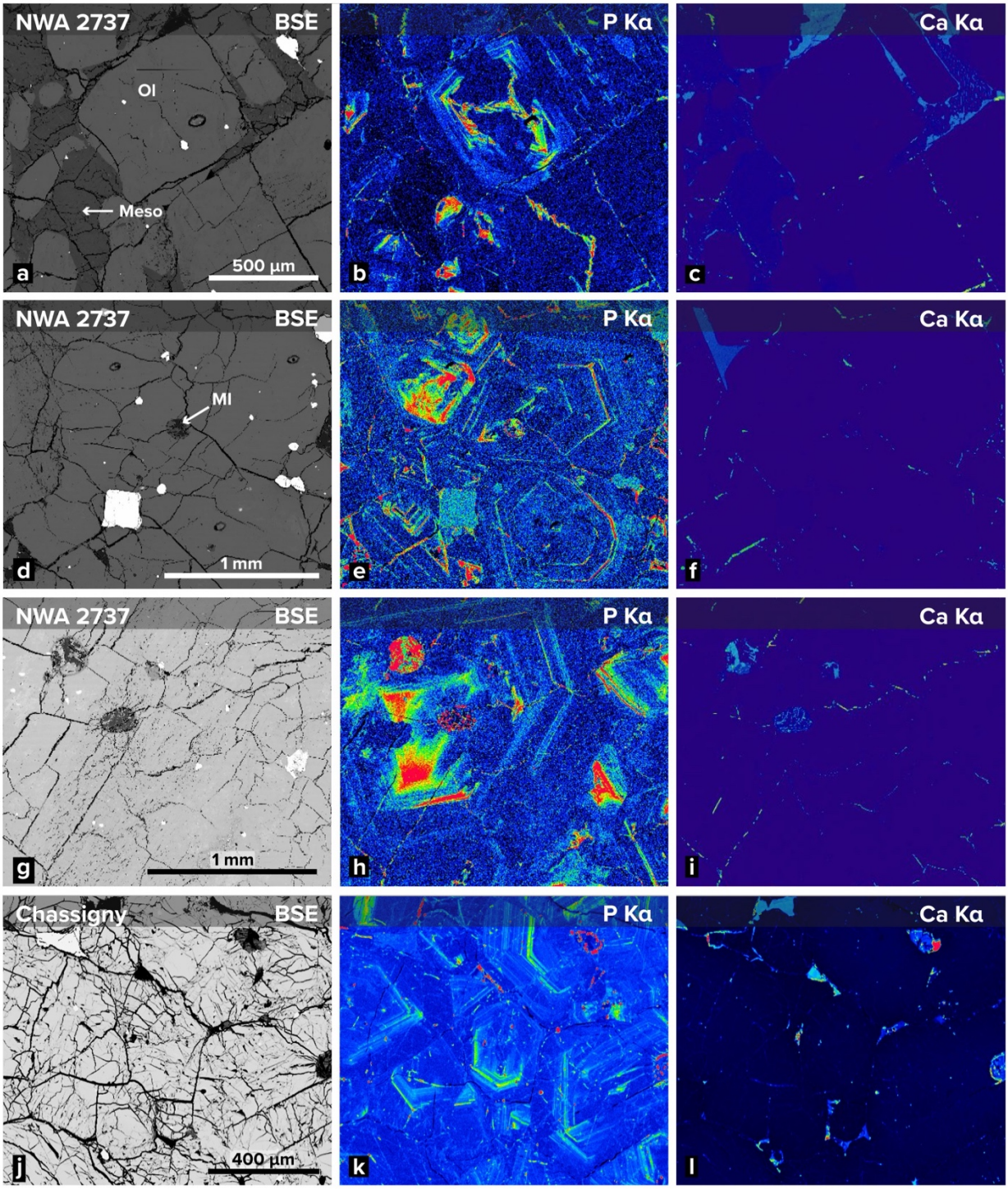

Figure 4.3: Backscattered electron (BSE) images and P and Ca X-ray Kα maps in olivine in chassignites NWA 2737 (a–i) and Chassigny (j–l). Olivine in NWA 2737 contain P-rich hopper and infill cores surrounded by thin oscillatory bands. Chassigny olivine are comprised only of fine P oscillatory bands. Abbreviations: Ol = olivine; Meso = mesostasis.

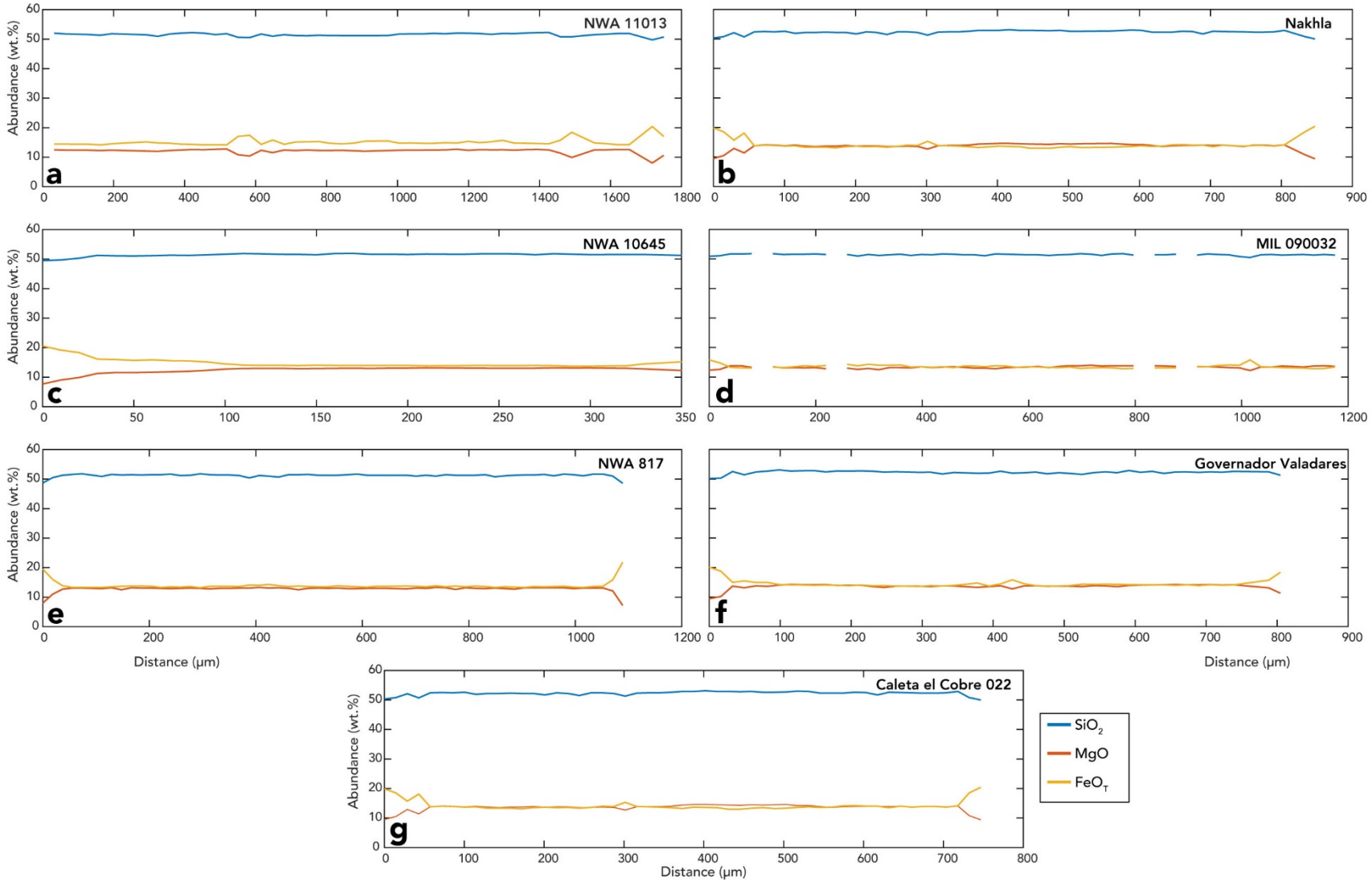

Figure 4.4: Major element traverse data for pyroxene in the nakhlites. Oxides MgO and FeO are largely spatially anti-correlated, with MgO enriched toward the rims. Calcium oxide concentrations appear independent of both MgO and FeO.

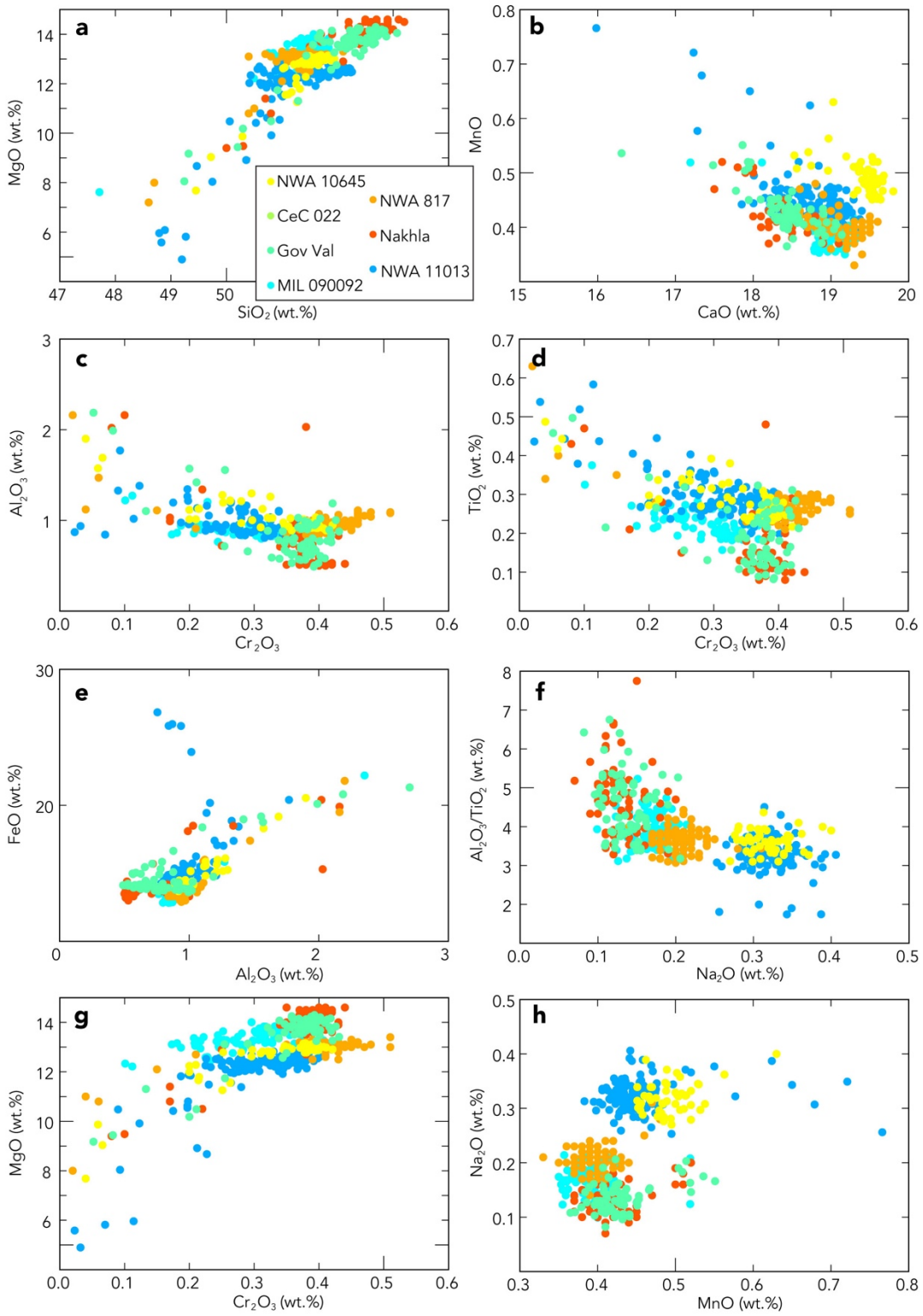

Figure 4.5: Comparison of oxide abundances from quantitative traverses in nakhlite pyroxene. Compositional Domain 1 (containing high Al and Ti) is positively correlated with FeO, but often negatively correlated with Cr_2O_3 (c–e). Domain 2 (high Mg and Si) is positively correlated with Cr_2O_3 (a, g). We observe two groupings of samples in terms of Na_2O abundances (h).

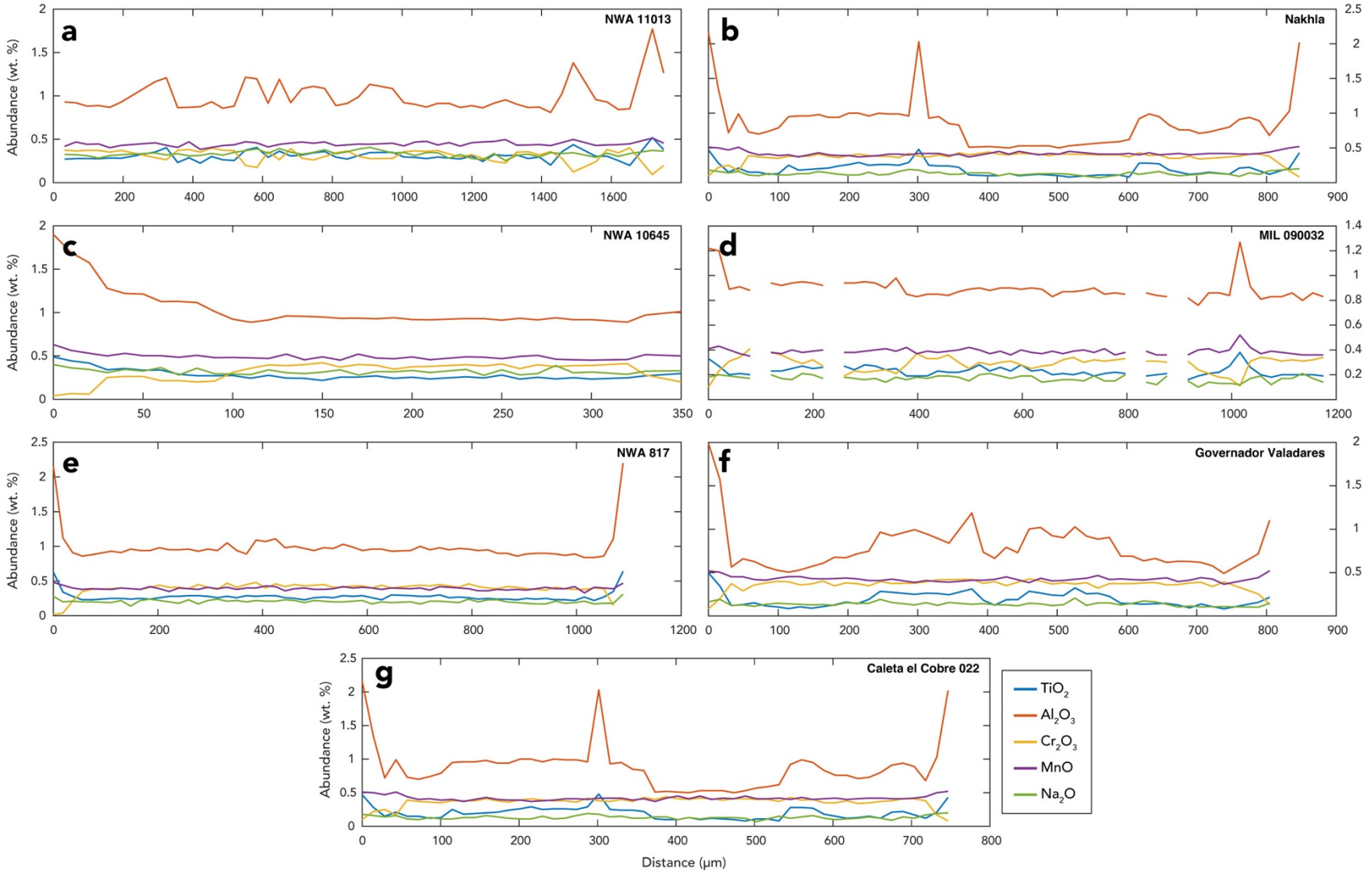

Figure 4.6: Minor element traverse data for pyroxene in the nakhlites. Alumina (Al_2O_3) is correlated with titanium oxide (TiO_2), both of which generally increase in pyroxene rims, and which are usually anti-correlated with Cr_2O_3.

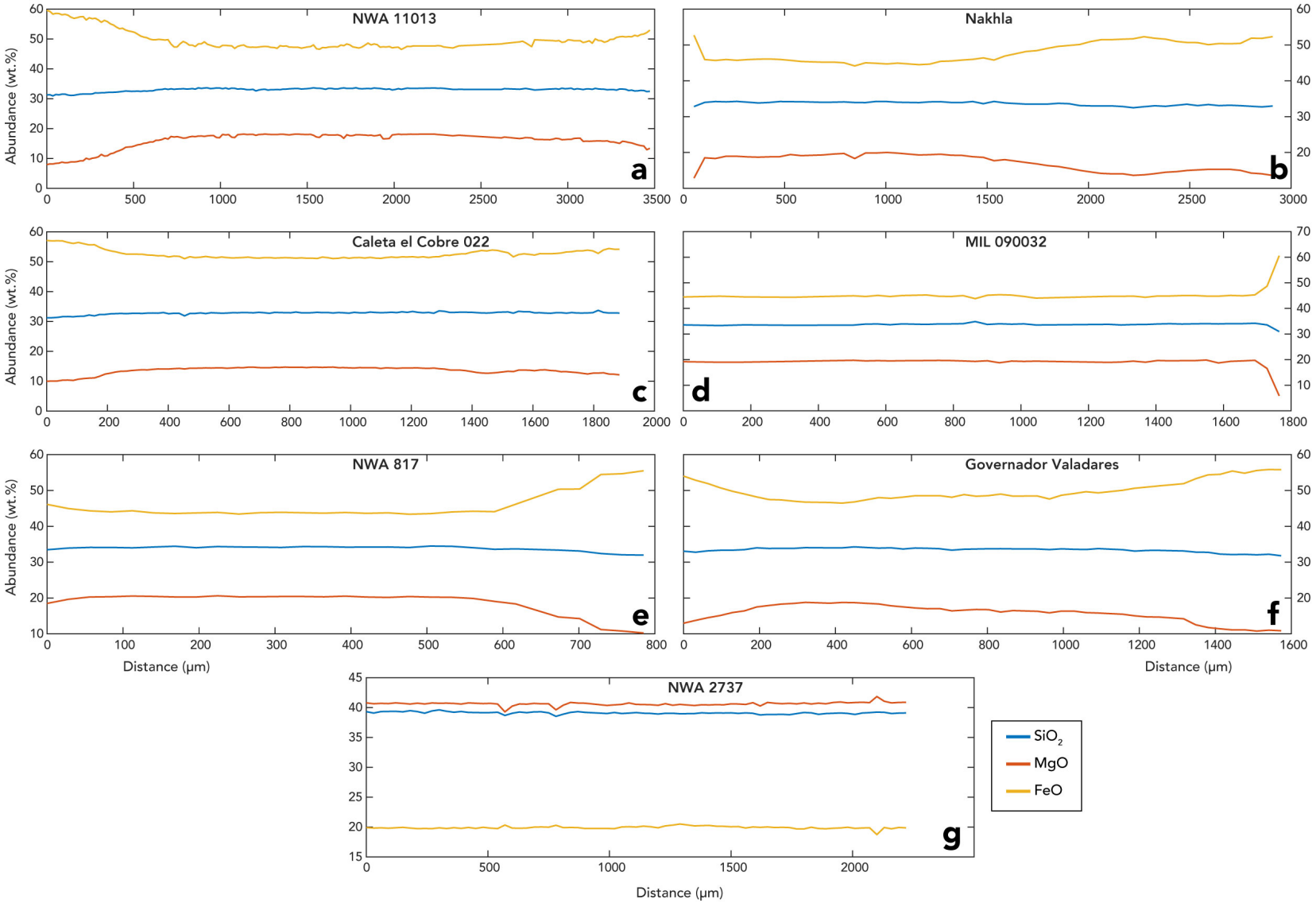

Figure 4.7: Major element quantitative traverse data for chassignite olivine and nakhlite olivine. Nakhlite olivine becomes MgO-poor and FeO-rich at the rim (7a–7f). Chassignite olivine is largely homogenous (7g).

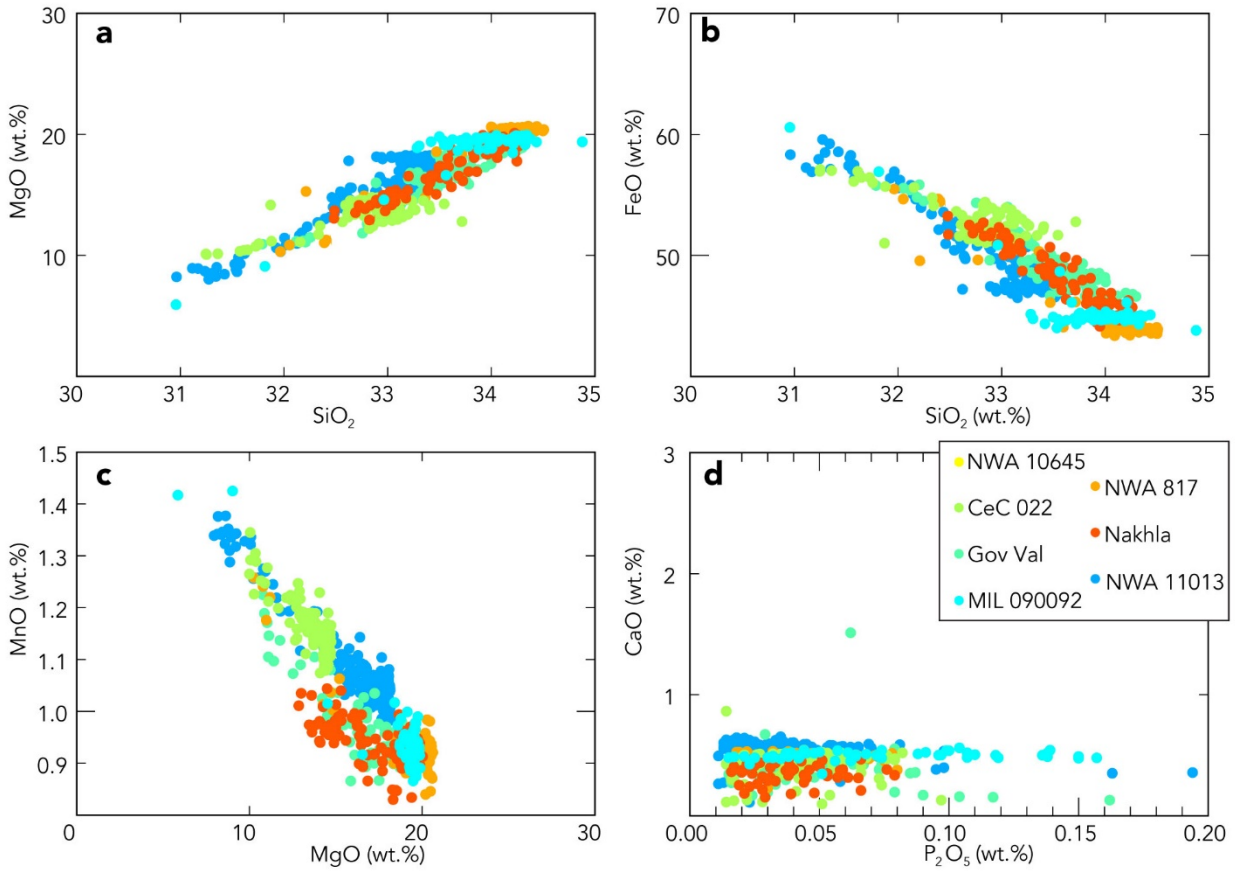

Figure 4.8: Comparison of oxide abundances from quantitative traverses in nakhlite olivine. Magnesium oxide (MgO) and silica (SiO_2) are positively correlated, while FeO and SiO_2 are positively correlated (a, b). Despite the presence of P zoning, P_2O_5 is not correlated with any other measured oxide (d).

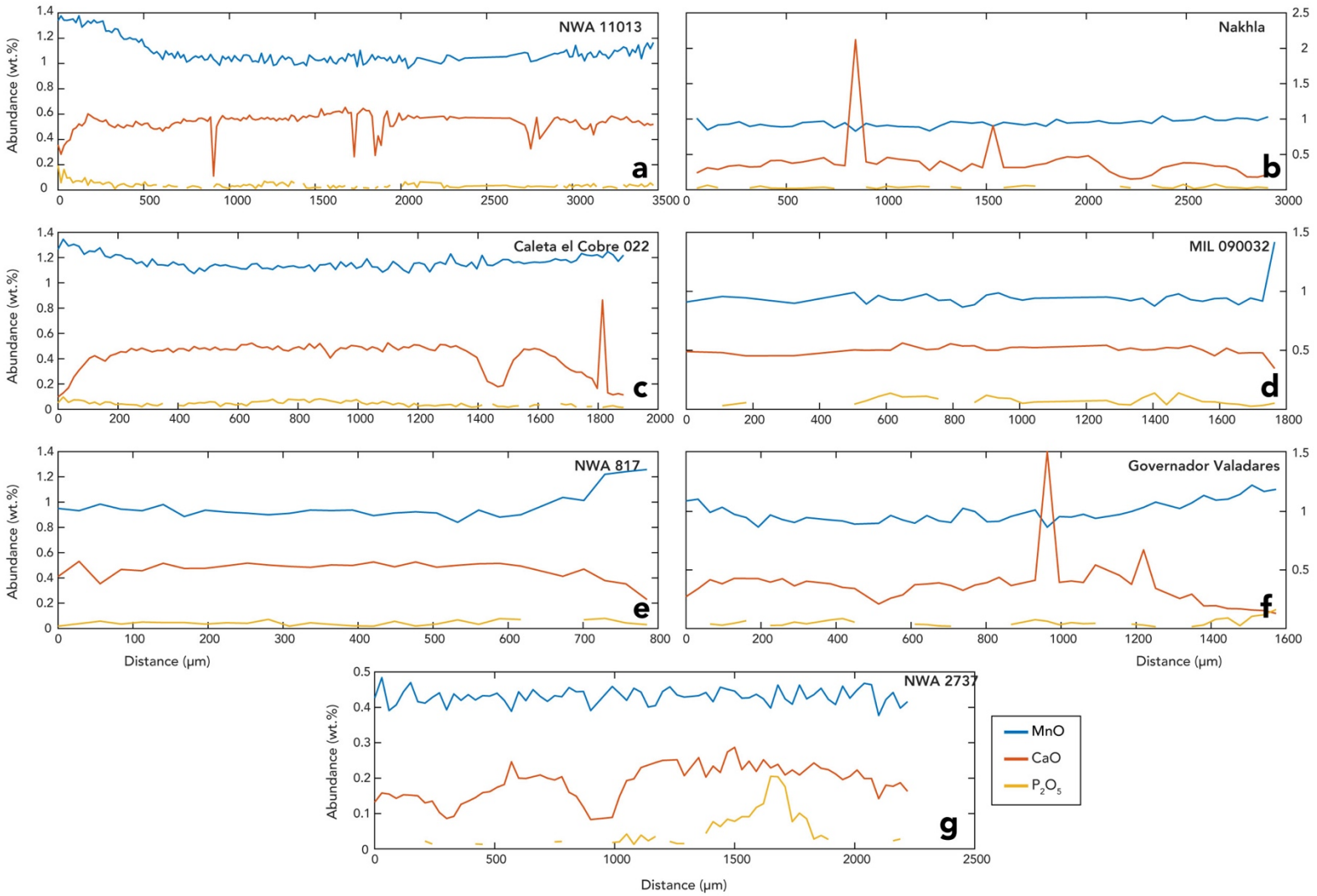

Figure 4.9: Minor element quantitative traverse data from nakhlite (9a–9f) and chassignite olivine (9g). Phosphorous zoning in maps is not apparent in quantitative traverses. Calcium traverse data appears to display zoning that is not visible in maps and which is not spatially correlated with any other element.

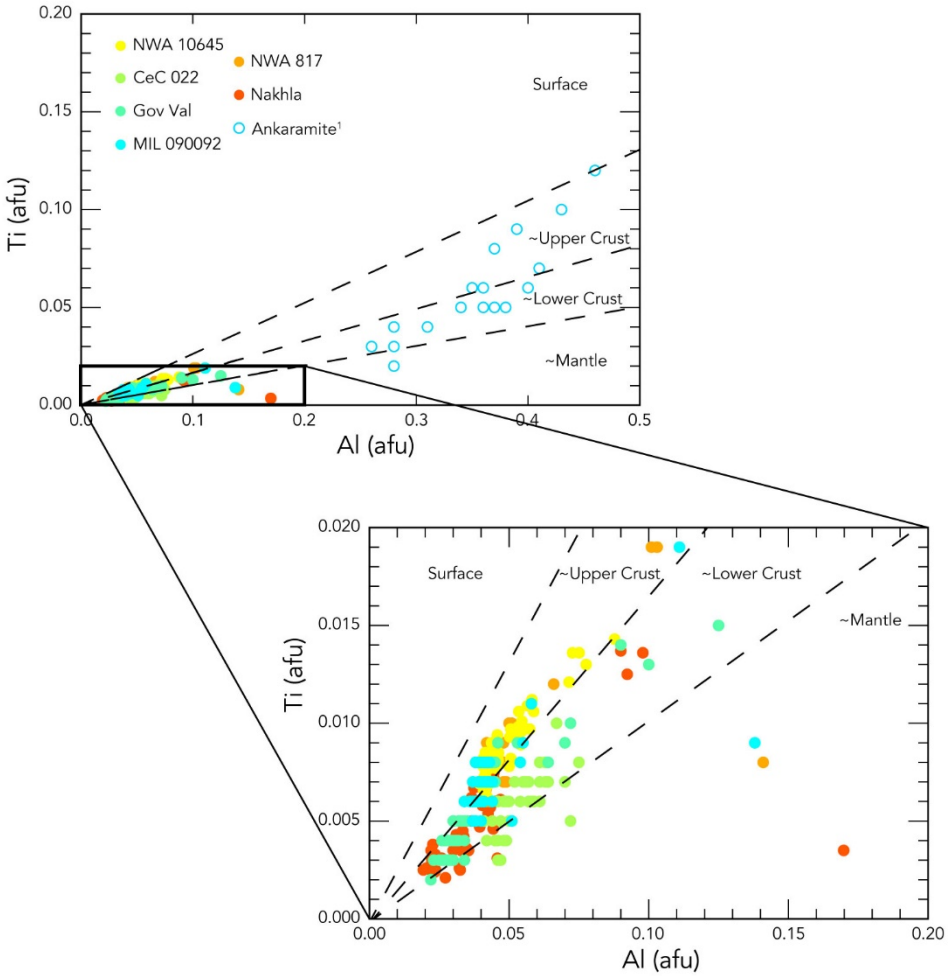

Figure 4.10: Single-pyroxene barometry for nakhlite pyroxene cores, using data obtained high-Mg measurements. Nakhlite data (solid circles) is compared to data obtained by Hammer et al. (2016) in Hawaiian ankaramite pyroxene. Pressure fields are empirically determined by Nekvasil et al. (2004) using terrestrial magma compositions, and adapted to pressures relevant to shergottites by Filiberto et al. (2010), so are only suggestive of relative pressures for nakhlites.

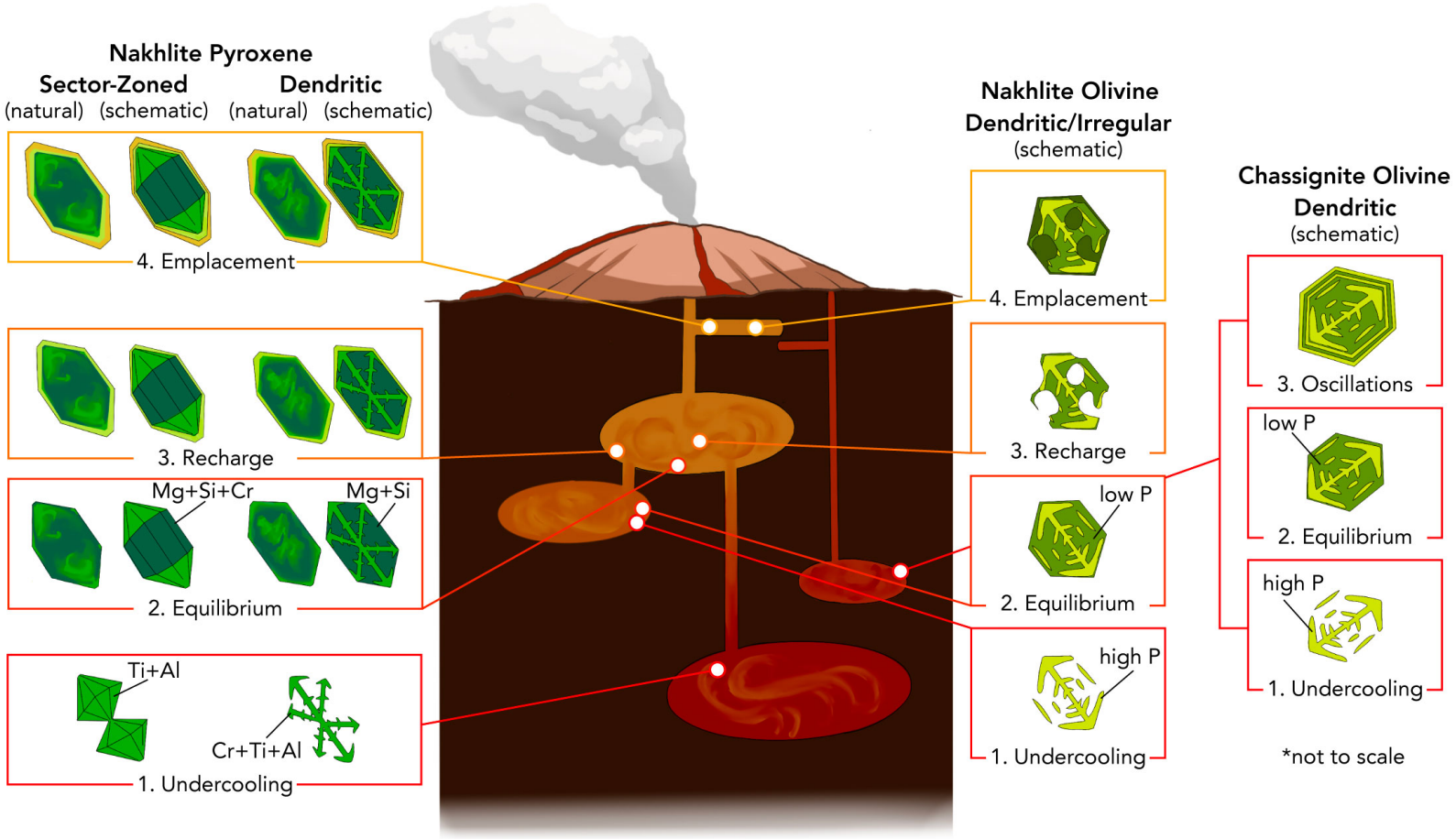

Figure 4.11: Summary figure representing petrogenesis of nakhlites and chassignites. Nakhlite pyroxene begins forming in effective undercooling conditions to result in two core morphologies: dendritic or hourglass (pyroxene [px] step 1). Infill in nakhlite pyroxene occurs under near-equilibrium conditions in relatively lower pressures (px step 2). Cores were stored and record magma mixing events resulting in inner rim formation (px step 3), while an outer rim forms upon emplacement (px step 4). Nakhlite olivine forms initially in undercooling conditions (ol step 1), and dendritic or skeletal cores infill in equilibrium conditions (ol step 2). Magma mixing possibly results in resorption and the formation of embayments (ol step 3). Final nakhlite olivine overgrowth occurs on emplacement (ol step 4). Chassignite olivine forms initially during undercooling to form dendritic cores (chassignite [ch.] step 1), which infill during equilibrium (ch. step 2). Oscillations occur from mantle to rim during rapidly changing thermal conditions (ch. step 3).

4.8 References

Balta, J.B., Sanborn, M., R, H.Y.M.C.S.J., and Wadhwa, M., 2013, Magmatic history and parental melt composition of olivine-phyric shergottite LAR 06319 : Importance of magmatic degassing and olivine antecrysts in Martian magmatism: v. 1382, p. 1359–1382, doi:10.1111/maps.12140.

Cohen, B.E., Mark, D.F., Cassata, W.S., Lee, M.R., Tomkinson, T., and Smith, C.L., 2017, Taking the pulse of Mars via dating of a plume-fed volcano: Nature Communications, v. 8, p. 1–9, doi:10.1038/s41467-017-00513-8.

Collinet, M., Charlier, B., Namur, O., Oeser, M., Médard, E., Weyer, S., 2017, Crystallization history of enriched shergottites from Fe and Mg isotope fractionation in olivine megacrysts: Geochimica et Cosmochimica Acta, p. 277–297.

Collinet, M., Plesa, A.C., Grove, T.L., Schwinger, S., Ruedas, T., and Breuer, D., 2021, MAGMARS: A Melting Model for the Martian Mantle and FeO-Rich Peridotite: Journal of Geophysical Research: Planets, v. 126, doi:10.1029/2021JE006985.

Corrigan, C.M., Velbel, M.A., and Vicenzi, E.P., 2015, Modal abundances of pyroxene, olivine, and mesostasis in nakhlites: Heterogeneity, variation, and implications for nakhlite emplacement: Meteoritics and Planetary Science, v. 50, p. 1497–1511, doi:10.1111/maps.12492.

Daly, L. et al., 2019, Boom boom pow: Shock-facilitated aqueous alteration and evidence for two shock events in the Martian nakhlite meteorites: Science Advances, v. 5, p. 1–12, doi:10.1126/sciadv.aaw5549.

Day, J.M.D., Tait, K.T., Udry, A., Moynier, F., Liu, Y., and Neal, C.R., 2018, Martian magmatism from plume metasomatized mantle: Nature communications, v. 9, p. 4799,

doi:10.1038/s41467-018-07191-0.

Day, J.M.D.D., Taylor, L.A., Floss, C., and McSween, H.Y., 2006, Petrology and chemistry of MIL 03346 and its significance in understanding the petrogenesis of nakhlites on Mars: v. 41, p. 581–606, doi:10.1111/j.1945-5100.2006.tb00484.x.

Donaldson, C.H., 1976, An experimental investigation of olivine morphology: Contributions to Mineralogy and Petrology, v. 57, p. 187–213, doi:10.1007/BF00405225.

Dreibus, G., and Wänke, H., 1985, Mars, a volatile-rich planet: Meteoritics, v. 20, p. 367–381.

Eckley, S.A., 2022, Magmatic thermal histories and emplacement mechanisms of Martian shergottite meteorites: 1–211 p.

Filiberto, J., Musselwhite, D.S., Gross, J., Burgess, K., Le, L., and Treiman, A.H., 2010, Experimental petrology, crystallization history, and parental magma characteristics of olivine-phyric shergottite NWA 1068: Implications for the petrogenesis of "enriched" olivine-phyric shergottites: Meteoritics and Planetary Science, v. 45, p. 1258–1270, doi:10.1111/j.1945-5100.2010.01080.x.

Goodrich, C.A., Treiman, A.H., Filiberto, J., Gross, J., and Jercinovic, M., 2013, K2O-rich trapped melt in olivine in the Nakhla meteorite: Implications for petrogenesis of nakhlites and evolution of the Martian mantle: Meteoritics and Planetary Science, v. 48, p. 2371–2405, doi:10.1111/maps.12226.

Griffin, S. et al., 2022a, Constraints on the Emplacement of Martian Nakhlite Igneous Rocks and Their Source Volcano From Advanced Micro-Petrofabric Analysis: Journal of Geophysical Research: Planets, v. 127, doi:10.1029/2021JE007080.

Griffin, S., Daly, L., Piazolo, S., Forman, L. V, and Cohen, B.E., 2022b, Can the Magmatic Conditions of the Martian Nakhlites be Discerned via Investigation of Clinopyroxene and

Olivine Intracrystalline Misorientations?, doi:10.1029/2021JE007082.

Gross, J., Filiberto, J., Herd, C.D.K., Daswani, M.M., Schwenzer, S.P., and Treiman, A.H., 2013, Petrography, mineral chemistry, and crystallization history of olivine-phyric shergottite NWA 6234: A new melt composition: Meteoritics & Planetary Science, v. 48, p. 854–871, doi:10.1111/maps.12092.

Harvey, R.P., and Mcsween, H.Y., 1992, The parent magma of the nakhlite meteorites: Clues from melt inclusions.:

Hewins, R.H., Humayun, M., Barrat, J., Zanda, B., and Lorand, J., 2020, ScienceDirect Northwest Africa 8694 , a ferroan chassignite : Bridging the gap between nakhlites and chassignites: Geochimica et Cosmochimica Acta, v. 282, p. 201–226, doi:10.1016/j.gca.2020.05.021.

Jambon, A., Sautter, V., Barrat, J.A., Gattacceca, J., Rochette, P., Boudouma, O., Badia, D., and Devouard, B., 2016, Northwest Africa 5790: Revisiting nakhlite petrogenesis: Geochimica et Cosmochimica Acta, v. 190, p. 191–212, doi:10.1016/j.gca.2016.06.032.

Kouchi, A., Sugawara, Y., Kashima, K., and Sunagawa, I., 1983, Laboratory growth of sector zones clinopyroxenes in the system $CaMgSi_2O_6$ – $CaTiAl_2O_6$: Contributions to Mineralogy and Petrology, v. 83, p. 177–184.

Lee, C.T.A., Sun, C., Sharton-Bierig, E., Phelps, P., Borchardt, J., Liu, B., Costin, G., and Johnston, A.D., 2022, Widespread phosphorous excess in olivine, rapid crystal growth, and implications for magma dynamics: Volcanica, v. 5, p. 433–450, doi:10.30909/vol.05.02.433450.

Lessel, J., and Putirka, K., 2015, New thermobarometers for martian igneous rocks, and some implications for secular cooling on Mars: American Mineralogist, v. 100, p. 2163–2171, doi:10.2138/am-2015-4732.

Maneta, V., Baker, D.R., and Minarik, W., 2015, Evidence for lithium - aluminosilicate

supersaturation of pegmatite - forming melts: Contributions to Mineralogy and Petrology, v. 170, p. 1–16, doi:10.1007/s00410-015-1158-z.

Mari, N., Hallis, L.J., Daly, L., and Lee, M.R., 2020, Convective activity in a Martian magma chamber recorded by P-zoning in Tissint olivine: Meteoritics & Planetary Science, v. 55, p. 1057–1072, doi:10.1111/maps.13488.

Marsh, B.D., 2007, Crust and Lithosphere Dynamics.: Elsevier Science & Technology, v. 6, 275–333 p., doi:10.1016/B978-044452748-6.00106-1.

Masotta, M., Pontesilli, A., Mollo, S., Armienti, P., Ubide, T., Nazzari, M., and Scarlato, P., 2020, The role of undercooling during clinopyroxene growth in trachybasaltic magmas: Insights on magma decompression and cooling at Mt. Etna volcano: Geochimica et Cosmochimica Acta, v. 268, p. 258–276, doi:10.1016/j.gca.2019.10.009.

McCubbin, F.M., Elardo, S.M., Shearer, C.K., Smirnov, A., Hauri, E.H., and Draper, D.S., 2013, A petrogenetic model for the comagmatic origin of chassignites and nakhlites: Inferences from chlorine-rich minerals, petrology, and geochemistry: Meteoritics and Planetary Science, v. 48, p. 819–853, doi:10.1111/maps.12095.

Mckay, G., Le, L., and Mikouchi, T. Al, Ti, and Cr: Complex zoning in synthetic and natural nakhlite pyroxenes:, https://ntrs.nasa.gov/search.jsp?R=20070022571.

Mikouchi, T., and Miyamoto, M., 2002, Comparative Cooling Rates of Nakhlites as Inferred from Iron-Magnesiumand Calcium Zoning of Olivines: Lunar and Planetary Science Conference, v. 33, p. Abst.#1343, internal-pdf://mikoucho_02a-3939258624/mikoucho_02a.pdf.

Mikouchi, T., Takenouchi, A., and Zolensky, M.. E., 2017, Multiple igneous bodies for Nakhlites and Chassignites as inferred from olivine cooling rates using calcium zoning: 80th Annual Meeting of the Meteoritical Society, v. 2017, p. Abstract# 5739.

Milman-Barris, M.S., Beckett, J.R., Baker, M.B., Hofmann, A.E., Morgan, Z., Crowley, M.R., Vielzeuf, D., and Stolper, E., 2008, Zoning of phosphorus in igneous olivine: Contributions to Mineralogy and Petrology, v. 155, p. 739–765, doi:10.1007/s00410-007-0268-7.

Nekvasil, H., Dondolini, A., Horn, J., Filiberto, J., Long, H., and Lindsley, D.H., 2004, The origin and evolution of silica-saturated alkalic suites: An experimental study: Journal of Petrology, v. 45, p. 693–721, doi:10.1093/petrology/egg103.

Nicklas, R.W., Day, J.M.D., Vaci, Z., Udry, A., Liu, Y., and Tait, K.T., 2021, Uniform oxygen fugacity of shergottite mantle sources and an oxidized martian lithosphere: Earth and Planetary Science Letters, v. 564, p. 116876, doi:10.1016/j.epsl.2021.116876.

Nyquist, L.E., Bogard, D.D., Greshake, A., and Eugster, O., 2001, The clan of Martian meteorites , formerly called SNCs after S hergotty , N akhla and C hassigny , now consists of 16 unpaired meteorites of magmatic origin (basalts and ultramafic cumulates). Generally young crystallization ages (with the exception of : , p. 105–165.

Paton, C., Hellstrom, J., Paul, B., Woodhead, J., and Hergt, J., 2011, Iolite: Freeware for the visualisation and processing of mass spectrometric data: Journal of Analytical Atomic Spectrometry, v. 26, p. 2508–2518, doi:10.1039/c1ja10172b.

Payré, V., and Dasgupta, R., 2022, Effects of phosphorus on partial melting of the Martian Mantle and compositions of the Martian Crust: Geochimica et Cosmochimica Acta, v. 327, p. 229–246, doi:10.1016/j.gca.2022.03.034.

Piazolo, S., La Fontaine, A., Trimby, P., Harley, S., Yang, L., Armstrong, R., and Cairney, J.M., 2016, Deformation-induced trace element redistribution in zircon revealed using atom probe tomography: Nature Communications, v. 7, p. 1–7, doi:10.1038/ncomms10490.

Plesa, A.C., Padovan, S., Tosi, N., Breuer, D., Grott, M., Wieczorek, M.A., Spohn, T., Smrekar,

S.E., and Banerdt, W.B., 2018, The Thermal State and Interior Structure of Mars: Geophysical Research Letters, v. 45, p. 12,198-12,209, doi:10.1029/2018GL080728.

Rahib, R.R., Udry, A., Howarth, G.H., Gross, J., Paquet, M., Combs, L.M., Laczniak, D.L., and Day, J.M.D., 2019, Mantle source to near-surface emplacement of enriched and intermediate poikilitic shergottites in Mars: Geochimica et Cosmochimica Acta, v. 266, p. 463–496, doi:10.1016/j.gca.2019.07.034.

Sautter, V. et al., 2015, In situ evidence for continental crust on early Mars: Nature Geoscience, v. 8, p. 605–609, doi:10.1038/ngeo2474.

Sautter, V., Toplis, M.J., Lorand, J.P., and Macri, M., 2012, Melt inclusions in augite from the nakhlite meteorites: A reassessment of nakhlite parental melt and implications for petrogenesis: Meteoritics and Planetary Science, v. 47, p. 330–344, doi:10.1111/j.1945-5100.2012.01332.x.

Shea, T., Hammer, J.E., Hellebrand, E., Mourey, A.J., Costa, F., First, E.C., Lynn, K.J., Melnik, O., and Shea, T., 2019, Phosphorus and aluminum zoning in olivine : contrasting behavior of two nominally incompatible trace elements: Contributions to Mineralogy and Petrology, v. 174, p. 1–24, doi:10.1007/s00410-019-1618-y.

Shearer, C.K., Aaron, P.M., Burger, P. V., Guan, Y., Bell, A.S., and Papike, J.J., 2013, Petrogenetic linkages among fO_2, isotopic enrichments-depletions and crystallization history in Martian basalts. Evidence from the distribution of phosphorus in olivine megacrysts: Geochimica et Cosmochimica Acta, v. 120, p. 17–38, doi:10.1016/j.gca.2013.06.034.

Stockstill, K.R., Mcsween, H.Y., and Bodnar, R.J., 2005, Melt inclusions in augite of the Nakhla martian meteorite: Evidence for basaltic parental melt:, http://meteoritics.org.

Streck, M.J., Dungan, M.A., Malavassi, E., Reagan, M.K., and Bussy, F., 2002, The role of basalt

replenishment in the generation of basaltic andesites of the ongoing activity at Arenal volcano, Costa Rica: Evidence from clinopyroxene and spinel: Bulletin of Volcanology, v. 64, p. 316–327, doi:10.1007/s00445-002-0209-2.

Tornare, E., Pilet, S., and Bussy, F., 2016, Magma differentiation in vertical conduitsrevealed by the complementary study of plutonic and volcanic rocks from Fuerteventura (Canary Islands): Journal of Petrology, v. 57, p. 2221–2250, doi:10.1093/petrology/egx004.

Treiman, A.H., 2005, The nakhlite meteorites: Augite-rich igneous rocks from Mars: Elsevier GmbH, v. 65, p. 203–270, doi:10.1016/j.chemer.2005.01.004.

Ubide, T., Caulfield, J., Brandt, C., Bussweiler, Y., Mollo, S., Di Stefano, F., Nazzari, M., and Scarlato, P., 2019, Deep Magma Storage Revealed by Multi-Method Elemental Mapping of Clinopyroxene Megacrysts at Stromboli Volcano: Frontiers in Earth Science, v. 7, doi:10.3389/feart.2019.00239.

Ubide, T., and Kamber, B.S., 2018, Volcanic crystals as time capsules of eruption history: Nature Communications, v. 9, doi:10.1038/s41467-017-02274-w.

Udry, A., and Day, J.M.D., 2018, 1.34 billion-year-old magmatism on Mars evaluated from the co-genetic nakhlite and chassignite meteorites: Geochimica et Cosmochimica Acta, v. 238, p. 292–315, doi:10.1016/j.gca.2018.07.006.

Udry, A., Howarth, G.H., Herd, C., Day, J., Lapen, T.J., and Filiberto, J., 2020, What martian meteorites reveal about the interior and surface of Mars: Earth and Space Science Open Archive, p. 55, https://doi.org/10.1002/essoar.10503123.2.

Welsch, B., Hammer, J., Baronnet, A., Jacob, S., Hellebrand, E., and Sinton, J., 2016, Clinopyroxene in postshield Haleakala ankaramite: 2. Texture, compositional zoning and supersaturation in the magma: Contributions to Mineralogy and Petrology, v. 171, p. 1–19,

doi:10.1007/s00410-015-1213-9.

Welsch, B., Hammer, J., and Hellebrand, E., 2014, Phosphorus zoning reveals dendritic architecture of olivine: Geology, p. 1–4, doi:10.1130/G35691.1.

Xing, C.M., Wang, C.Y., and Tan, W., 2017, Disequilibrium growth of olivine in mafic magmas revealed by phosphorus zoning patterns of olivine from mafic–ultramafic intrusions: Earth and Planetary Science Letters, v. 479, p. 108–119, doi:10.1016/j.epsl.2017.09.005.

Xing, C., Yan, C., Charlier, B., and Namur, O., 2022, Ubiquitous dendritic olivine constructs initial crystal framework of mafic magma chamber: Earth and Planetary Science Letters, v. 594, p. 117710, doi:10.1016/j.epsl.2022.117710.

Chapter 5: Conclusion

In Chapter 1 of this dissertation, I conducted assimilation and fractional crystallization modeling of Mars magmas in martian-relevant conditions to determine its role in the formation of felsic materials on Mars. We found that assimilation and fractional crystallization together evolved magmas to felsic compositions more efficiently (i.e., at a lower degree of solid fractionation) than fractional crystallization alone. The extent to which crustal wallrock is melted and assimilated is controlled in part by its initial temperature, which means that magmas emplaced in ancient, hot crust may have been more likely to prompt assimilation and drive evolution. These findings fit observations of the martian crust by rovers and orbiters: evolved and felsic materials are more likely to be found on older surfaces. Other terrestrial planets like Venus (with its hot crust) and Mercury (with graphite- and sulfide-rich crust) may also have crust formed in part by assimilation and fractional crystallization.

In Chapter 2 of this dissertation, I analyzed melt inclusions in a representative suite of martian nakhlite and chassignite meteorites in order to constrain the initial composition of the magmas which formed them. I found that melt inclusion bulk compositions in both nakhlites and chassignites have been likely affected by open-system processes in crystal mushes, which means that the magma which initially formed the minerals either significantly changed in composition, was replaced locally by, or was mixed with a new magma. With that change in surrounding magma, the melt inclusions likely changed in composition irreversibly in order to achieve equilibrium with the host mineral. These findings are significant in that they provide evidence that minerals in the nakhlites and chassignites had been stored in magma chambers prior to eruption, and that most martian magmas undergo mush storage as well.

In Chapter 3, I examined chemical zoning patterns in nakhlite and chassignite cumulus minerals. I found that zoning of most elements had been functionally erased by diffusion of those elements throughout the minerals over time, indicating that minerals in both meteorite classes had been stored in magma chambers. Because the magmas that formed the cumulus minerals in nakhlites and chassignites are not the same magmas which erupted them, those cumulus minerals are antecrystic (as opposed to phenocrystic, or formed from one magma). All cumulus minerals in the nakhlites and chassignites were formed initially very rapidly by a process called undercooling, which adds to a growing body of evidence that undercooling is commonplace in martian magma chambers. I found that nakhlite pyroxene grains were formed over a range of crustal pressures under very similar conditions for all samples, but nakhlite olivine grains were formed under conditions unique to each sample. Nakhlite olivine and pyroxene were therefore formed separately, but emplaced together, and late-stage mineral growth occurred during emplacement which sometimes entrapped one phase in the other. Chassignite olivine grains likely formed in a very dynamic magma environment, which lead to rapid oscillatory changes in chemistry.

In this dissertation, I applied a variety of analytical and modeling techniques to rover observations of igneous targets and to martian meteorite samples in order to better understand what magmatic processes formed them. I find that processes like assimilation and fractional crystallization as well as magma storage and magma mixing, which are common processes on Earth, also likely drive diversity of crustal rocks on Mars.

Appendix A

A1. Magma Chamber Simulator Assimilation Modeling and Application of Rhyolite-MELTS to Martian Compositions

All models were conducted using the Magma Chamber Simulator (or MCS; Bohrson et al., 2014). The MCS is capable of conducting fractional crystallization models with or without the open-system processes of assimilation and recharge. Possible modeled subsystems include the magma, a fractionated cumulate reservoir, and an assimilated phase (wallrock). Magma, wallrock, and recharge subsystem phase equilibria calculations are conducted in individual MELTS windows while the user interacts with a numerically coded Excel sheet that carries out executive functions (Bohrson et al., 2014). MELTS is a thermodynamic phase equilibria calculator with several algorithms available for use in the MCS, including Rhyolite-MELTS (v. 1.0.x, v. 1.1.x, v. 1.2.x) and pMELTS (Ghiorso et al., 2002; Ghiorso and Gualda, 2015; Gualda et al., 2012).

As the MCS models fractionation, cumulate material (including solid minerals and fluid phases) is removed both thermally and chemically from the magma subsystem. A closed cumulate subsystem is an assumption made for model simplicity. Cumulate reservoirs in natural systems interact with the magma and wallrock subsystems to generate more wallrock partial melt than would form if the cumulate reservoir were closed (Bohrson et al., 2014). As the closed cumulate reservoir simplification underestimates wallrock partial melting, all results for changes to the bulk magma composition due to AFC are conservative estimates.

The MCS calculates relative volumes of subsystems in ratios against a default of 100 g of magma (Bohrson et al., 2014). The user cannot model absolute magma and wallrock volumes, thus, any calculations of residual magma volumes are relative. Furthermore, all magma mixing (including mixing of partially melted wallrock into the bulk magma subsystem) is complete at each

temperature decrement calculation (Bohrson et al., 2014). Compositional and thermal gradients are not estimated in either the magma or the wallrock.

Liquidus calculations reported in this study are determined by the MCS to be the temperature at which the entire magma subsystem is molten (Bohrson et al., 2014). The phase to first appear on the liquidus in models is chromite, with silicate materials crystallizing at lower temperatures (~1400°C) more consistent with experimental literature values (Filiberto et al., 2010). While chromite appears as the liquidus phase in other martian MELTS modeling literature, the total volume of early spinel fractionation is typically small and has little effect on the liquid line of descent (Balta and McSween, 2013; Udry et al., 2014). In addition to high-temperature spinel crystallization, Balta and McSween (2013) found that the MELTS algorithm underestimates multiple saturation pressures compared to experimental martian compositions. Otherwise, Balta and McSween (2013) find that MELTS reproduces martian compositions effectively. Rhyolite-MELTS relies on an expanded MELTS calibration database (containing extraterrestrial materials) and is and is effective for modeling systems represented in meteorites (Ashcroft and Wood, 2015; Gualda et al., 2012).

A2. The Role of Oxygen Fugacity in AFC Models

Model Parameters

The MCS only allows users to conduct constrained fO_2 modeling along buffers. As such, we conducted constrained models at the fayalite-magnetite-quartz (FMQ) buffer, which falls within high and low values for known martian magmas at crustal depths (Herd et al., 2002; McCubbin et al., 2013; Udry et al., 2020). To test the effects of relevant high and low initial fO_2 values, we conducted unconstrained fO_2 models in addition to the ones constrained at FMQ. To do

so, we calculated the ratio Fe^{3+}/Fe^{2+} equivalent to FMQ, FMQ–3, and FMQ+2 for the magma subsystems at all model pressures using Equation 7 from Kress and Carmichael (1991):

$$\ln\left(\frac{X_{Fe_2O_3}}{X_{FeO}}\right) = a\ln(fO_2) + \frac{b}{T} + c + \sum_i (d_i X_i) + e\left[1 - \frac{T_o}{T} - ln\left(\frac{T}{T_o}\right)\right] + f\frac{P}{T} + g\left(\frac{(T-T_o)P}{T}\right) + h\frac{P^2}{T}$$

where a, b, c, d_i, f, g, and h are empirical constants (i includes Al_2O_3, FeO, CaO, Na_2O, and K_2O), T is temperature, and P is pressure. The resulting compositions are normalized with 0.07, 0.50, and 1.0 wt.% H_2O and are used as the initial magma compositions.

Oxygen Fugacity Model Results and Discussion

The oxygen fugacity range of FMQ–3 to +2 was selected to bracket estimates of magmas generated at the crust-mantle boundary and the shallowly-emplaced martian nakhlite meteorites (Herd et al., 2002; McCubbin et al., 2013). Measurements of ferrous to ferric components in meteorite samples and on the surface of Mars are subject to error, and thus constraining fO_2 allows us to conduct models by forcing them to evolve chemically around a consistent fO_2 buffer using FeO* (= FeO + Fe_2O_3). Constrained fO_2, however, does not accurately represent natural evolution that occurs in a magmatic system wherein the fO_2 may vary with processes, such as autooxidation and degassing, thereby affecting what phases are in equilibrium (e.g., Anenburg and O'Neill, 2019).

The abundance and activity of O_2 in Mars-relevant magma compositions and conditions is difficult to model using the MCS. However, we found that higher fO_2 (more oxidizing conditions) in initial magmas result in lower silica and evolution overall than in magmas with more reducing

conditions. Most fO_2-unconstrained models crashed the MELTS engine consistently, particularly after thermal equilibrium between the magma and wallrock subsystems. This is likely because the database upon which MELTS is built lacks empirically-based solutions for Mars-relevant compositions and conditions. Constraining models along fO_2 buffers minimizes the Khorzhinskii potential (which fixes the abundance and chemical potential of O_2 in the system), rather than minimizing the Gibbs energy (Bohrson et al., 2014). Removing two variables (abundance and chemical potential) from the Gibbs equation reduces some model resolution and limits some phases (like olivine), but otherwise the constrained models provide similar liquid lines of descent (LLD) and undergo significantly more fractional crystallization steps after thermal equilibrium and so are resolved more completely. As a general rule, increasingly oxidizing magmas will likely contain less silica than their reduced counterparts (Fig. A3). However, improving the model database with a wider array of Mars-relevant magma compositions would elucidate many more magmatic processes, particularly what solid phases are fractionated.

A3. Residual Wallrock Calculations and Model

The wallrock subsystem, as it partially melts, is modeled as chemically homogenous throughout the model. The MCS does not track the bulk compositional changes of the wallrock subsystem (only the partial melt it generates), but it can be calculated with the "Cumulate and residual wallrock major element calculation tool" by Jussi Heinonen (available at: https://mcs.geol.ucsb.edu/code, accessed 07 Oct 2021). We found that wallrock undergoes minimal change throughout all models, with variation between LLDs falling within fractions of a single weight percent (Fig. A2). For instance, higher pressure models featuring residual NWA 7034 wallrock and Fastball initial magma (4–6 kbar, ~48.5 wt.% SiO_2) are slightly more depleted

in silica than low pressure models (1–2 kbar, ~48.2 wt.% SiO_2). Wallrock compositions do not approach any observed Gale crater felsic or alkaline targets, and it is unlikely that exhumed wallrock contributes to evolved crustal compositions.

A4. Root Mean Square (RMS) Best Fit Modeling

We elected to conduct RMS calculations by averaging the squared differences between target and model compositions for all oxides at individual temperature decrements (model calculation steps) to best constrain at what single crystallinity the models best replicate the target compositions. Similar statistical techniques used in modeling literature (i.e., Udry et al., 2014; Udry et al., 2018; Wu et al., 2021) sum or average the squared differences between model and target oxides across all temperature decrements to find best fit model parameters (composition, pressure, etc.) as well. Any application of this method (or similar methods) weighs all population values (i.e., all oxides) the same. The ultimate effect of this may be to select a model that is best fit toward low-abundance oxides and oxide measurements with high error (e.g., TiO_2) rather than to weigh the fit toward abundant oxides of interest (e.g., SiO_2). To investigate this effect in our own RMS application in each best fit model, we found the minima value of the squared differences between a single target oxide and modeled oxide at each temperature decrement, which we take to be the best fit of that individual oxide. We plotted the crystallinity at each oxide minima along with the bulk averaged best fit crystallinity for each target composition in Fig. A7. Best fit model data are found in Table A3. We observe that individual oxide best fits are scattered, and that no best fit averaged across all oxides is specifically weighed toward low-abundance oxides (Fig. A7). Instead, the averaged best fit represents the local minima across all oxides, which tends toward higher degrees of crystallinity near the end of the model (Fig. A7).

Importantly, we are not using this method to assign error or accuracy to our models. Modeled compositions are not absolute compositions, and oxide estimations are subject to upwards of 1 wt.% error using MELTS modeling (Udry et al., 2018; Balta and McSween, 2013). Although target uncertainties are not included in best fit calculations, best fit models are quantitatively compared to high-precision, generally low-accuracy targets. The targets Sledgers, Chakonipau, Becraft, Sparkle, Angmaat, and Harrison are also subject to the error (upwards of ~7 wt.% for SiO_2) inherent to ChemCam onboard the Curiosity rover (Clegg et al., 2017; Cousin et al., 2017; Payré et al., 2017). Highly precise statistical methods, when applied to high error measurements and models, can only be used to make recommendations for magmatic behavioral trends.

A5. Tables

Table A1. Pressure and temperature gradient estimates used in models.

Initial Pressure (kbar)	Initial Depth (km)	Initial Temperature (°C)(21°C/km estimate)*[1]	Initial Temperature (°C)(15°C/km estimate)*[2]	Initial Temperature (°C)(6.0°C/km estimate)*[1]
1	8.3	174.3	124.5	49.8
2	16.6	348.6	249.0	99.6
4	33.2	697.2	498.0	199.2
6	49.8	1045.8	747.0	298.8
8	66.4	1394.4	996.0	398.4
10	83.0	1743.0	1245.0	498.0

*Surface temperature = 0°C

[1] Babeyko & Zharkov, 2000

[2] Hahn et al., 2011

Table A2. Iron compositions for Fastball magma at equivalent high and low fO_2 estimates.

	Pressure	1 kbar	2 kbar	4 kbar	6 kbar
FMQ	Fe_2O_3	2.47	2.26	2.21	2.17
	FeO	16.5	16.7	16.8	19.0
	Molar Fe^{3+}/Fe_{tot}	0.12	0.12	0.12	0.11
FMQ–3	Fe_2O_3	0.73	0.73	0.71	0.70
	FeO	18.7	18.7	19.0	18.7
	Molar Fe^{3+}/Fe_{tot}	0.03	0.03	0.03	0.03
FMQ+2	Fe_2O_3	5.99	5.93	5.82	5.72
	FeO	16.0	16.0	16.1	16.1
	Molar Fe^{3+}/Fe_{tot}	0.25	0.25	0.25	0.24

Table A3. Best fit models, compositions, and RMS values.

	Best-fit model details					Model composition (normalized to 100%)									
Target Name	RMS Value	Initial Magma	Wallrock Composition	Pressure	Wt.% H_2O	SiO_2	TiO_2	Al_2O_3	FeO_T	MgO	CaO	Na_2O	K_2O	% Magma	% Solids
Sledgers	2.0	Adirondack basalt	Average Mars crust	6 kbar	0.07	62.5	0.01	13.4	5.14	0.07	2.99	5.33	1.17	10.5	90.1
Chakonipau	2.5	Adirondack basalt	Average Mars crust	6 kbar	0.07	61.2	0.01	14.0	6.24	0.15	3.28	5.34	1.06	12.4	88.1
Becraft	2.2	Adirondack basalt	Average Mars crust	6 kbar	0.50	60.1	0.11	12.5	10.0	0.27	4.01	5.86	1.79	16.0	84.5
Sparkle	3.1	Adirondack basalt	Average Mars crust	4 kbar	1.00	59.0	0.02	14.5	8.30	0.46	4.27	5.18	0.91	21.1	79.6
Angmaat	2.0	Adirondack basalt	Average Mars crust	2 kbar	1.00	61.5	0.06	12.7	9.12	0.63	5.25	4.42	1.12	33.2	67.2
Harrison	1.5	Adirondack basalt	Average Mars crust	6 kbar	0.07	54.1	0.08	16.3	12.5	0.71	5.10	4.75	0.69	24.0	76.5
NWA 6963 Type 1	3.0	Adirondack basalt	NWA 7034	1 kbar	1.00	74.0	0.03	7.19	2.70	0.05	3.50	5.12	1.54	22.8	77.2
NWA 6963 Type 2	3.0	Adirondack basalt	NWA 7034	1 kbar	1.00	74.2	0.03	6.97	2.57	0.04	3.49	5.21	1.63	21.5	78.5

A6. Figures

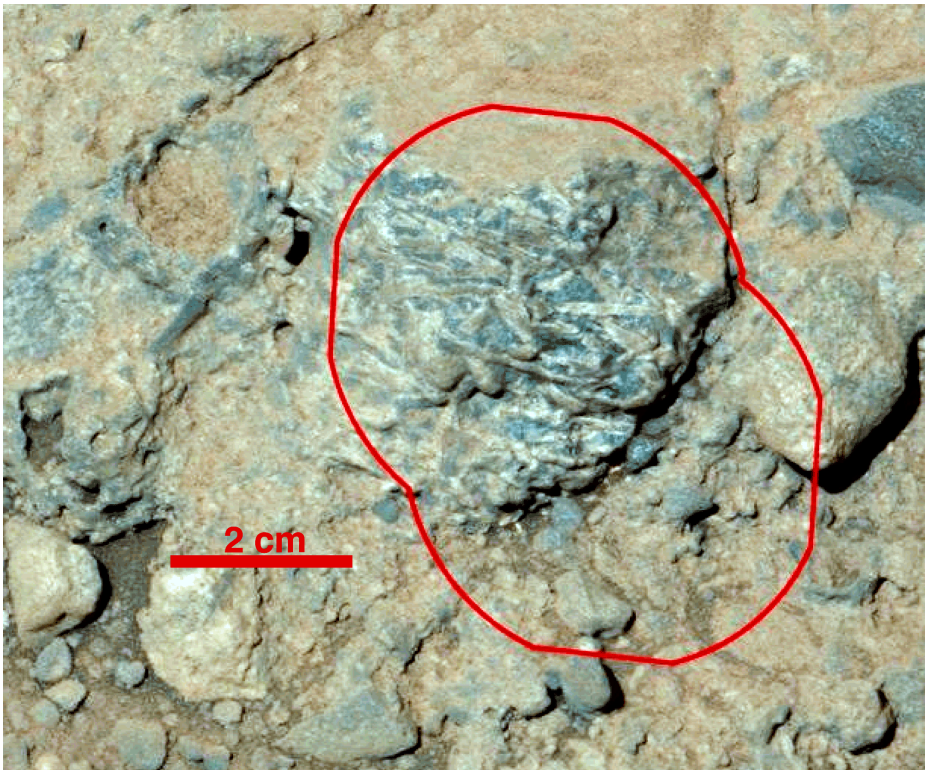

Figure A1: ChemCam RMI contour product featuring Curiosity target “Harrison” on Sol 514. Elongated plagioclase grains are surrounded by a dark matrix. Mosaic footprint is outlined in red.

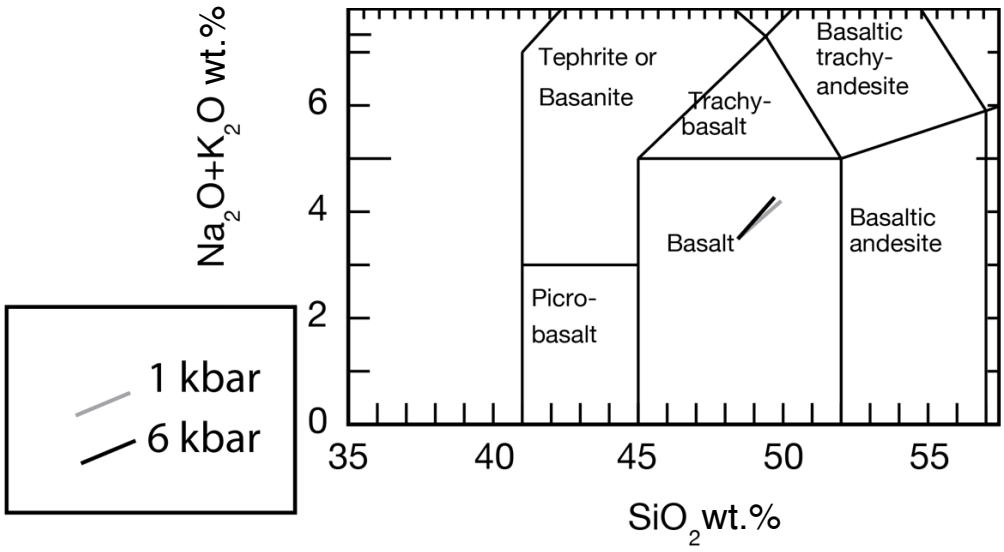

Figure A2: Total alkali versus silica composition diagram including residual wallrock (NWA 7034) after assimilation by Fastball magma containing 0.07 wt.% H2O. Increasing pressure corresponds to increasing depth and longer duration assimilation. Thus, higher pressure wallrock is more depleted than its lower pressure equivalent.

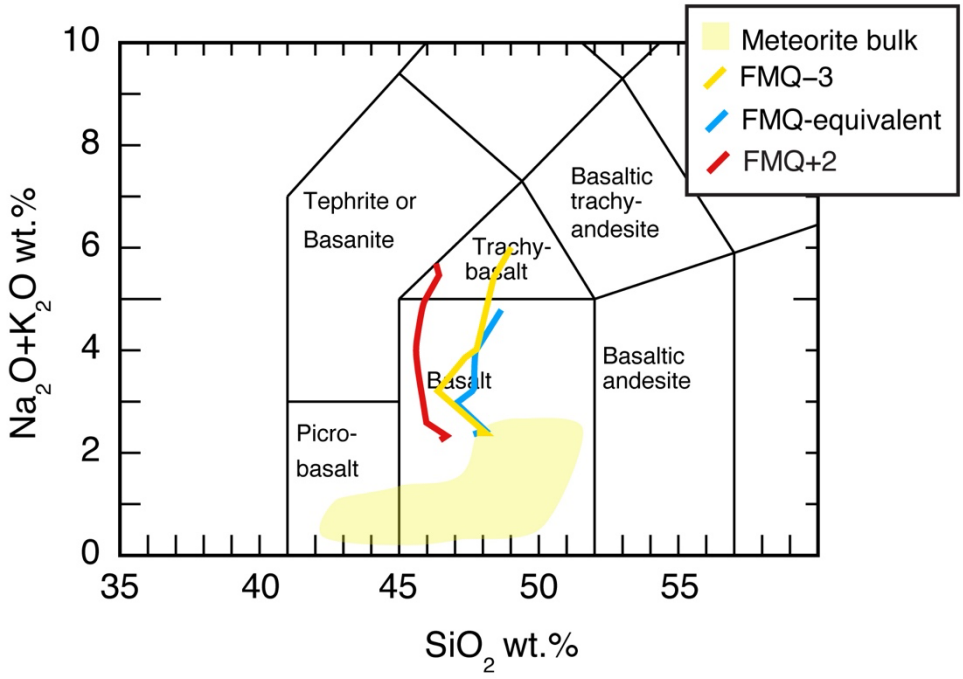

Figure A3: Total alkali versus silica composition diagram including Fastball magma assimilating NWA 7034 wallrock under different initial unconstrained magmatic redox conditions. Oxidizing magmas are more silica-depleted than reduced magmas or magmas with initial iron contents equivalent to the fayalite-magnetite-quartz (FMQ) buffer.

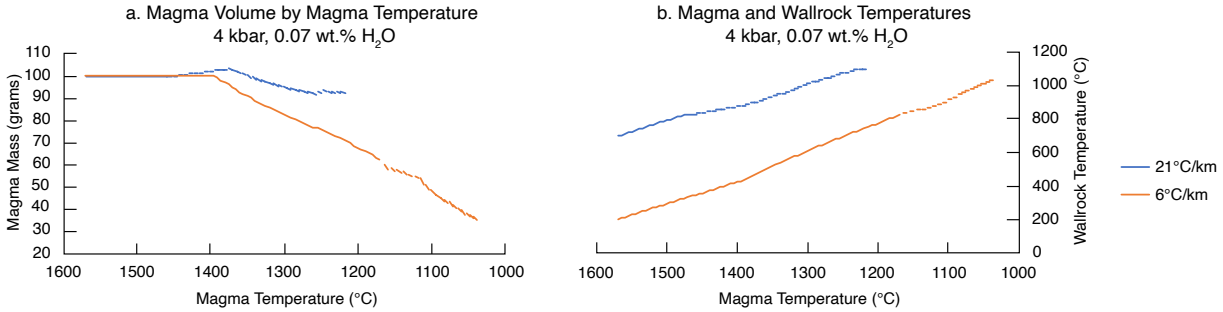

Figure A4: a) Mass and b) thermal evolution of a Fastball magma intruding a NWA 7034 wallrock at 4 kbar depth along a 21°C/km areotherm (blue) and 6°C/km areotherm (orange). All models presented are run from the onset of magma crystallization until the wallrock and magma subsystems reach thermal equilibrium. Hotter areothermal gradients result in thermal equilibrium at larger masses of residual magma than cooler ones. Wallrock in both settings heats up at a similar rate (slope –1.58 for 6°C/km, –1.15 for 21°C/km).

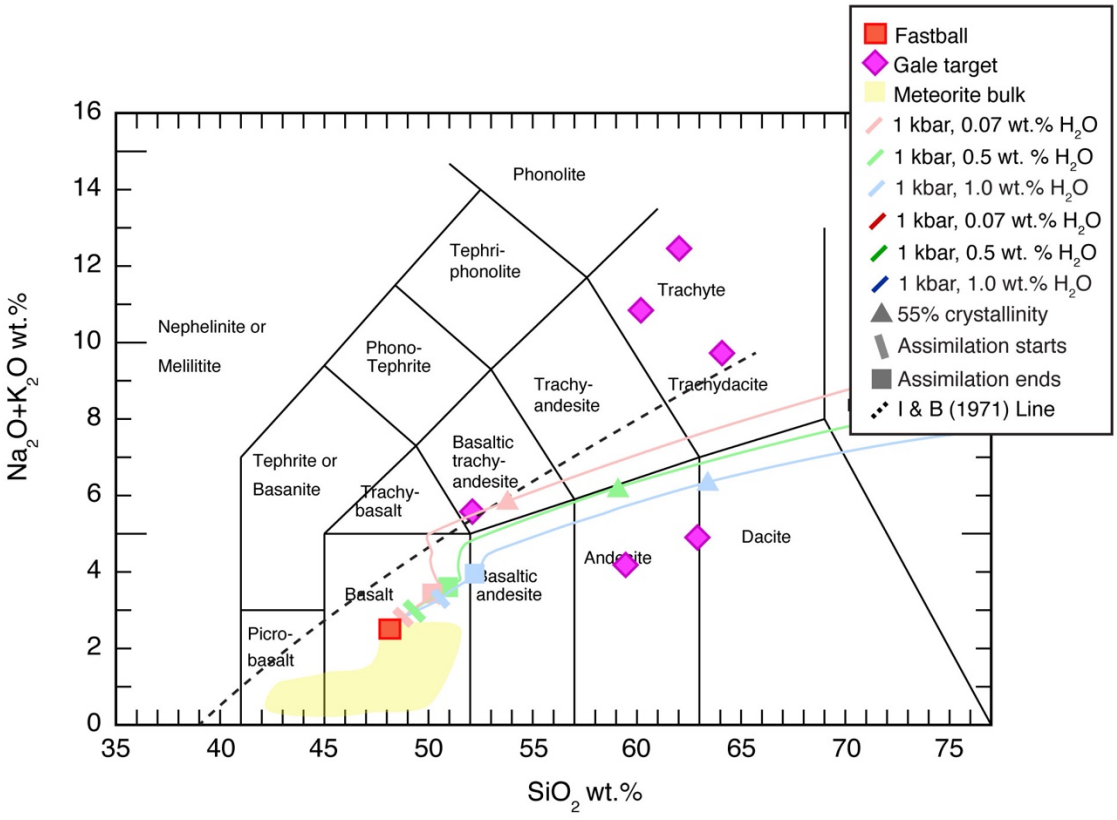

Figure A5: AFC models of Fastball magma intruding NWA 7034 wallrock at a mass ratio of 10:3 (magma to wallrock at 1) 1 kbar pressure. Increasing permeability prompts rapid partial melting of the wallrock subsystem even at shallow depths (<10 km), leading to increased amounts of silica in the magma at lower degrees of crystallinity.

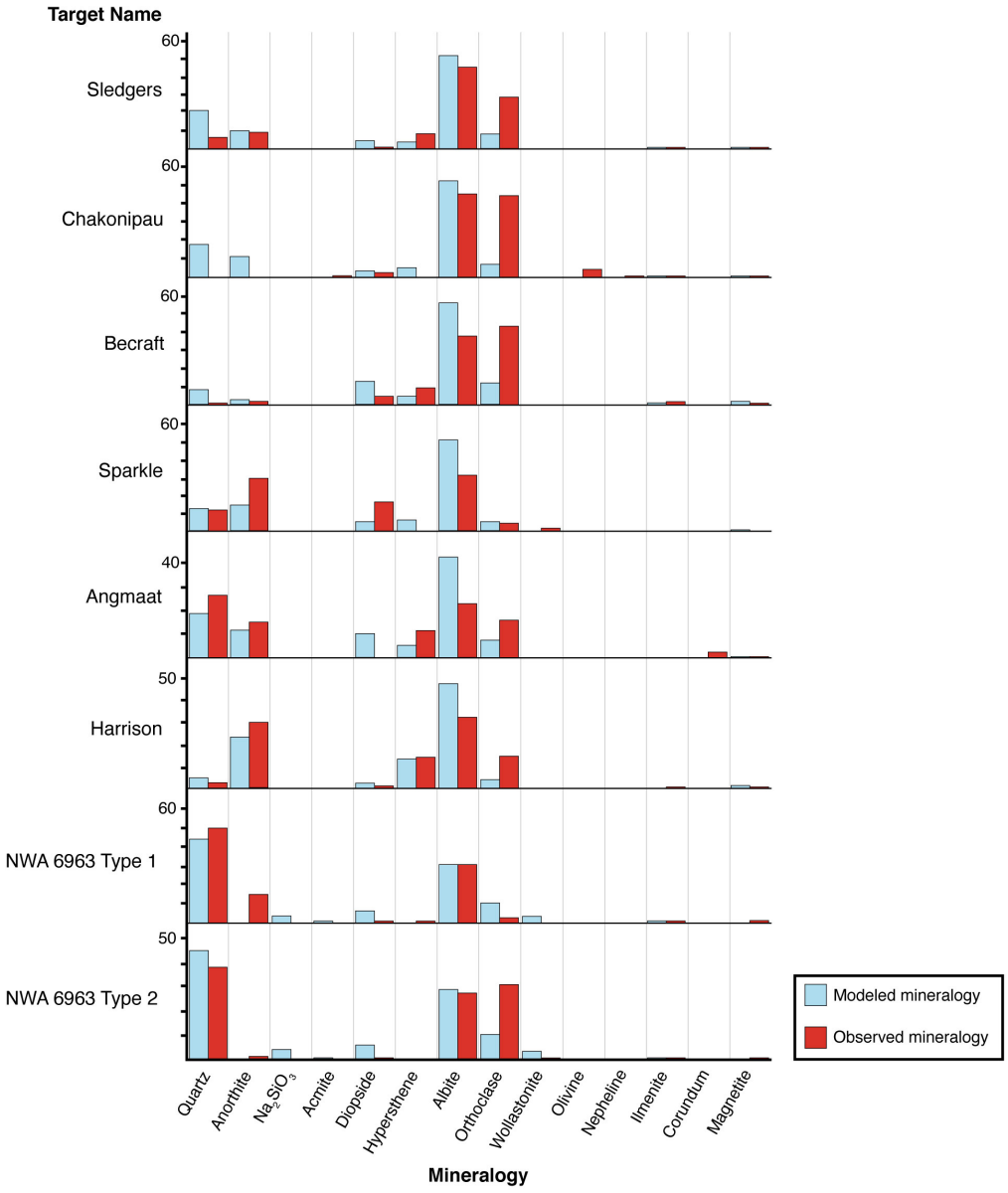

Figure A6: Modeled normative mineralogy (blue bars) against normative mineralogy for Gale crater and NWA 6963 granitic glass compositions (orange bars). Despite underpredicting orthoclase formation, the model replicated predicted phases in observed targets and samples.

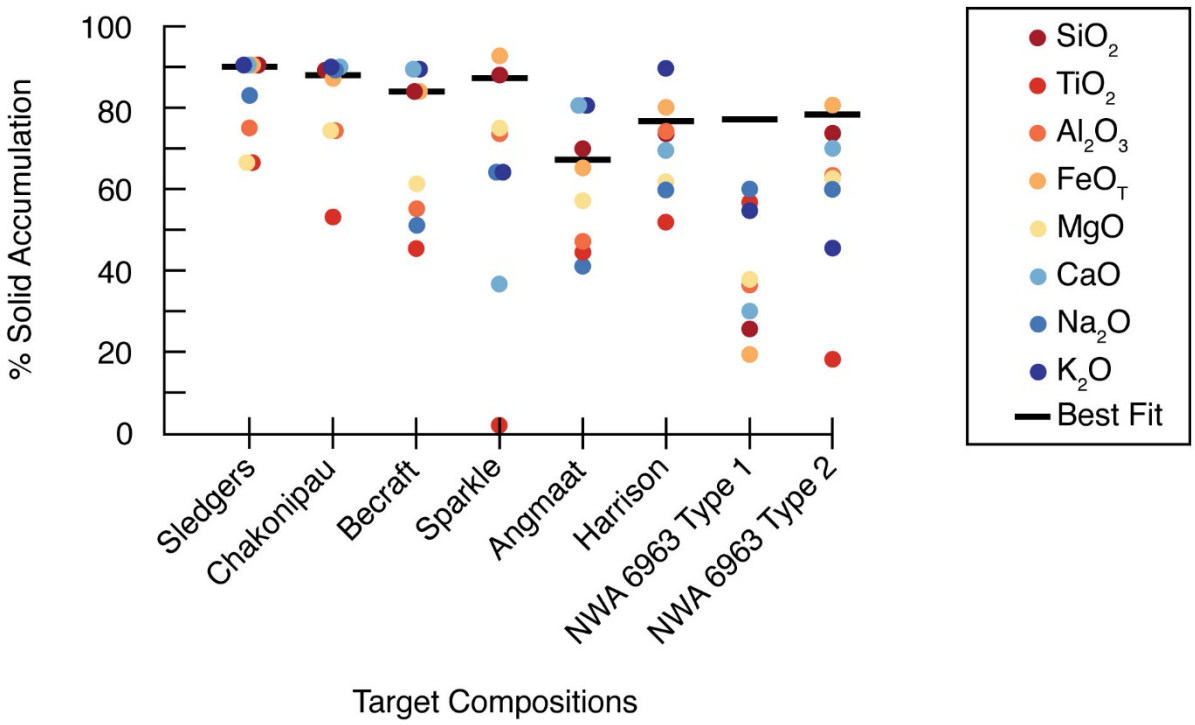

Figure S7: Crystallinity (percent solid accumulation) for averaged best fit models selected by RMS (black bars) and the overall minima for the difference between modeled and target oxides for each best fit model (dots). All data is arranged by target on the x-axis. Best fit model parameters by target are described in Table A3.

A7. References

Anenburg, M., and O'Neill, H.S.C., 2019, Redox in Magmas: Comment on a Recent Treatment of the Kaiserstuhl Volcanics (Braunger et al., Journal of Petrology, 59, 1731-1762, 2018) and Some Other Misconceptions: Journal of Petrology, v. 60, p. 1825–1832, doi:10.1093/petrology/egz046.

Ashcroft, H.O., and Wood, B.J., 2015, An experimental study of partial melting and fractional crystallization on the HED parent body: Meteoritics and Planetary Science, v. 50, p. 1912–1924, doi:10.1111/maps.12556.

Balta, B.J., and McSween, H.Y., 2013, Application of the MELTS algorithm to martian compositions and implications for magma crystallization: Journal of Geophysical Research E: Planets, v. 118, p. 2502–2519, doi:10.1002/2013JE004461.

Bohrson, W.A., Spera, F.J., Ghiorso, M.S., Brown, G.A., Creamer, J.B., and Mayfield, A., 2014, Thermodynamic model for energy-constrained open-system evolution of crustal magma bodies undergoing simultaneous recharge, assimilation and crystallization: The magma chamber simulator: Journal of Petrology, v. 55, p. 1685–1717, doi:10.1093/petrology/egu036.

Clegg, S.M. et al., 2017, Recalibration of the Mars Science Laboratory ChemCam instrument with an expanded geochemical database: Spectrochimica Acta - Part B Atomic Spectroscopy, v. 129, p. 64–85, doi:10.1016/j.sab.2016.12.003.

Filiberto, J., Dasgupta, R., Kiefer, W.S., and Treiman, A.H., 2010, High pressure, near-liquidus phase equilibria of the Home plate basalt Fastball and melting in the Martian mantle: Geophysical Research Letters, v. 37, p. 1–4, doi:10.1029/2010GL043999.

Ghiorso, M.S., and Gualda, G.A.R., 2015, An H2O–CO2 mixed fluid saturation model compatible with rhyolite-MELTS: Contributions to Mineralogy and Petrology, v. 169, p. 1–30, doi:10.1007/s00410-015-1141-8.

Ghiorso, M.S., Hirschmann, M.M., Reiners, P.W., and Kress, V.C., 2002, The pMELTS: A revision of MELTS for improved calculation of phase relations and major element partitioning related to partial melting of the mantle to 3 GPa: Geochemistry, Geophysics, Geosystems, v. 3, p. 1–35, doi:10.1029/2001gc000217.

Gualda, G.A.R., Ghiorso, M.S., Lemons, R. V., and Carley, T.L., 2012, Rhyolite-MELTS: A modified calibration of MELTS optimized for silica-rich, fluid-bearing magmatic systems: Journal of Petrology, v. 53, p. 875–890, doi:10.1093/petrology/egr080.

Herd, C.D.K., Borg, L.E., Jones, J.H., and Papike, J.J., 2002, Oxygen fugacity and geochemical variations in the martian basalts: Implications for martian basalt petrogenesis and the oxidation state of the upper mantle of Mars: Geochimica et Cosmochimica Acta, v. 66, p. 2025–2036, doi:10.1016/S0016-7037(02)00828-1.

Kress, V.C., and Carmichael, I.S.E., 1991, The compressibility of silicate liquids containing Fe2O3 and the effect of composition, temperature, oxygen fugacity and pressure on their redox states: Contributions to Mineralogy and Petrology, v. 108, p. 82–92, doi:10.1007/BF00307328.

McCubbin, F.M., Elardo, S.M., Shearer, C.K., Smirnov, A., Hauri, E.H., and Draper, D.S., 2013, A petrogenetic model for the comagmatic origin of chassignites and nakhlites: Inferences from chlorine-rich minerals, petrology, and geochemistry: Meteoritics and Planetary Science, v. 48, p. 819–853, doi:10.1111/maps.12095.

Udry, A., Balta, J.B., and McSween, H.Y., 2014, Exploring fractionation models for Martian magmas: Journal of Geophysical Research E: Planets, v. 119, p. 1–18, doi:10.1002/2013JE004445.

Udry, A., Howarth, G.H., Herd, C., Day, J., Lapen, T.J., and Filiberto, J., 2020, What martian meteorites reveal about the interior and surface of Mars: Earth and Space Science Open Archive, p. 55, https://doi.org/10.1002/essoar.10503123.2.

Appendix B

B1. Figures

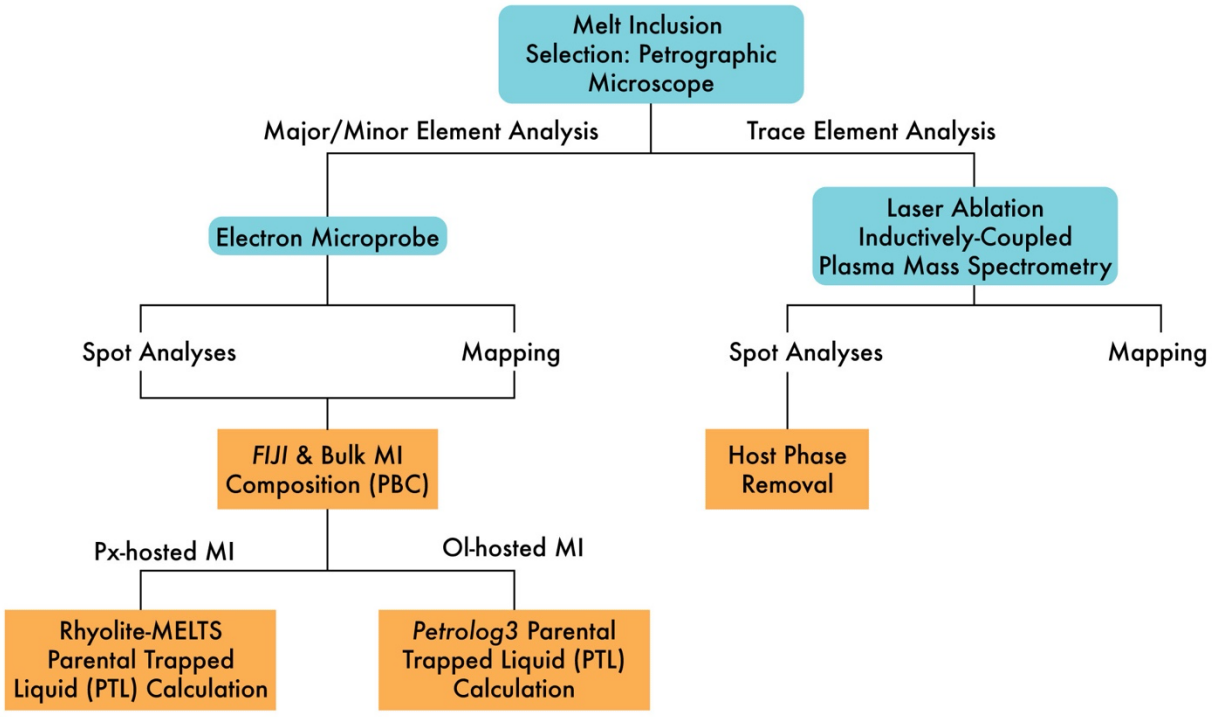

Figure B1: Methods flowchart describing steps to determining major, minor, and trace element abundances present in melt inclusions. Orange boxes indicate a step involving modeling or calculation. Blue rounded boxes indicate steps involving instrument analysis. Acronyms: MI = melt inclusion; PBC = present bulk composition, Px = pyroxene, Ol = olivine, PTL = parental trapped liquid.

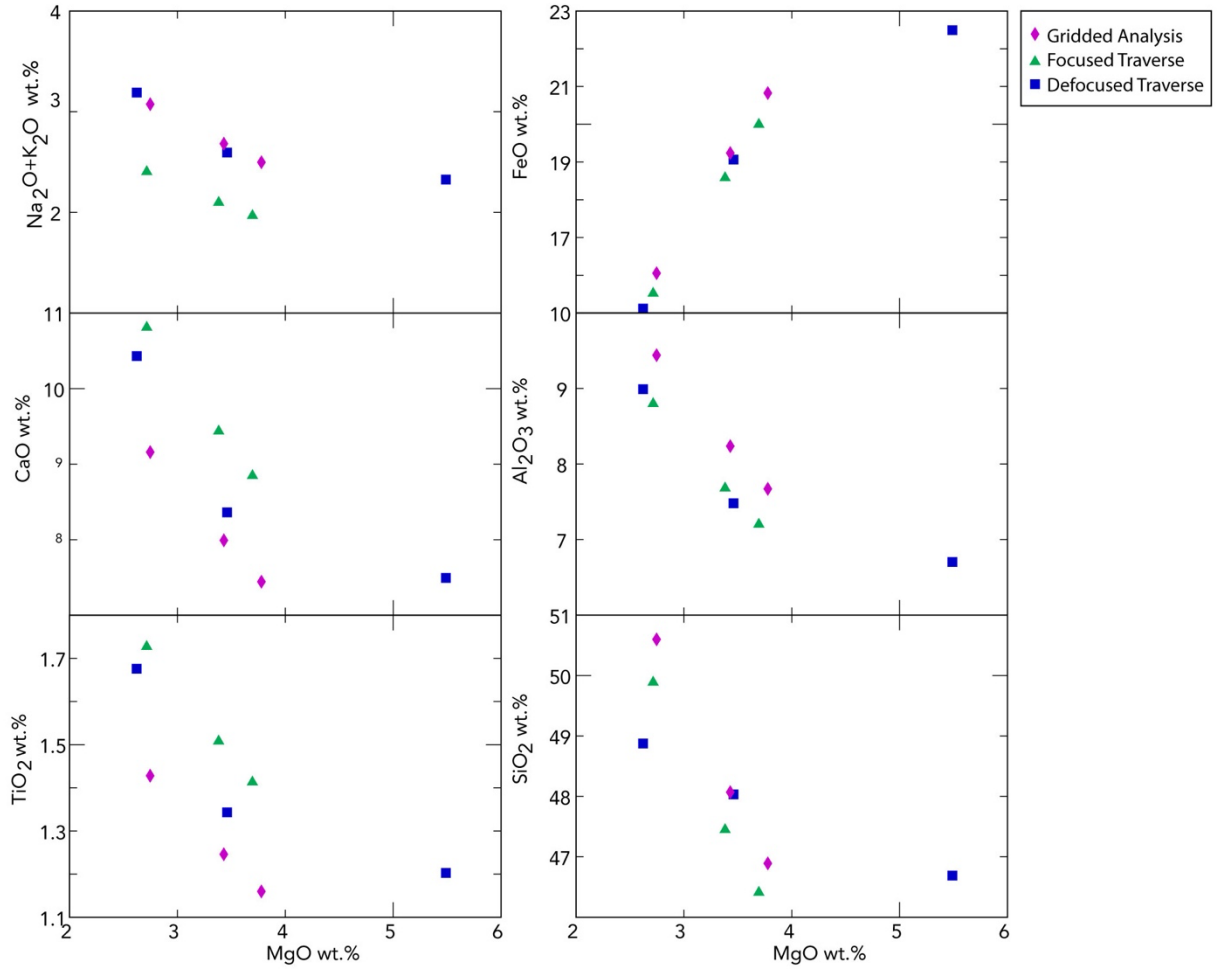

Figure B2: Comparison PTLs derived from different analytical techniques applied to melt inclusion analysis of olivine-hosted inclusion in nakhlite MIL 090030. Gridded analyses are conducted by averaging gridded points across an inclusion and averaged. The focused traverse was conducted with a 1 µm beam size and averaged. The defocused traverse was conducted with a 5 µm beam size and averaged. Each analysis is presented as three separate PTLs, each modeled with a high, middling, and low FeO_T value. High value = 28.9 wt.% (Goodrich et al., 2013); mid-range value = 26.9 wt.% (Stockstill et al., 2005); low value = 22.2 wt.% (Imae and Ikeda, 2007). In all oxides, variability is greater between high and low FeOT-determined PTLs than between analytical techniques. Poorly constrained initial compositional conditions of melt inclusions create more uncertainty in PTLs than the uncertainties imparted by analyses.

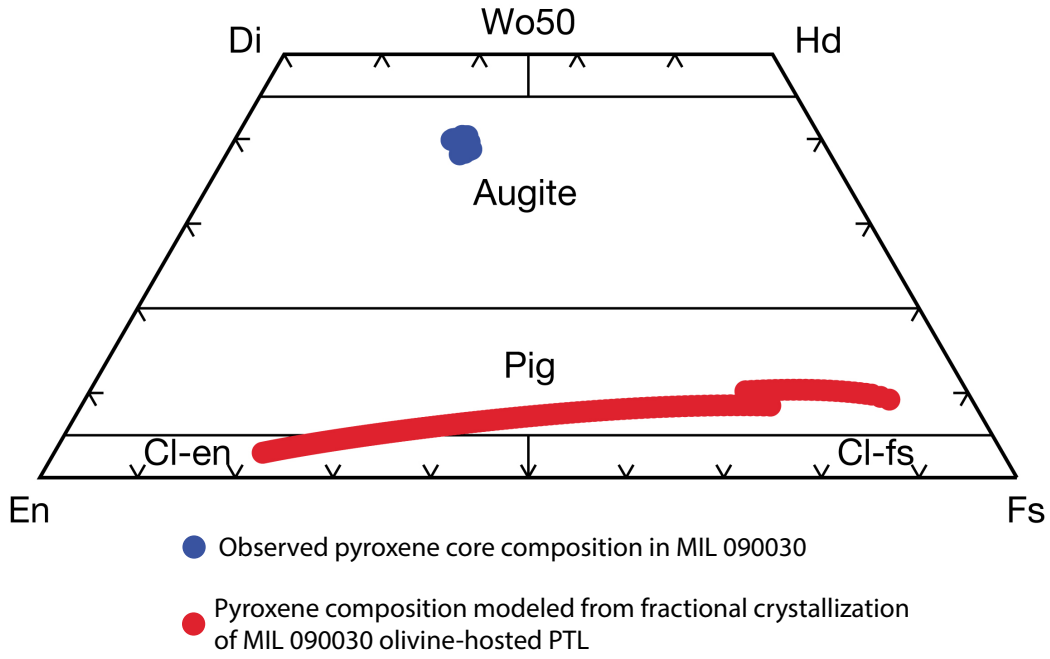

Figure B3: Pyroxene quadrilateral showing fractional crystallization results for a model conducted with an initial magma composition consisting of a nakhlite olivine-hosted melt inclusion in MIL 090030. The modeled results are for a pyroxene composition, plotted in red, against a measured MIL 090030 pyroxene core (EMPA results). The model does not approach the measured composition, as it forms only one pyroxene population that remains too calcium-depleted throughout the model. Thus, nakhlite olivine-hosted melt inclusion PTLs and pyroxene-hosted PTLs are petrogenetically distinct, if the PTL calculations are representative of the parental magma composition.

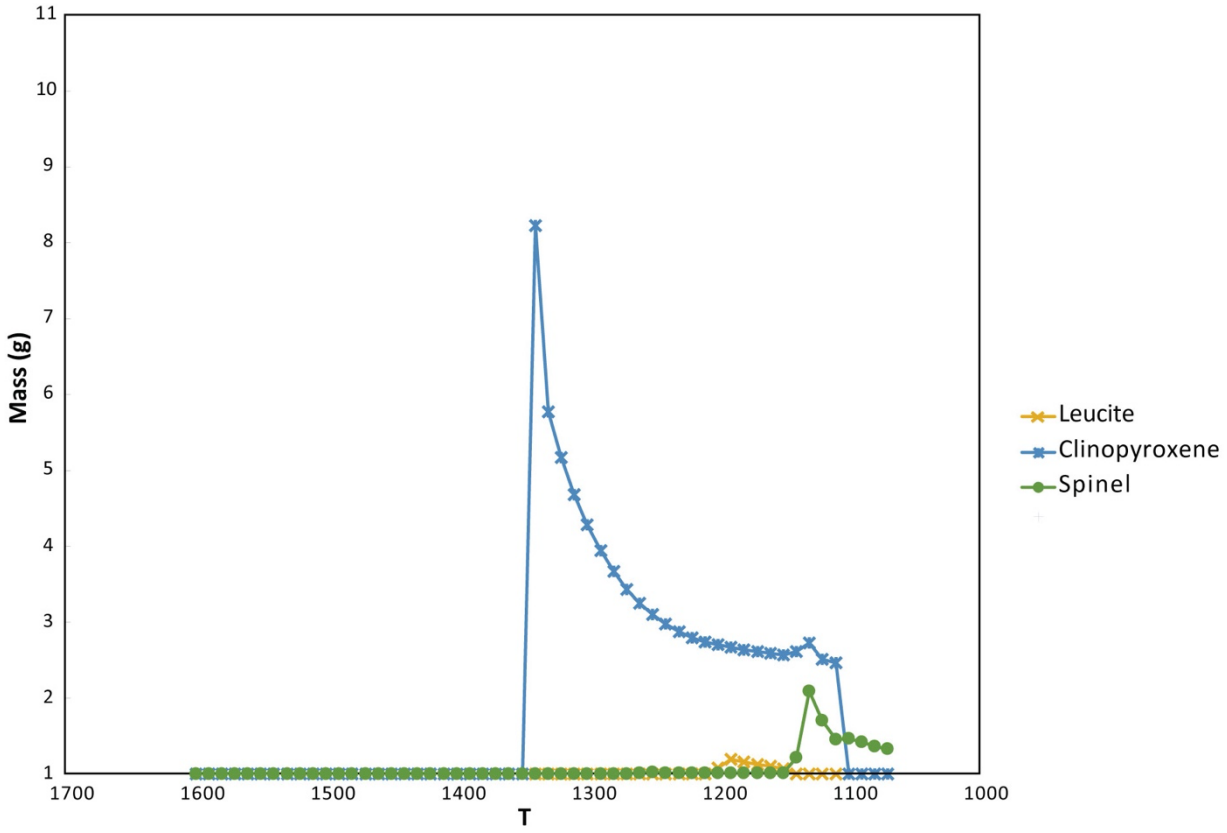

Figure B4: Solid cumulate mass abundances (g) versus temperature (T) in a fractional crystallization model at 1kbar (fO_2 constrained at FMQ) of a pyroxene-hosted melt inclusion in nakhlite MIL 090030. Olivine is never an equilibrium phase, and it is therefore unlikely that olivine and pyroxene are generated from one parental magma if the PTLs are representative of parental magma compositions.

B3. References

Goodrich, C.A., Treiman, A.H., Filiberto, J., Gross, J., Jercinovic, M., 2013. K2O-rich trapped melt in olivine in the Nakhla meteorite: Implications for petrogenesis of nakhlites and evolution of the Martian mantle. Meteorit. Planet. Sci. 48, 2371–2405. https://doi.org/10.1111/maps.12226

Imae, N., Ikeda, Y., 2007. Petrology of the Miller Range 03346 nakhlite in comparison with the Yamato-000593 nakhlite, Meteoritics & Planetary Science.

Stockstill, K.R., McSween, H.Y., Bodnar, R.J., 2005. Melt inclusions in augite of the Nakhla martian meteorite: Evidence for basaltic parental melt, Meteoritics & Planetary Science.

Appendix C

C1. Figures

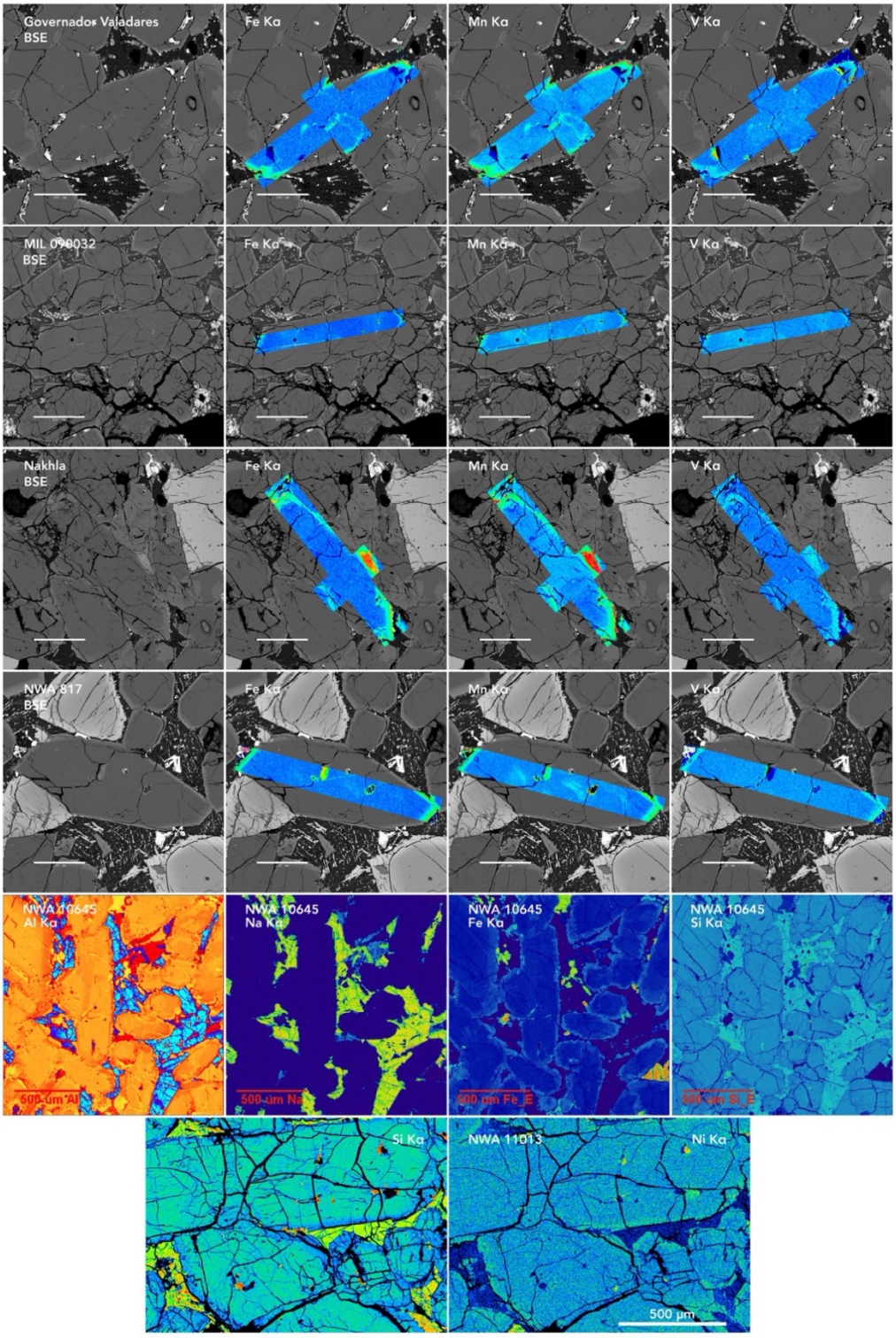

Figure C1: Characteristic Kα X-Ray maps of pyroxene in nakhlite samples. From top to bottom, samples Governador Valadares, Miller Range (MIL) 090032, Nakhla, Northwest Africa (NWA) 817, NWA 10645, and NWA 11013.

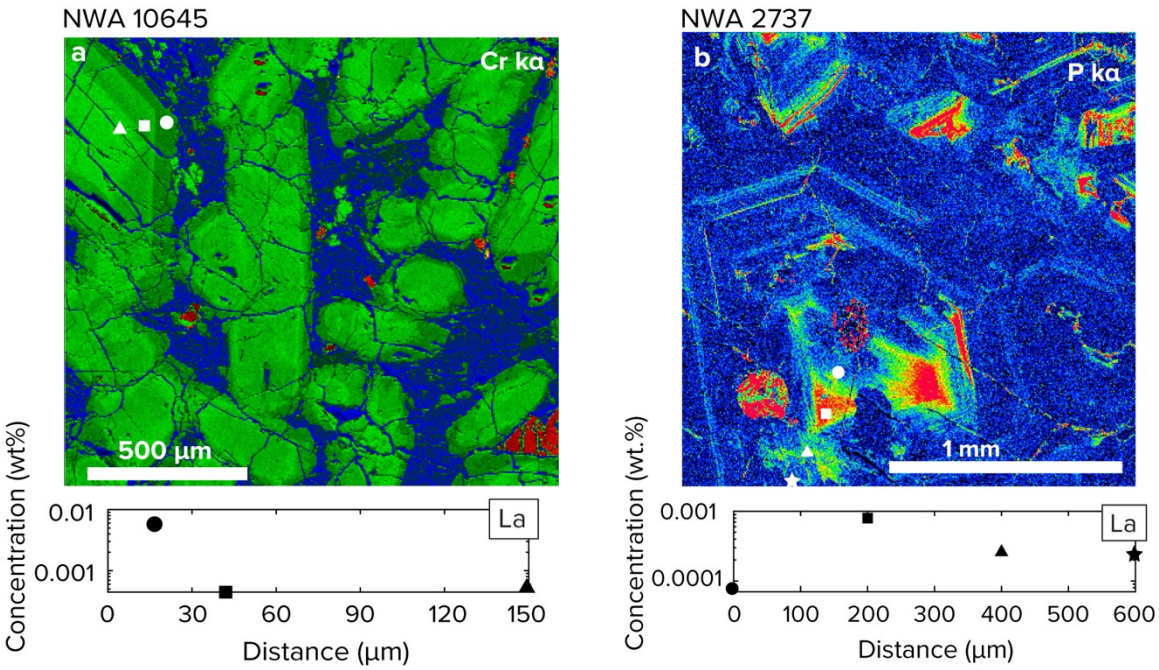

Figure C2: Trace element compositions measured in nakhlite pyroxene in NWA 10645 (a) and chassignite olivine NWA 2737 (b). Compositional X-Ray maps with points for reference above. Lanthanum (La) abundances plotted against relative distances below. Data are processed using the trace element reduction scheme in iolite 4 (Paton et al., 2011).

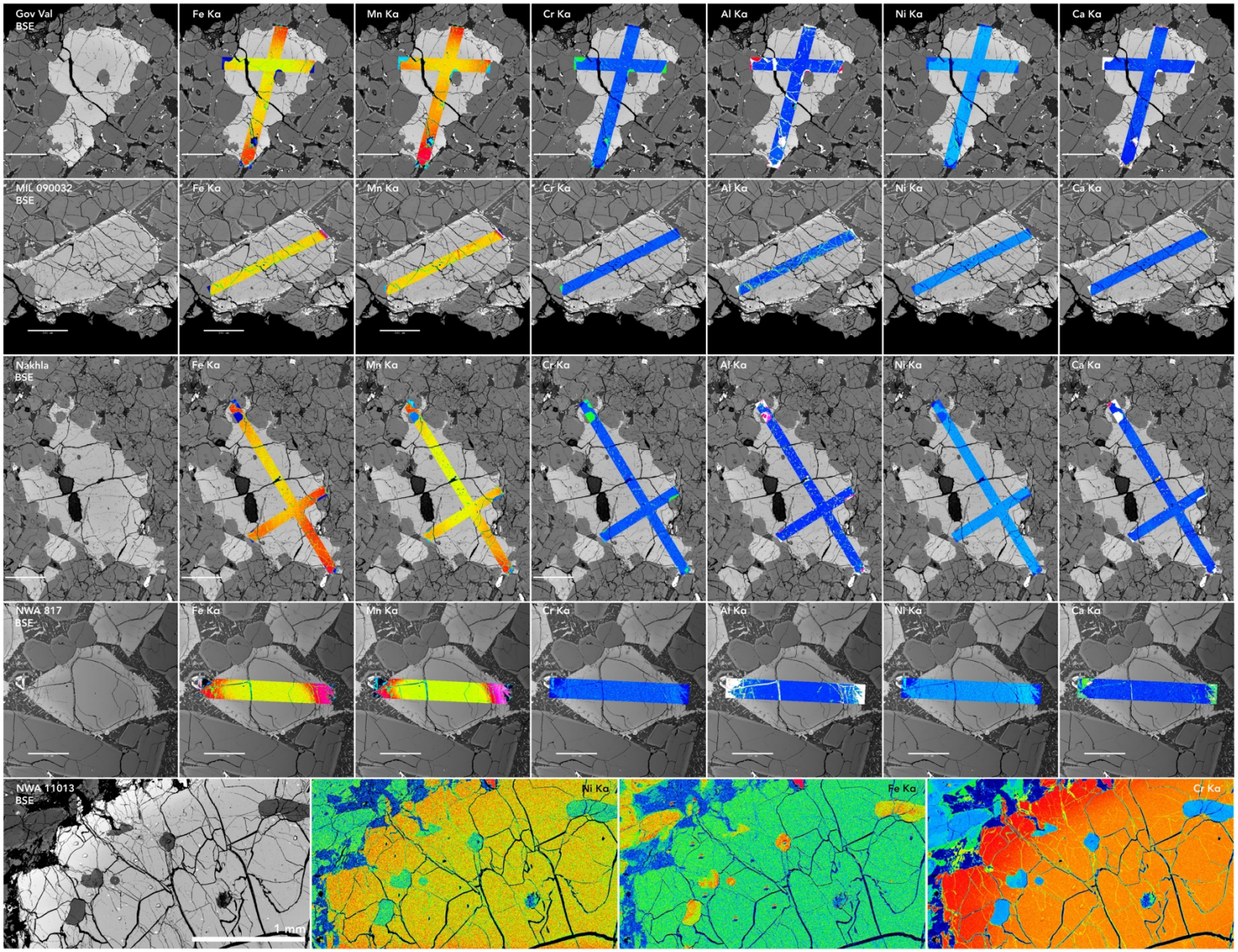

Figure C3: Characteristic Kα X-Ray maps of olivine in nakhlite samples. From top to bottom, samples Governador Valadares (Gov Val), MIL 090032, Nakhla, NWA 817, NWA 10645, and NWA 11013.

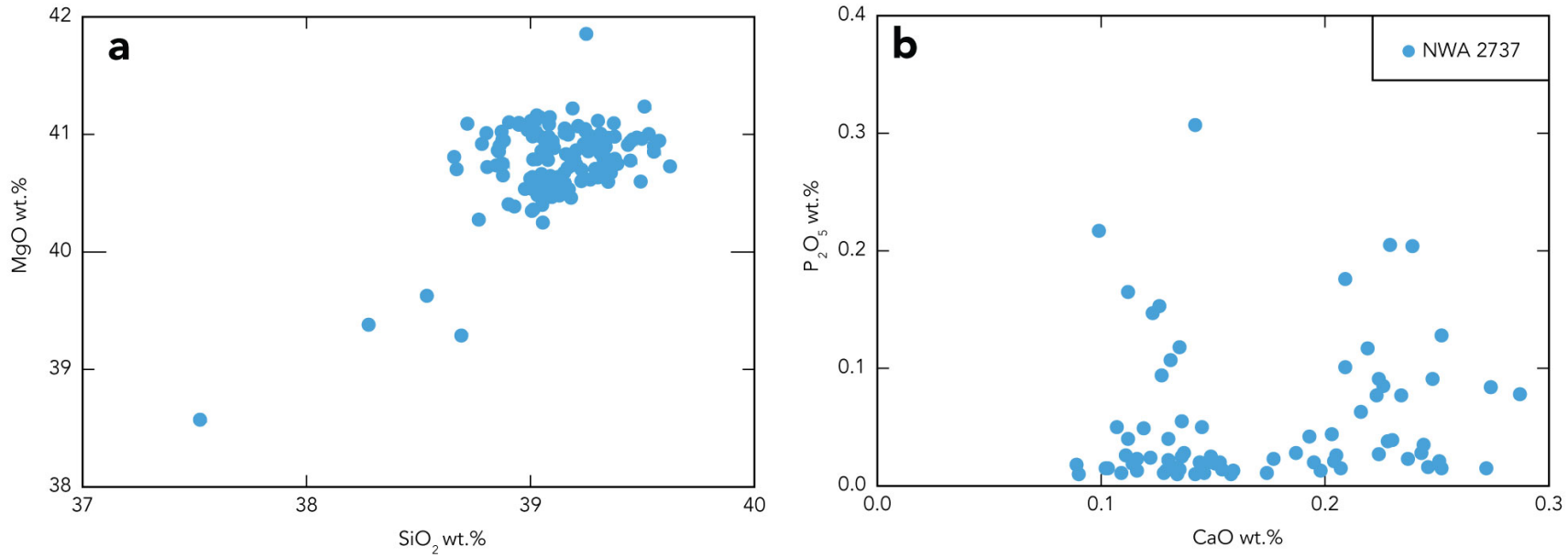

Figure C4: Quantitative traverse data for olivine in chassignite NWA 2737. There is a slight positive correlation between MgO and SiO_2, but no other observable relationships between oxides.

References

Paton, C., Hellstrom, J., Paul, B., Woodhead, J., and Hergt, J., 2011, Iolite: Freeware for the visualisation and processing of mass spectrometric data: Journal of Analytical Atomic Spectrometry, v. 26, p. 2508–2518, doi:10.1039/c1ja10172b.

Curriculum Vitae

Amanda Ostwald
Department of Geoscience
University of Nevada, Las Vegas
4505 S Maryland Pkwy, Las Vegas, NV 89154
amanda.m.ostwald@gmail.com

Education
- PhD. Student, Geological Sciences
  - University of Nevada, Las Vegas, 2018-present
  - Dissertation Topic: Magmatic processes leading to compositional diversity in the Mars crust
  - Advised by Dr. Arya Udry
- B.S. Geological Sciences
  - University of Texas at El Paso, 2014–2017
  - *Summa Cum Laude*

Research Interests
Planetary geology with a focus on igneous petrology and martian meteorites.

Research and Professional Experience
- Mars 2020 (Perseverance) mission student collaborator (Spring 2022–current)
- Research Assistant (UNLV, Fall 2019–current)
  - Performed thermodynamic modeling of martian magmatic systems.
    - Project title: "The role of assimilation and fractional crystallization in the evolution of the Mars crust"
  - Analyzed martian meteorite samples using electron microprobe analysis and laser-ablation inductively coupled plasma mass spectrometry.
    - Project title: "The parental melts of the nakhlite and chassignite Mars meteorites"
- Teaching Assistant (UNLV, Fall 2018–Spring 2019)
  - Taught lab portion of online introductory course: GEOL 104.
  - Taught lab portion of Igneous and Metamorphic Petrology: GEOL 327.
- Mars Research Scientist (Jacobs, February 2018–August 2018)
  - Conducted research in alteration products of Mars-like basalts in open and closed hydrologic systems.
  - Analyzed synthesized samples using X-ray diffraction.
- Mars Research Intern (Jacobs/UTEP, Fall 2017)
  - Prepared and analyzed sample standards using X-ray diffraction for full-pattern quantitative analysis library.
  - Conducted mineralogical alteration experiments in simulated Mars environments using both column and batch methods.

- Undergraduate Student Researcher for Doctor Diane Doser, "University of Texas at El Paso: Research Experience for Community College Students" (REU, Spring and Summer 2017)
  - Conducted field and laboratory research on El Paso Oligocene intrusive bodies with petrological, structural, and geophysical analysis.
  - Taught field methods, mapping, and structural geology to two-year community college students.
- Research Assistant for Doctor Jose Hurtado (UTEP, Fall 2016–Summer 2017)
  - Constructed 3D models using structure-from-motion photogrammetry and image sets from the Mars Science Laboratory (Curiosity).
- Research Assistant for Doctor Tom Gill (UTEP, Fall 2015–Spring 2016)
  - Prepared and processed sediment samples using laser grain-size analysis.

Peer-reviewed Publications

Beyssac, O., Forni, O., Cousin, A., Udry, A., Kah, L. C., Mandon, L., Clavé, E., Liu, Y., Poulet, F., Quantin Nataf, C., Gasnault, O., Johnson, J., Benzerara, K., Beck, P. Dehouck, E., Mangold, N., Alvarez Llamas, C., Anderson, R., Arana, G., Barnes, R., Bernard, S., Bosak, T., Brown, A.J., Castro, K., Chide, B**.,** Clegg, S., Cloutis, E., Fouchet, T., Gabriel, T., Gupta, S., Lacombe, G., Lasue, J., Le Mouelic, S., Lopez-Reyes, G., Madariaga, J.M., McCubbin, F.M., McLennan, S., Manrique, J.A., Meslin, P.Y., Montmessin, F., Núñez, J., Ollila, A.M., **Ostwald, A.**, Pilleri, P., Pinet, P., Royer, C., Sharma, S.K., Schröder, S., Simon, J.I., Toplis, M.J., Veneranda, M., Willis, P.A., Maurice, S., Wiens, R.C., The SuperCam Team (2023), Petrological traverse of the olivine cumulate Séítah formation at Jezero crater, Mars: A perspective from SuperCam onboard Perseverance. *Journal of Geophysical Research: Planets*, 128: e2022JE007638.

Ramsey S. R., **Ostwald A. M.**, Udry A., O'Neal E., Day J. M. D., Wilbur Z., Barnes J. J., Griffin S. (submitted), Northwest Africa 13669, a Reequilibrated Nakhlite from a Previously Unsampled Portion of the Nakhlite Igneous Complex. In review.

O'Neal, E. W., **Ostwald, A. M.**, Udry, A., Gross, J., Righter, M., Lapen, T. J., Darling, J., Howarth, G. H., Johnsen, R., McQuaig, D. R. (submitted), Source and parental melts of poikilitic shergottites: Implications for martian magmatism. In review.

Ostwald, A. M., Udry, A., Day, J. M. D., Gross, J. (2023), Melt inclusion heterogeneities in the nakhlite and chassignite martian meteorite suite and evidence for complicated, multi-generational magmas. In review.

Ralston, S. J., Peretyazhko, T. S., Sutter, B., Ming, D. W., Morris, R. V., Garcia, A., **Ostwald, A.** (2022), Phyllosilicate formation on early Mars via open-system acid alteration of basaltic glass. *Earth and Planetary Science Letters*. 10.10/j.epsl.2022.117987

Udry, A., **Ostwald, A. M.**, Sautter, V., Cousin, A., Beyssac, O., Forni, O., Dromart, G., Benserara, K., Nachon, M., Horgan, B., Mandon, L., Clavé, E., Dehouck, E., Gibbons, E., Alwmark, S., Ravanis, E., Wiens, R. C., Legett, C., Anderson, R., Pilleri, P., Mangold, N., Schmidt, M., Liu, Y., Nuñez, J. I., Castro, K., Madariaga, J. M., Kizovski, T., Beck, P., Bernard, S., Bosak, T., Brown, A., Clegg, S., Cloutis, E., Cohen, B., Connell, S., Crumpler, L., Debaille, V., Flannery, D., Fouchet, T., Gabriel, T. S. J., Gasnault, O., Herd, C. D. K., Johnson, J., Manrique, J. A., Maurice, S., McCubbin, F. M., McLennan, Ollila, A., Pinet, P., Quantin-Nataf, C., Royer, C., Sharma, S., Simon, J. I., Steele, A., Tosca, N., Treiman, A., and the SuperCam team (2022), A Mars 2020 Perseverance SuperCam perspective on the igneous nature of the Máaz formation

at Jezero crater and link with Séítah, Mars. *Journal of Geophysical Research: Planets*, 127: e2022JE007440. https://doi-org.ezproxy.library.unlv.edu/10.1029/2022JE007440

Ostwald, A.M., Udry, A., Payré, V., Gazel, E., Wu, P. (2021), The role of assimilation and fractional crystallization in the evolution of the Mars crust. *Earth and Planetary Science Letters*, 585: 117514. https://doi.org/10.1016/j.epsl.2022.117514

Wu, P., Gazel, E., Udry, A., Setera, J.B. and **Ostwald, A.M.** (2021), Melt inclusions in chassignite NWA 2737: A link between processes recorded in Martian meteorites and rocks at Gale crater. *Meteoritics and Planetary Science*, 56: 1328-1349. https://doi.org/10.1111/maps.13700

Published Reports

Hurtado, J.M, Young, K.E., **Ostwald, A.M.**, Ward, F.S., Henderson, M.J.B., Morse, Z.R. (2021), Lunar Surface Science Workshop (LSSW) Session VIII: Structuring Real-Time Science Support of Artemis Crewed Operations. https://lunarscience.arc.nasa.gov/lssw/downloads/LSSW-8-Report-April-2021.pdf

Conference Abstracts

Ostwald, A. M., Udry, A., Day, J. M. D., Gross, J., Griffin, S. (2023). *Complexly zoned crystals in the nakhlite and chassignite meteorites and implications for petrogenesis*. Talk presented at the Lunar and Planetary Science Conference, Houston, Texas. Abstract #1123.

Ramsey, S., **Ostwald, A.**, Udry, A., Day, J. M. D. (2023). *Parental melt composition of the Northwest Africa 13669 nakhlite from pyroxene and olivine-hosted melt inclusions*. Talk presented at the Lunar and Planetary Science Conference, Houston, Texas. Abstract #1030.

Ralston, S. J., Peretyazhko, T. S., Sutter, B., Ming, D. W., Morris, R. V., Garcia, A. H., **Ostwald, A. M.** (2023) *Phyllosilicate formation on early Mars via open-system acid alteration of basaltic glass*. Talk presented at the Lunar and Planetary Science Conference, Houston, Texas. Abstract #1496.

Ostwald A. M., Udry A., Day J. M. D., Gross J. (2022). *Chemical heterogeneities among melt compositions hosted in melt inclusions in nakhlites and chassignites.* Talk presented at the Meteoritical Society Meeting, Glasgow, Scotland. Abstract #6124.

Udry A., **Ostwald A. M.**, Sautter V., et al. (2022). *A comparison of the igneous Máaz formation at Jezero crater with martian meteorites.* Talk presented at the Meteoritical Society Meeting, Glasgow, Scotland. Abstract #6089.

O'Neal E. W., **Ostwald A. M.**, Udry A., Gross J., Righter M., Mcquaig D. R., Lapen T. J., Howarth G. H., and Johnsen R. (2022). *The evolution of poikilitic shergottite magmas from mantle to crust.* Talk presented at the Meteoritical Society Meeting, Glasgow, Scotland. Abstract #6178.

Ramsey S., Udry A., Day J. M. D., and **Ostwald A.** (2022). *Formation and emplacement of the Northwest Africa 13669 nakhlite.* Poster presented at the Meteoritical Society Meeting, Glasgow, Scotland. Abstract #6028.

Ostwald A. M., Udry A., Day J. M. D., and Gross J. (2022) *Complex zoning in the nakhlite and chassignite martian meteorites*. Poster presented at the Meteoritical Society Meeting, Glasgow, Scotland. Abstract #6125.

Ostwald, A.M., Udry, A., Gross, J., Day, J.M.D. (2022). *Chemical Heterogeneities Among Melt Inclusions in Nakhlites and Chassignites*. Poster presented at the Lunar and Planetary Science Conference, Houston, TX. Abstract #1206.

Ostwald, A.M., Udry, A., Gazel, E., Payré, V., Wu, P. (2022). *The Role of Assimilation and Fractional Crystallization in the Formation of the Mars Crust*. Poster presented at the Lunar and Planetary Science Conference, Houston, TX. Abstract #1203.

Ramsey, S., Udry A., J.M.D. Day, **Ostwald, A.M.** (2022). *Major and Trace Element Bulk Rock and Mineral Chemistry of Northwest Africa 13669, a New Nakhlite.* Poster presented at the Lunar and Planetary Science Conference, Houston, TX. Abstract # 1127.

O'Neal, E.W., **Ostwald, A.M.**, Udry, A., Gross, J., Righter, M. (2022) *Melt Inclusion, Trace Element, and Isotopic Analyses of a Poikilitic Shergottite Suite: Implications for Martian Magmatism*. Poster presented at the Lunar and Planetary Science Conference, Houston, TX. Abstract #2449.

Ostwald, A.M., Udry, A., Gross, J., Day, J.M.D. (2021). *Nakhlite and Chassignite Parental Melt Compositions Compared*. Talk presented at the Meteoritical Society Meeting, Chicago, IL. Abstract # 6209.

Ostwald, A.M., Henderson, M.J.B., Hurtado, J.M., Young, K.E., Morse, Z.R., Ward, F.S. (2021). *Results and Recommendations from Lunar Surface Science Workshop 8: Structuring Real-Time Support of Artemis Crewed Operations.* Poster presented at the NASA Exploration Science Forum & European Lunar Symposium virtual conference.

Ostwald, A.M., Udry, A., Gazel, E., Payré, V., Wu, P. (2021). *The Role of Assimilation and Fractional Crystallization in Evolved Martian Crustal Compositions*. Oral presentation given at the Lunar and Planetary Science Conference, virtual. Abstract #1132.

Ostwald, A.M., Udry, A., Gross, J., Day, J.M.D. (2021). *Parental Melts of Nakhlites and Chassignites Determined from Analysis of Melt Inclusions.* Poster presented at the Lunar and Planetary Science Conference, virtual. Abstract #1079.

Udry, A., **Ostwald, A. M.**, Howarth, G. H., Paquet, M., Forman, L. V., Day, J. M. D., and Taylor, A. (2021). *The Plagioclase-bearing Poikilitic Shergottite Northwest Africa 12241, a Not-So Shocked Martian Meteorite*. Oral presentation given at the Lunar and Planetary Science Conference, Houston, TX. Abstract #1033.

Udry, A., Howarth, G. H., Herd, C. D. K., Day, J. M. D., Lapen, T. J., Filiberto, J., and **Ostwald, A. M.** (2021). *What Have We Learned About the Interior and Surface of Mars from Martian Meteorites.* Poster presented at the Lunar and Planetary Science Conference, Houston, TX. Abstract #1046.

O'Neal, E. W., Udry, A., Howarth, G. H., Gross, J., and **Ostwald, A.M.** (2021). *Characterization of Poikilitic Shergottite Parental Melts and What They Can Tell Us About Martian Magmatism.* Poster presented at the Lunar and Planetary Science Conference, Houston, TX. #1065.

Ostwald, A.M., Udry, A., Gazel, E., Payré, V., Wu, P. (2020). *Assimilation-fractional crystallization modeling using known martian compositions*. Poster presented at the American Geophysical Union virtual meeting. Abstract P055-0012.

Ralston, S. J., Sutter, B., Ming, D. W., Garcia, A., **Ostwald, A.**, Peretyazhko, T. (2020). *Clay Mineral Formation on Early Mars via Open-System Acid Alteration of Basaltic Glass.* Poster presented at the American Geophysical Union virtual meeting. Abstract EP017-09.

O'Neal, E. W., Udry, A., Howarth, G. H., Gross, J., and **Ostwald, A.** (2020). *Constraining Martian Magmatism and Shergottite Formation through Melt Inclusion Analyses of a Poikilitic Shergottite Suite.* Poster presented at the Geological Society of America Conference, virtual.

Ostwald, A.M., Udry, A., Gazel, E., Payré, V. (2020). *Assimilation-fractional crystallization on Mars as a formation process for felsic rocks.* Accepted for oral presentation to Lunar and Planetary Science Conference, Houston, TX (canceled due to coronavirus pandemic).

Ostwald, A.M., Udry, A., Gross, J., Day, J.M.D. (2020). *Chassignite and nakhlite parental melts determined from melt inclusion analysis.* Accepted for poster presentation to Lunar and Planetary Science Conference, Houston, TX (canceled due to coronavirus pandemic).

O'Neal, E. W., Udry, A., Howarth, G. H., Gross, J., and **Ostwald, A.** (2020). *Source and Parental Melts of a Poikilitic Shergottite Suite: Implications for Martian Magmatism.* Accepted for poster presentation to Lunar and Planetary Science Conference, Houston, TX (canceled due to coronavirus pandemic).

Ostwald, A.M., Udry, A., Gross, J. (2019). *Melt inclusion analyses to constrain parental magma compositions of the nakhlite meteorites*. Talk presented at the Meteoritical Society Meeting, Sapporo, Japan. Abstract #6106.

Ostwald, A.M., Udry, A., Gross, J. (2019). *The parental melt of nakhlites as determined from melt inclusions.* Poster presented at the Lunar and Planetary Science Conference, Houston, TX. Abstract #1431.

Ostwald, A.M., Sutter, B., & Peretyazhko, T.S. (2018). *Open Hydrologic Assessment of Phyllosilicate Formation on Early Mars*. Poster presented at the Lunar and Planetary Science Conference, Houston, TX.

Ostwald, A.M., & Hurtado, J.M. (2017). *3D models from structure-from-motion photogrammetry using Mars Science Laboratory images: methods and implications*. Poster presented at the Lunar and Planetary Science Conference, Houston, TX.

Ostwald, A.M., et al. (2016). *Petrology of the proterozoic Castner marble, Franklin Mountains, West Texas, USA*. Poster presented at the UTEP Geoscience Colloquium, El Paso, TX.

Invited Seminars and Colloquia

- Center for Meteorite Studies, Arizona State University, Virtual talk, July 2020.
- School of Geographical and Earth Sciences, University of Glasgow, Virtual talk, July 2020.

Scientific Session Organization

- Lunar and Planetary Science Meeting "Petrology, Petrogenesis, and Geochemistry of Martian Meteorites, Crust, and Mantle" session moderator, March 7, 2022.
- Meteoritical Society Meeting "Mars" session co-chair, August 17, 2021.
- Lunar Surface Science Workshop, Breakout Discussion facilitator, "Guiding Principles and Exploration Strategies" session chair, February 24-25, 2021.

Technical Expertise

Instruments: Electron Microprobe Analyzer (EMPA), Laser-Ablation Inductively Coupled Plasma Mass Spectrometry (LA-ICP-MS), X-Ray Diffraction (XRD), Scanning Electron Microscopy (SEM), Petrographic Microscopy, Spectrophotometry.

Modeling and Mathematics: alphaMELTS, Magma Chamber Simulator, MATLAB, HTML, CSS.

Image and Design Software: Photoshop, Illustrator, Indesign, Dreamweaver, Igpet.

Remote Sensing Software: QGIS, Agisoft Photoscan Professional.

Grants and Awards (Total: $63,783.89)

- Graduate and Professional Student Association sponsorship. Summer 2023. $2000.
- Best Graduate Oral Presentation, UNLV Geosymposium. Spring 2023. $1000.

- Jack and Fay Ross Fellowship. Fall 2022–Spring 2023. $40,810.00.
- Graduate Academic Achievement Award, UNLV Geosymposium. Spring 2022. $1500.
- Best Oral Presentation, UNLV Geosymposium. Spring 2022. $1500.
- McKay Award for best talk at Meteoritical Society Conference 2021 held in Chicago in August, 2021. $1000.
- General Sciences Scholarship. Fall 2021. $1500.
- Barnada French Scholarship. University of Nevada, Las Vegas. Fall 2021. $1250.
- NASA Planetary Sciences Division Travel Grant. Meteoritical Society Conference, Summer 2021. $1500.
- Geosymposium Research Award: Robinson Mine. Spring 2021. $1500.
- Runner-up Best Oral Presentation, UNLV Geosymposium. Spring 2021.
- Growth, Inclusivity, Voice, and Excellence (GIVE) Award from UNLV Women's Council for work done with UNLV Chapter of Association for Women Geoscientists. Spring 2021.
- Runner-up Best Oral Presentation, Graduate & Professional Student Association Research Forum. Spring 2021. $250.
- Graduate & Professional Student Association Research Sponsorship. Fall 2020. $1123.89.
- Career Development Award from the Lunar and Planetary Institute. Lunar and Planetary Science Conference, Spring 2020. $1000 award contingent upon attendance to the conference that was canceled due to coronavirus pandemic.
- Graduate & Professional Student Association Research Sponsorship. Fall 2019. $1250.
- NASA Planetary Sciences Division Travel Grant. Meteoritical Society Conference, Summer 2019. $1800.
- Geosymposium Research Award: Jacobs. Spring 2019. $1000.
- Steven E. Dwornik Award: Graduate Student Poster Honorable Mention. Spring 2019.
- Bernada French Scholarship. University of Nevada, Las Vegas. Fall 2018. $1100.
- Outstanding Graduating Senior in Geology. University of Texas at El Paso. Winter 2017.
- Alpha Phi Omega. *Walter R. Roser Award*. University of Texas at El Paso. Spring 2017. $1200.
- El Paso Mineralogical Society. *Best Undergraduate Poster, Colloquium 2017.* University of Texas at El Paso. Spring 2017. $100.
- GEO Surveys, Inc. *W. P. Nash Scholarship*. University of Texas at El Paso. Spring 2014-Fall 2016. $1400 per semester (total: $8400).

Workshops and Short Courses

- **Hosted**: Modeling Open System Processes on the Magma Chamber Simulator, online, April 2021.
- Thermodynamic Modeling of Magmatic Processes with alphaMELTS 2: Online, December 2020.
- Melts, Glasses, and Magmas (MGM) Short Course: Online Edition, Ludwig Maximilian University of Munich, July 2020.
- Reservoir characterization and modeling short course, ExxonMobil, University of Arizona, September 2018.

Professional Memberships and Contributions

- Association of Women Geoscientists (member)
  - UNLV Chapter co-founder, president (Fall 2019-Spring 2021)
- Geological Society of America (member)
- Meteoritical Society (member)
- Served on multiple NASA funding review panels (Spring 2023)

Outreach and Science Communication

- Astronomy in the Park at Mt. Charleston with the Las Vegas Astronomical Society (June 2023): gave a 30-minute outdoor talk and answered questions for a general audience of ~200 attendees
- Astronomy in the Park at Lake Mead with the Las Vegas Astronomical Society (February 2023): gave a 15-minute outdoor talk and answered questions for a general audience of ~30 attendees
- Letters to a Pre-Scientist (Spring 2023): participated in a science pen pal program for K–12 students
- Astronomy in the Park at Mt. Charleston with the Las Vegas Astronomical Society (September 2022): gave a 30-minute outdoor talk and answered questions for a general audience of ~500 attendees.
- Astronomy in the Park at Mt. Charleston with the Las Vegas Astronomical Society (July 2022): gave a 30-minute outdoor talk and answered questions for a general audience of ~200 attendees.
- Las Vegas Astronomical Society Meeting (July 2022): gave a one-hour lecture for a general audience of ~30 attendees.
- GEAR UP ASPIRE (Summer 2021): developed and presented 8 hours of lecture material on planetary geology and geologic hazards for 9th grade students.
- Skype a Scientist (Fall 2020-Fall 2022): answered questions for five classes of 5th-6th grade children.
- Las Vegas Regional Science Fair judge (February 2020).
- Association of Women Geoscientists UNLV Chapter volunteer for Burkholder Middle School UNLV visit: taught middle school students about principles of water conservation and how to interpret topographic maps (February 2020).
- Invited speaker for Astronomy on Tap: Las Vegas (October 2019).
- Inclusion Rocks volunteer: taught middle school and high school students about planetary geology, meteorites, fluvial morphology, and topographic map interpretation (Fall 2018-Spring 2019).
- Rock identification for UNLV Department of Geoscience: identified rocks for department visitors (Fall 2018).
- We Are Girls Conference Speaker, Hogg Middle School, Houston (April 2018).
- Celebration of Our Mountains tour coordinator for Bishop's Cap (New Mexico) and Franklin Mountain State Park Tin Mine (Texas) tours (2016).